12-2010

Age and petrogenesis of the Roaring Mountain rhyolites, Yellowstone Volcanic Field, Wyoming

Kathleen Marie Wooton
University of Nevada, Las Vegas

AGE AND PETROGENESIS OF THE ROARING MOUNTAIN RHYOLITES, YELLOWSTONE VOLCANIC FIELD, WYOMING

by

Kathleen Marie Wooton

Bachelor of Science
The College of William & Mary
2005

A thesis submitted in partial fulfillment
of the requirements for the

Master of Science Degree in Geoscience
Department of Geoscience
College of Sciences

Graduate College
University of Nevada, Las Vegas
December 2010

UNLV
UNIVERSITY OF NEVADA LAS VEGAS

THE GRADUATE COLLEGE

We recommend the thesis prepared under our supervision by

Kathleen Marie Wooton

entitled

Age and Petrogenesis of the Roaring Mountain Rhyolites, Yellowstone Volcanic Field, Wyoming

be accepted in partial fulfillment of the requirements for the degree of

Master of Science in Geoscience

Terry L. Spell, Committee Chair

Eugene Smith, Committee Member

Michael L. Wells, Committee Member

Stephen H. Lepp, Graduate Faculty Representative

Ronald Smith, Ph. D., Vice President for Research and Graduate Studies
and Dean of the Graduate College

December 2010

ABSTRACT

Age and Petrogenesis of the Roaring Mountain Rhyolites, Yellowstone Volcanic Field, Wyoming

By

Kathleen Marie Wooton

Dr. Terry L. Spell, Examination Committee Chair
Associate Professor of Geology
University of Nevada, Las Vegas

Extracaldera rhyolites in the Norris-Mammoth Corridor of the Yellowstone Volcanic Field (YVF) appear to be unrelated to intracaldera volcanism, resulting instead from a new crustal magma source derived from northeastward propagation of the Yellowstone "melting anomaly." The youngest extracaldera rhyolite unit, the Roaring Mountain Member (RM), is chemically distinct from the previous extracaldera lavas, reverting to more primitive compositions.

This study suggests that the majority of the RM rhyolites erupted from the same large-scale silicic magma system. Based on geochemistry and $^{40}Ar/^{39}Ar$ geochronology, the Crystal Spring mingled rhyolite and Obsidian Cliff rhyolite erupted concurrently at 59.1 ± 2.0 ka. The mafic enclaves within the Crystal Spring mingled rhyolite are compositionally similar to the Swan Lake Flat basalts. Their presence confirms mafic magmatism persisted after the latest basalt eruptions at 209 ka. The residual Obsidian Cliff magma subsequently underwent fractional crystallization and erupted as the main flow of the Gibbon River rhyolites in 52.0 ± 8.5 ka. Two other flows within the Gibbon River rhyolites may have evolved as small, independent melts that erupted concurrently with the main Gibbon River flow. $^{238}U/^{230}Th$ zircon geochronology indicates magma residence times of up to 160 ka.

ACKNOWLEDGMENTS

This research was possible thanks to the Nevada Isotope Geochronology Laboratory, University of Nevada, Las Vegas, and the Department of Geoscience, University of Nevada, Las Vegas.

I would like to thank Terry Spell for, first, allowing me to work on this research, and second, for all the knowledge and insight he imparted with respect to volcanology, geochronology, and the Yellowstone Volcanic Field. I would also like to thank Terry for giving up a great deal of his time to provide me with extensive help and comments while writing this thesis. I would like to thank Kathy Zanetti for patiently teaching me the ins and outs of an Ar-geochronology lab, and for her friendship. I would like to thank the many interesting and knowledgeable professors at UNLV for expanding and enhancing my knowledge and understanding of geology. Of these professors, I would really like to thank Gene Smith for our many interesting classes, field trips, and conversations. Finally, I would especially like to thank my thesis committee members, Gene Smith, Michael Wells, and Stephen Lepp, for their patience and time.

TABLE OF CONTENTS

LIST OF TABLES

LIST OF FIGURES

CHAPTER 1

INTRODUCTION

After decades of research, the origin and evolution of large-scale silicic magma systems is still debated. Specifically, the ability of such systems to develop and maintain large magma reservoirs for more than 100 ka is uncertain. Early research on granites and rhyolites considered plutons and silicic magma systems as large, upper crustal, convecting magma bodies that are thermally sustained by mafic sills over millions of years (i.e. Hildreth, 1981; Lipman, 1984). More recently, the time frame of production and evolution, and the nature of the magma chambers from which large volume silicic magmas are erupted have been called into question. Isotopic dating of some large silicic lavas suggest magma systems are long-lived and can evolve relatively homogeneously over several 100 ka prior to eruption (Halliday *et al.*, 1989; Christensen and DePaolo, 1993; Christensen and Halliday, 1996). However, other studies indicate magma systems are developed rapidly and silicic magmas are erupted shortly after formation, with minimal or no interaction between temporally-related magmas (Bindeman *et al.*, 2001; Vazquez and Reid, 2002; Gibler, 2007). For example, geochemistry and geochronology from the Jemez Volcanic Field indicate the post-collapse rhyolite domes were generated separately, in small magma batches and were not maintained in a single large coherent system (Wolff and Gardner, 1995; Gibler, 2007). Even research on the products of a single eruption is conflicting. Rb/Sr ages suggest that the Long Valley caldera's Bishop Tuff magma was generated and maintained for over 300 ka (Halliday *et al.*, 1989; Christensen and DePaolo, 1993; Christensen and Halliday, 1996). However, zircon U/Pb ages do not support a long Bishop Tuff magma residence time. The U/Pb ages indicate

zircons grew less than 100 ka prior to the Bishop Tuff eruption (Simon and Reid, 2005). Zircons are typically the first phenocrysts to grow in a magma, suggesting either a very prolonged period lacking crystal growth or incorrect Rb/Sr ages (Reid and Coath, 2000; Simon and Reid, 2005).

The Yellowstone Volcanic Field, Wyoming (YVF, Figure 1.1), is one of three large-scale caldera-forming volcanic fields in the western United States, along with the Long Valley and Jemez Volcanic Fields (California and New Mexico, respectively). The YVF has been the site of three caldera collapse events over the last 2.2 Ma. Magma production in the crust beneath the YVF is driven by a melting anomaly in the mantle (Christiansen and Blank, 1972; Christiansen, 2001) and has repeatedly produced large volumes of silicic magma. Both basaltic and rhyolitic lava flows are present in the field. The last volcanic activity occurred at ~70 ka (Obradovich, 1992), but Yellowstone is currently the site of vigorous hydrothermal activity (Christiansen, 2001). Seismic low-velocity anomalies beneath the Norris-Mammoth Corridor north of the Yellowstone caldera, and beneath the Yellowstone caldera, suggest the presence of magma bodies in the crust beneath Yellowstone (Husen *et al.*, 2004).

Early work on the YVF (Figure 1.2) classified the young rhyolite flows and domes north of the Yellowstone caldera (Obsidian Creek, OC, and Roaring Mountain, RM, Members) as post-collapse, extracaldera rhyolites related to the third-cycle caldera eruptions at Yellowstone (Christiansen and Blank, 1972). Hildreth and others (1991), however, suggested that extracaldera rhyolites are distinct from the intracaldera rhyolites, and formed as small, independent crustal melt magma batches associated with basaltic magmatism north of the caldera. Recent work by Nastanski (2005) also indicated that

extracaldera rhyolites are chemically unrelated to the Yellowstone intracaldera rhyolites, but instead suggests most of the extracaldera rhyolites were erupted from a single, large-scale magma system. The presence of a young, distinct volcanic system north of the Yellowstone caldera suggests that the YVF may be in the initial stages of a fourth caldera cycle (Nastanski and Spell, 2004a; Spell *et al.*, 2004).

This study will focus on the geochemistry, timing of establishment, and evolution of the RM magma system to test the hypothesis that the extracaldera rhyolites were derived from a single, large-scale, long-lived magma system beneath the Norris-Mammoth Corridor (Spell *et al.*, 2004; Nastanski, 2005). The youngest basaltic eruption in the YVF is the Panther Creek volcano which erupted at 209 ka (Smith and Bennett, 2006). However, a recently discovered mafic-silicic mingled lava in the youngest RM flow (Nastanski, 2005), the Crystal Spring rhyolite (~80 ka, Obradovich, 1992), records the continued presence of younger mafic magmas beneath the Norris-Mammoth Corridor. Understanding the evolution of the most recent rhyolites in the Norris-Mammoth Corridor and determining possible causes of their eruption may provide better constraints on the cause, timing, and location of the next Yellowstone volcanic eruption.

This study will also add to the ongoing research into the cause and nature of large-scale silicic magmatism. U/Pb zircon ages argue for a residence time of less than 100 ka for the Lava Creek Tuff in Yellowstone (Bindeman *et al.*, 2001; Vazquez and Reid, 2002). However, U/Pb zircon ages from the post-Lava Creek Tuff extracaldera rhyolites indicate the OC & RM Member rhyolites evolved from a single coherent magma system that was active for up to 350 ka (Spell and Nastanski, 2004; Nastanski, 2005). This research contributes additional information to the large-scale silicic magma system

lifetime vs. thermal sustainability controversy by determining whether the RM rhyolites were derived from small independent magma batches, from a single, magma system with a short lifespan of <~100 ka, or from the same single long lived, large-scale magma system as the OC rhyolites.

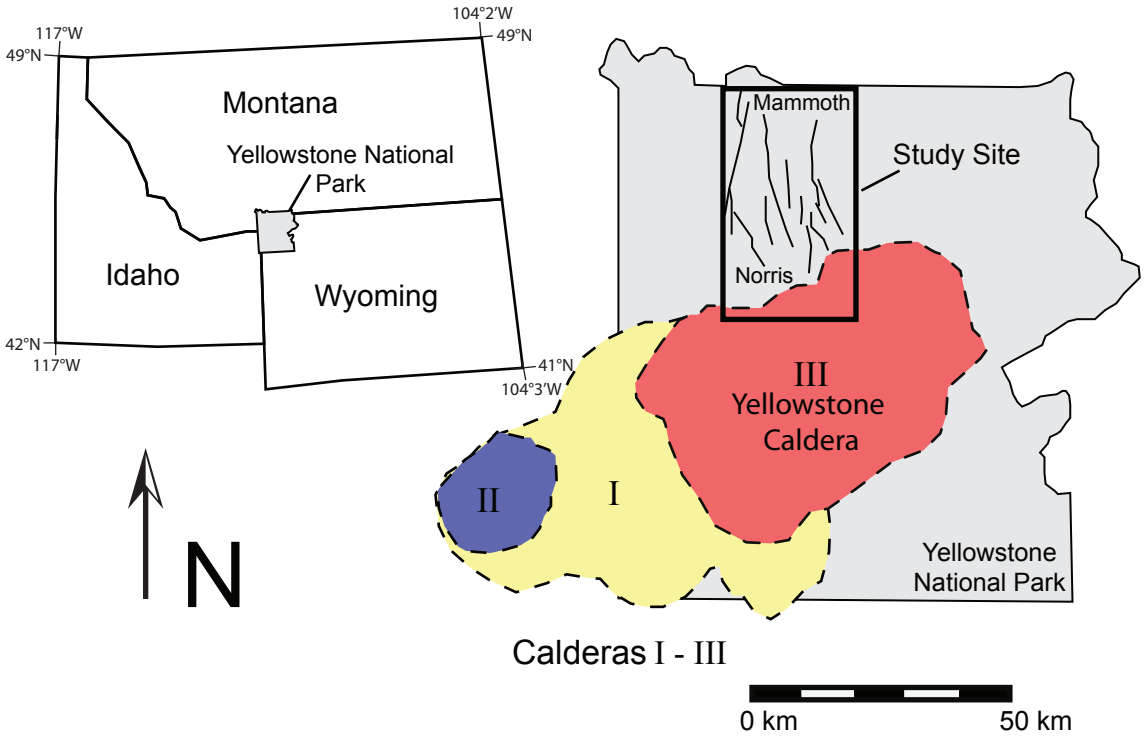

Figure 1.1. Map showing the three calderas of the Yellowstone Volcanic Field. The third caldera is the Yellowstone caldera. The boxed area north of the Yellowstone caldera is the Norris-Mammoth Corridor where the extracaldera rhyolites were erupted. Modified from Christiansen (2001).

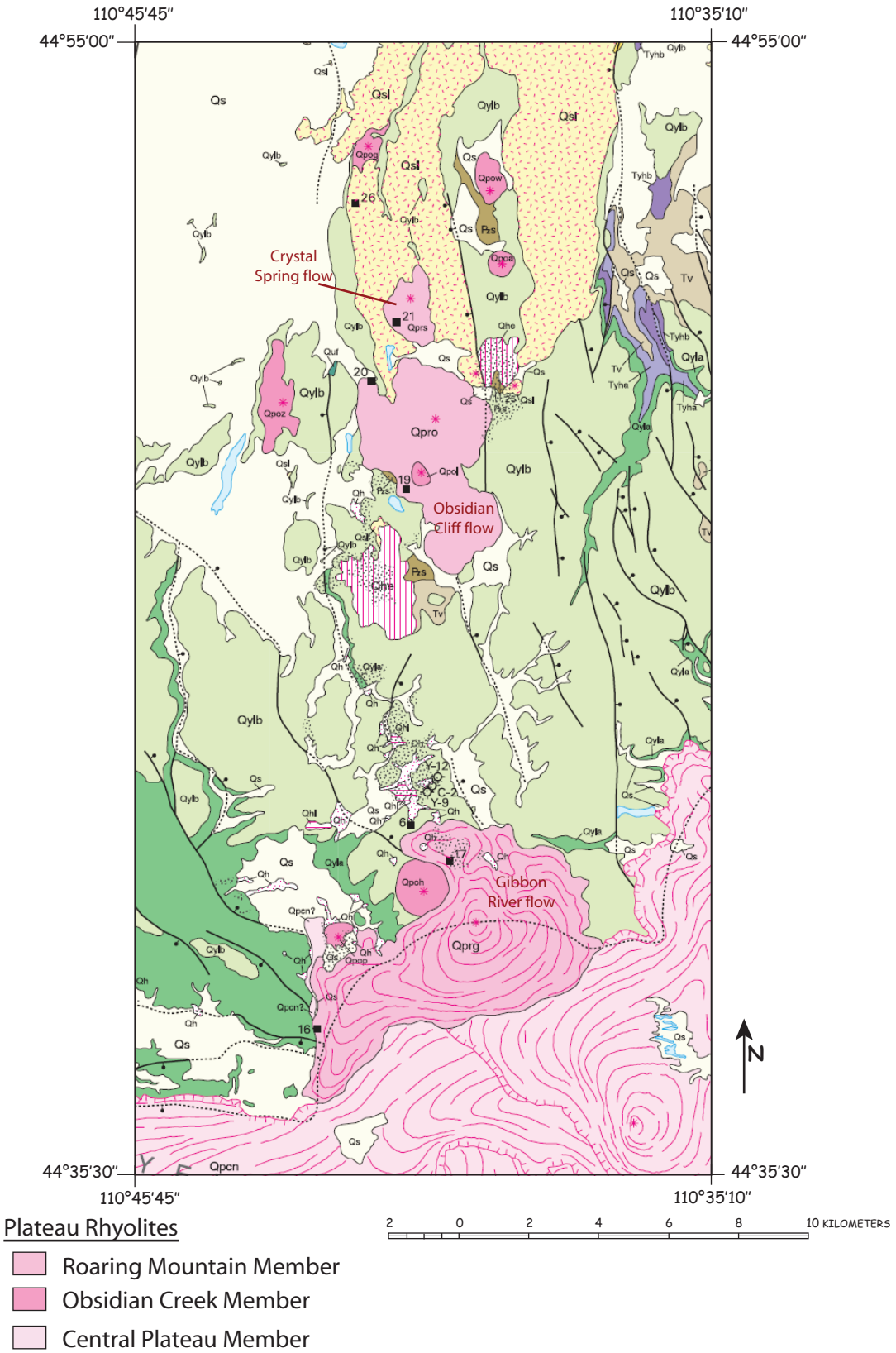

Figure 1.2. Geologic map of Norris-Mammoth Corridor in the Yellowstone Volcanic Field. The three rhyolite flows of this study are labeled. Map from Christiansen (2001).

CHAPTER 2

GEOLOGIC BACKGROUND

The Yellowstone Volcanic Field (YVF) is a large-scale, bimodal continental volcanic field located at the northeastern end of a propagating 16.6 Ma "hotspot" track (Hooper *et al.*, 2002). This track originates at the Columbia River flood basalts and defines the over 500 km long Snake River Plain, before terminating at the YVF (Armstrong *et al.*, 1975). Although originally considered a classic continental mantle plume hotspot (Morgan, 1972; Lowry *et al.*, 2000), some investigators suggest an origin as a melting "anomaly" based on Yellowstone volcanism characteristics and geophysical observations that are inconsistent with plume models (Christiansen, 2001; Christiansen *et al.*, 2002). However, there is still debate regarding the origin of the Yellowstone "hotspot" (Pierce and Morgan, 2009; Smith *et al.*, 2009).

The YVF is located within an area of Archean gneissic granitoids (2.8 Ga high-grade metasedimentary and metavolcanic rocks) that are exposed in the Teton Mountain Range to the south and the Beartooth Mountains to the northeast (Hildreth *et al.*, 1991). These Archean granitoids are overlain by Cambrian to Cretaceous marine sedimentary rocks, exposed to the north and south of the YVF, and by Eocene andesites of the Absaroka Mountain Range, east of the YVF (Hildreth *et al.*, 1991). Precambrian mafic dike swarms also intrude the region (Hildreth *et al.*, 1991). In the Yellowstone area, the maximum thickness of the Phanerozoic marine sediments is ~2.5 km and the Absaroka volcanic rocks are up to ~1.5 km thick (Hildreth *et al.*, 1991). Since current modeling indicates a top depth of 8 km for the active magma system beneath the Yellowstone Caldera (Husen *et al.*, 2004), any magma reservoir beneath the Yellowstone Caldera

would likely be located in Archean gneissic granitoid basement (Hildreth *et al.*, 1991). However, a magma system northwest of the Yellowstone Caldera could be located at a much shallower depth (>2 km) and within shallower country rock (Husen *et al*., 2004).

The YVF is characterized by three caldera collapse events over the last 2.2 Ma (Figure 1.1) (Christiansen and Blank, 1972; Obradovich, 1992; Christiansen, 2001). The oldest volcanic rocks in the Yellowstone area are the 2.2-2.1 Ma Junction Butte basalt and the Rhyolite of Snake River Butte (Figure 2.1) (Christiansen, 2001). At 2.06 Ma the Huckleberry Ridge Tuff erupted forming a 2,500 km^3 ash-flow tuff that covered 17,000 km^2 (Hildreth *et al*., 1984; Lanphere *et al*., 2002) and resulted in the first caldera collapse event, forming a caldera with dimensions of 75 km by 95 km (I, Figure 1.1) (Christiansen, 2001). Volcanism continued after caldera collapse with the Big Bend Ridge postcaldera rhyolite flows, erupted between 1.8 and 1.3 Ma (Christiansen, 2001). Following the eruption of the 280 km^3 Mesa Falls Tuff at 1.29 Ma, a second caldera collapse occurred, this time creating the small 16 km diameter Henry's Fork caldera (II, Figure 1.1) in the western YVF (Hildreth *et al*., 1984; Christiansen, 2001; Lanphere *et al*., 2002). Postcollapse volcanism continued with the 1.3 to 1.2 Ma Island Park rhyolites, erupted concurrently with continued regional basaltic volcanism (Christiansen, 2001). Between 1.2 and 0.61 Ma, the Mount Jackson rhyolite erupted from fissures in the area of the youngest YVF caldera (Christiansen, 2001). With the eruption of the 1,000 km^3 Lava Creek Tuff at 639 ka, the Yellowstone caldera collapse event occurred, forming an elliptical, 85 km by 45 km compound caldera (III, Figure 1.1) (Hildreth *et al*., 1984; Christiansen, 2001; Lanphere *et al.*, 2002).

Post-Lava Creek eruptions produced two resurgent rhyolite domes and several other rhyolite flows within the caldera as early as 516 ka, infilling the caldera with the Plateau Rhyolite (Figure 2.1) until ~70 ka (Obradovich, 1992; Christiansen, 2001). The Riverside and Cougar Creek extracaldera rhyolites (classified as part of the Roaring Mountain Member) erupted at 526 ka and 356 ka, respectively, northwest of the Yellowstone caldera (Christiansen and Blank, 1972; Christiansen, 2001; Nastanski, 2005). The Obsidian Creek extracaldera rhyolites (Figure 1.2) erupted north of the Yellowstone caldera from 326 ka until 134 ka, with an apparent lull in volcanism before the 134 ka eruption (Spell and Nastanski, 2004; Nastanski, 2005). Basaltic volcanism north of the Yellowstone Caldera ceased at 209 ka with the eruption of the Swan Lake Flat basalts (Nastanski and Spell, 2004b; Bennett, 2006; Smith and Bennett, 2006). The Roaring Mountain extracaldera rhyolites (Figure 1.2), Gibbon River, Obsidian Cliff, and Crystal Spring flows, erupted from 118 ka to 80 ka along the Norris-Mammoth Corridor (Obradovich, 1992; Nastanski, 2005).

Currently, the YVF is the site of vigorous hydrothermal activity, exhibiting hundreds of geysers, hot springs, mud pots, and fumaroles. The hydrothermal sites are focused around Yellowstone Lake, within the Yellowstone caldera, and in the Norris-Mammoth Corridor – most notably at Norris Geyser Basin and Mammoth Hot Springs (Kharaka *et al.*, 2000; Christiansen *et al.*, 2007). The chemical composition of the gases (dominantly CO_2) discharged at these sites indicate a mantle-derived magmatic source for the hydrothermal heat (Kharaka *et al.*, 2000).

Though the ash-flow tuffs have a low permeability, numerous faults and fractures (Figure 2.2) allow for the water circulation vital in sustaining the hydrothermal features

(Jaworowski *et al.*, 2006). The YVF is characterized by numerous small ($M \leq 3$) earthquakes each year, but historically has had several large earthquakes. The largest historical earthquake, the Hebgen Lake earthquake ($M = 7.5$) in 1959, caused as much as 6 m of offset along faults (Christiansen *et al.*, 2007). The last large earthquake ($M = 6.1$) was located within the Norris Geyser Basin in 1975 (Christiansen *et al.*, 2007).

In the 1970s, it was recognized that the YVF was exhibiting continuous crustal uplift across the area of the Yellowstone caldera (Christiansen *et al.*, 2007). In 1986, uplift changed to subsidence in the caldera region (Christiansen *et al.*, 2007) and in the 1990s, a complex period of crustal deformation, interpreted as magma movement beneath the region, began in the area of the Norris-Mammoth Corridor and the north rim of the Yellowstone caldera (Figure 2.3) (Wicks *et al.*, 2006). Since 2002, the dynamic deformation of the YVF has halted and stabilized (Wicks *et al.*, 2006).

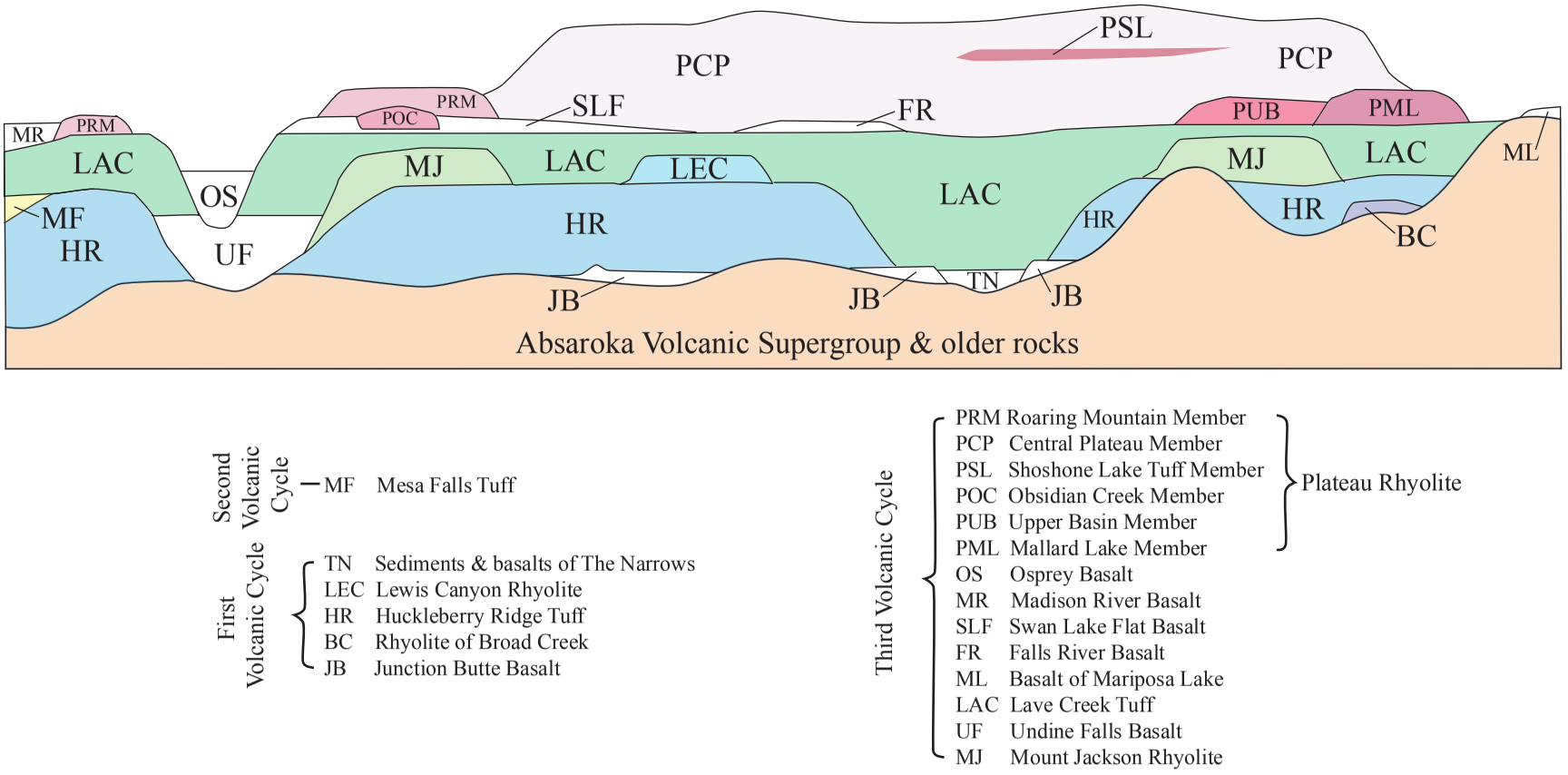

Figure 2.1. Generalized stratigraphic cross-section of the Yellowstone Volcanic Field. Modified from Christiansen and Blank (1972).

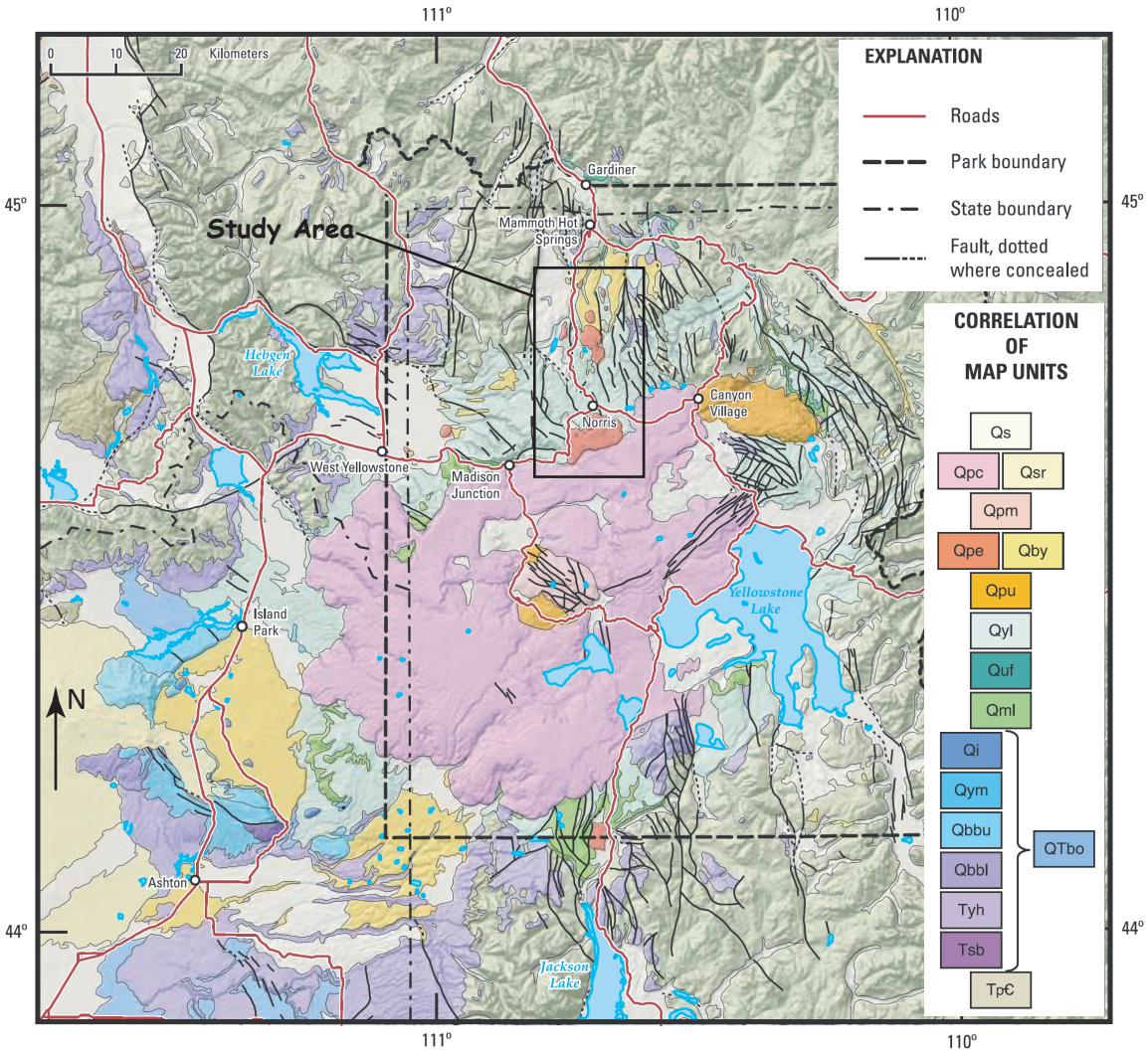

Figure 2.2. Geologic map of Yellowstone Volcanic Field showing major faults. Geologic units are: Qs, surficial deposits; Qpc, Central Plateau Member of Plateau Rhyolites; Qsr, Snake River Group basalts; Qpm, Mallard Lake Member of Plateau Rhyolites; Qpe, extracaldera rhyolites; Qby, young extracaldera basalts; Opu, Upper Basin Member of Plateau Rhyolites; Qyl, Lava Creek Tuff; Quf, Undine Falls Basalt; Qml, Mount Jackson and Lewis Canyon Rhyolites; Qi, Island Park Rhyolite; Qym, Mesa Falls Tuff; Qbbu, upper lavas of Big Ridge Rhyolite; Qbbl, lower lavas of Big Bend Ridge Rhyolite; Tyh, Huckleberry Ridge Tuff; Tsb, Snake River Butte rhyolite; QTbo, older basalts; TpC, rocks predating the Yellowstone Volcanic Field. Modified after Christiansen *et al.*, 2007, with geology from Christiansen (2001). Details of study area shown in Figure 1.2.

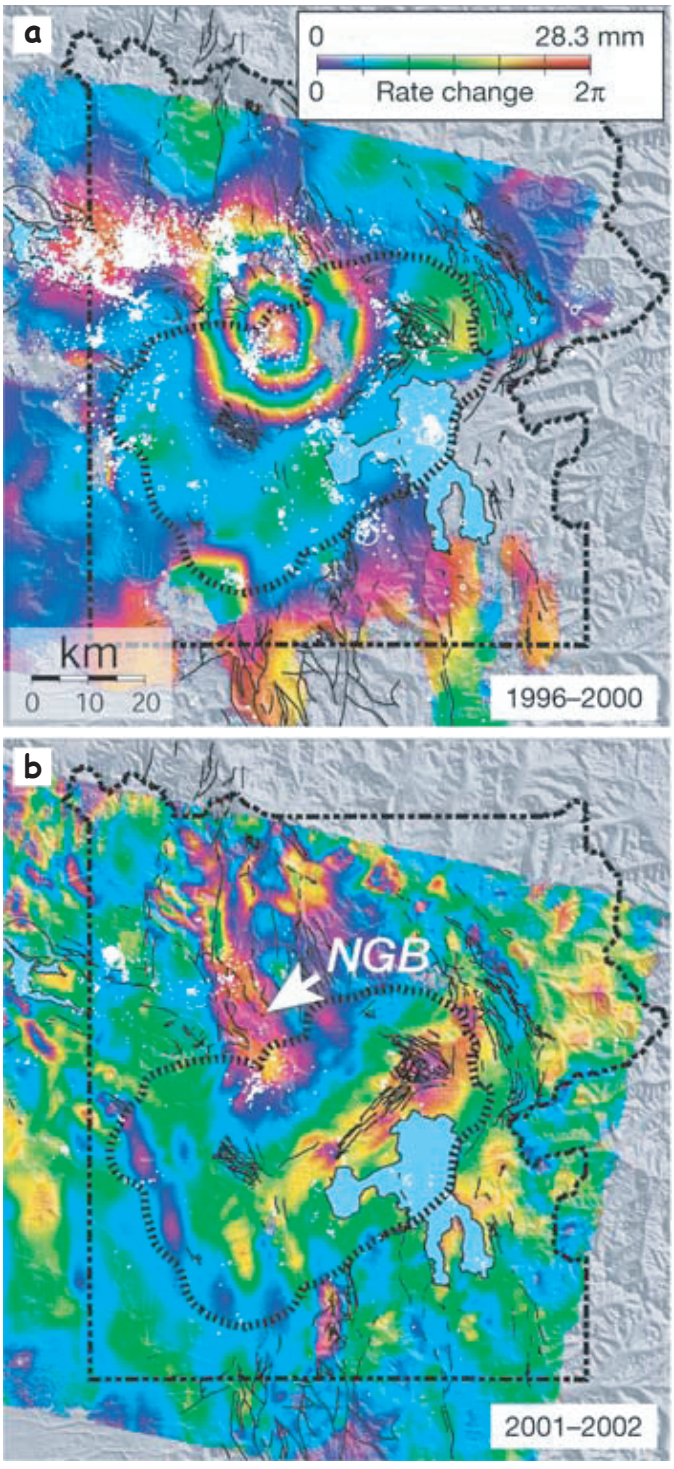

Figure 2.3. Interferograms documenting change in elevation from (a) summer 1996 to summer 2000 and (b) summer 2001 to summer 2002. One color succession from violet to red indicates a distance change of 28.3 mm between the monitoring satellite to the ground. The white dots mark the epicenters of earthquakes recorded during the time span of the interferograms. The black dotted boundary marks Yellowstone National Park and the black hashed boundary outlines the Yellowstone caldera rim. NGB is Norris Geyser Basin. From Wicks *et al.*, 2006.

CHAPTER 3

PREVIOUS WORK

Fenner (1938) first described mafic-silicic mingled lavas within the extracaldera rhyolites of the Yellowstone Caldera. However, Christiansen and Blank (1972) actually mapped and named the Central Plateau, Obsidian Creek (OC), and Roaring Mountain (RM) Members of the Plateau Rhyolite (Figure 2.2). They grouped the Cougar Creek, Riverside, Obsidian Cliff, and Crystal Spring rhyolite flows into the extracaldera RM Member of the Plateau Rhyolite, and the Gibbon River flow was placed in the Central Plateau Member (Figure 2.2) of the Plateau Rhyolite. This classification was based on stratigraphic relationships, petrographic similarities, and initial geochronology (Christiansen and Blank, 1972).

Hildreth and others (1991) published preliminary geochemistry on the OC and RM rhyolites. They observed that the extracaldera rhyolites are isotopically and chemically distinct from the Central Plateau rhyolites and other Yellowstone Caldera rhyolites (Hildreth *et al.*, 1991). Hildreth and others (1991) also suggested that the extracaldera rhyolites were produced from independent melt batches, which were unrelated to each other and unrelated to the Yellowstone Caldera's post-collapse rhyolites.

Obradovich (1992) used K/Ar geochronology to date the Plateau Rhyolite flows, including the Cougar Creek (399 ± 3 ka), Obsidian Cliff (183 ± 3 ka), Gibbon River (90 ± 2 ka) and Crystal Spring (80 ± 2 ka) flows (all reported uncertainties are 1σ). After reexamining the Plateau Rhyolite flows, Christiansen (2001) placed the Gibbon River flow (Figure 2.2) within the RM Member.

More recent work by Nastanski and Spell (2004a), Nastanski and Spell (2004b), Spell and Nastanski (2004), and Nastanski (2005) produced new interpretations of the Yellowstone Caldera's extracaldera lavas. Evaluation by Nastanski (2005) of previous geochemistry (Hildreth *et al.*, 1991) and new analyses (Nastanski and Spell, 2004a; Nastanski, 2005) of the OC and RM rhyolites indicate that the extracaldera rhyolites exhibit $(^{87}Sr/^{86}Sr)_i$, ε_{Nd}, Pb isotope ratios, and $\delta^{18}O$ values that are inconsistent with derivation from the same magma system as the coeval rhyolites erupted within the Yellowstone caldera. These results agree with the conclusions of Hildreth and others (1991). New dates and redating of the extracaldera rhyolites by $^{40}Ar/^{39}Ar$ geochronology provided new ages for the Roaring Mountain Member rhyolites (Riverside: 525.8 ± 3.3 ka; Cougar Creek: 368.2 ± 2.0 ka; Gibbon River: 118.0 ± 10.0 ka; and Obsidian Cliff: 105.6 ± 1.0 ka, all reported uncertainties are 1σ) (Nastanski, 2005). Some of these new $^{40}Ar/^{39}Ar$ ages indicate that the ages Obradovich (1992) obtained by K/Ar were off by as much as 75 ka (e.g. Obsidian Cliff flow) (Nastanski, 2005).

The OC flows are porphyritic rhyolites that erupted between 326-134 ka (Nastanski, 2005). Ion microprobe $^{230}Th/^{238}U$ and $^{206}Pb/^{238}U$ zircon ages indicate that the OC silicic magma system was established as early as 450 ka (Spell and Nastanski, 2004). Geochemical modeling suggests that the OC rhyolite magma system was injected with mafic magma represented by the Swan Lake Flat basalts (Nastanski, 2005), and several mingling events occurred between 326 and 263 ka (Nastanski, 2005). After the mingling events, geochemical modeling indicates the OC magma continued to evolve by simple fractional crystallization (Figure 3.1) (Nastanski, 2005).

The RM Member rhyolites post-date the OC Member rhyolites and consist of five rhyolite flows (as defined by Christiansen, 2001). However, Nastanski and Spell (2004b) and Nastanski (2005) found that the Cougar Creek and Riverside flows are chemically, temporally, and spatially unrelated to the youngest three flows, the Gibbon River, Obsidian Cliff, and Crystal Spring rhyolites. The RM rhyolite (as described by Nastanski, 2005) consists of aphyric to sparsely porphyritic lavas that erupted between 118 and 80 ka (Obradovich, 1992; Nastanski, 2005). Between the last OC flow, the Gibbon Hill rhyolite, and the first RM flow, the Gibbon River rhyolite, the RM rhyolites revert to more primitive, less-evolved compositions (Figure 3.1) (Nastanski, 2005). This sudden change in chemistry before the onset of eruption of the RM rhyolites suggests that the magma system may have undergone a mafic recharge event resulting in mafic-silicic magma mixing and production of less-evolved magma compositions (Nastanski, 2005). This hypothesis is supported by the recently discovered mafic-silicic mingled lava in the Crystal Spring flow (Nastanski and Spell, 2004a; Nastanski, 2005). However, the exact timing of the mingling event represented in the Crystal Spring lava flow is uncertain; the mingling event could have triggered the eruption, occurring immediately prior to eruption of the Crystal Spring flow, or mingling could have happened at any greater time before eruption (with something else triggering the eruption). Based on three geochemical analyses, the RM rhyolites appear to record simple fractional crystallization after mafic-silicic mixing and mingling in the system (Nastanski, 2005).

The three younger RM rhyolites are the flows that are pertinent to this study. The Gibbon River rhyolite contains phenocrysts of sanidine, quartz, plagioclase, clinopyroxene, and orthopyroxene (Christiansen and Blank, 1972; Nastanski, 2005). The

Obsidian Cliff and Crystal Spring rhyolites are mostly aphyric glass with sparse phenocrysts of plagioclase and zircon (Christiansen and Blank, 1972; Nastanski, 2005). The mingled lavas in the Crystal Spring rhyolite contain plagioclase and clinopyroxene phenocrysts (Christiansen and Blank, 1972; Nastanski, 2005). The mafic enclaves within the Crystal Spring lava are sub-spherical clots of fine-grained plagioclase and clinopyroxene groundmass that exhibit crenulate margins (Nastanski, 2005).

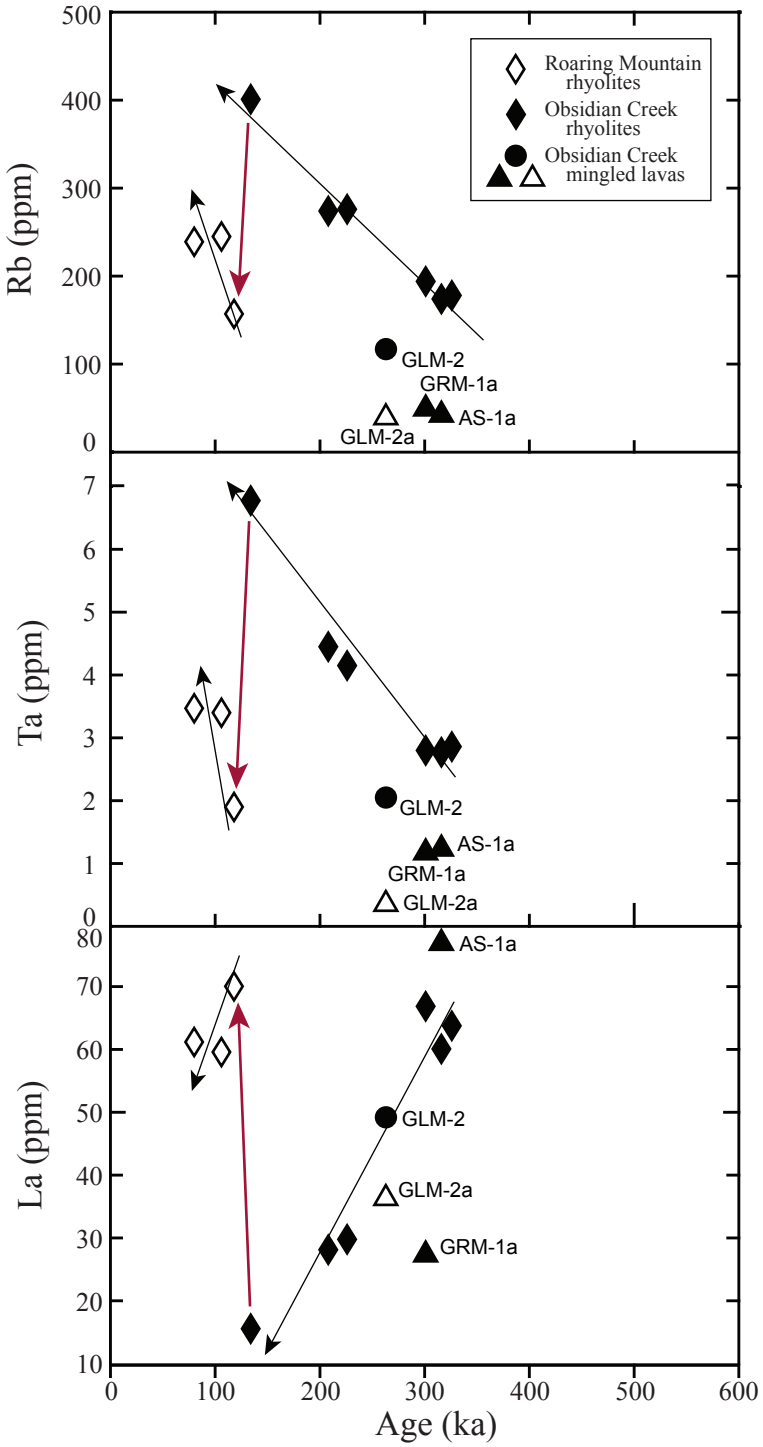

Figure 3.1. Eruption age vs. trace element concentration (Rb, Ta, and La) plots showing increasing/decreasing trends with age for the Obsidian Creek and Roaring Mountain Member rhyolites. Black arrows are fractional crystallization trends. Mingled lavas from the Obsidian Creek Member commonly plot off trends (samples GLM-2, GLM-2a, GRM-1a and AS-1a). Filled-diamonds are samples from the Obsidian Creek Member and open-diamonds are samples from the Roaring Mountain Member. Red arrows indicate sudden chemistry change between Gibbon Hill (OC) and Gibbon River (RM) flows. Modified from Nastanski (2005).

CHAPTER 4

ANALYTICAL METHODS

Rock samples from all three Roaring Mountain rhyolite flows were collected from Yellowstone National Park, Wyoming, during June of 2006. Sample collection was based on the mapping of the Roaring Mountain flows by Christiansen (2001). An attempt was made to collect representative samples from across the entire surface area of each rhyolite flow, however, fallen logs and new growth from the 1988 Yellowstone forest fire made some areas completely inaccessible. Four enclave-rich obsidian samples and four corresponding fresh enclave samples were collected from the Crystal Spring flow (Figure 4.1). Fourteen unaltered, black obsidian and several pumiceous samples were collected from the Obsidian Cliff flow (Figure 4.1). From the Gibbon River flow, fifteen rhyolite, obsidian and pumiceous rhyolite samples were collected (Figure 4.2). Thin section billets were cut from each sample and sent to Quality Thin Sections in Tucson, Arizona, where polished thin sections were made. A portion of the remaining sample material was broken into 2-4 cm chips using a jaw crusher fitted with tungsten carbide plates.

XRF Geochemistry

Clean, unaltered rock chips were picked for each sample and sent to Washington State University's GeoAnalytical Lab where loss on ignition, XRF and ICP-MS analyses were performed. At the GeoAnalytical Lab the chips were ground into powder in an agate container. The powdered sample was then mixed with dilithium tetraborate ($Li_2B_4O_7$) in a 2:1 $Li_2B_4O_7$ to sample mix (Johnson *et al.*, 1999). The $Li_2B_4O_7$ is used as a flux when fusing the sample into a bead. The mixture was placed in a graphite crucible,

then fused in a muffle furnace at 1000°C. The glass sample was reground in an agate swing mill and refused at 1000°C in an attempt to achieve homogeneity throughout the sample bead. The bead was then polished with a diamond lap to achieve a flat analysis surface before being analyzed in the XRF spectrometer.

A ThermoARL XRF was used to measure X-ray intensity and compares 29 element concentrations of the sample unknowns to 2 of 9 USGS standards and 2 pure vein quartz standards. Analysis conditions were kept stable with a Rh-target run at 50 kV and 50 mA under vacuum, and a mask of 25 mm was used (Johnson *et al.*, 1999). Interferences from the vacuum line and absorption effects caused by other elements were accounted for automatically. These stable conditions are good for measuring all 29 elements, except Sc, V, Nb, and Ba, which lose precision and accuracy under these particular conditions (Johnson *et al.*, 1999). The GeoAnalytical Lab's XRF is recalibrated every three weeks and two internal standards are analyzed every other day to monitor the spectrometer's performance (Johnson *et al.*, 1999).

ICP-MS Geochemistry

For ICP-MS analyses, complete dissolution of the sample is required. A portion of the clean, unaltered rock chips sent to the GeoAnalytical Lab at Washington State University was ground in an iron swing mill and then mixed with $Li_2B_4O_7$ flux in a 1:1 blend. The sample mixture was fused at 1000°C in a carbon crucible in a muffle furnace. The glass sample beads were then reground and 250 mg of sample powder was dissolved in 6 ml HF, 2 ml HNO_3, and 2 ml $HClO_4$ in an open Teflon vial on a hotplate at 110°C (Knaack *et al.*, 1994). The mixture was then evaporated to dryness and re-evaporated after being mixed with 2 ml $HClO_4$ at 165°C (Knaack *et al.*, 1994). The dry mixture was

mixed with 3 ml HNO_3, 8 drops of H_2O_2, 5 drops of HF, and In, Re, and Ru standards and then diluted to 1:240 (Knaack *et al.*, 1994). This process completely dissolves zircons and refractory minerals, such as garnet, and volatizes silica and boron as gaseous fluorides (Knaack *et al.*, 1994).

The sample dilution was analyzed in a HP4500 ICP-MS with an argon plasma ion source. Twenty-seven elements were analyzed after ionization at 7000°C (Knaack *et al.*, 1994). Seventeen unknown samples were analyzed between one acid blank and two analyses of each of three Washington State University rock standards. The In, Re, and Ru standards mixed into the sample are used to monitor and correct for instrument drift (Knaack *et al.*, 1994). Elemental intensities were also corrected for oxide and isobaric interferences. Using the six Washington State University rock standards and the acid blank, calibration curves were constructed for each analyzed element (Knaack *et al.*, 1994). These curves were used to calculate elemental concentrations (Knaack *et al.*, 1994). ICP-MS assumes that the isotopic proportions of samples and standards deviate only slightly from the average isotopic proportions of the Earth's crust (Knaack *et al.*, 1994).

$^{40}Ar/^{39}Ar$ Geochronology

The chips remaining after geochemistry from samples GRWY6, OCWY2, and CSWY1E were pulverized to ~3 mm fragments with a disk pulverizer fitted with steel plates. These fragments were then sieved to sizes >2000, 2000-1400, 1400-850, 850-710, 710-600, 600-425, 425-250, and <250 μm in stainless steel sieves. For GRWY6, a rhyolite from the Gibbon River flow, 60 sanidine grains were hand-picked from the 2.0-1.4 mm fraction, 40 sanidine grains were hand-picked from the 850-710 μm fraction, and

200 mg of sanidines were hand-picked from the 600-425 μm size fraction. From OCWY2, a sample of unaltered glass from the Obsidian Cliff flow, 70 grains of glass were hand-picked from the 850-710 μm fraction and 600 mg of glass was hand-picked from the 600-425 μm size fraction. Sample CSWY1E, a basaltic enclave from the Crystal Spring flow, had 600 mg of groundmass hand-picked from the 600-425 μm sieve fraction. The sanidine samples were cleaned for 2 minutes with a 5% hydrofluoric acid ultrasonic wash and the basalt sample was washed with a 10% nitric acid bath for 5 minutes. Finally, all six samples were cleaned three times in an ultrasonic bath of acetone.

These six samples were wrapped individually in aluminum foil and placed in fused quartz tubes. The tubes were sealed and wrapped in aluminum foil and placed in an aluminum tube, which was then irradiated in the central position of the reactor at the Oregon State University's Radiation Center for one hour. The irradiation vessel was lined with Cd to shield the samples from thermal neutrons and reduce the production of $^{40}Ar_K$ from ^{40}K (Tetley *et al.*, 1980). To measure the neutron fluence during irradiation (the J-factor), sanidines from the Fish Canyon Tuff in Colorado (Australian National University 92-176, 27.9 ± 1.2 Ma, 2σ) (Cebula *et al*., 1986; McDougall and Harrison, 1999) were included in the irradiation package. K-glass and CaF_2 samples were also packaged with the samples. K-glass is used to measure the production of $^{40}Ar_K$ from ^{40}K during irradiation, however, with a Cd-lining this correction should be very low. CaF_2 is used to measure the interfering Ar isotopes produced by neutron interactions with Ca isotopes. During irradiation, neutron interaction with ^{42}Ca and ^{43}Ca produces $^{39}Ar_{Ca}$, and $^{36}Ar_{Ca}$ is produced by neutron interaction with ^{40}Ca.

Upon returning from the nuclear reactor, the furnace step-heat samples were removed from the Al-foil, and three separates of each sample were packaged in Sn-foil (which melts at 231.9°C compared to Al at 660.3°C). These were then analyzed as nine furnace step heating runs at UNLV's Nevada Isotope Geochronology Lab. Single grains of sanidine and glass from the 850-710 μm and 2.0-1.4 mm samples were placed in a copper laser tray and fused with a 20-W CO_2 laser.

Gas from the furnace step heats and laser fusions was cleaned with two Zr-V SAES getters and then admitted into a MAP 215-50 mass spectrometer for argon isotopic analysis. During analysis, each Ar-isotope (36, 37, 38, 39, 40) was measured seven times per step or laser grain. To correct for outgassing of surfaces inside the extraction line and the mass spectrometer, blanks were analyzed. For furnace step-heat analyses, blank runs were measured in increments of 200°C, from 600°C to 1400°C, the temperature range used for the analyses. Furnace blanks were measured every other day. During single crystal laser fusion analyses, blank runs were measured every hour. For the single crystal fusion analyses of sample GRWY6, the ^{36}Ar blank measurement was ~20% of the total measured ^{36}Ar. To avoid potential age miscalculations due to anomalous blanks, a daily average of all hourly blanks was used to correct GRWY6 #4 and GRWY6 #5. However, the use of daily blanks vs. hourly blanks did not greatly affect the ages calculated for this data (Figure 4.3), suggesting that the ages calculated are not blank sensitive. Lastly, to determine the discrimination of the mass spectrometer, several aliquots of atmospheric argon ($^{40}Ar/^{36}Ar$ = 295.5) were analyzed and averaged over the analysis period. The discrimination for each analysis is listed in Appendix J in the individual analyses tables.

The seven Ar-isotope measurements were regressed to obtain abundances at the time of gas inlet, and the data was reduced using LabSpec, written by B. Idleman at Lehigh University, Pennsylvania. Microsoft Excel was used to calculate plateau ages, an error-weighted mean of the step ages that define a plateau. A plateau consists of contiguous steps of indistinguishable calculated ages (overlapping by $<2\sigma$) that together comprise $\geq$50% of the ^{39}Ar released. Isoplot 3.0 (Ludwig, 2003) was used to calculate inverse isochrons, MSWD (Wendt and Carl, 1991), and relative probability plots for the analyses.

$^{238}U/^{230}Th$ Geochronology

The chips not used for geochemistry for samples CSWY4, OCWY2, OCWY5, and OCWY14 were pulverized with a disk pulverizer fitted with steel plates to ~1 mm fragments. The samples were then sieved to sizes >250, 250-150, 150-53, and <53 μm in brass sieves. The <250 μm sieve fraction from GRWY6 was re-sieved to >212, 212-150, 150-53, and <53 μm size fractions in brass sieves. All five samples of size fraction 150-53 μm were dropped in 3.4ρ Methylene Iodide and the sink from each sample was exposed to a magnet to remove Fe-oxides. Zircons were then hand-picked from the non-magnetic sink of each sample. Only GRWY6 provided zircons for further analysis. The zircons were washed with 5% hydrofluoric acid for 8 minutes in an ultrasonic bath and then were washed three times with acetone.

The zircons were then lined up on tape and placed in an epoxy disk. The surface of the epoxy was then removed with 1 μm Al_2O_3 grit to expose and flatten the interior surfaces of the zircons. The epoxy disk with zircons was then coated in gold and placed in the sample chamber of UCLA's Cameca IMS 1270. An O^- ion beam was used to sputter a 30-35 μm spot on the zircons. $^{238}U^{16}O^+$, $^{232}Th^{16}O^+$, $^{90}Zr_2O_4^+$, 244.036 amu and

246.028 amu were analyzed for 20 spots on 11 grains. AS-3 zircons (1099.1 ± 0.5 Ma, 2σ; Paces and Miller, 1993) were analyzed to calibrate the microprobe's measured ThO/UO to the actual Th/U (Reid *et al*, 1997; Schmitt *et al*, 2006).

Finally, cathodoluminescence (CL) images were taken of all 11 analyzed zircons in an effort to reveal compositional zoning and internal features, which may be correlated with ages obtained. These images were taken using the JEOL JXA-8900 electron microprobe at UNLV's Electron Microanalysis and Imaging Laboratory.

Electron Microprobe

Uncovered thin sections from samples GRWY1, GRWY6, GRWY7P, OCWY6, CSWY1, CSWY1E, and CSWY2 were polished with 1 μm Al_2O_3 grit. The thin sections were then carbon coated, placed in brass holders, and the thin sections were grounded with copper tape to the holders. The samples were then placed in a JEOL JXA-8900 electron microprobe at UNLV's Electron Microanalysis and Imaging Laboratory. The samples were analyzed at an acceleration voltage of 15keV and current of 30nA. Elements were measured on peak for 30 sec and backgrounds for 10 sec. All minerals were analyzed with a 1 μm spot size, except plagioclase, sanidine, and Fe-oxides, which were analyzed with a defocused beam of 5 μm to minimize alkali loss from the energy of the beam (for feldspars, Jurek and Gedeon, 2003) and in an attempt to determine the magmatic, pre-exsolution (i.e. bulk) Fe-oxide compositions.

For the Gibbon River samples, GRWY1, GRWY6, and GRWY7P, the SiO_2, Al_2O_3, CaO, Na_2O, and K_2O composition of rim and center points were analyzed for sanidine and plagioclase, and the SiO_2, CaO, Na_2O, Al_2O_3, FeO, MgO, MnO, and TiO_2 composition of pyroxene, amphibole, olivine, and Fe-oxide phenocrysts was point

analyzed. Rim to rim line traverses of sanidine and plagioclase phenocrysts were analyzed for SiO_2, Al_2O_3, CaO, Na_2O, K_2O, MgO, BaO, and SrO at points spaced 10 μm apart and rim to rim line traverses of quartz phenocrysts were analyzed for SiO_2 and TiO_2 at 10 μm spaced points. CL and secondary electron (SEM) images of several quartz and sanidine phenocrysts were generated as well.

For the Obsidian Cliff sample, OCWY6, point analyses of phenocrysts were attempted, but all phenocrysts were 10 μm or less and provided very poor analytical data.

For CSWY1E, a Crystal Spring mafic enclave sample, rim and center point analyses were measured for SiO_2, CaO, Na_2O, Al_2O_3, FeO, MgO, MnO, and TiO_2 compositions of olivine, clinopyroxene, and Fe-oxide phenocrysts, and SiO_2, Al_2O_3, CaO, Na_2O, and K_2O compositions of plagioclase phenocrysts. Plagioclase from sample CSWY1, an obsidian with mafic enclaves and mafic phenocrysts from Crystal Spring, was analyzed along two perpendicular line traverses from rim to rim. Points were analyzed 5 μm apart and were measured for SiO_2, Al_2O_3, CaO, Na_2O, K_2O, MgO, BaO, and SrO compositions. CSWY2 did not contain plagioclase phenocrysts that were useful for analysis.

Scanning Electron Microscope

Grains from the non-magnetic heavy mineral separate extracted from OCWY14's 150-53 μm sieve size were attached to tape on a small holder and coated in gold. The sample and holder were then placed in UNLV's Electron Microanalysis and Imaging Laboratory's JEOL JSM-5610 scanning electron microscope and the sample's elemental composition was analyzed. Images of several grains were taken with the secondary and backscatter electron detectors (BSE).

Figure 4.1. Topographic map of the Crystal Spring (top) and Obsidian Cliff (bottom) rhyolite flows, Yellowstone Volcanic Field, Wyoming. Sample locations are marked in blue (Crystal Spring) and pink (Obsidian Cliff). Map modified from U.S.G.S. (1986b).

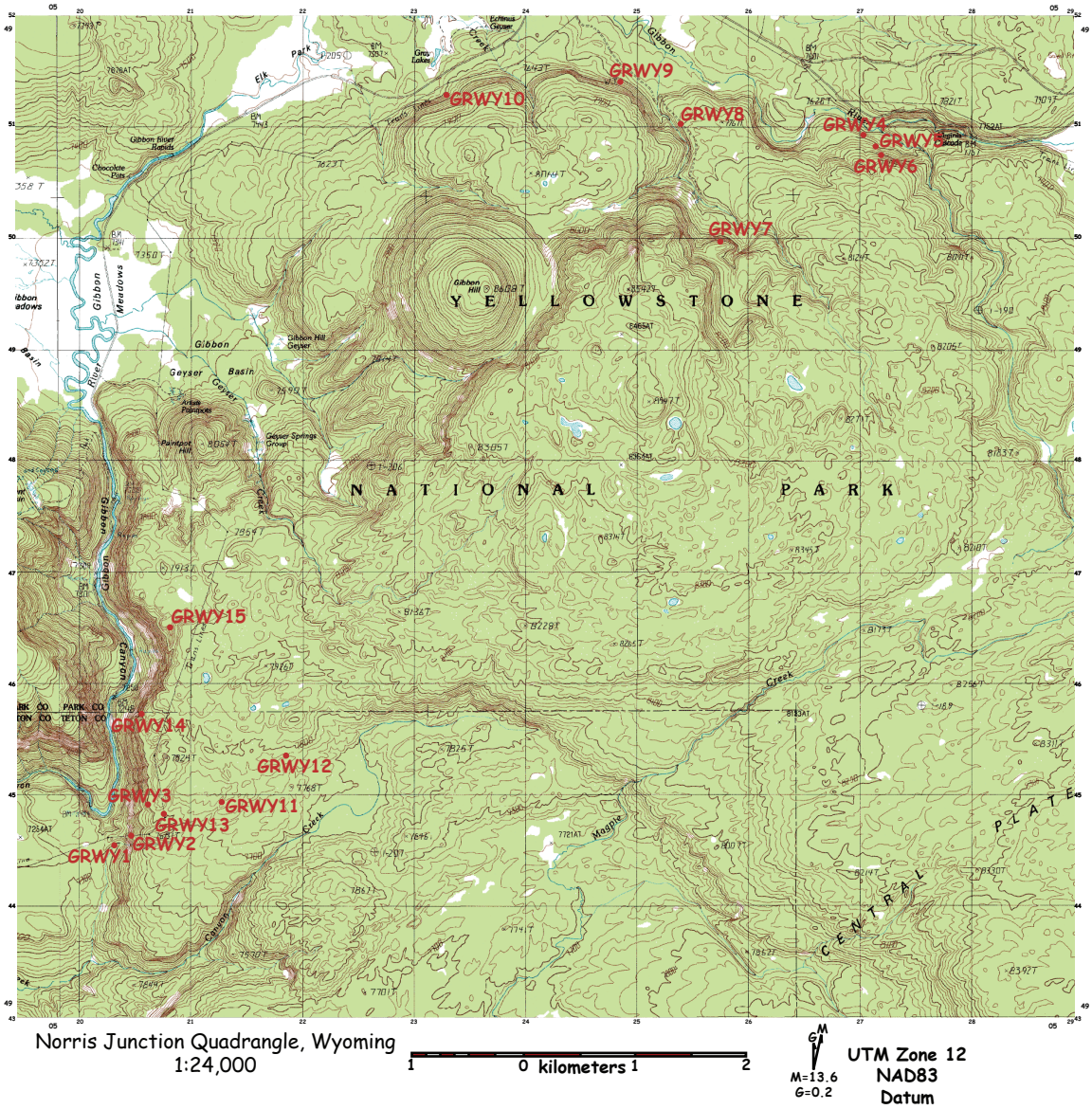

Figure 4.2. Topographic map of the Gibbon River rhyolite flow, Yellowstone Volcanic Field, Wyoming. Sample locations are marked in red. Map modified from U.S.G.S. (1986a).

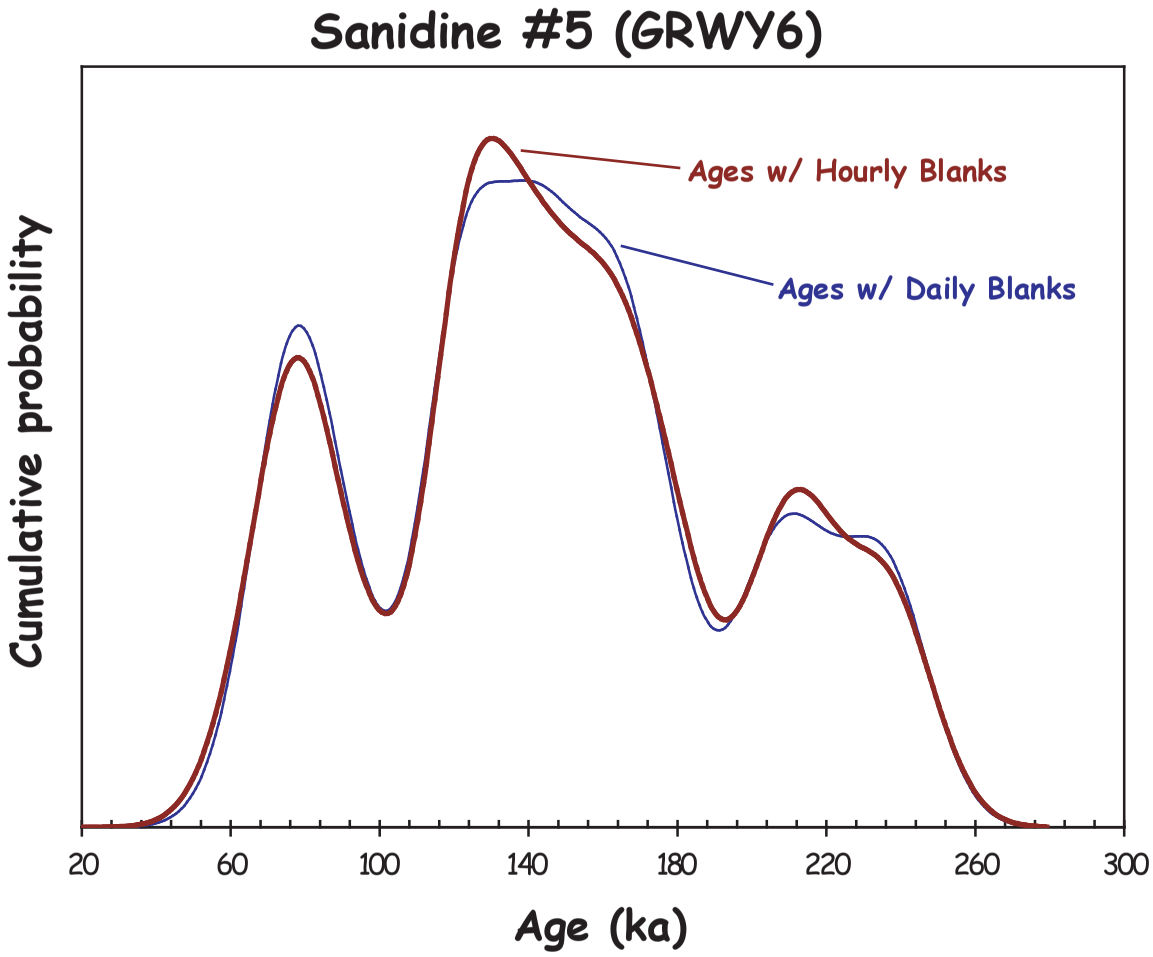

Figure 4.3. Age vs. cumulative probability plot of GRWY6 #5 showing $^{40}Ar/^{39}Ar$ ages calculated with hourly blanks and ages calculated with daily blanks.

CHAPTER 5

PETROGRAPHY

Numerous samples were collected from the Gibbon River, the Obsidian Cliff, and the Crystal Spring rhyolites. An attempt was made to collect from all regions of each flow for representative coverage, but sample collection was prohibited by the inaccessibility of some areas due to the 1988 Yellowstone National Park forest fires. Sampling locations are shown in Figures 4.1 and 4.2.

Gibbon River Flow

From the Gibbon River rhyolite 15 samples were collected (Figure 4.2), consisting of sparsely porphyritic to porphyritic grey rhyolite and obsidian (Figure 5.1). Phenocrysts include sanidine and quartz with sparse plagioclase. Most samples are unaltered to slightly devitrified. Sample GRWY7 consists of both obsidian and a pumiceous rhyolite of the flow's carapace (Figure 5.2). Sample GRWY6 is more coarsely porphyritic than the other samples of the flow (Figure 5.3), and the southwest flow front contains mahogany obsidian and areas of brecciated obsidian.

Examination of thin sections from each sample reveals three petrographically distinct rhyolites within the Gibbon River flow (Table 5.1). The main flow (defined by samples GRWY4, GRWY5, GRWY7O, GRWY7P, GRWY8, GRWY9, GRWY10, GRWY11, GRWY12, GRWY13, GRWY14, and GRWY15) consists of dense glass with phenocrysts of large sanidine (~5% of the rock), sparse quartz (<1%), plagioclase (<1%), opaque minerals (<1%), rare amphibole, olivine, and zircon. The sanidine (2-3 mm) is unzoned. Both the sanidine and quartz (~1 mm) are euhedral to subhedral and are

moderately resorbed and embayed. Plagioclase (~2 mm) is less common and is subhedral, unzoned, embayed and exhibits corroded interiors. Devitrification is exhibited by spherulites that are slightly altered to clay.

The southwest flow front and samples GRWY1 and GRWY3 consist of a dense glass with phenocrysts of large sanidine (~10% of the rock), quartz (~5%), sparse opaque minerals (~2%), plagioclase (~1%), rare amphibole, and zircon. The sanidine (up to 4 mm) is euhedral to subhedral and optically unzoned. Quartz (1-3 mm) is euhedral and often shattered and broken. Plagioclase (1-3 mm) is subhedral and embayed.

A single sample (GRWY6) from the northern front of the Gibbon River flow (Figure 4.2) is distinctly more coarsely porphyritic with phenocrysts of sanidine (~6% of the rock), opaque minerals (~3%), sparse quartz (<1%), rare olivine, amphibole, and zircon. Sanidine (2-3 mm) is euhedral to subhedral and slightly resorbed. Quartz (~3 mm) is subhedral to anhedral and typically shattered and broken. Amphibole is brownish green in polarized light and subhedral. Olivine is small (<50 μm) and anhedral.

Table 5.1. Point counts and phenocryst percentage of Gibbon River rhyolite samples

Gibbon River Thin Section Point Counts			
	GRWY3	GRWY6	GRWY7O
Sanidine	47	35	22
Quartz	24	4	2
Plagioclase	3	0	3
Opaque Minerals	11	14	1
Olivine	0	2	0
Amphibole	2	1	0
Glass	513	544	572
Total	600	600	600

Gibbon River Phenocryst Percentages			
	GRWY3	GRWY6	GRWY7O
Sanidine	7.8%	5.8%	3.7%
Quartz	4%	0.7%	<0.5%
Plagioclase	0.5%	0%	0.5%
Opaque Minerals	1.8%	2.3%	<0.5%
Olivine	0%	<0.5%	0%
Amphibole	<0.5%	<0.5%	0%
Glass	85.5%	90.7%	95.3%
Total	100%	100%	100%

Obsidian Cliff Flow

Fourteen samples were collected from the Obsidian Cliff rhyolite (Figure 4.2). Eleven of these samples are black, aphyric obsidian (Figure 5.4) with sparse lithophysae (sample OCWY12). The other three samples are fresh grey pumiceous rhyolite from the flow carapace (Figure 5.5). All collected samples, except OCWY14, are unaltered with up to ~2% spherulites in some samples. OCWY14 is a boulder collected from the Obsidian Cliff and is extensively devitrified (>60% of the boulder). The only mineralogy discernable to the unaided eye is small Fe-oxide minerals in the pumiceous rhyolite samples.

The thin sections from the Obsidian Cliff rhyolites reveal that the aphyric obsidian is characterized by abundant to sparse, unidentifiable microcrysts (≤10 μm), possibly consisting of quartz and feldspar. In OCWY12 and OCWY14, olivine phenocrysts (up to 250 μm) are observable (Figure 5.6). In a few samples, glomerocrysts with phenocrysts of plagioclase, clinopyroxene, and olivine are present, and in the pumiceous rhyolite samples, phenocrysts of opaque Fe-oxide minerals are present. Based on the aphyric nature of the Obsidian Cliff rhyolites no mineral point counts were performed on these samples.

Crystal Spring Flow

From the Crystal Spring mingled rhyolite, four sites were sampled, with samples of mafic enclaves and rhyolitic obsidian collected at each site. Enclave abundance and size increase from south to north in the flow, with up to ~20% mafic enclave abundance and ~1 meter-wide mafic enclaves at the site where CSWY1 was collected. Enclaves exhibit crenulate margins at the obsidian/enclave contact (Figures 5.7 & 5.8). All the enclave samples are fresh grey basalt or andesite (Figure 6.1; Chapter 6) (Figure 5.9). Sample CSWY1ME is a darker, more vesicular portion of a large enclave. The obsidian samples are aphyric and fresh with slight devitrification in samples CSWY2 and CSWY3.

The Crystal Spring rhyolite thin sections reveal glass with phenocrysts and microcrysts of plagioclase, clinopyroxene, and olivine, and mafic enclaves that range from several centimeters to only millimeters in diameter. Glomerocrysts of plagioclase, olivine and clinopyroxene are also present and are rimmed by an aphyric glass that is darker than the rhyolitic glass matrix. Plagioclase (up to 0.5 mm) is albite twinned,

euhedral to subhedral laths that define flow banding within the rhyolite (Figure 5.10). Clinopyroxene and olivine are common microcrysts. The mafic enclaves are often enclosed in a rim of dark, aphyric glass, like the glomerocrysts, and vary in size between samples. Sample CSWY2 contains a single, extensively resorbed quartz grain (Figure 5.10) and a single, 0.5 mm sieved plagioclase grain. While most microcrysts within the Crystal Spring mingled rhyolites are identifiable, some are not (similar to Obsidian Cliff microcrysts); to avoid bias due to incorrect identification of microcrysts, no mineral point counts were performed on these samples.

The Crystal Spring mafic enclave thin sections reveal a holocrystalline basalt or andesite with a groundmass of plagioclase, olivine, clinopyroxene, and opaque minerals. Plagioclase (up to 0.5 mm) are albite twinned, euhedral to subhedral laths (Figure 5.11). Olivine and clinopyroxene are subhedral (Figure 5.11).

In the area of sample CSWY3, the surface of the ground is covered in fragments of black vesicular obsidian (sample CSWY3V; Figure 5.12) containing aphyric grey mafic enclaves up to 8 mm in size. The enclaves have crenulate edges defined by sharp contacts. The fragments are commonly oxidized on the surface and along cracks.

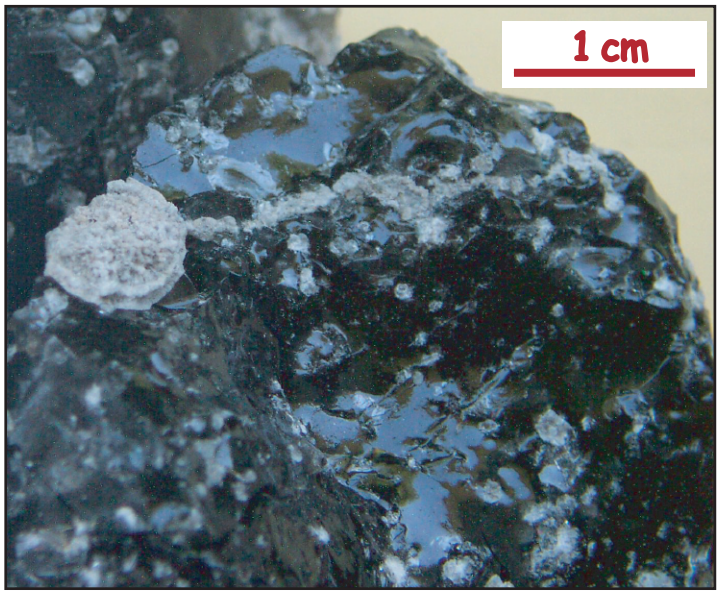

Figure 5.1. Obsidian sample from the Gibbon River flow (GRWY11). Sanidine, quartz, and plagioclase phenocrysts, and spherulites are visible. Large grey lithophysae in the upper left corner.

Figure 5.2. Pumiceous sample from the Gibbon River flow (GRWY7P). Sanidine, quartz, and plagioclase phenocrysts are visible.

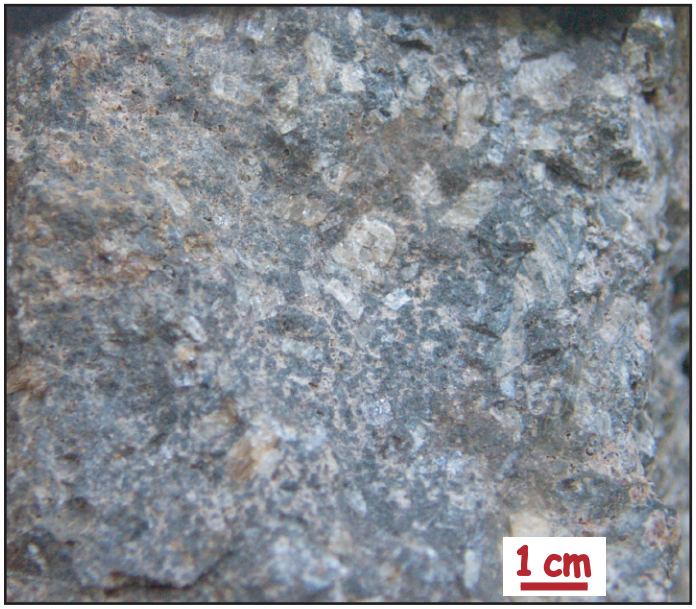

Figure 5.3. Porphyritic rhyolite sample from the Gibbon River flow (GRWY6). Sanidine and quartz phenocrysts are visible.

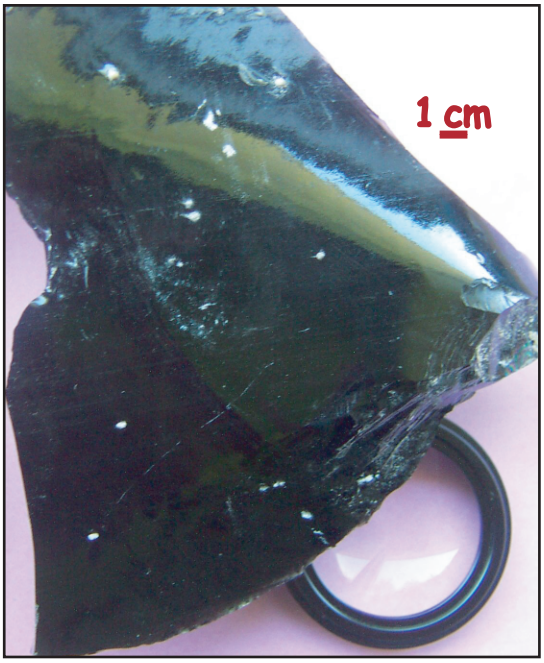

Figure 5.4. Obsidian sample from the Obsidian Cliff flow (OCWY2). Small white spherulites are visible.

Figure 5.5. Pumice sample from the Obsidian Cliff flow (OCWY5).

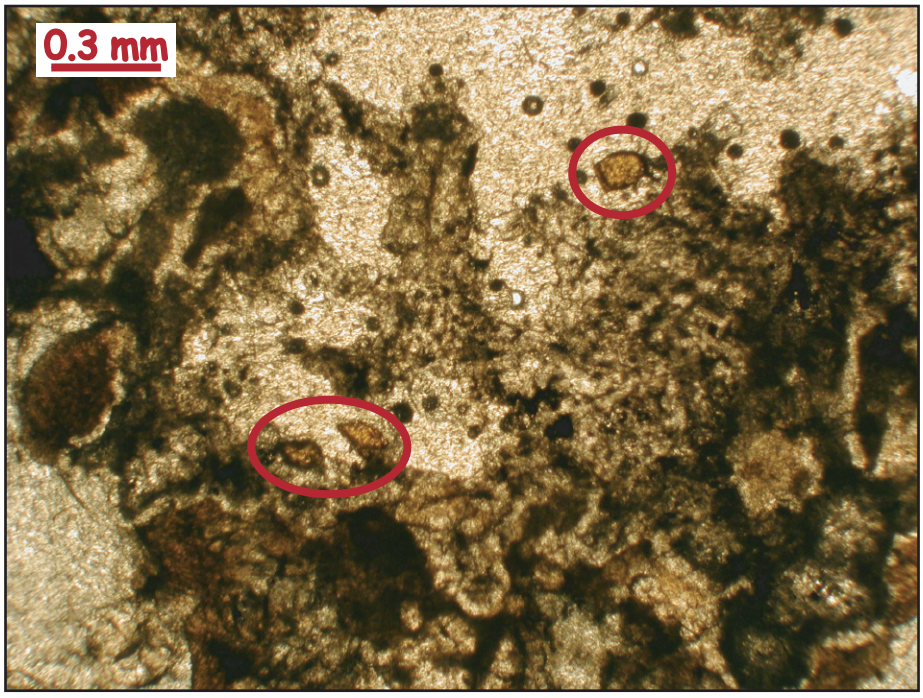

Figure 5.6. Photomicrograph of an altered Obsidian Cliff sample (OCWY14). Orange minerals are olivine phenocrysts (circled in red).

Figure 5.7. Mingled rhyolite sample from the Crystal Spring flow (CSWY1). Grey regions are crenulated basaltic enclaves in obsidian.

Figure 5.8. Basaltic enclave (light grey) with quenched rim (medium grey) in the mingled lava sample CSWY1 from the Crystal Spring flow.

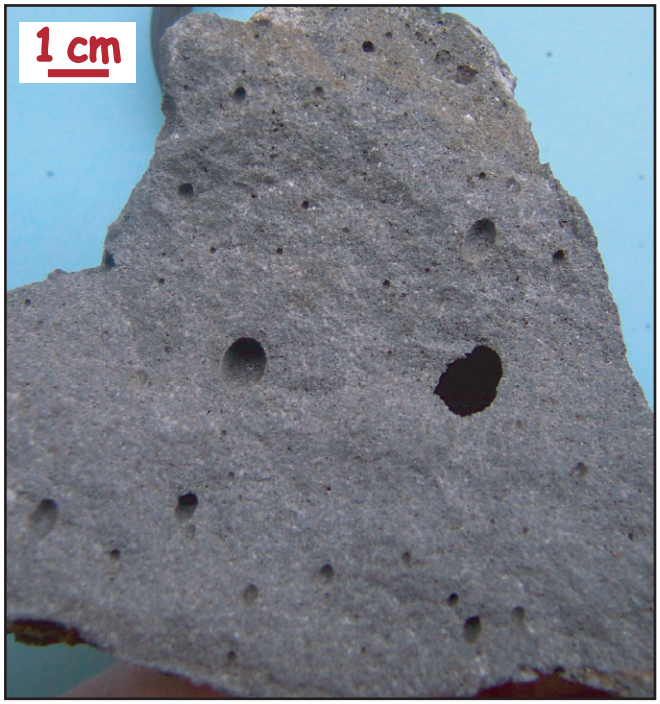

Figure 5.9. Basaltic enclave from the Crystal Spring mingled rhyolite (CSWY1ME).

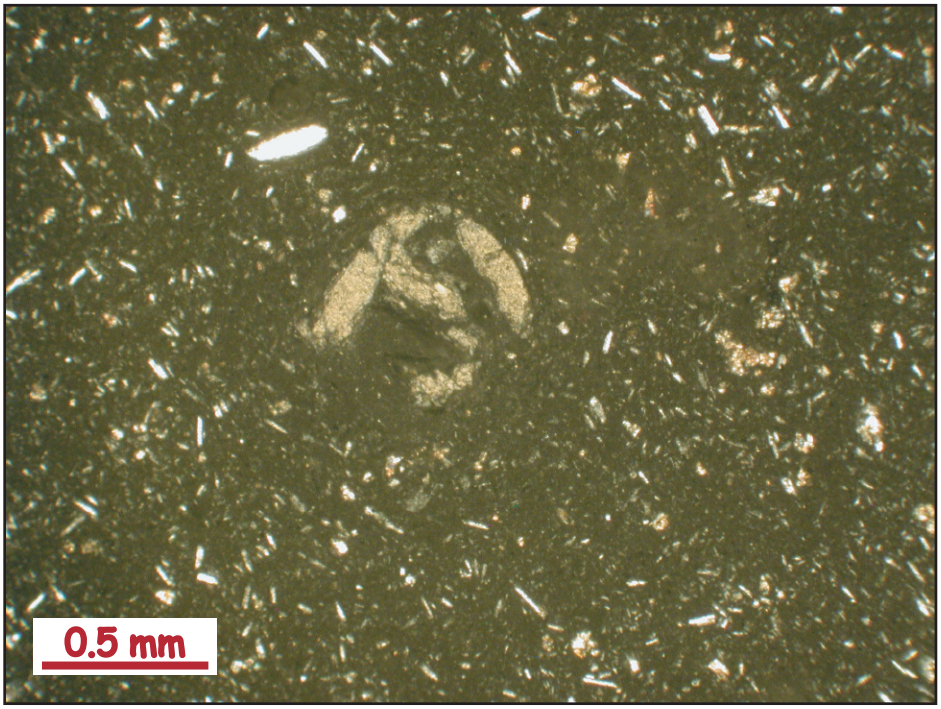

Figure 5.10. Photomicrograph of a resorbed quartz in the obsidian of the Crystal Spring mingled rhyolite sample CSWY2.

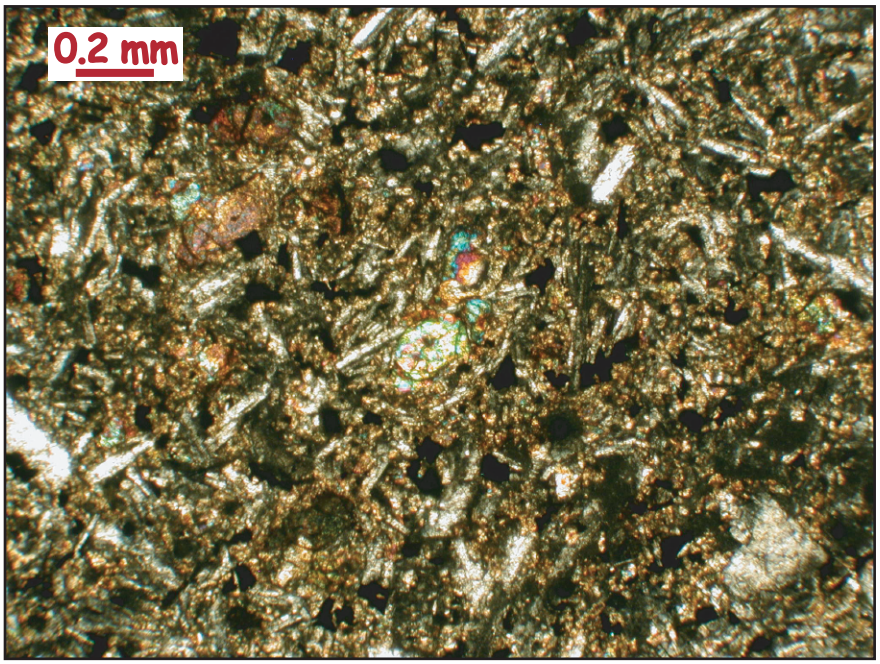

Figure 5.11. Photomicrograph of olivine, clinopyroxene, and plagioclase groundmass in a basaltic enclave of the Crystal Spring mingled rhyolite samples (CSWY1E).

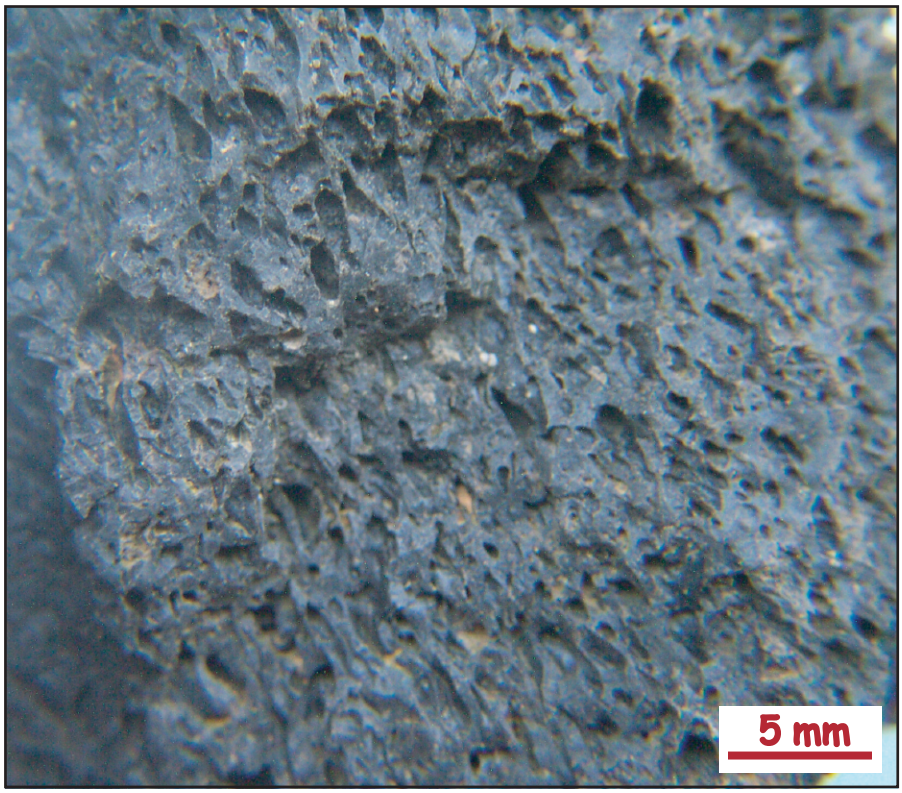

Figure 5.12. Vesicular obsidian from the Crystal Spring mingled rhyolite (CSWY3V).

CHAPTER 6

GEOCHEMISTRY

Eight samples from the Gibbon River flow (GRWY1, GRWY3, GRWY6, GRWY7O, GRWY9, GRWY10, GRWY12, & GRWY15), seven samples from the Obsidian Cliff flow (OCWY2, OCWY5, OCWY6, OCWY8, OCWY11, OCWY12, & OCWY14), five obsidian samples (CSWY1, CSWY2, CSWY3, CSWY3V, & CSWY4) and three enclave samples (CSWY1E, CSWY1GE, CSWY1ME) from the Crystal Spring mingled lavas were analyzed by XRF and ICP-MS (Appendix B). The major element analyses of each sample were normalized to 100% of the volatile-free whole rock composition (Appendix B). During XRF analysis, the oxidation state of iron is ignored and all analyzed Fe is expressed as FeO (denoted as FeO*) (Johnson *et al.*, 1999).

Following the classification of LaBas and others (1986), all of the Gibbon River and Obsidian Cliff samples are rhyolite, as are the five Crystal Spring obsidians (Figure 6.1). The Crystal Spring enclave sample, CSWY1GE is an andesite, and samples CSWY1E and CSWY1ME are both basalts (Figure 6.1).

Gibbon River Flow

All of the Gibbon River rhyolite samples are generally similar in composition, however, minor variations in chemistry permit three separate rhyolite compositions to be defined: 1) the main flow (GRWY7O, GRWY9, GRWY10, GRWY12, & GRWY15), 2) the southwestern flow (GRWY1 & GRWY3), and 3) sample GRWY6.

The Main Flow

The main flow of the Gibbon River rhyolites has a mean wt.% SiO_2 of 77.31 ± 0.19 (Table 6.1; Appendix B) and is indistinguishable within uncertainty with the Obsidian Cliff rhyolites (Figure 6.2). Like all the Gibbon River rhyolite samples, the MgO and MnO contents of the main flow are less than 0.1 wt.% of the normalized composition (Figure 6.2; Appendix B). The main flow has the lowest FeO* concentration of the three Gibbon River rhyolites (Figure 6.2; Table 6.1). The main flow rhyolites are enriched in rare-earth elements (REEs) compared to chondrites and exhibits an extreme negative Eu-anomaly (Figure 6.3; Table 6.2). They are also enriched in large-ion lithophile (LIL) and high-field strength (HFS) elements, except for Sr, Ba, and TiO_2, which are depleted compared to chondrites (Figure 6.4; Table 6.2). The main flow has the lowest Sr concentration of the three Gibbon River rhyolites (Figure 6.4).

The Southwestern Flow

The southwestern flow of the Gibbon River rhyolite is less evolved than the main flow of the Gibbon River rhyolites, with a mean wt.% SiO_2 of 77.06 ± 0.19 (Figure 6.2; Appendix B). The southwestern flow has the highest K_2O and the lowest Na_2O of the three Gibbon River rhyolites, and the average FeO* concentration falls between the main flow of the Gibbon River rhyolites and sample GRWY6 (Figure 6.2; Table 6.1). The southwestern flow is enriched in REEs compared to chondrites and exhibits a moderate negative Eu-anomaly (Figure 6.3; Table 6.2). The southwestern flow also has the highest Sr concentration of all three Gibbon River rhyolites (Figure 6.4).

Sample GRWY6

Sample GRWY6 is the least evolved of the Gibbon River samples at 76.13 ± 0.19 wt.% SiO_2 (Appendix B) and has the highest FeO* concentration of all the Gibbon River samples (Figure 6.2; Table 6.1). It is enriched in REEs compared to chondrites and exhibits a shallow negative Eu-anomaly (Figure 6.3; Table 6.2). Sample GRWY6 is also enriched in both LIL and HFS elements, and GRWY6's Sr concentration falls between the southwestern flow and the majority of the Gibbon River flow (Figure 6.4; Table 6.2).

Gibbon River Rhyolites

Major, minor, and trace element data also confirm the three rhyolite compositions within the Gibbon River flow as discussed above (Figures 6.2, 6.5 & 6.6). The main flow of the Gibbon River rhyolites is the most evolved and sample GRWY6 is the least evolved (Figures 6.2 & 6.3). TiO_2, Zr, and Ba concentrations decrease (Figure 6.2), and Rb, Th, and U concentrations increase with increasing SiO_2.

By themselves, the major and trace element data of the Gibbon River rhyolites exhibit no consistent pattern or trend between all three rhyolites. Linear trends are exhibited with trace elements like Tb, Lu, and Th (Figures 6.6 & 6.7). However, the order of the three flows along these linear trends varies between elements (Gibbon River flow order of Lu vs. Ta in Figure 6.6 compared to the flow order of Th vs. Rb in Figure 6.7).

When combined with the data from the Crystal Spring and Obsidian Cliff flows, however, obvious geochemical associations emerge. For major, minor and trace elements, the main flow of the Gibbon River analyses fall at the most evolved end of a linear trend between the Obsidian Cliff obsidians, the Crystal Spring mingled rhyolites, and the Crystal Spring mafic enclaves (Figures 6.2, 6.5 & 6.6). The light REEs of the

main flow of the Gibbon River rhyolites (La, Ce, Pr & Nd) do not fall along this linear trend. The main flow is lower in La, Ce, and Nd concentration than the southwestern flow and sample GRWY6 analyses.

For major and minor elements, the southwestern flow analyses fall between the Crystal Spring mafic enclaves and the Crystal Spring mingled rhyolites along a linear trend connecting the main Gibbon River flow, the Obsidian Cliff obsidians, the Crystal Spring mingled rhyolites, and the Crystal Spring mafic enclaves (Figures 6.2, 6.5 & 6.6). Most of the southwestern flow trace element analyses (Sc, V, Cr, Ni, Cu, Zn, Sr, Ba, Zr, Pb, Th, La, Ce, & Nd), however, do not fall into this linear trend (e.g. Pb vs. Y in Figure 6.5). The major, minor, and trace element analyses of the southwestern flow (except trace elements Ni, Zn, Sr, Ba, La, Ce, & Nd) do fit along a second linear trend that excludes the Crystal Spring mingled rhyolites, the Obsidian Cliff flow, and sample GRWY6. This second linear trend extends between the Crystal Spring mafic enclaves and the main Gibbon River flow, with the southwestern flow in the middle (e.g. Nb vs. Y in Figure 6.5).

Sample GRWY6 does not consistently plot on any of the previous mentioned linear trends (Figure 6.2, 6.5 & 6.6). However, for SiO_2, CaO, FeO, MgO, TiO_2, P_2O_5, Sc, V, Cr, Ni, and Cu, the GRWY6 analyses do fall along a linear trend connecting the Crystal Spring mafic enclaves, GRWY6, the southwestern Gibbon River flow, and the main Gibbon River flow (Figure 6.2).

Obsidian Cliff Flow

All seven of the Obsidian Cliff analyses cluster within uncertainty of each other for all major elements, except Na and K, which are mobile during hydration. The Obsidian Cliff rhyolites have a mean of 77.38 ± 0.19 wt.% SiO_2, 12.12 ± 0.082 wt.% Al_2O_3, 1.13 ± 0.18 wt.% FeO*, 0.44 ± 0.043 wt.% CaO, 0.083 ± 0.012 wt.% TiO_2, 0.04 ± 0.073 wt.% MgO, and 0.023 ± 0.002 wt.% MnO (Table 6.1; Appendix B) and are indistinguishable within uncertainty with the main flow of the Gibbon River rhyolites (Figure 6.2; Table 6.1). For Na_2O and K_2O, the most devitrified of the Obsidian Cliff samples, OCWY14 falls outside the analytical error of the sample cluster (Figure 6.2). Excluding OCWY14, the Obsidian Cliff rhyolites are composed of an average of 4.98 ± 0.015 wt.% K_2O and 3.77 ± 0.036 wt.% Na_2O (Figure 6.2; Table 6.1; Appendix B). The Obsidian Cliff analyses, for both major and minor elements, fall at the most evolved end of a linear trend with the Crystal Spring mafic enclaves and the Crystal Spring mingled rhyolites (Figures 6.2 & 6.5). This linear trend extends from the Crystal Spring mafic enclaves to the Crystal Spring mingled rhyolite, to the Obsidian Cliff rhyolite, and ending with the main flow of the Gibbon River rhyolites.

The Obsidian Cliff trace elements also cluster tightly (Figures 6.3, 6.4 & 6.6). These analyses, like the major and minor elements, fall at the most evolved end of the linear trend between the Crystal Spring mafic enclaves and the main flow of the Gibbon River rhyolites (Figures 6.5 & 6.6).

The Obsidian Cliff samples are enriched in REEs compared to chondrites and have a well-developed negative Eu-anomaly (Figure 6.3; Table 6.2). With the exception of Sr and TiO_2, the Obsidian Cliff rhyolites are enriched in LIL and HFS elements (Figure 6.4;

Table 6.2). The samples are depleted in Sr and slightly depleted in TiO_2 compared to chondrites, and Ba is not as enriched in the Obsidian Cliff samples as the other LIL elements (Figure 6.4).

Crystal Spring Flow

The Crystal Spring mingled rhyolites decrease in mafic enclave content from north (sample CSWY1) to south (sample CSWY4) (Figure 6.1). The site where sample CSWY1 was collected contains ~20% enclaves and CSWY1 contains 71.77 ± 0.19 wt.% SiO_2 (Figure 6.2; Table 6.1; Appendix B). The most silicic Crystal Spring mingled rhyolite sample, CSWY4 contains 76.97 ± 0.19 wt.% SiO_2, similar in composition to the Obsidian Cliff cluster of rhyolite analyses (Figures 6.2; Table 6.1; Appendix B).

The Crystal Spring rhyolites are enriched in REEs and have a negative Eu-anomaly that ranges from a moderate (sample CSWY1) to an extreme (samples CSWY4) anomaly (Figure 6.3; Table 6.2). The samples are enriched in LIL and HFS elements, with the exception of Sr which is depleted in the most silicic rhyolite sample (Figure 6.4). Ba, Sr, and TiO_2 concentration decrease with decreasing mafic enclave content (Figure 6.4).

For all of the Crystal Spring major, minor, and trace element analyses, the Crystal Spring mingled rhyolites extend along a linear trend to their mafic enclaves (Figures 6.2, 6.5, 6.6 & 6.7). The linear trend stretches from the most mafic Crystal Spring basaltic enclave to the most evolved Crystal Spring rhyolite (Figures 6.5, 6.6 & 6.7).

Crystal Spring Mafic Enclaves

The Crystal Spring mafic enclaves are basalts (and in some cases, andesites like sample CSWY1GE) (Figure 6.1). The mafic enclaves (represented by sample

CSWY1ME) contain 49.04 ± 0.19 wt.% SiO_2, 7.49 ± 0.073 wt.% MgO, and 10.88 ± 0.043 wt.% CaO (Figure 6.2; Appendix B) and are tholeiitic in composition (Figure 6.8). The mafic enclave composition is similar to the Swan Lake Flat and Hepburn Mesa basalts (Figure 6.9) (Fenner, 1938; Hildreth *et al.*, 1991; Christiansen, 2001; Bennett, 2006).

The Crystal Spring mafic enclaves (CSWY1E & CSWY1ME) are enriched in REEs and show a slightly positive Eu-anomaly (Figure 6.3; Table 6.2). The Crystal Spring mafic enclave samples are enriched in all LIL and HFS elements (Figure 6.4; Table 6.2).

Table 6.1. Major Element Composition of the Roaring Mountain Lava Flows

	SiO_2 (wt.%) [a]	K_2O (wt.%) [a]	Na_2O (wt.%) [a]	FeO* (wt.%) [a]	MgO + MnO (wt.%) [a]
Gibbon River Flow					
Main	77.31 ± 0.19	4.86 ± 0.015	3.96 ± 0.036	1.11 ± 0.18	< 0.1
Southwestern	77.06 ± 0.19	5.19 ± 0.015	3.44 ± 0.036	1.28 ± 0.18	< 0.1
GRWY6	76.13 ± 0.19	5.13 ± 0.015	3.66 ± 0.036	2.08 ± 0.18	< 0.1
Obsidian Cliff Flow					
Obsidian	77.38 ± 0.19	4.98 ± 0.015 [c]	3.77 ± 0.036 [c]	1.13 ± 0.18	< 0.1
Crystal Spring Flow					
Mingled Rhyolite [d]	71.77 to 76.97 ± 0.19	4.01 to 4.89 ± 0.015	3.57 to 3.76 ± 0.036	1.28 to 3.04 ± 0.18	0.192 to 1.708

[a] Figure 6.2.
[b] Data listed in Appendix B.
[c] Average of all Obsidian Cliff samples except OCWY14.
[d] Concentration ranges are for rhyolite samples CSWY1, CSWY2, CSWY3, CSWY3V, and CSWY4.

Table 6.2. Trace Element Composition of the Roaring Mountain Lava Flows

	REEs vs. Chondrites [a]	Negative Eu-Anomaly [a]	LIL [b]	HFS [b]	La/Lu [a]
Gibbon River Flow					
Main	enriched	extreme	enriched	enriched	35.2
Southwestern	enriched	moderate	enriched	enriched	122.2
GRWY6	enriched	shallow	enriched	enriched	80.9
Obsidian Cliff Flow					
Obsidian	enriched	extreme	enriched	enriched	61.8
Crystal Spring Flow					
Mingled Rhyolite	enriched	moderate to extreme	enriched	enriched	62.3
Mafic Enclaves	enriched	slightly positive	enriched	enriched	42.7

[a] Figure 6.3.
[b] Figure 6.4.

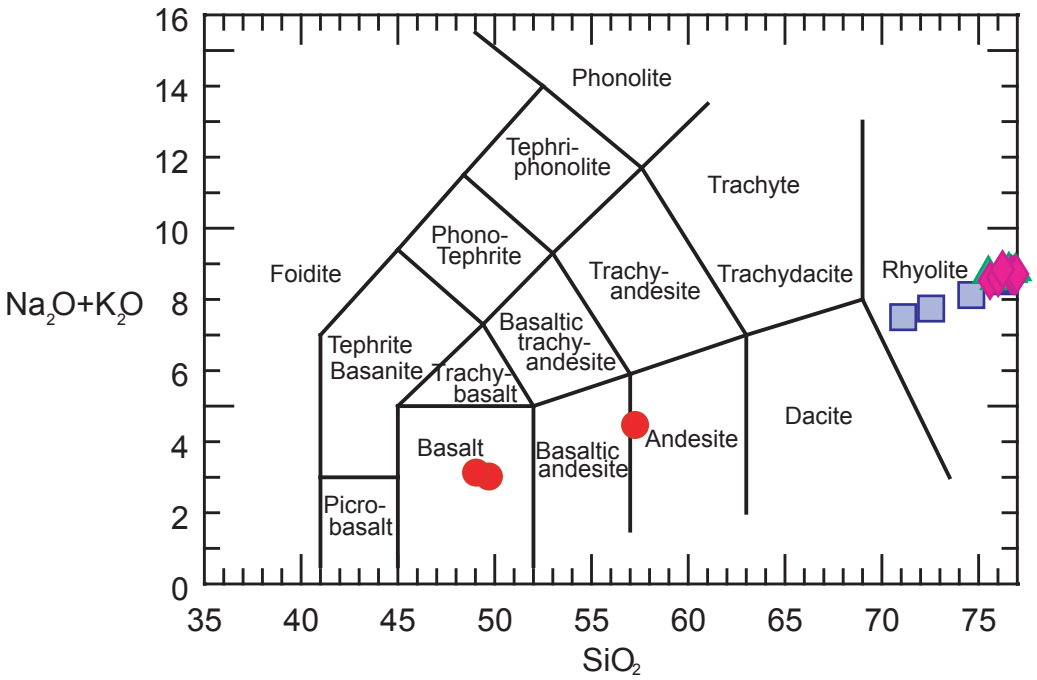

Figure 6.1. Rock classification of the Gibbon River lavas (▲), Obsidian Cliff lavas (♦), Crystal Spring minged rhyolites (▣), and mafic enclaves (●) following LaBas *et al.* (1986).

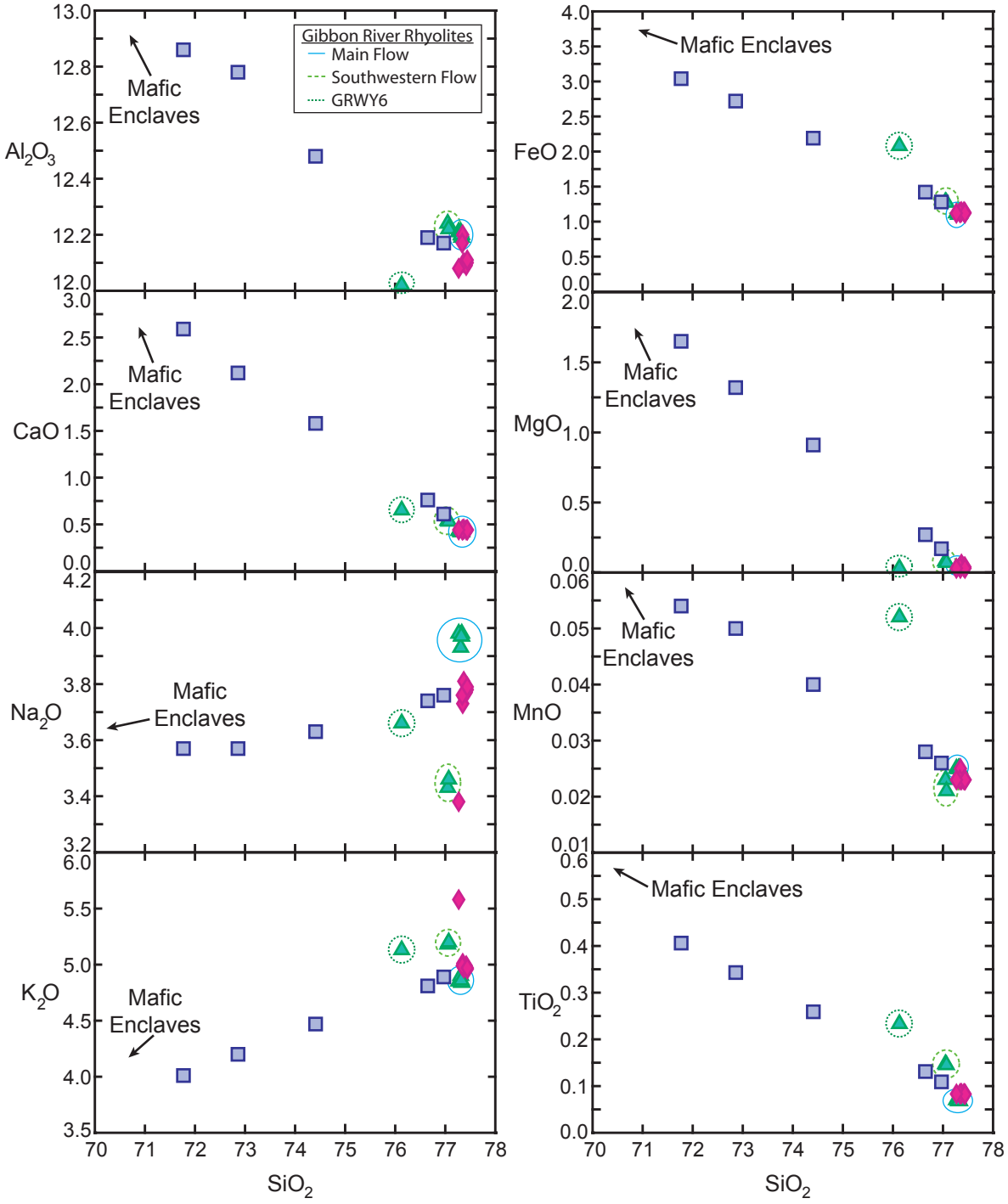

Figure 6.2. Major element diagrams for the Gibbon River lavas (▲), Obsidian Cliff lavas (♦), and Crystal Spring mingled rhyolites (□) from XRF analyses. Crystal Spring mafic enclaves plot off scale between 49-58 wt.% SiO_2.

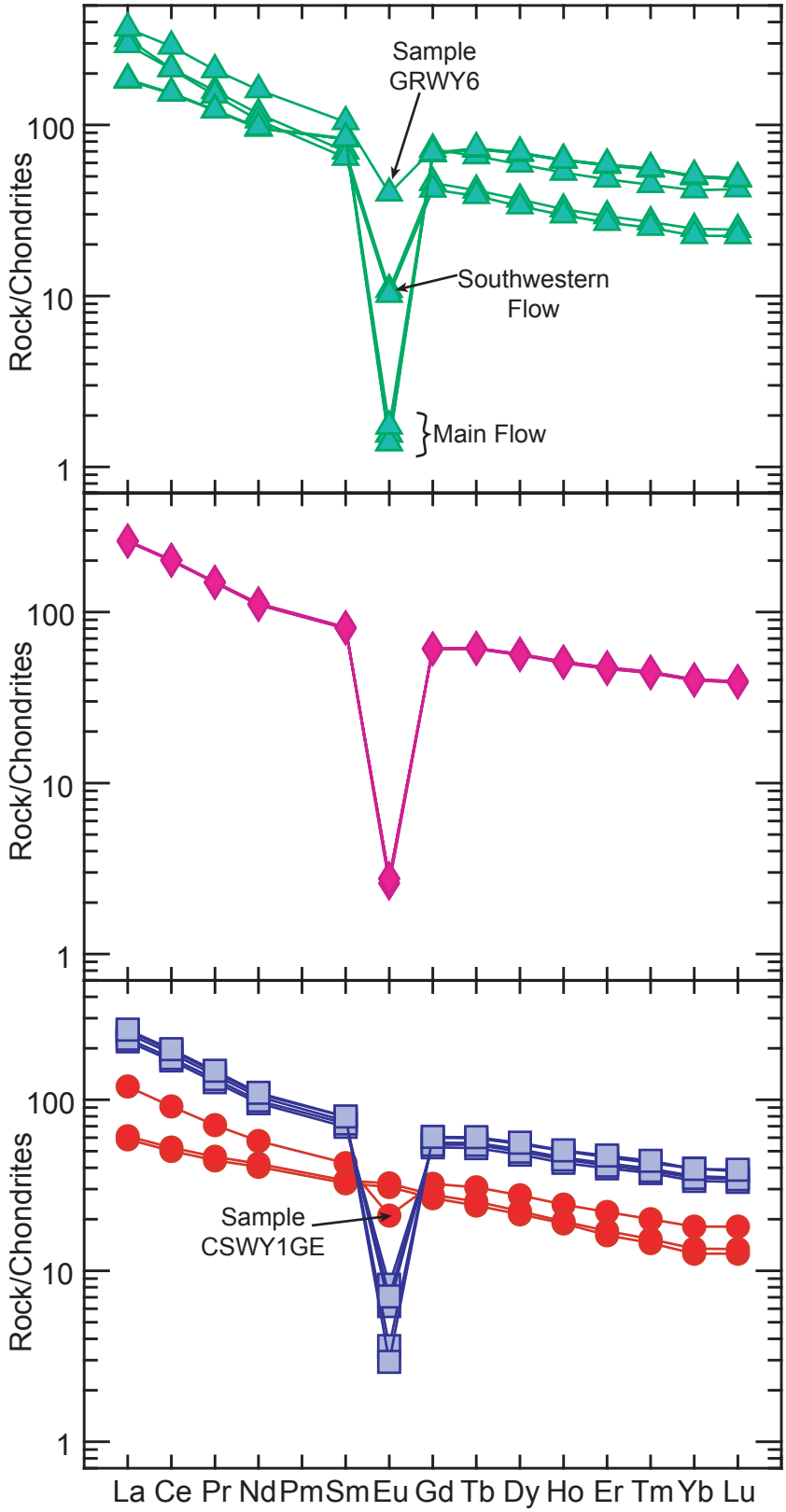

Figure 6.3. Rare earth element diagrams (formatted after Sun & McDonough, 1989) for the Gibbon River lavas (▲), Obsidian Cliff lavas (◆), Crystal Spring mingled rhyolites (■), and mafic enclaves (●) from ICP-MS analyses.

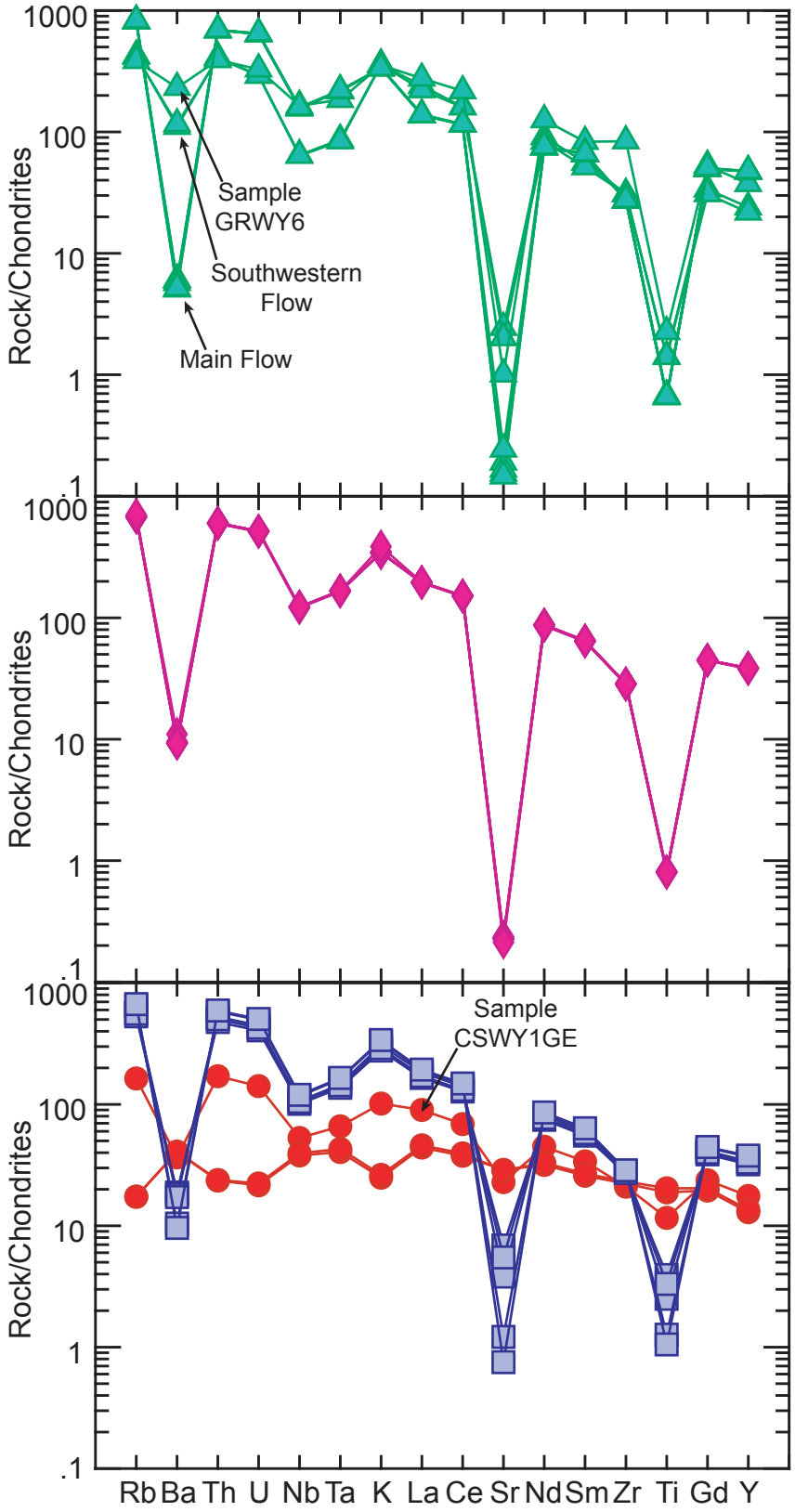

Figure 6.4. Large-ion lithophile and high-field strength element diagrams (formatting after Sun, 1980) for the Gibbon River lavas (▲), Obsidian Cliff lavas (♦), Crystal Spring mingled rhyolites (■), and mafic enclaves (●) from ICP-MS analyses.

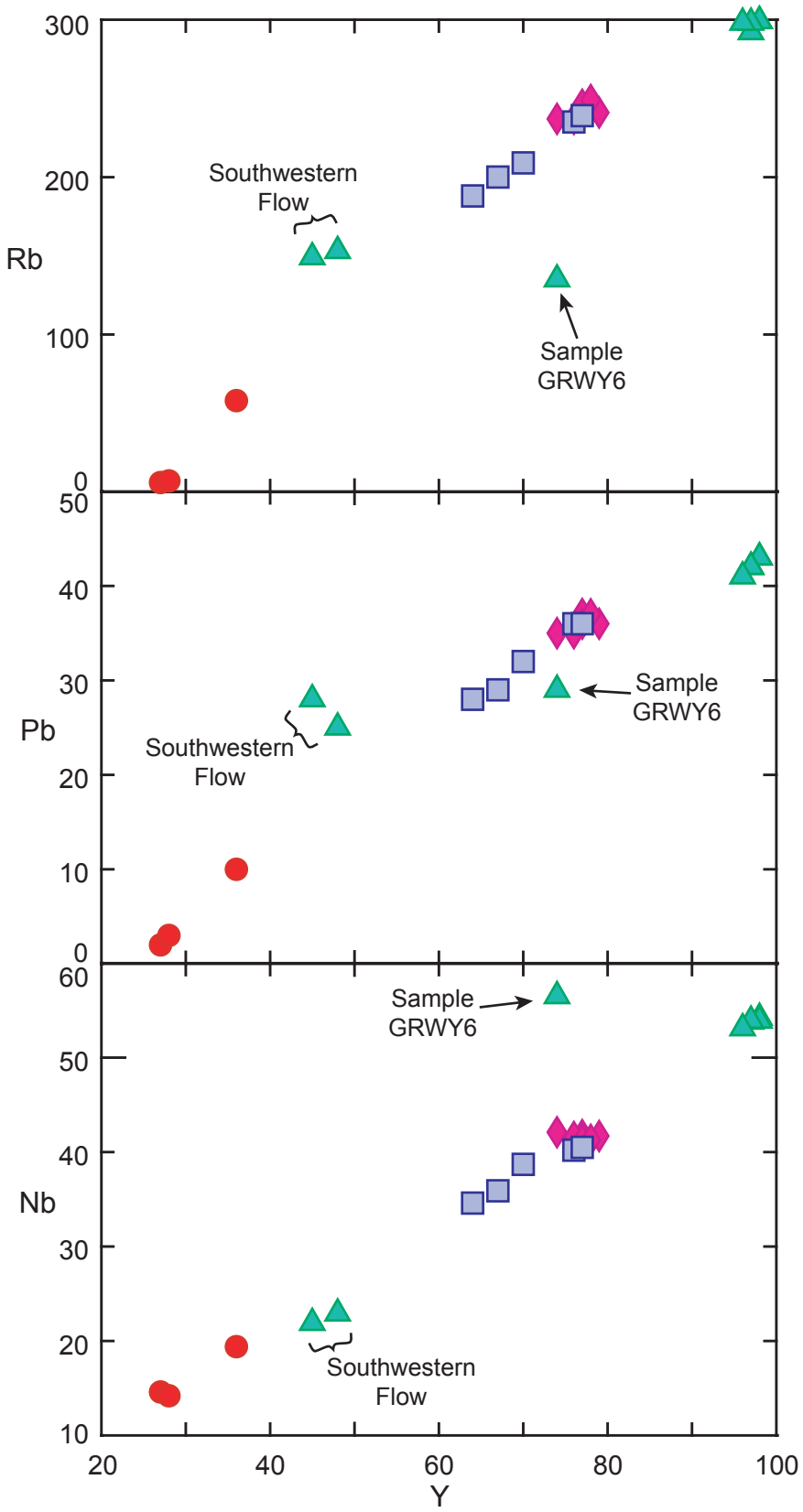

Figure 6.5. Trace element diagrams for the Gibbon River lavas (▲), Obsidian Cliff lavas (♦), Crystal Spring mingled rhyolites (■), and mafic enclaves (●) from XRF analyses.

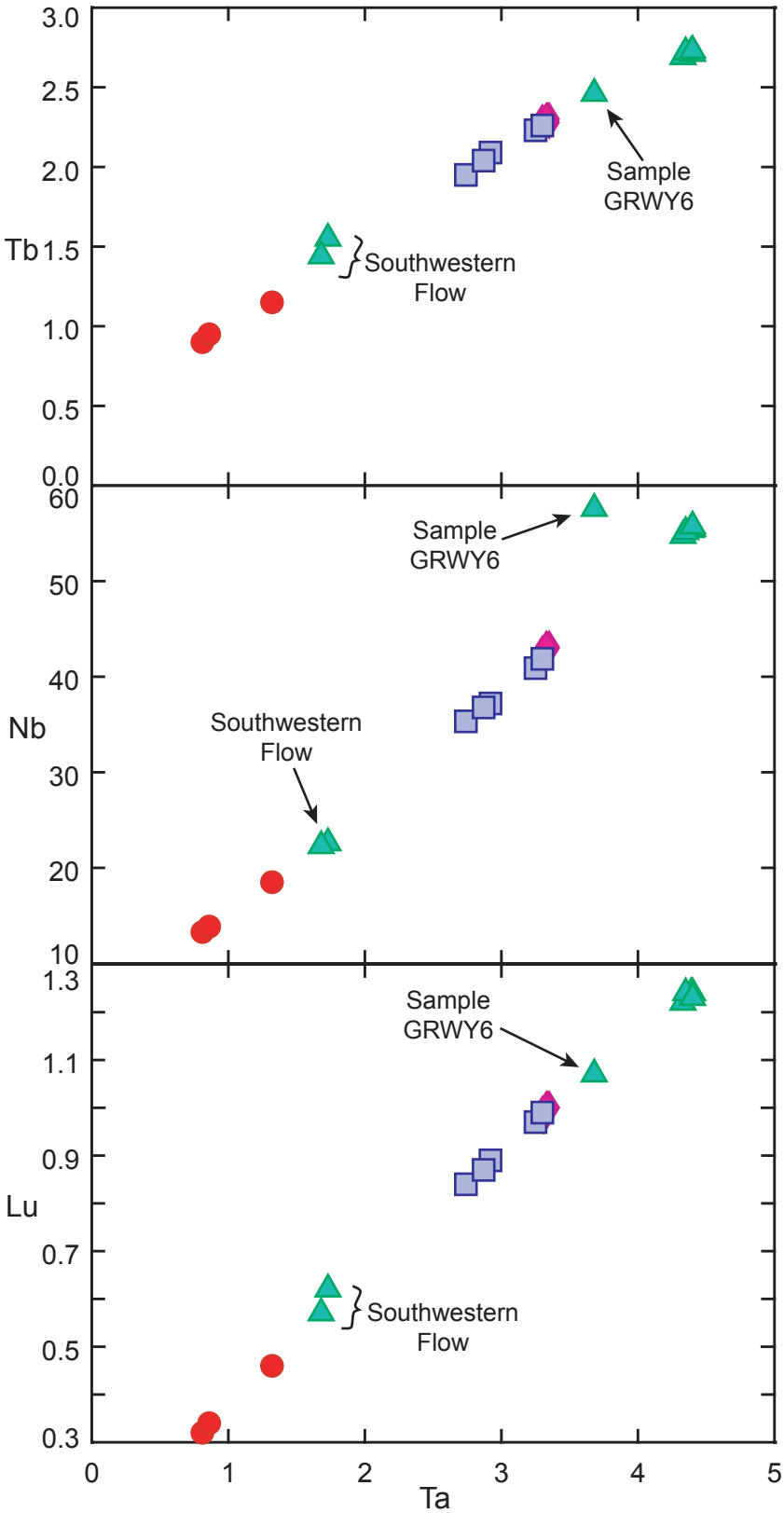

Figure 6.6. Trace element diagrams for the Gibbon River lavas (▲), Obsidian Cliff lavas (♦), Crystal Spring mingled rhyolites (■), and mafic enclaves (●) from ICP-MS analyses.

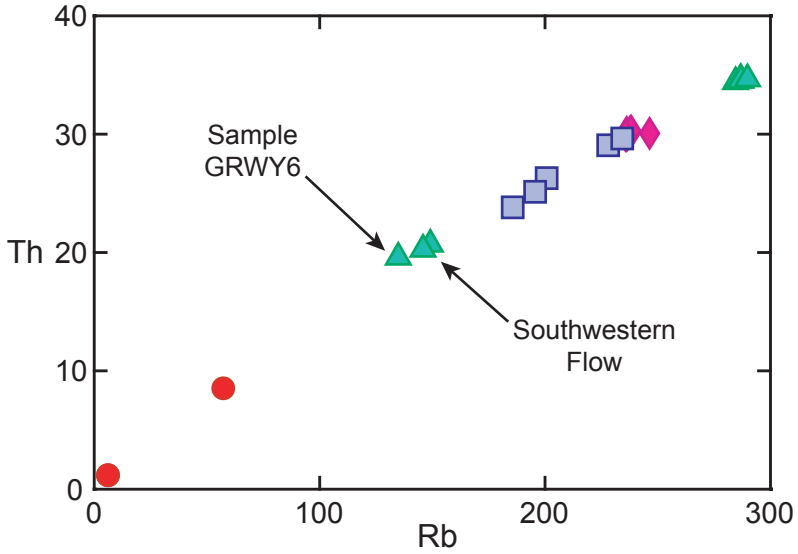

Figure 6.7. Trace element diagrams for the Gibbon River lavas (▲), Obsidian Cliff lavas (◆), Crystal Spring mingled rhyolites (▣), and mafic enclaves (●) from ICP-MS analyses.

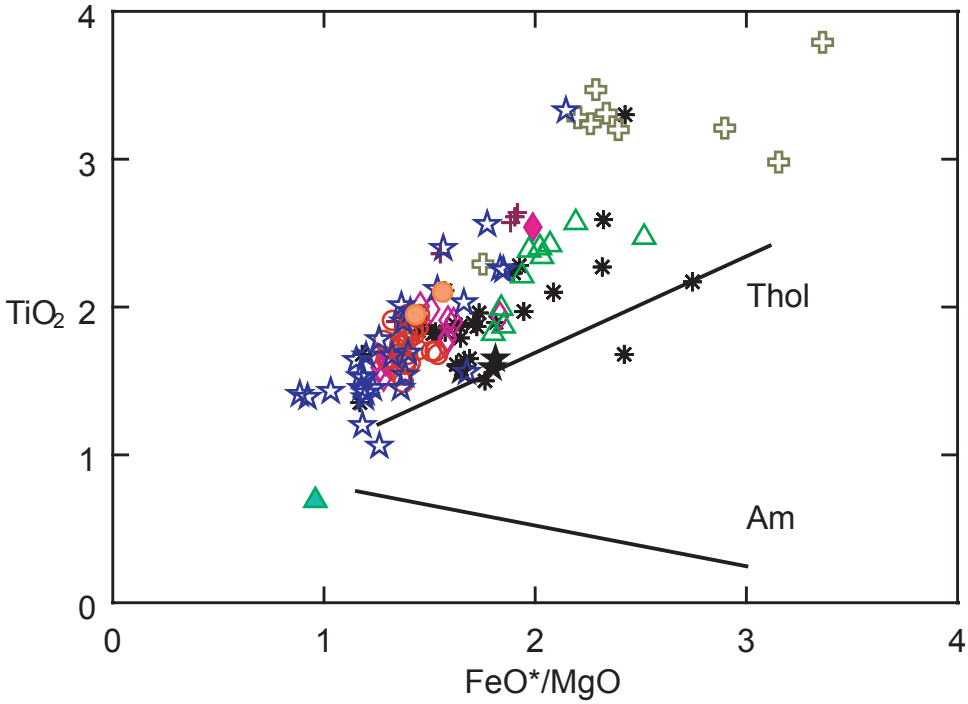

Figure 6.8. Chemical composition of Crystal Spring mafic enclaves (CSWY1E & CSWY1ME, ●) and other Yellowstone Volcanic Field basalts. Composition lines after Miyashiro (1974) represent the chemical trends of tholeiitic (Thol) basalts and the calc-alkaline (Am) basalts of the Amagi Volcano, Japan. Basalts include pre-Lava Creek Tuff basalts (✳), Falls River Basalt (+), Basalt of Grizzly Lake (◆), Basalt of Geode Creek (★), Basalt of Mariposa Lake (▲), Gerrit Basalt (☆), Madison River Basalt (△), Osprey and Hepburn Mesa Basalts (◇), Swan Lake Flat Basalt (○), and Basalts of Snake River Group (✜). Analyses are from Fenner (1938), Hamilton (1963), Hamilton (1965), Hildreth *et al.* (1991), Christiansen (2001), and Bennett (2006).

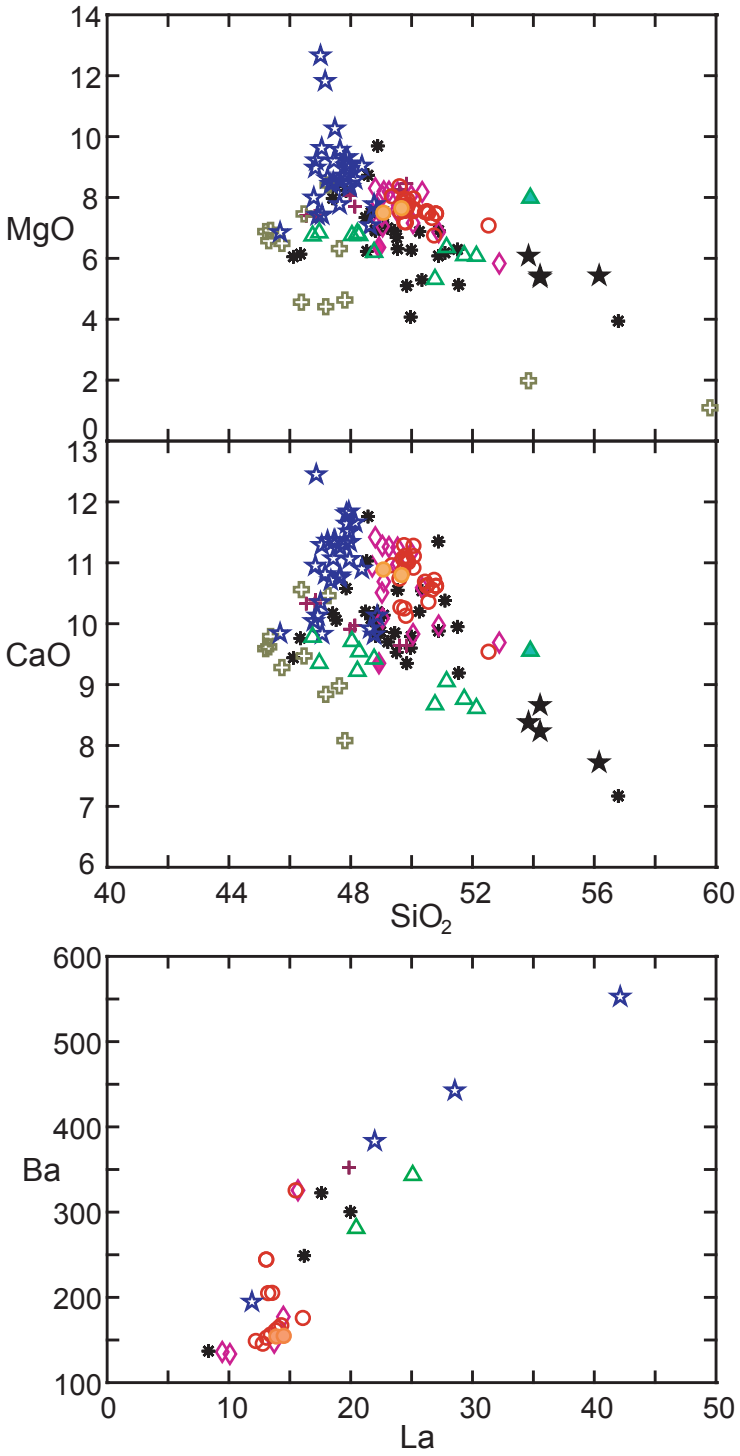

Figure 6.9. Major and trace element diagrams for the Crystal Spring mafic enclaves (CSWY1E & CSWY1ME, ●) and other Yellowstone Volcanic Field basalts. Basalts include pre-Lava Creek Tuff basalts (✳), Falls River Basalt (+), Basalt of Grizzly Lake (♦), Basalt of Geode Creek (★), Basalt of Mariposa Lake (▲), Gerrit Basalt (☆), Madison River Basalt (△), Osprey and Hepburn Mesa Basalts (◇), Swan Lake Flat Basalt (○), and Basalts of Snake River Group (✚). Analyses are from Fenner (1938), Hamilton (1963), Hamilton (1965), Hildreth *et al.* (1991), Christiansen (2001), and Bennett (2006).

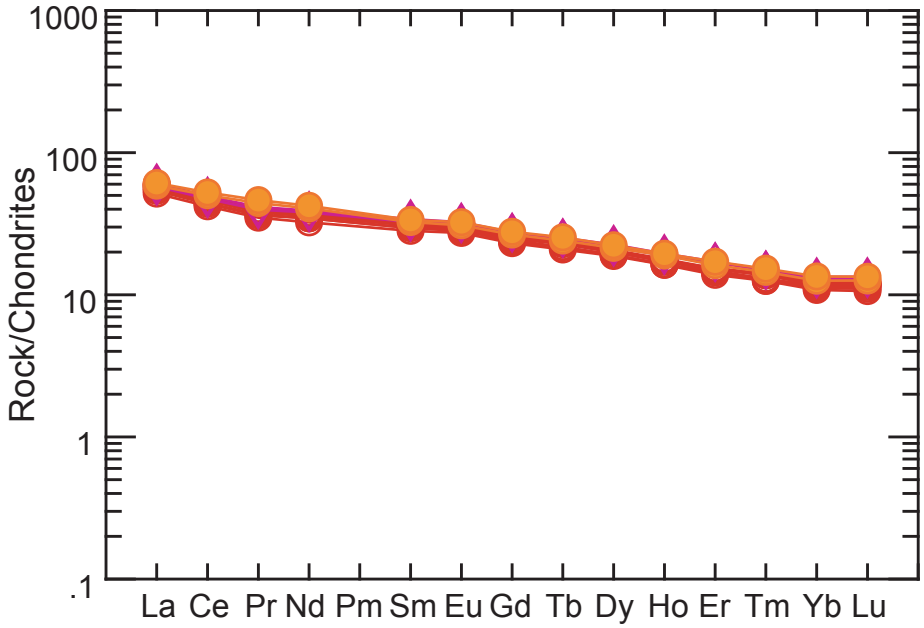

Figure 6.10. Rare earth element diagram (formatted after Sun & McDonough, 1989) for the Crystal Spring mafic enclaves (CSWY1E & CSWY1ME,●) with Swan Lake Flat Basalt (○) samples YSLF0301, YSLF0309, YSLF0311 through YSLF0314, YSLF0316, and Osprey Basalt (◊) samples YO0301 and YO0304 from Bennett (2006) for comparison.

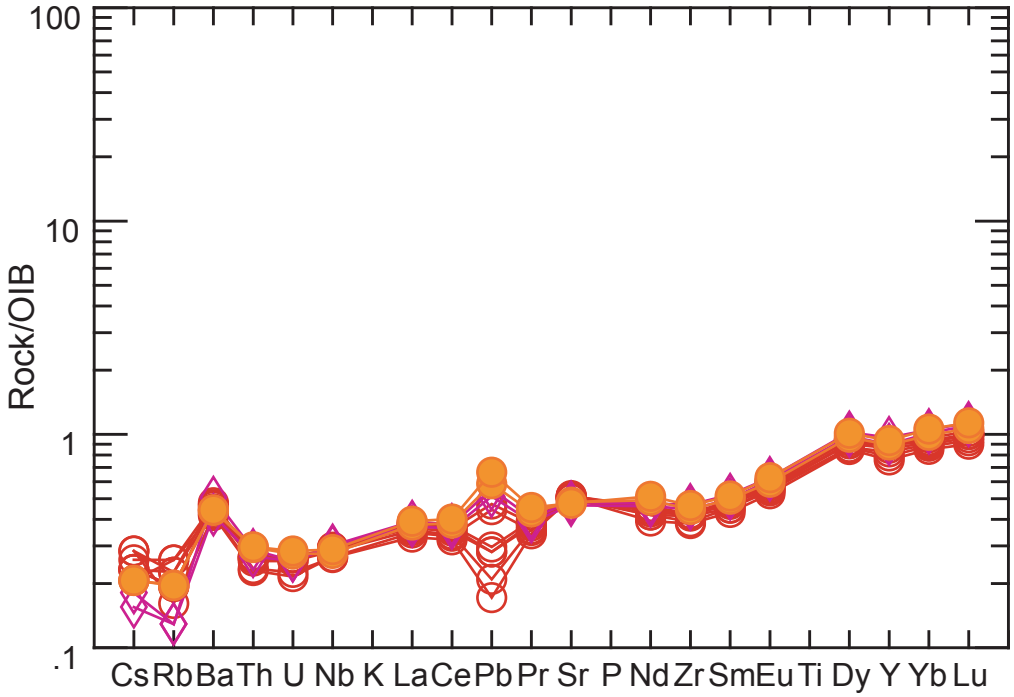

Figure 6.11. Trace element diagram (formatted after Sun & McDonough, 1989) for the Crystal Spring mafic enclaves (CSWY1E & CSWY1ME,●) with Swan Lake Flat Basalt (○) samples YSLF0301, YSLF0309, YSLF0311 through YSLF0314, YSLF0316, and Osprey Basalt (◊) samples YO0301 and YO0304 from Bennett (2006) for comparison. OIB is Ocean Island Basalt.

CHAPTER 7

PHENOCRYST GEOCHEMISTRY

To further constrain the composition and evolution of the Roaring Mountain rhyolites, thin sections from each unit were analyzed by electron microprobe. A thin section representative of each of the three Gibbon River units, as identified by petrography and geochemistry (Chapters 5 & 6), was also analyzed. Point analyses of individual minerals were measured to determine specific mineralogy. In many cases, points on both a mineral's rim and core were analyzed to evaluate changes in the magma composition during phenocryst growth. Traverse analyses of individual feldspar from the Gibbon River and Crystal Spring rhyolites, and a pyroxene from the Crystal Spring flow were done to provide further information into each magmas's chemical evolution during mineral precipitation. Analyses with measured elemental totals between 98% and 102% were considered acceptable and are included in Appendices C through F. Measurements with elemental totals less than 98% or greater than 102% were rejected and not included in further investigation.

Gibbon River Flow – Main Rhyolite

Three thin sections were analyzed from the Gibbon River rhyolites. GRWY7P was chosen to represent the main Gibbon River flow (Chapters 5 & 6). Point analyses of the cores and rims of six sanidines were chemically indistinguishable, with compositions of Or_{58} (average of all analyses) (Figure 7.1 & Table 7.4; Appendix C). Point analyses were done of the core and rim of one plagioclase (Appendix C). The core analyses are slightly more calcic oligoclase (An_{25}, average of core analyses) than the more potassic oligoclase

rims (An_{21}, average of rim analyses) (Figure 7.1 & Table 7.4; Appendix C). The pyroxenes of GRWY7P are ferroan augite ($Wo_{39}En_{24}Fs_{36}Ac_{1}$, average of all analyses) (Figure 7.2 & Table 7.4; Appendix C) and the amphiboles are ferro-actinolite (Table 7.4; Appendix C). GRWY7P also contains magnetite that has been altered to ulvöspinel (Table 7.4; Appendix C).

Four sanidines and one plagioclase grain from GRWY7P were analyzed by rim to rim traverses. The plagioclase composition is slightly more calcic oligoclase (An_{28}; most calcic analysis of traverse) at the core and becomes more sodic oligoclase (An_{21}; most sodic analysis at edge of traverse) at the edges (Figure 7.3; Appendix D). All four analyzed sanidines have a relatively similar composition across the crystal and all are chemically indistinguishable with compositions averaging Or_{60} (Figure 7.4 & Table 7.1; Appendix D). Sanidine S5 has one edge that is more Na-rich than the main portion of the crystal (Figure 7.5; Appendix D).

The BaO profiles of the four sanidines analyzed from GRWY7P do show zoning in three of the phenocrysts (Figure 7.6; Appendix D). Sanidine S2 has a low-Ba core that increases before gradually decreasing to a low-Ba composition at the crystal's edge (Figure 7.7; Appendix D). Sanidine S3 has a high-Ba core that gradually decreases towards the edge and then increases again right at the crystal rim (Figure 7.7; Appendix D). The BaO composition of sanidine S5 has a similar pattern to S3, with a high-Ba core that gradually decreases towards the edge and then, increases at the phenocryst rim (Figure 7.7; Appendix D). The BaO composition of S6 does show changes in Ba across the crystal but the pattern is not symmetrical from rim to rim (Figure 7.7; Appendix D). The Ba concentration along the analysis traverse of S6 increases from left to right (Figure

7.7; Appendix D). The Ba concentration of most of the rims of the analyzed sanidines range between ~0.4 to 0.6 wt. % BaO (Figure 7.6; Appendix D).

Table 7.1. Average composition of sanidines analyzed from sample GRWY7P

Sanidine	Composition
S2	$An_2Ab_{39}Or_{59}$ [a]
S3	$An_2Ab_{39}Or_{59}$ [a]
S5	$An_2Ab_{39}Or_{59}$ [a]
S6	$An_2Ab_{40}Or_{58}$ [a]

[a] average of traverse analyses

Gibbon River Flow – Southwestern Rhyolite

GRWY1 was analyzed from the southwestern flow (Chapters 5 & 6). Point analyses of the cores and rims of six sanidines were done, and the cores (Or_{54}, average of core analyses) are slightly more potassic than the rims (Or_{53}, average of rim analyses) (Figure 7.1 & Table 7.4; Appendix C). Point analyses of the core and rim of one plagioclase produced chemically indistinguishable An_{27} (average of all analyses) oligoclase results (Figure 7.1 & Table 7.4; Appendix C). GRWY1 contains fayalite (Fo_3Fa_{97}) and magnetite that has been altered to ulvöspinel (Table 7.4; Appendix C). The pyroxenes in GRWY1 are ferroan augite ($Wo_{40}En_{26}Fs_{34}Ac_1$) (Figure 7.2 & Table 7.4; Appendix C).

Five sanidines from GRWY1 were analyzed from rim to rim. Four of the five analyzed sanidines exhibit distinct compositional zoning (Figure 7.8; Appendix D). Sanidines S1 and S2 have anorthoclase inclusions (Or_{32} and Or_{34}, respectively; Table 7.2) surrounded by sanidine rims of relatively similar composition (Or_{50} and Or_{53}, respectively; Table 7.2) (Figure 7.9; Appendix D). Sanidine S4 grades in composition from Or_{55} (Table 7.2) at the core to a more sodic Or_{40} (Table 7.2) composition at the grain edge (Figure 7.9; Appendix D). Sanidine S4 overlaps in composition with the rims

of sanidines S1 and S2 (Figure 7.9; Appendix D). The majority of sanidine S5 is a relatively similar Or_{58} (Table 7.2) composition with a rim that becomes more sodic (Or_{43}, Table 7.2) towards the edge of the grain (Figure 7.10; Appendix D). Sanidine S6 has an oligoclase inclusion (An_{20}, Table 7.2) and a compositional zone of sanidine (Or_{57}, Table 7.2) (Figure 7.10) that is chemically indistinguishable from the majority of sanidine S5 (Figure 7.8; Appendix D). Sanidine S6 also has a compositional rim that becomes more sodic (Or_{44}, Table 7.2) towards the edge of the grain (Figure 7.10; Appendix D). In fact, the most sodic analysis at the edge of both sanidine S6 and S5 are chemically indistinguishable (Figure 7.8 & Table 7.2; Appendix D).

Three of the BaO profiles of the five sanidines analyzed from GRWY1 are asymmetrical from rim to rim (Figure 7.11; Appendix D). The Ba concentration of sanidine S1 increases from the left edge to a BaO high and then gradually decreases across the center of the crystal before suddenly dropping off to zero (Figure 7.12; Appendix D). The region of Ba absence corresponds to the anorthoclase inclusion and the right edge of S1 (Figure 7.12; Appendix D). Sanidine S2 has a low-Ba concentration across the majority of the crystal, with slight variation and like S1, suddenly drops to zero along the far right side of the phenocryst (Figure 7.12; Appendix D). This area of no Ba, like S1, corresponds to the anorthoclase inclusion and the right edge of S2 (Figure 7.12; Appendix D). The BaO profile of sanidine S4 is fairly symmetrical, with a relatively stable BaO composition across the center of the phenocryst and a slight drop in Ba at the crystal's edges (Figure 7.12; Appendix D). Sanidine S5 has an asymmetrical BaO pattern that from left to right gradually decreases from a high-Ba concentration to a low-Ba concentration at the right edge of the phenocryst (Figure 7.12; Appendix D). The BaO

profile of sanidine S6 generally reflects the major element composition of S6 (Figure 7.13; Appendix D). No Ba was measured along the region of the oligoclase inclusion and along the majority of the phenocryst the Ba composition is highly variable, slightly decreasing towards the crystal edges, between 0.2 and 0 wt. % BaO (Figure 7.13; Appendix D). At the edges of sanidine S6, the Ba composition increases sharply, corresponding to the decrease in Or % at the phenocryst edges (Figure 7.13; Appendix D).

Table 7.2. Compositional zones of sanidines analyzed from sample GRWY1

Sanidine	Inclusion Composition	Inner Zone Composition	Rim Composition
S1	$An_5Ab_{65}Or_{30}$ [a]	-	$An_2Ab_{49}Or_{49}$ [b]
S2	$An_5Ab_{63}Or_{32}$ [a]	-	$An_2Ab_{46}Or_{52}$ [b]
S4	-	$An_3Ab_{44}Or_{53}$ [c]	$An_3Ab_{58}Or_{39}$ [d]
S5	-	$An_2Ab_{41}Or_{57}$ [e]	$An_3Ab_{55}Or_{42}$ [d]
S6	$An_{18}Ab_{74}Or_8$ [a]	$An_2Ab_{42}Or_{56}$ [f]	$An_4Ab_{54}Or_{42}$ [d]

[a] most sodic analysis of traverse
[b] average of traverse analyses without anorthoclase inclusion analyses
[c] most potassic analysis at center of traverse
[d] most sodic analysis at edge of traverse
[e] average of traverse analyses without rim analyses
[f] average of traverse analyses without oligoclase inclusion and rim analyses

Gibbon River Flow – Sample GRWY6

Thin section GRWY6 from the Gibbon River flow was determined to be chemically distinct based on its petrography and geochemistry (Chapters 5 & 6). Thin section GRWY6 was further analyzed as a separate unit within the Gibbon River flow. Point analyses of the cores and rims of four sanidines produced chemically indistinguishable Or_{44} (average of all analyses) sanidine results (Figure 7.1 & Table 7.4; Appendix C). Point analyses of the cores and rims of two amphiboles were done. The amphibole cores

are more magnesian than the rims, however, both cores and rims were ferro-actinolite (Appendix C). Two of the three pyroxenes analyzed are hedenbergite ($Wo_{41}En_{10}Fs_{48}Ac_1$, average) and the other is ferrosilite ($Wo_3En_{27}Fs_{70}$) (Figure 7.2 & Table 7.4; Appendix C). GRWY6 also contains two distinct olivine compositions (Fo_3Fa_{97} & $Fo_{29}Fa_{71}$), magnetite that has been altered to ulvöspinel, and ilmenite (Table 7.4; Appendix C).

Three sanidines from GRWY6 were analyzed from rim to rim by electron microprobe. Sanidines S2 and S4 have a relatively similar composition across the grain and are chemically indistinguishable Or_{47} sanidines (Figure 7.14 & Table 7.3; Appendix D). The largest grain, sanidine S1 has three compositional zones (Figure 7.15 & Table 7.3; Appendix D). The core is variable in composition (Figure 7.15), generally varying around a similar composition (Or_{43}; assumed to be the average composition) but includes compositions up to Or_{52} and anorthoclase (An_9) inclusions (Figure 7.15 & Table 7.3; Appendix D). Surrounding the Na-rich core of S1 is a relatively compositionally similar, more potassic sanidine zone that is rimmed by a more sodic sanidine at the edges (Figure 7.15 & Table 7.3; Appendix D). The composition of the core and the edge of S1 are chemically indistinguishable (Figure 7.14 & Table 7.3; Appendix D).

Two of the three sanidines analyzed have asymmetrical rim to rim BaO profiles (Figure 7.16; Appendix D). The highest Ba concentration of sanidine S1 is at the very edges of the phenocryst (Figure 7.17; Appendix D). From left to right, the Ba-concentration of S1 is variable between 1.0 to 0.8 wt.% BaO across the majority of the phenocryst, then drops to a low-Ba composition before rising slightly and compositionally steadying out towards the phenocryst edge (Figure 7.17; Appendix D). The lower Ba concentration of S1 corresponds to the right-side of the inner potassic zone

(Figure 7.17; Appendix D). The BaO profile of sanidine S2 is also asymmetrical, with the Ba concentration gradually increasing from the center of the phenocryst towards the edges (Figure 7.17; Appendix D). Along the right-side of the BaO traverse, the Ba continues to increase to the phenocryst edge (Figure 7.17; Appendix D). Towards the left-side of the phenocryst, the Ba concentration decreases towards the sanidine edge (Figure 7.17; Appendix D). The BaO composition of sanidine S4 is relatively constant around 0.2 wt.% BaO (Figure 7.17; Appendix D).

Table 7.3. Compositional zones of sanidines analyzed from sample GRWY6

Sanidine	Core Composition	Inner Zone Composition	Rim Composition
S1	$An_4Ab_{55}Or_{41}$ [a]	$An_3Ab_{50}Or_{47}$ [b]	$An_4Ab_{56}Or_{40}$ [c]
S2	-	$An_2Ab_{53}Or_{45}$ [d]	-
S4	-	$An_2Ab_{52}Or_{46}$ [d]	-

[a] average of compositionally variable core analyses
[b] average of compositionally similar rim analyses
[c] most sodic analysis at edge of traverse
[d] average of traverse analyses

Table 7.4. Summary of compositions of Gibbon River rhyolite phenocrysts

Sample	Sanidine Cores	Sanidine Rims	Plagioclase Cores	Plagioclase Rims
GRWY1	$An_2Ab_{45}Or_{53}$	$An_3Ab_{46}Or_{51}$	$An_{24}Ab_{69}Or_7$	$An_{25}Ab_{68}Or_7$
GRWY6	$An_4Ab_{54}Or_{42}$	$An_4Ab_{54}Or_{42}$	-	-
GRWY7O	$An_2Ab_{41}Or_{57}$	$An_2Ab_{41}Or_{57}$	$An_{23}Ab_{70}Or_7$	$An_{19}Ab_{71}Or_{10}$

Sample	Pyroxene	Amphibole	Olivine	Magnetite	Ilmenite
GRWY1	$Wo_{40}En_{26}Fs_{34}Ac_1$ ferroan augite	-	$Fo_3Fa_{94}Tp_3$ fayalite	present	-
GRWY6	$Wo_{41}En_{10}Fs_{48}Ac_1$ hedenbergite; $Wo_3En_{27}Fs_{70}$ ferrosilite	ferro-actinolite	$Fo_3Fa_{94}Tp_3$ fayalite; $Fo_{28}Fa_{69}Tp_3$	present	present
GRWY7O	$Wo_{39}En_{24}Fs_{36}Ac_1$ ferroan augite	ferro-actinolite	-	present	-

"Present" indicates the mineral was identified by electron microprobe analysis (Appendix C & D).

Obsidian Cliff Rhyolite

The thin section for OCWY6 was analyzed by electron microprobe, however, all microphenocrysts were less than 10 μm in diameter. Very poor analyses (measured elemental totals less than 97%) qualitatively indicate that the microphenocrysts are feldspar, pyroxene, and olivine.

While attempting to separate zircons from Obsidian Cliff sample OCWY14, a dark orange, heavy mineral was collected. This sample was analyzed in a scanning electron microscope (SEM) and identified as fayalite (Figure 7.18). These fayalites are between 150 and 53 μm in size.

Crystal Spring Rhyolite

Three thin sections from the Crystal Spring rhyolite samples were analyzed by electron microprobe, CSWY1, CSWY2, and CSYW4. Point analyses of the cores and rims of two plagioclase phenocrysts from CSWY1 were done. The core analyses were bytownite (An_{72}, average of core analyses) and the rims were labradorite (An_{70}, average of rim analyses) (Figure 7.19; Appendix E). A rim to rim traverse analysis of a pyroxene phenocryst in CSWY2 was compositionally enstatite with a Mg-rich core ($Wo_4En_{77}Fs_{19}$; average of core analyses) and Fe-rich rims ($Wo_4En_{70}Fs_{26}$; average of rim analyses) (Figure 7.20; Appendix F). Poor analyses (measured elemental totals less than 98%) of phenocrysts within CSWY4 indicate the Crystal Spring obsidians also contain microphenocrysts of feldspar, olivine, and iron oxides.

Plagioclase Traverse Analyses

Three plagioclase grains from CSWY1 were analyzed from rim to rim along two perpendicular traverses (Figure 7.21; Appendix F). The edges of all three plagioclase grains are indistinct and optically grade into the surrounding glass matrix (viewed under BSE, CL, and SEM). To assure the traverse only analyzed the plagioclase grain, the stoichiometric chemistry of the analyses at the grains' edges were verified as plagioclase. If an analysis was not plagioclase in composition (having 20 ± 0.20 oxygen in its formula), then it was not included in the data set (Appendix F). Nine analyses were excluded from the plagioclase traverse data for sample CSWY1; nearly all analyses excluded were either the first or last analyses of the traverse (CSWY1-5PB had one non-edge analysis that was not plagioclase).

The analyses of traverse A of CSWY1-P1 are a compositionally similar bytownite (An_{72}) across the middle of the grain (Figure 7.22 & Table 7.5; Appendix F). Continuing towards the edges, the plagioclase composition of traverse A varies between bytownite composition (An_{73}) and more Na-rich labradorite compositions (An_{66}) (Figure 7.22 & Table 7.5; Appendix F). At the crystal edges of traverse A, the plagioclase composition decreases in Ca content to a high-Na labradorite (An_{54}) (Figure 7.22 & Table 7.5; Appendix F). The analyses of traverse B of CSWY1-P1 have a bytownite core (An_{76}) that decrease to a low-Ca bytownite composition (An_{72}) that overlaps in composition with the middle analyses of traverse A (Table 7.22 & Table 7.5; Appendix F). The analyses of traverse B maintain the low-Ca bytownite composition to the edge of the grain, except for a few irregular decreases in Ca to a Na-rich labradorite composition (Figure 7.22 & Table 7.5; Appendix F).

The analyses of traverse A along CSWY1-P5 vary in composition between a low-Ca bytownite (An_{73}) of similar composition to the middle analyses and low-Ca composition of CSWY1-P1 (A & B, respectively) and a very low-Ca bytownite composition (An_{70}) (Figure 7.22 & Table 7.5; Appendix F). The analyses of traverse A (CSWY1-P5) decrease in Ca-concentration at the edges (Figure 7.22 & Table 7.5; Appendix F). The analyses of traverse B (CSWY1-P5) are a compositionally similar An_{71} across the entire grain with a slight gradation in composition from low-Ca bytownite (An_{75}) to high-Na labradorite (An_{69}) from left to right (Figure 7.22 & Table 7.5; Appendix F). The analyses show a drop in Ca-concentration to a labradorite composition (An_{67}) at the grain edges (Figure 7.22 & Table 7.5; Appendix F).

The analyses of both traverse A and B of CSWY1-P6 have a bytownite center (An_{80} & An_{82}, traverse A & B, respectively) surrounded by a compositionally similar low-Ca bytownite (An_{74} & An_{74}, traverse A & B, respectively) across the majority of the crystal (Figure 7.22 & Table 7.5; Appendix F). One edge of traverse B increases in Ca concentration (~5% higher An composition) to a An_{78} bytownite plateau (Figure 7.22; Appendix F). The composition of the other crystal edge of traverse B decreases in Ca to a high-Ca andesine (An_{49}), and the crystal edges of traverse A decrease in Ca concentration to labradorite compositions (An_{66}) (Figure 7.22 & Table 7.5; Appendix F).

Table 7.5. Compositional zones of plagioclases analyzed from sample CSWY1

Plagioclase Traverse	Core Composition	Constant Inner Zone Composition	Variable Inner Zone Composition	Rim Composition
1PA	-	$An_{71}Ab_{28}Or_1$ [a]	$An_{72}Ab_{27}Or_1$ / $An_{65}Ab_{33}Or_2$ [b] ave.: $An_{70}Ab_{29}Or_1$ [c]	$An_{53}Ab_{45}Or_3$ [d]
1PB	$An_{75}Ab_{24}Or_1$ [a]	$An_{71}Ab_{28}Or_1$ [a] sep.: $An_{72}Ab_{28}Or_1$ / $An_{66}Ab_{33}Or_1$ [e]	-	-
5PA	-	-	$An_{72}Ab_{27}Or_1$ / $An_{70}Ab_{30}Or_1$ [b] ave.: $An_{71}Ab_{29}Or_1$ [c]	$An_{60}Ab_{38}Or_2$ [d]
5PB	-	$An_{70}Ab_{29}Or_1$ [a] from $An_{74}Ab_{25}Or_1$ [f] to $An_{68}Ab_{31}Or_1$ [g]	-	$An_{66}Ab_{33}Or_2$ [h]
6PA	$An_{79}Ab_{20}Or_0$ [i]	$An_{74}Ab_{26}Or_0$ [a]	-	$An_{65}Ab_{34}Or_1$ [h]
6PB	$An_{82}Ab_{18}Or_0$ [j]	$An_{73}Ab_{26}Or_1$ [a]	plateau: $An_{78}Ab_{22}Or_1$ [k]	$An_{48}Ab_{49}Or_3$ [d]

[a] average of compositionally similar middle analyses
[b] average of bytownite compositional zone analyses and average of labradorite compositional zone analyses in compositionally variable core region, respectively
[c] average of compositionally variable core analyses
[d] most sodic analysis at edge of traverse
[e] compositional averages with Ca decreases separated and compositions calculated as in b. above
[f] most calcic analysis at edge of compositionally similar middle analyses of traverse
[g] most sodic analysis at edge of compositionally similar middle analyses of traverse
[h] average of edge analyses
[i] most calcic analysis of traverse
[j] average of most calcic analyses at core of traverse
[k] average of compositional plateau at edge of traverse

Crystal Spring Mafic Enclaves

Thin section CSWY1E was chosen as representative of the Crystal Spring mafic enclaves. Point analyses of the cores and rims of five plagioclase grains were done. The core analyses are bytownite (An_{72}, average of core analyses) in composition and the rims are more sodic labradorite (An_{65}, average of rim analyses) (Figure 7.19; Appendix E). The composition of CSWY1E plagioclase is chemically indistinguishable from the

composition of the plagioclase analyzed from CSWY1 (Figure 7.19; Appendix E). Point analyses of the cores and rims of the olivine phenocrysts are all forsterite and the rims are more iron-rich than the cores ($Fo_{77}Fa_{23}$ cores; $Fo_{63}Fa_{37}$ rims; averages of core and rim analyses, respectively) (Appendix E). The majority of the point analyses of pyroxene phenocrysts are augite ($Wo_{37}En_{45}Fs_{17}Ac_{1}$), except one phenocryst that is pigeonite ($Wo_{8}En_{57}Fs_{35}$) (Figure 7.20; Appendix E). CSWY1E also contains magnetite (Appendix E).

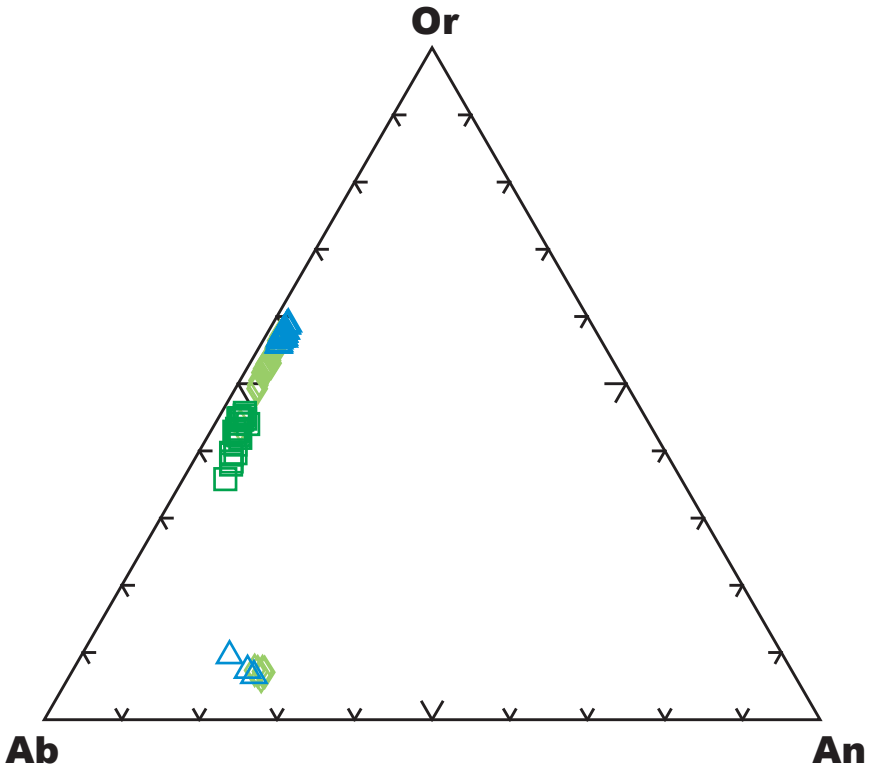

Figure 7.1. Electron microprobe point analyses of feldspar compositions of GRWY7P (△), GRWY1 (◊), and GRWY6 (□).

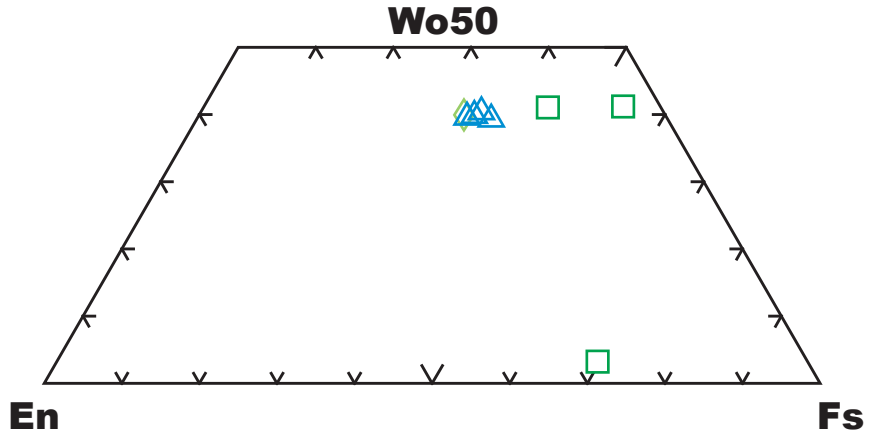

Figure 7.2. Electron microprobe analyses of pyroxene compositions of GRWY7P (△), GRWY1 (◊), and GRWY6 (□).

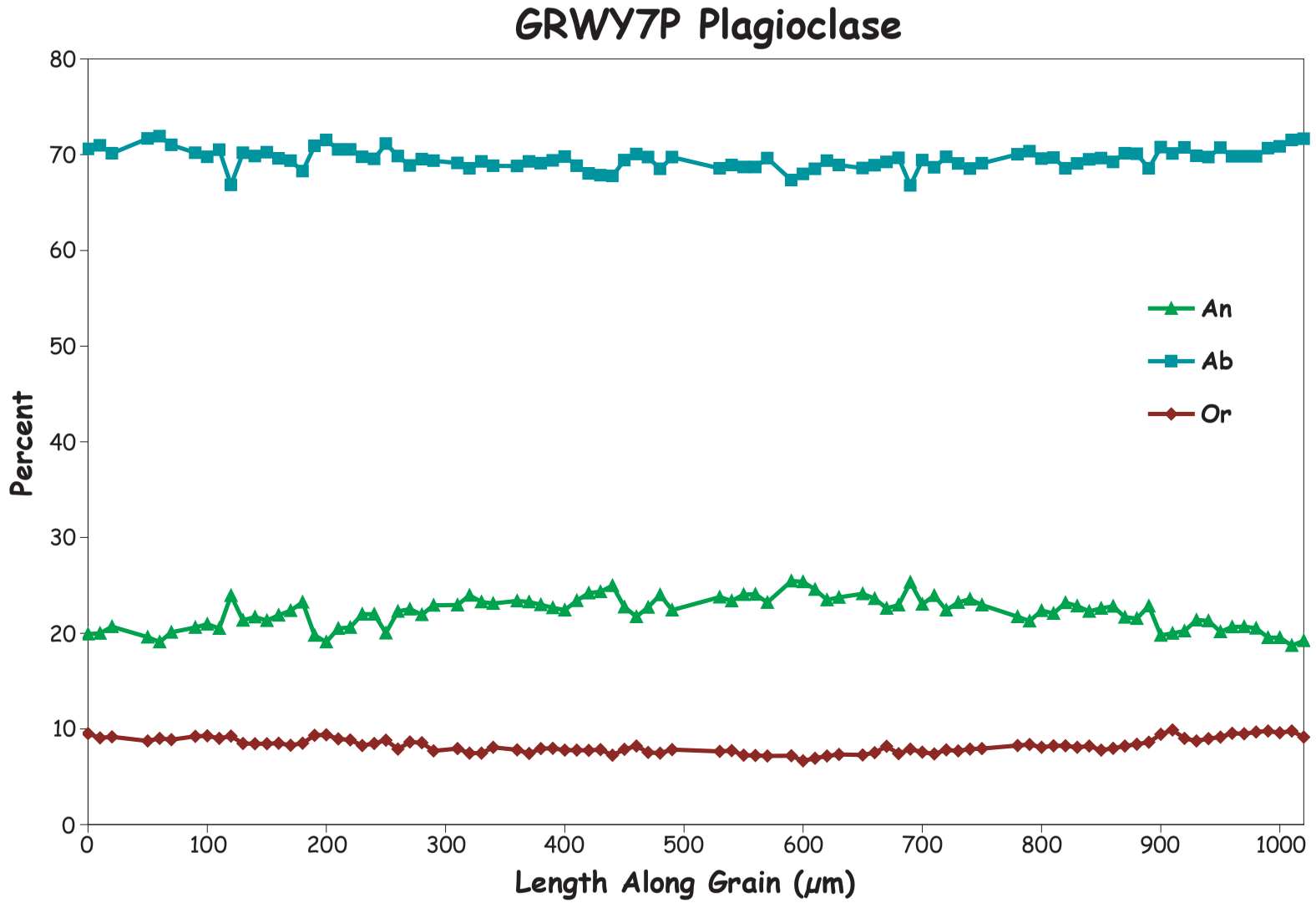

Figure 7.3. Electron microprobe traverse analyses of a plagioclase from GRWY7P. Traverses are from rim to rim.

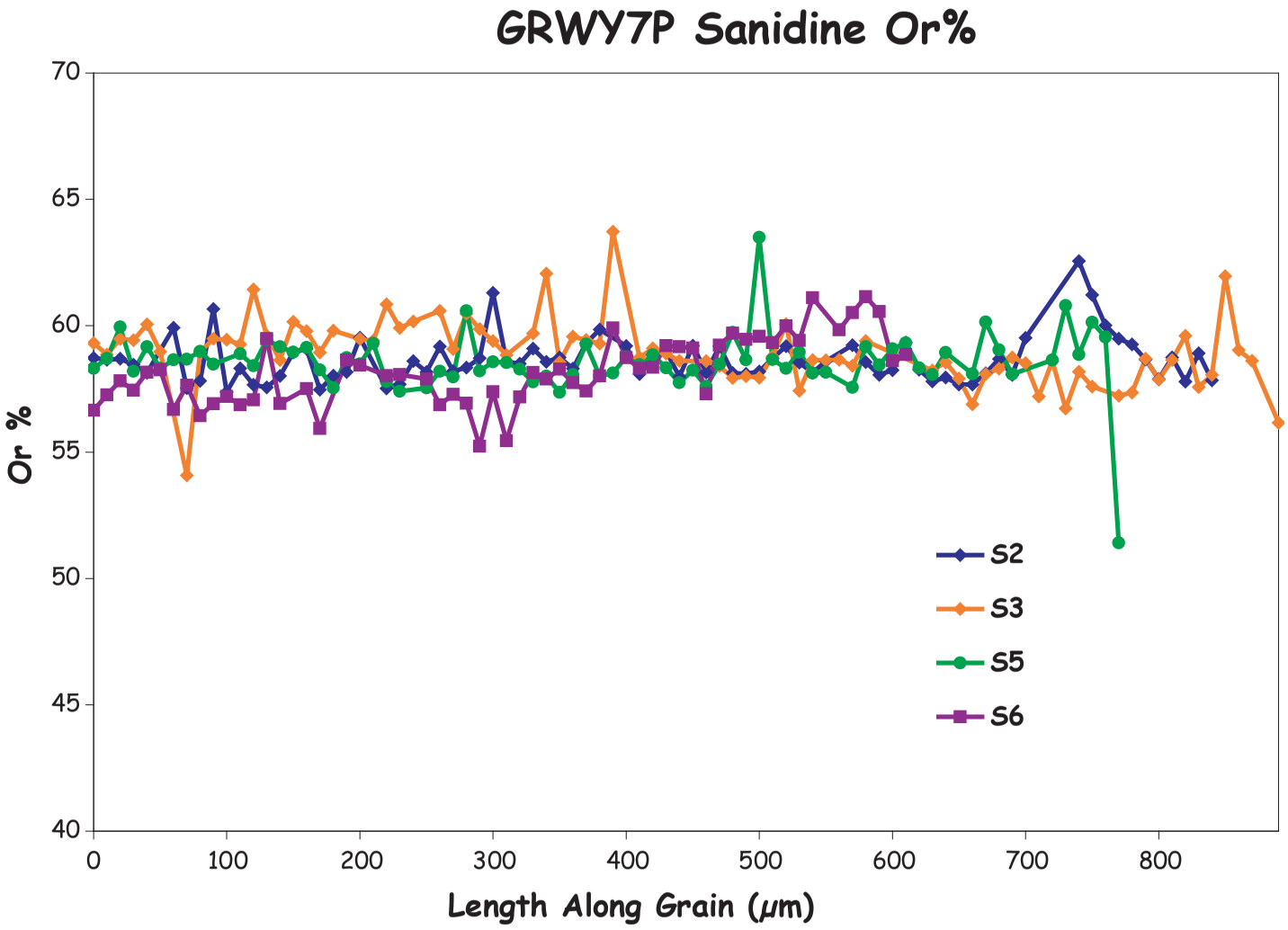

Figure 7.4. Electron microprobe traverse analyses of the Or composition of 4 sanidines from GRWY7P, presented together for comparison. Traverses are from rim to rim.

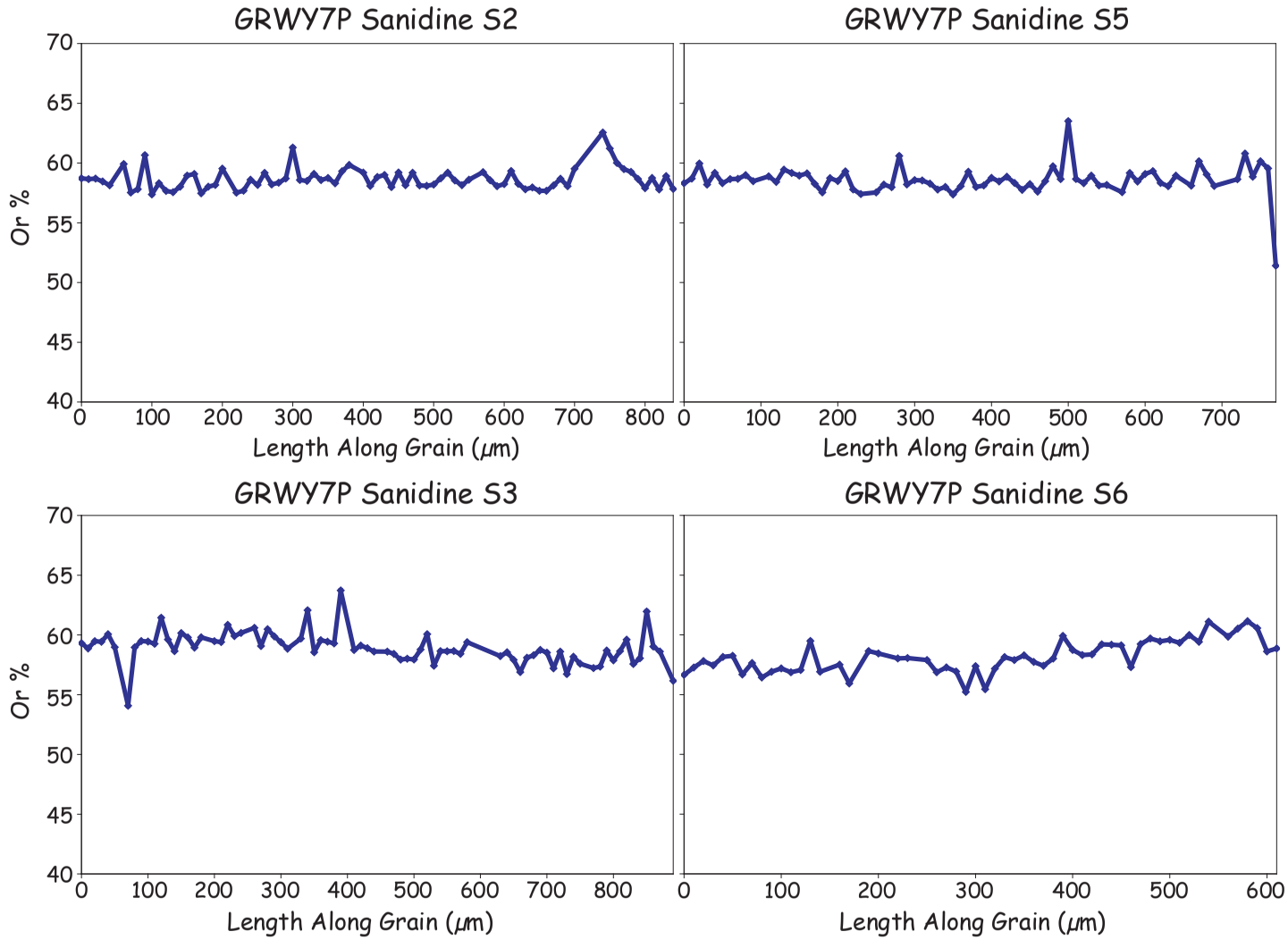

Figure 7.5. Detail of electron microprobe traverse analyses of the Or composition of 4 sanidines from GRWY7P. Traverses are from rim to rim.

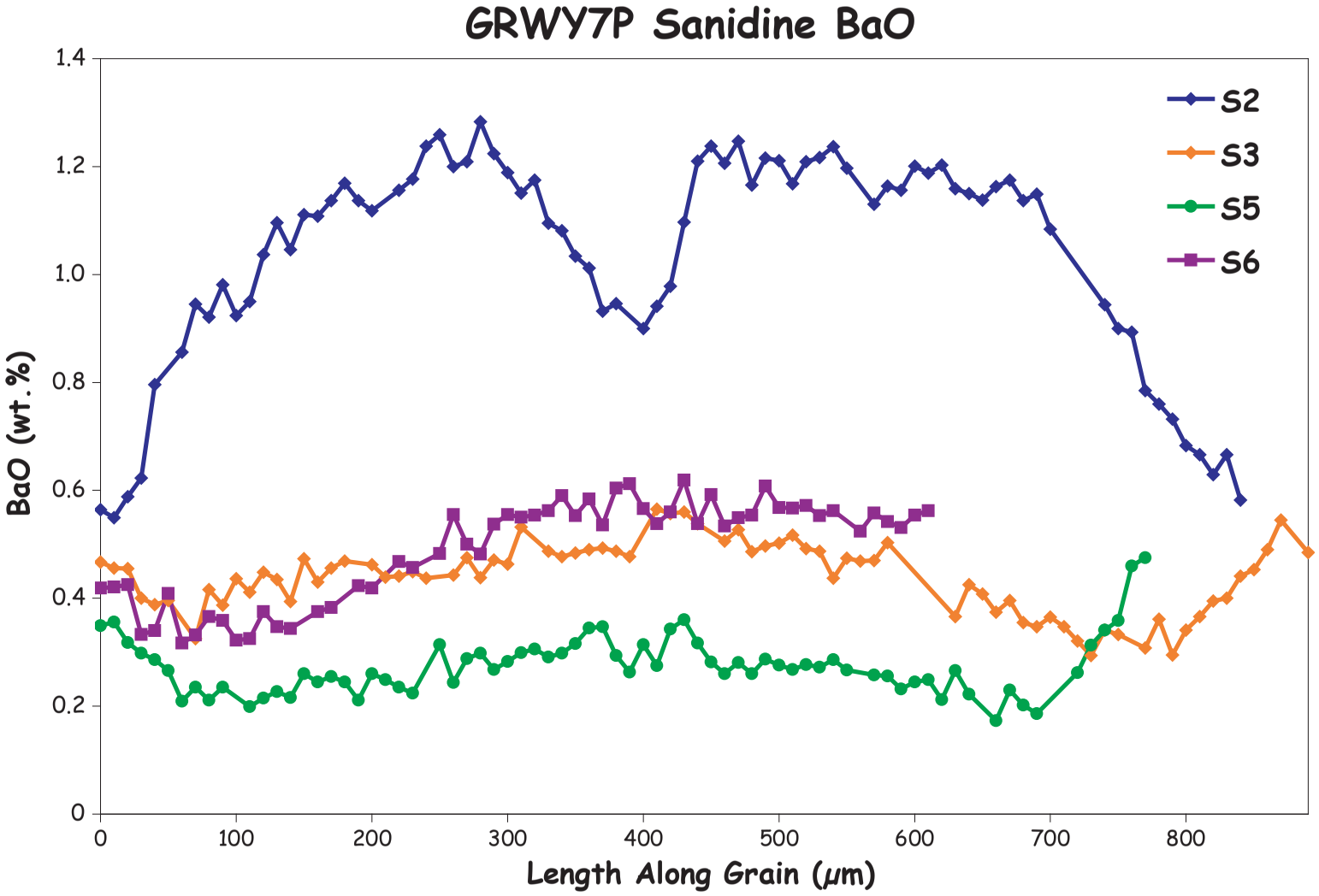

Figure 7.6. Electron microprobe traverse analyses of the BaO composition of 4 sanidines from GRWY7P, presented together for comparison. Traverses are from rim to rim.

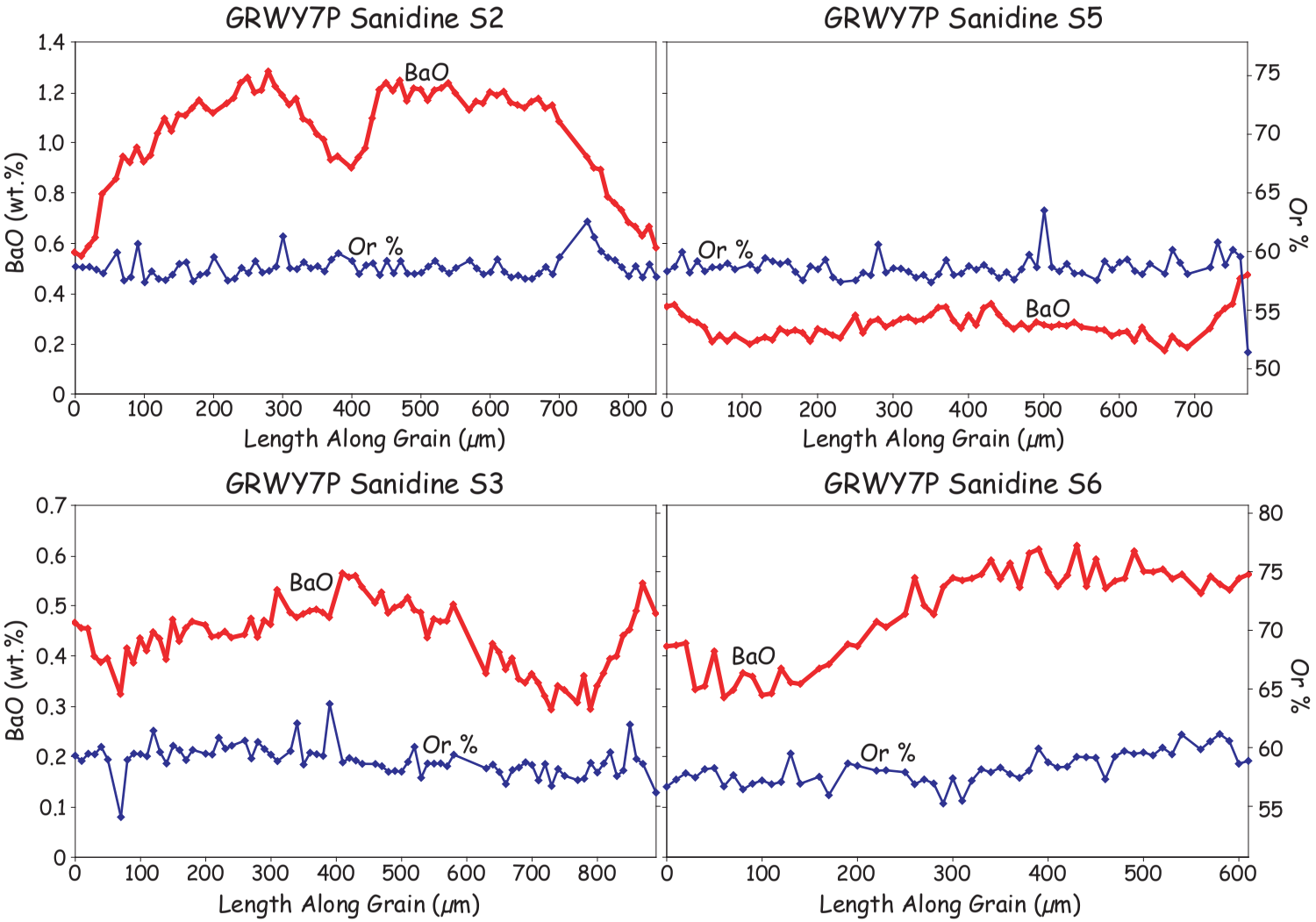

Figure 7.7. Detail of electron microprobe traverse analyses of the BaO composition (red, thick line) of 4 sanidines from GRWY7P overlaid with the Or composition (blue, thin line) of those sanidines. Traverses are from rim to rim.

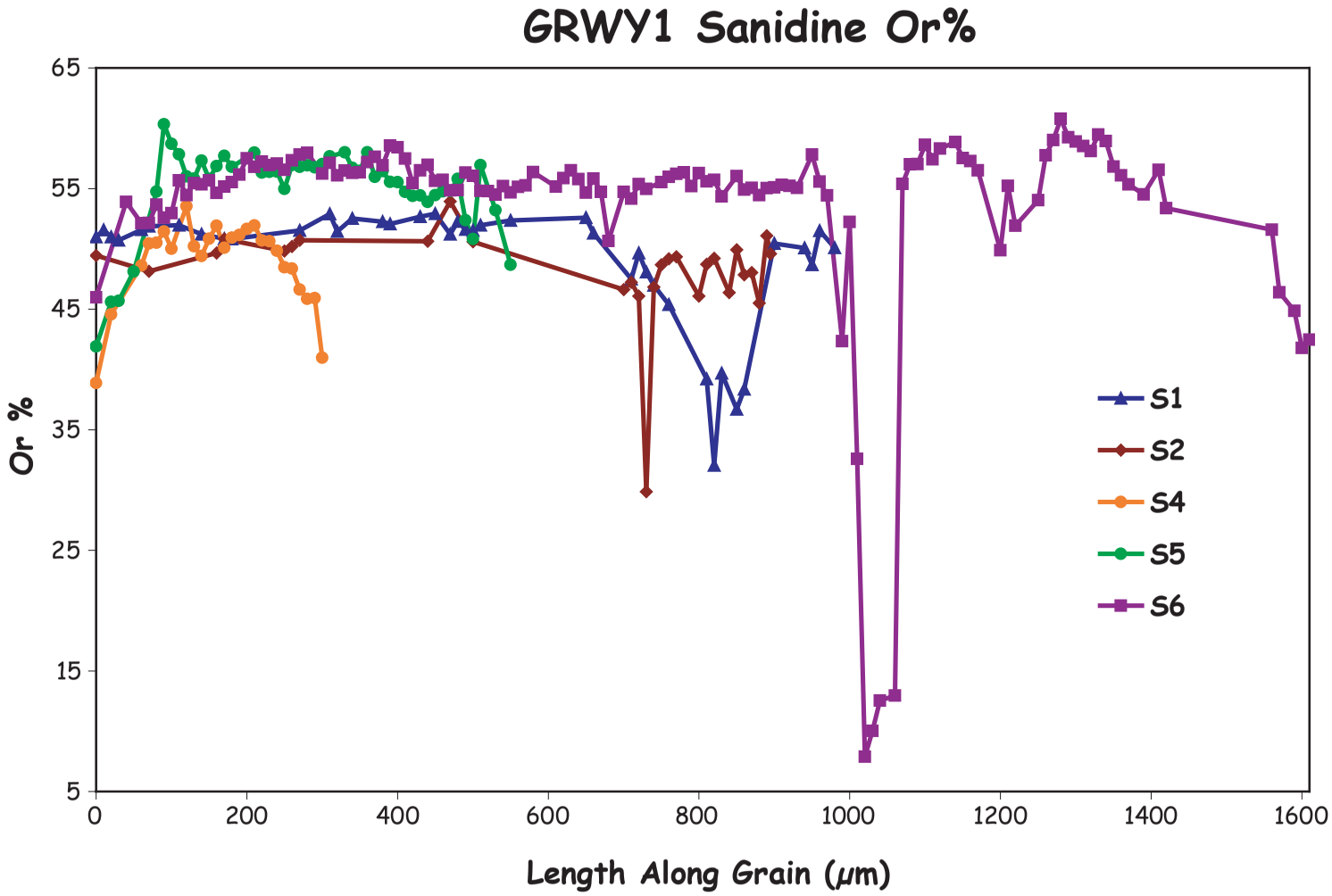

Figure 7.8. Electron microprobe traverse analyses of the Or composition of 5 sanidines from GRWY1, presented together for comparison. Traverses are from rim to rim.

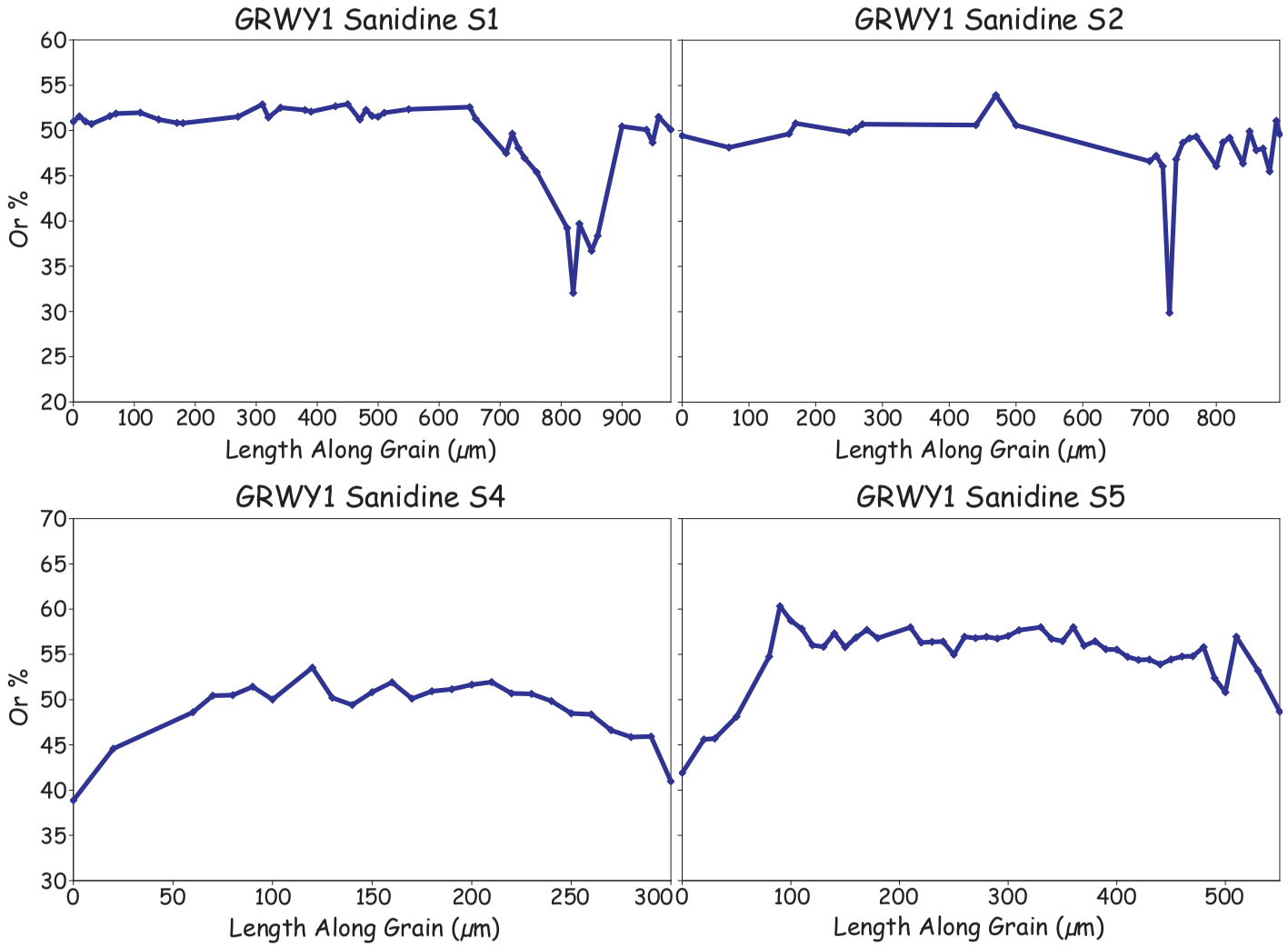

Figure 7.9. Detail of electron microprobe traverse analyses of the Or composition of 4 of the 5 sanidines analyzed from GRWY1. Notice the plagioclase inclusions of grains S1 and S2, and the increase in albite content at edges of grains. Traverses are from rim to rim.

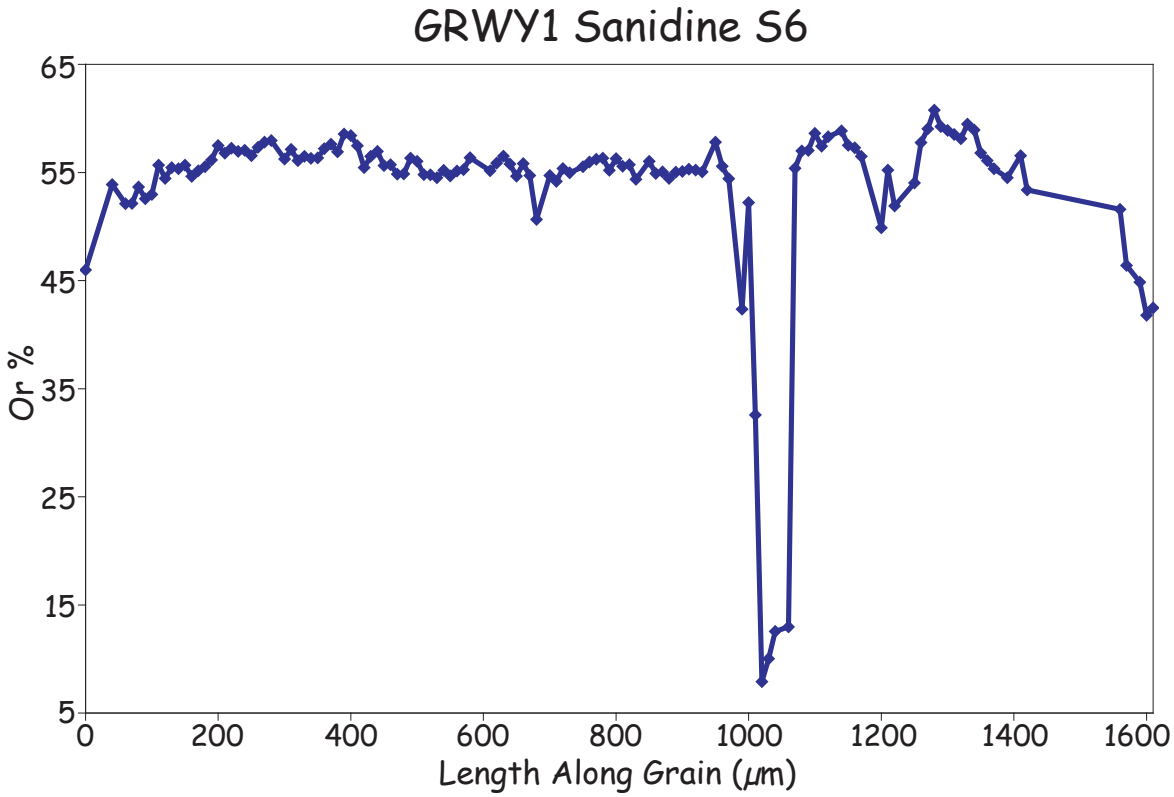

Figure 7.10. Detail of electron microprobe traverse analyses of the Or composition of the 5th sanidine analysed from GRWY1. Notice the plagioclase inclusion, and the increase in albite content at edges of grains. Traverse is from rim to rim.

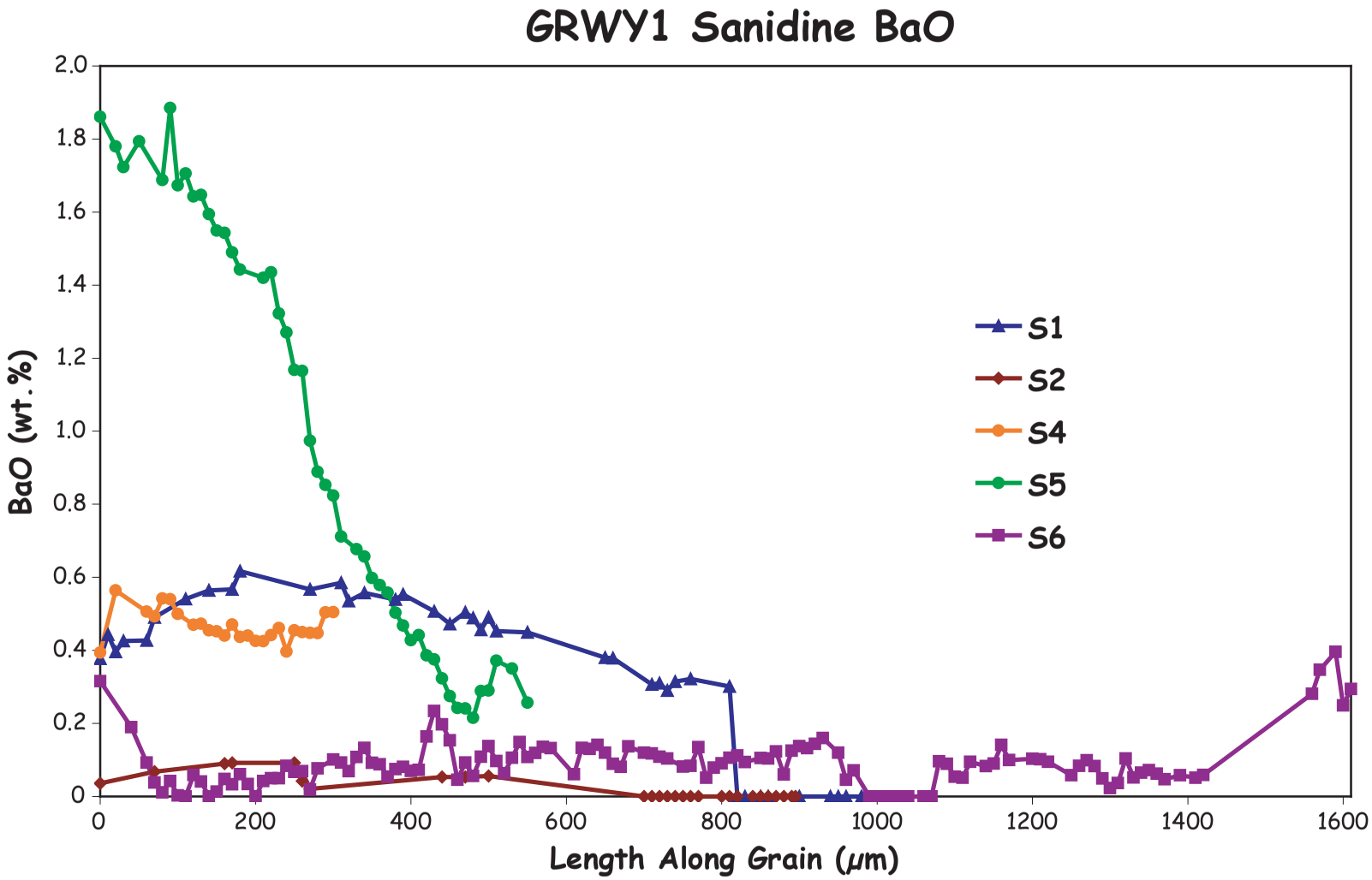

Figure 7.11. Electron microprobe traverse analyses of the BaO composition of 5 sanidines from GRWY1, presented together for comparison. Traverses are from rim to rim.

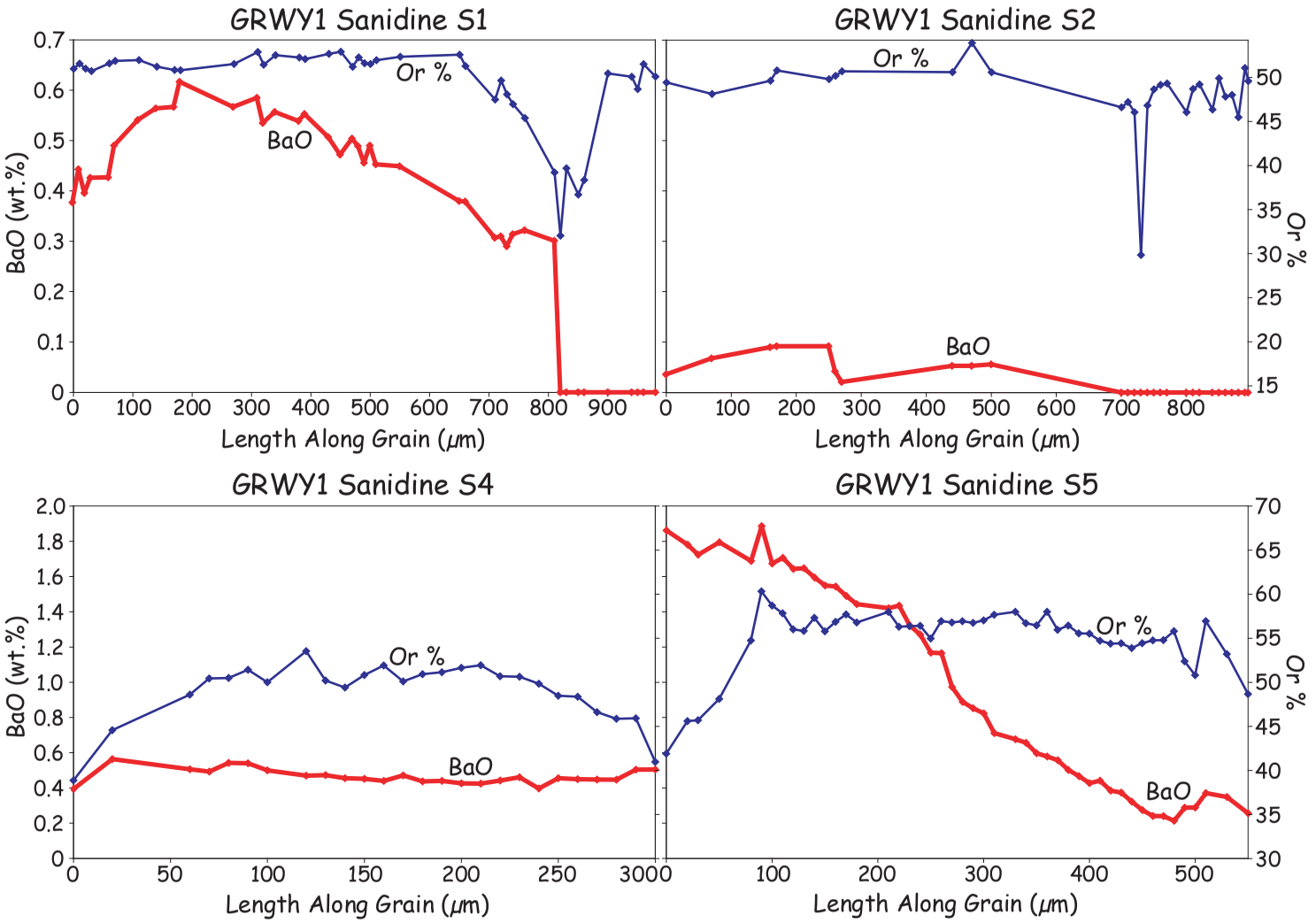

Figure 7.12. Detail of electron microprobe traverse analyses of the BaO composition (red, thick line) of 4 of the 5 sanidines analyzed from GRWY1 overlaid with the Or composition (blue, thin line) of those sanidines. Traverses are from rim to rim.

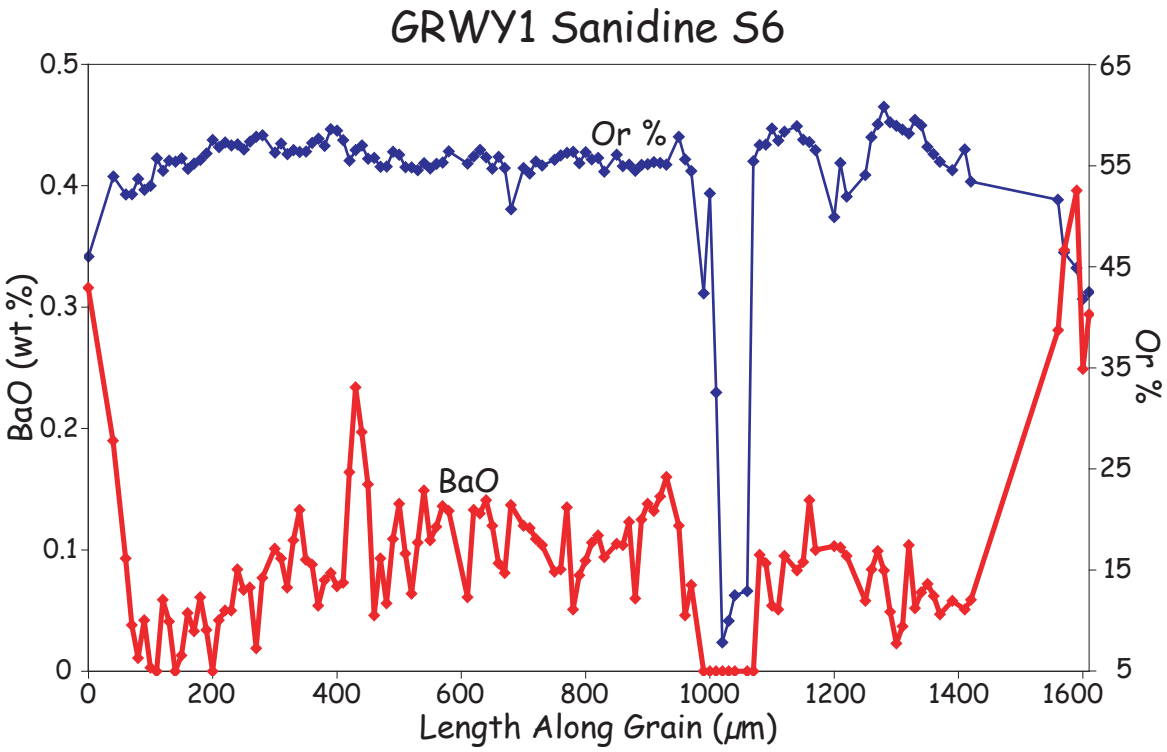

Figure 7.13. Detail of electron microprobe traverse analyses of the BaO composition (red, thick line) of the 5th sanidine analyzed from GRWY1 overlaid with the Or composition (blue, thin line) of those sanidines. Traverses are from rim to rim.

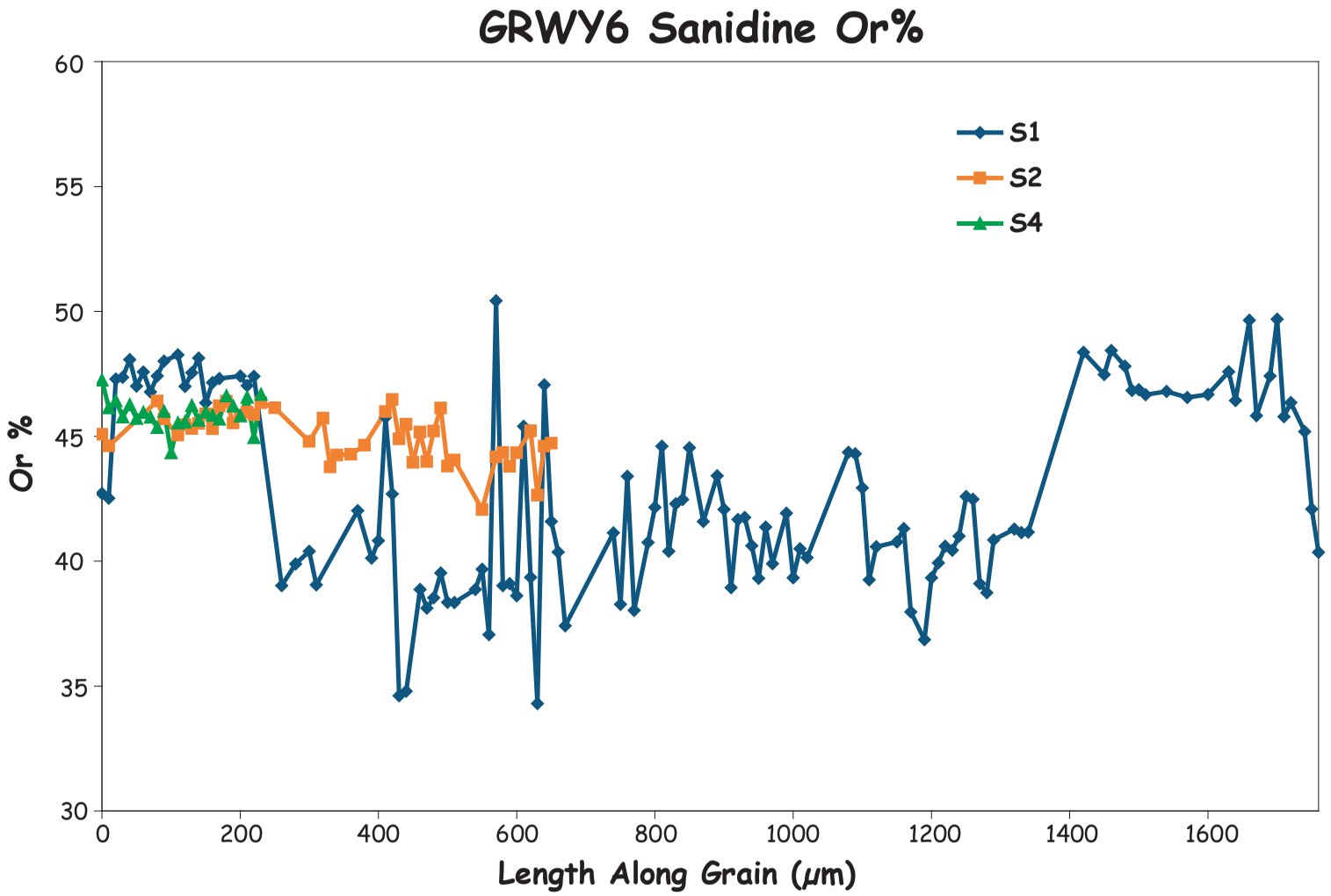

Figure 7.14. Electron microprobe traverse analyses of the Or composition of 3 sanidines from GRWY6, presented together for comparison. Traverses are from rim to rim.

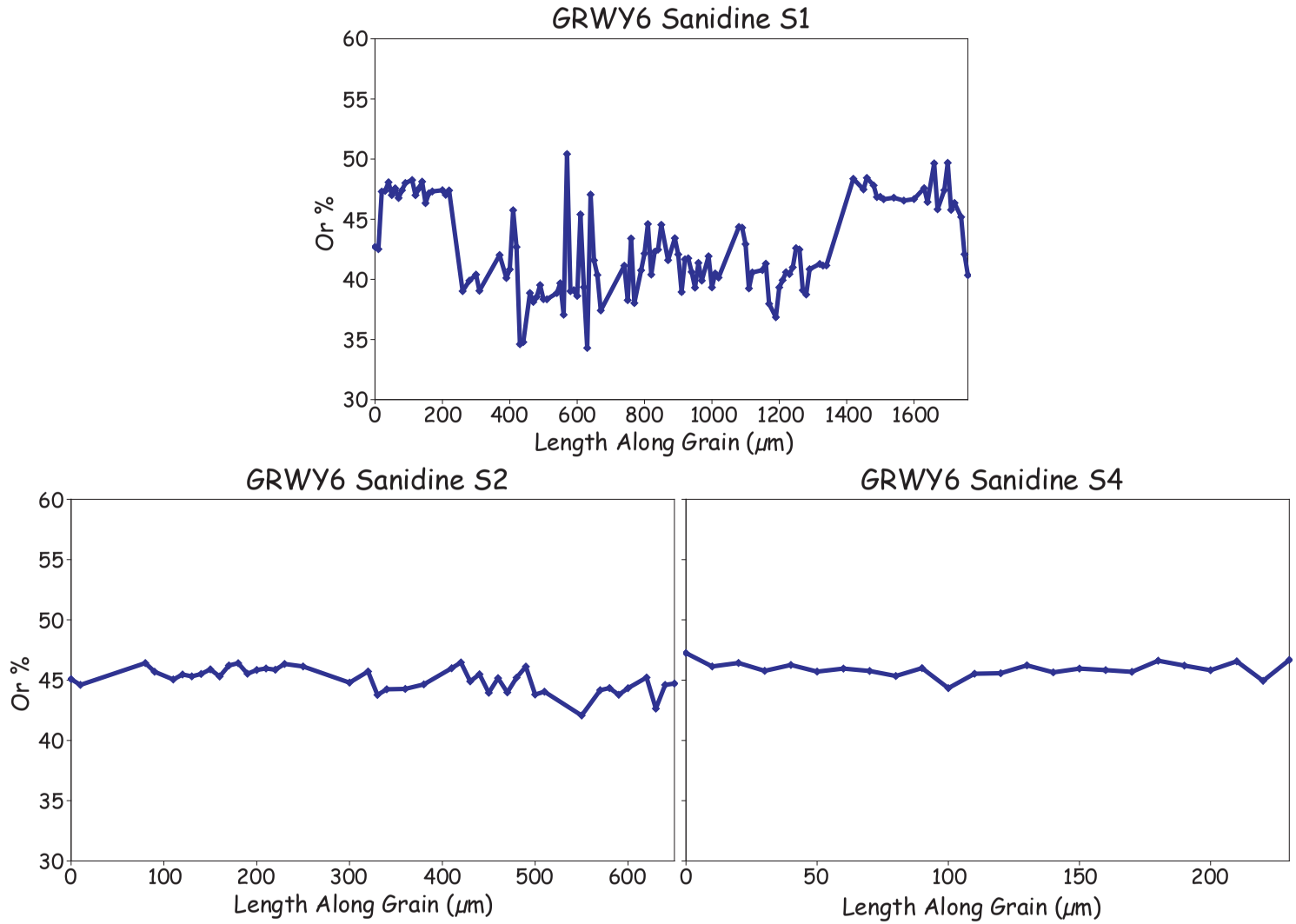

Figure 7.15. Detail of electron microprobe traverse analyses of the Or composition of 3 sanidines from GRWY6. Traverses are from rim to rim.

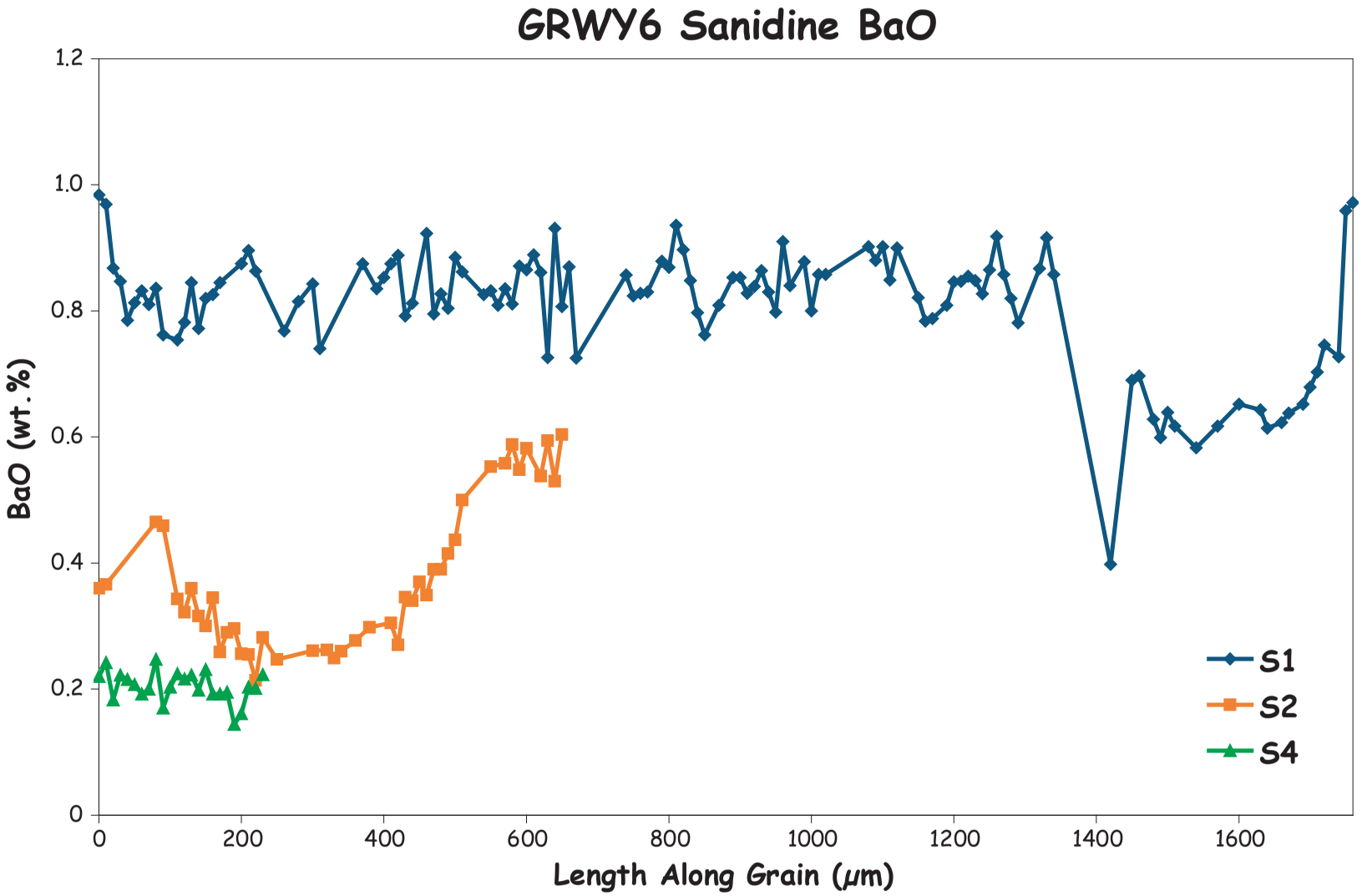

Figure 7.16. Electron microprobe traverse analyses of the BaO composition of 3 sanidines from GRWY6, presented together for comparison. Traverses are from rim to rim.

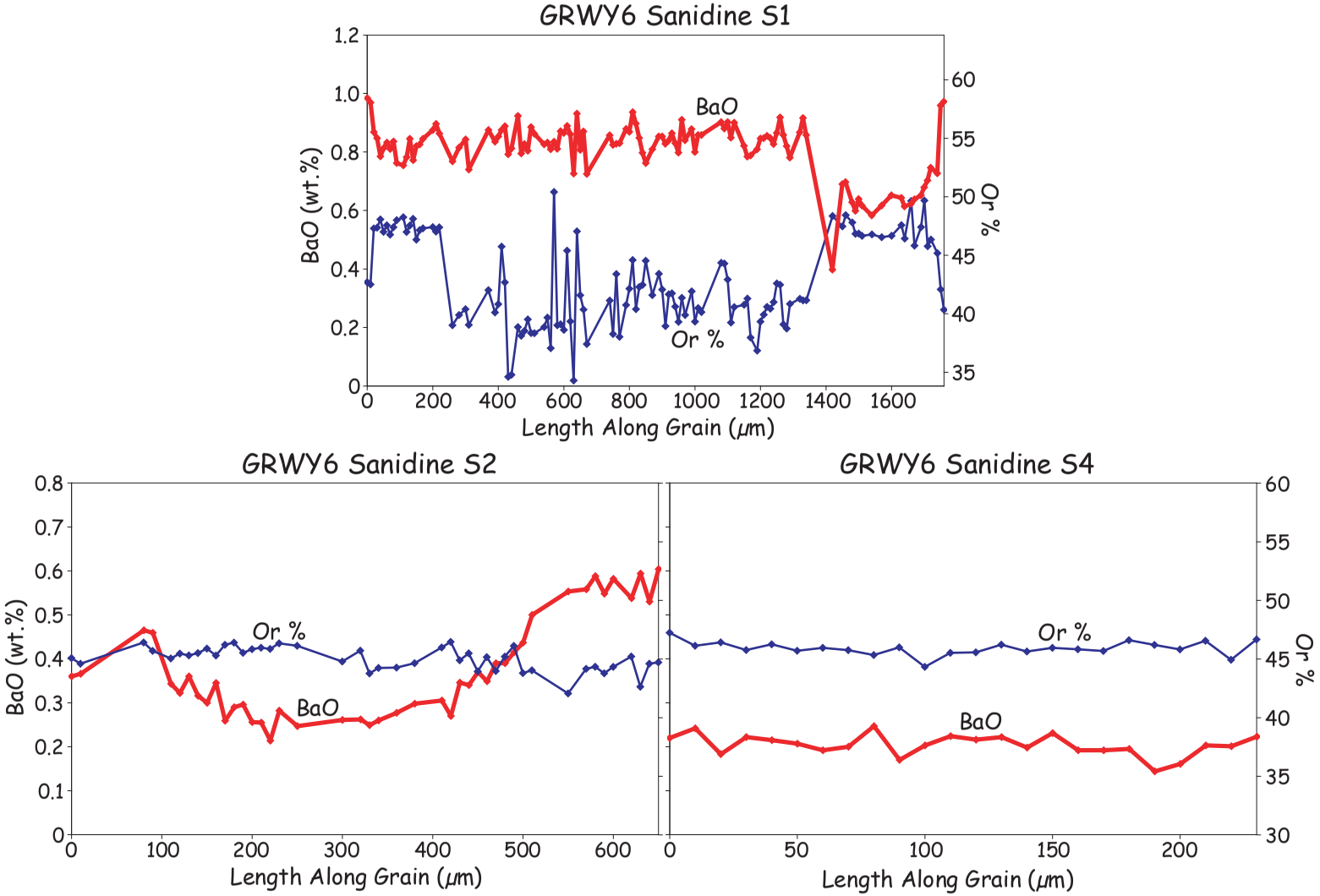

Figure 7.17. Detail of electron microprobe traverse analyses of the BaO composition (red, thick line) of 3 sanidines from GRWY6 overlaid with the Or composition (blue, thin line) of those sanidines. Traverses are from rim to rim.

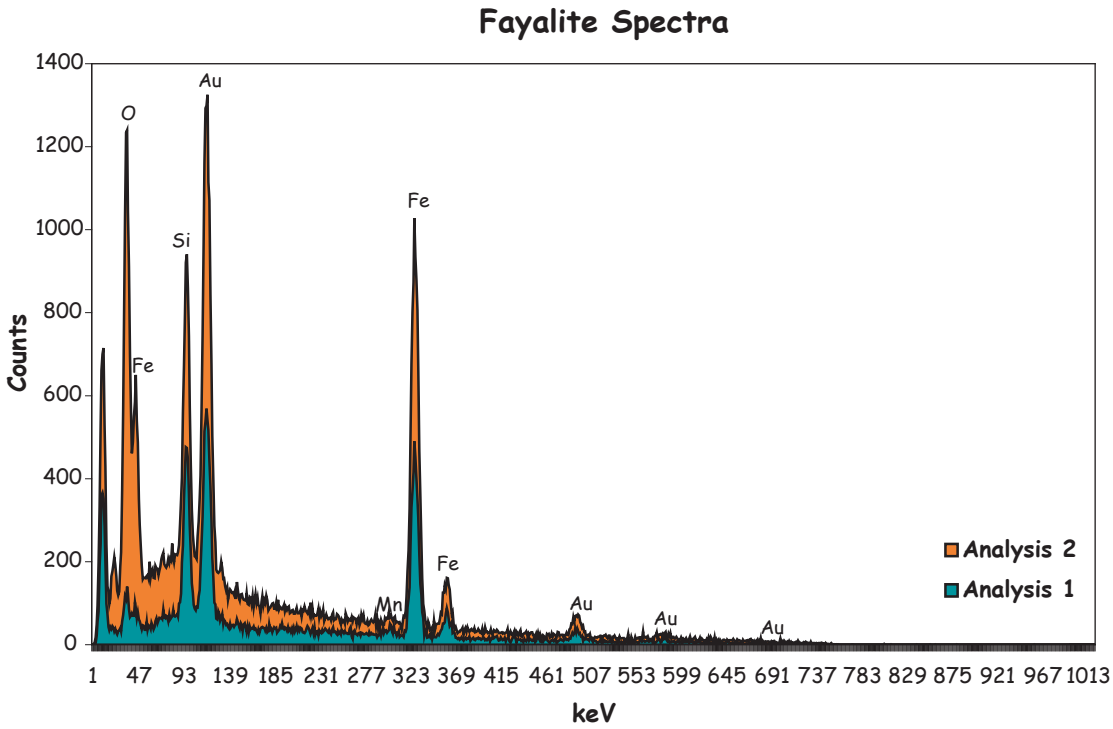

Figure 7.18. SEM analyses of two fayalite grains separated from altered obsidian sample OCWY14. Sample was coated in gold before analysis.

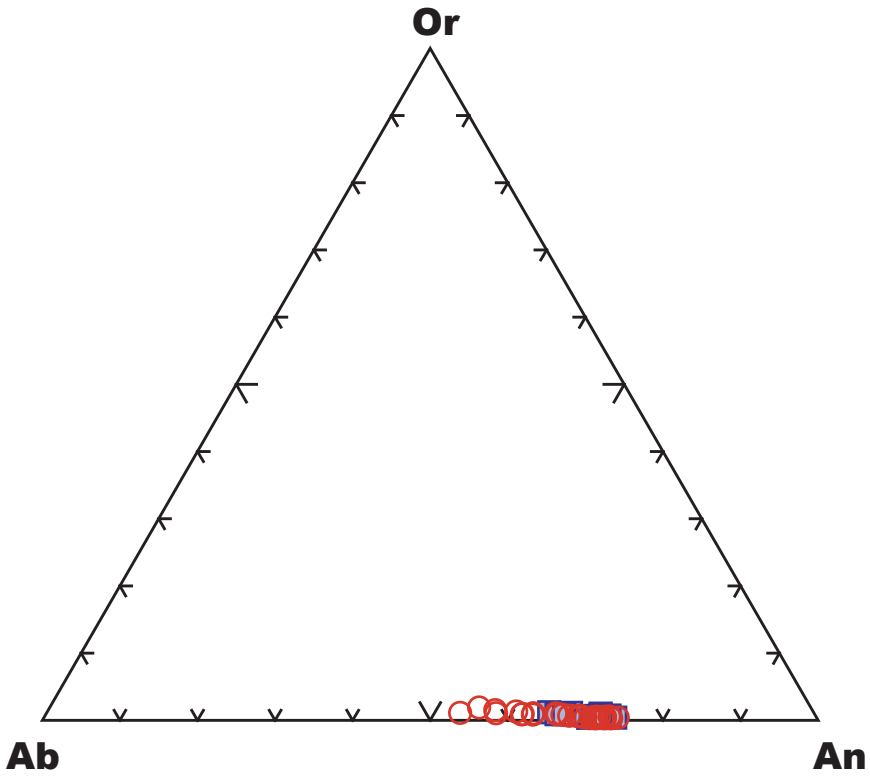

Figure 7.19. Electron microprobe point analyses of feldspar compositions of CSWY1 (▣) and CSWY1E (○). Notice CSWY1 plagioclases compositionally group with the CSWY1E plagioclases.

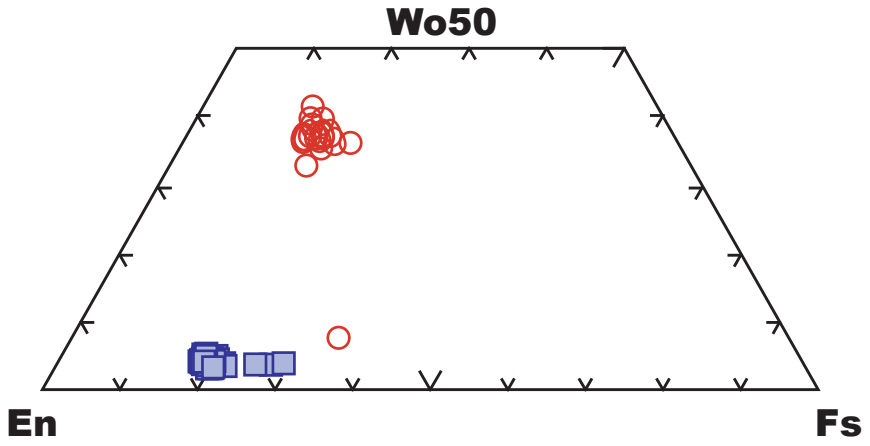

Figure 7.20. Electron microprobe traverse analyses of pyroxene compositions of CSWY2 (▣) and point analyses of pyroxene compositions of CSWY1E (○).

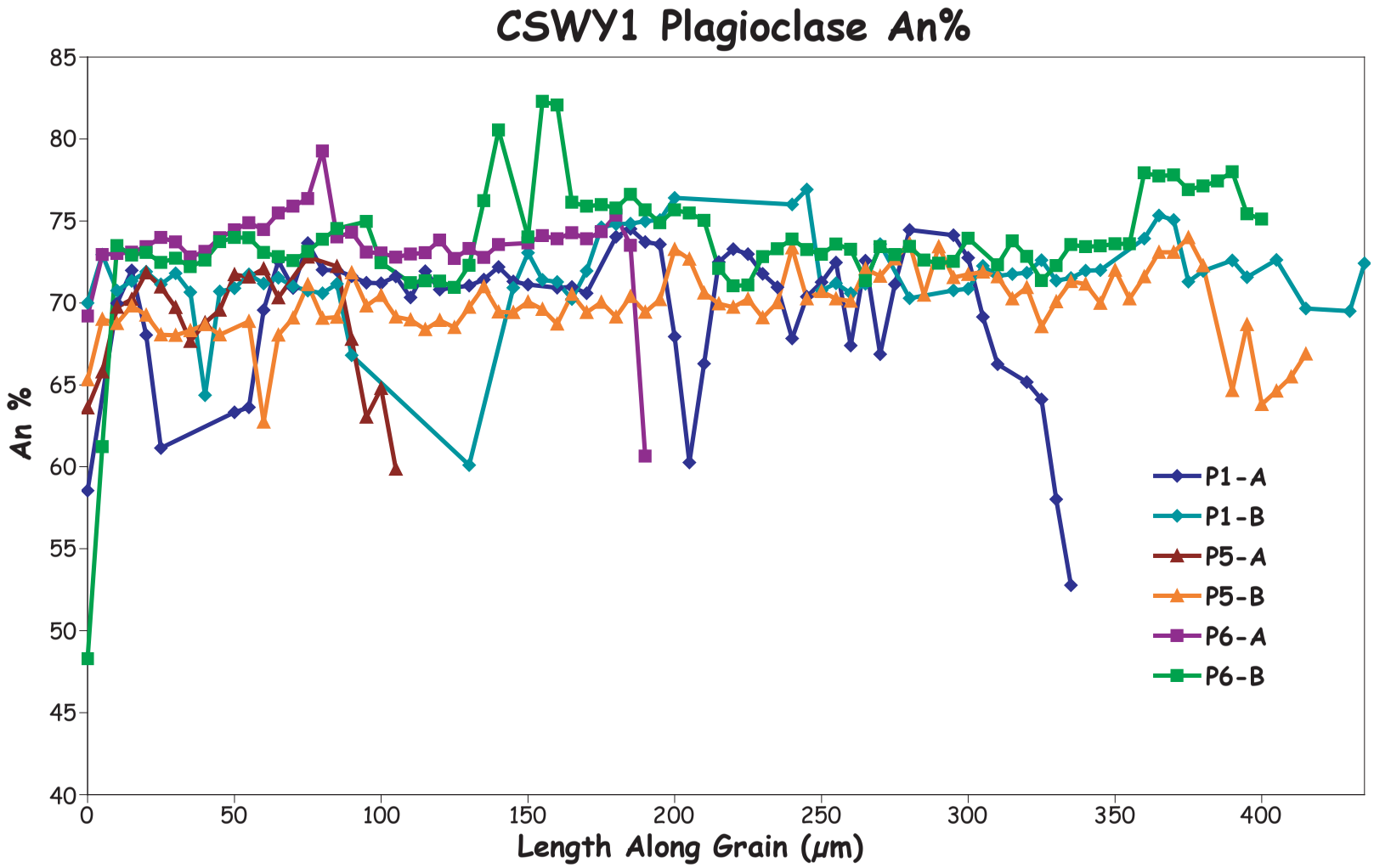

Figure 7.21. Electron microprobe traverse analyses and respective perpendicular traverse analyses of 3 plagioclases from CSWY1. Traverses are from rim to rim.

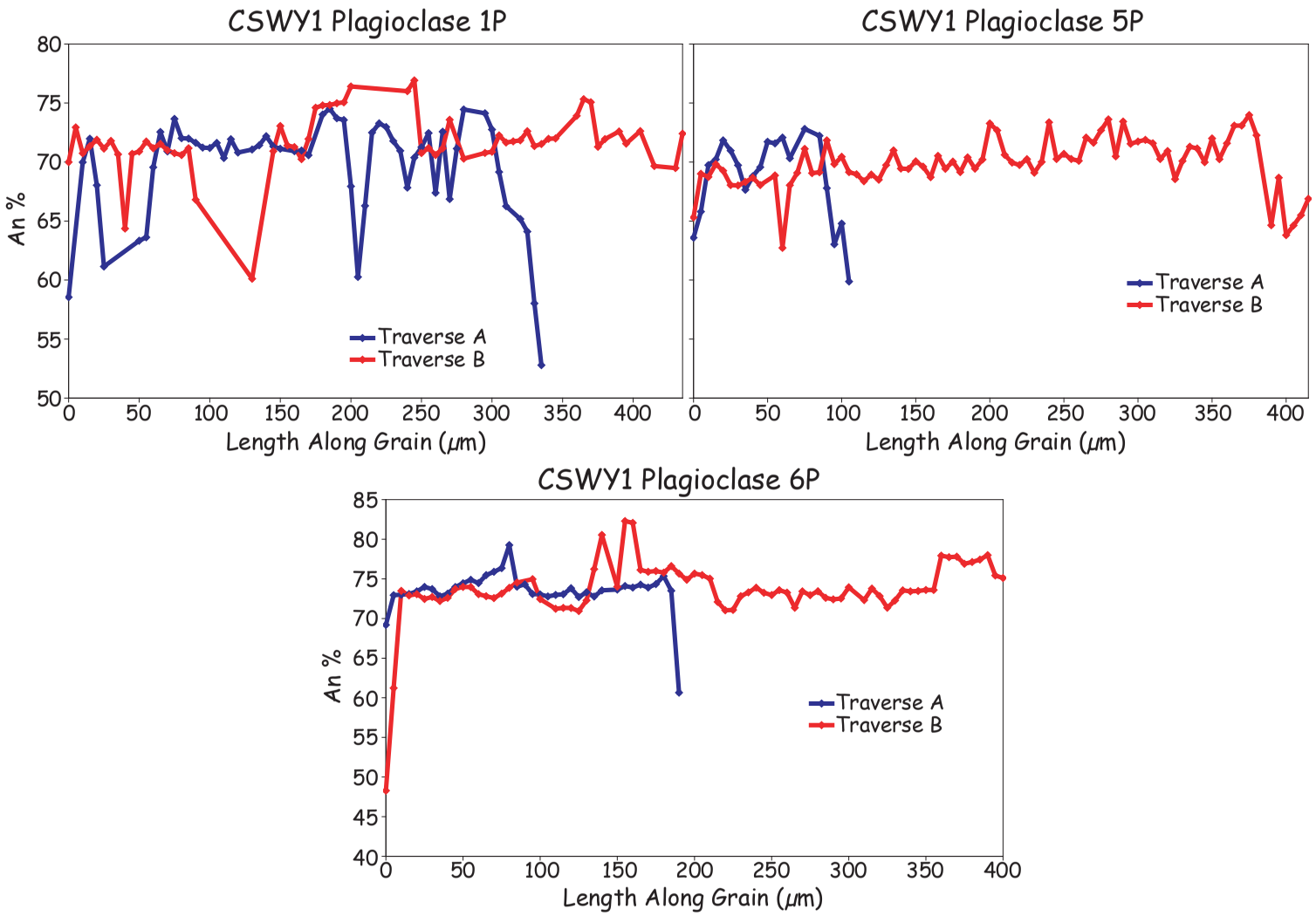

Figure 7.22. Detail of electron microprobe traverse analyses and respective perpendicular traverse analyses of 3 plagioclases from CSWY1. Notice decrease in anorthite content at edges of grains.. Traverses are from rim to rim.

CHAPTER 8

GEOTHERMOMETRY

Two samples of Gibbon River rhyolite analyzed by electron microprobe provided compositional data for both sanidine and plagioclase, GRWY7P and GRWY1. Gibbon River sample GRWY6 did not contain plagioclase. Assuming the outer edge of all the feldspar phenocrysts are in equilibrium within a single sample (Fuhrman and Lindsley, 1988), the electron microprobe analyses were used to calculate a feldspar crystallization temperature for the main Gibbon River flow (sample GRWY7P) and the southwestern flow of the Gibbon River rhyolites (sample GRWY1).

Further analysis by electron microprobe was preformed on quartz phenocrysts from three samples from the Gibbon River rhyolites, GRWY1, GRWY6, and GRWY7P. Rim to rim traverse analyses of each quartz phenocryst focused on analyzing titanium concentration across the grain. These titanium concentrations were then used to calculate quartz crystallizations temperatures along the analysis traverse (Wark and Watson, 2006).

The calculated two-feldspar temperatures are included in Appendix G. The electron microprobe analyses of the Gibbon River quartz samples and their respective calculated TitaniQ temperatures (Wark and Watson, 2006) are included in Appendix H.

Feldspar Geothermometry

In order to calculate feldspar crystallization temperatures using Fuhrman and Lindsley's two-feldspar geothermometry method (1988), an estimate of the magma's pressure during feldspar crystallization is required. Geophysical modeling and tomography presented in Husen and others (2004) indicate that the magma system

beneath the Yellowstone Caldera is ~8 km beneath the surface, with a gas-filled rock body 2 to 5 km beneath the surface of the Norris Geyser region. Modeling by Chang and others (2007) indicates a magma system between 6 and 14 km beneath the Yellowstone Caldera, with an expanding and contracting mass 6 to 16 km beneath the Norris Geyser region. Using these magma depths to estimate the depth of the system that produced the Gibbon River rhyolites, a depth of ~9 km would likely be within the upper or middle portion of a Gibbon River magma system. This depth corresponds to a pressure of ~3 kbar (assuming a geobarometric gradient of ~0.33 kbar/km). All of the feldspar crystallization temperatures below were calculated at 3 kbar.

Gibbon River Flow – Main Rhyolite

Data from nine sanidine and one plagioclase point analyses and seven sanidine and two plagioclase "edge" of traverse analyses (see Chapter 7) were used to calculate two-feldspar temperatures at 3 kbar in SolvCalc (Wen & Nekvasil, 1994). An eighth "edge" analysis from sanidine traverse GRWY7P-S5 was also used to calculate feldspar crystallization temperatures, but its calculated temperatures were omitted from the sample's average feldspar crystallization temperature. Two of the feldspar crystallization temperature sets calculated using this analysis from GRWY7P-S5 (T23 & T40, Appendix G) gave temperatures with more than ± 40°C variation, indicating this analysis' composition was not in equilibrium with the two of the three analyzed plagioclase compositions (Fuhrman and Lindsley, 1988). The third feldspar crystallization temperature set calculated using the "edge" analysis from GRWY7P-S5 (T06, Appendix G) was omitted since its equilibrium composition is suspect and if included, it increases the average crystallization temperature for GRWY7P feldspars by only 0.5°C. The

calculated feldspar crystallization temperatures ranged between 795.7°C and 827.1°C with an average crystallization temperature for GRWY7P feldspars of 813.5°C ± 30°C (uncertainty based on Fuhrman and Lindsley, 1988).

Gibbon River Flow – Southwestern Rhyolite

The electron microprobe analyses of sample GRWY1 from the southwestern flow of the Gibbon River rhyolites provided rim analyses from both plagioclase and sanidine (Chapter 7). The sanidine compositions used to calculate the two-feldspar crystallization temperatures varied quite a bit (Or ± 8%) and with only one plagioclase composition available to calculate two-feldspar crystallization temperatures, it is unlikely that all the sanidine compositions are in equilibrium with the plagioclase analysis. Data from four sanidine and one plagioclase point analyses and ten sanidine "edge" of traverse analyses (see Chapter 7) were used to calculate two-feldspar temperatures at 3 kbar in SolvCalc (Wen & Nekvasil, 1994). None of the two-feldspar crystallization calculations gave concordant, equilibrium temperatures (Fuhrman and Lindsley, 1988). Three of the calculated feldspar crystallization temperature sets gave close-to-equilibrium calculated temperatures, with two concordant temperatures and a third temperature within ± 100°C of the concordant two (Fuhrman and Lindsley, 1988). Using the mean of the two concordant temperatures as the calculated feldspar crystallization temperature for these three analyses, the average crystallization temperature calculated for GRWY1 feldspars is 818.6°C ± 40°C (uncertainty based on Fuhrman and Lindsley, 1988).

Titanium-in-Quartz Geothermometry

The TitaniQ titanium-in-quartz geothermometry method developed by Wark and Watson (2006) used rutile to fix the activity of TiO_2 ($a_{TiO_2} = 1$) while developing their temperature curves. Rutile was not identified within any of the Gibbon River rhyolites and so to utilize the TitaniQ method to calculate quartz crystallization temperatures, an estimate of the activity of TiO_2 within a particular magma is required (Wark and Watson, 2006). Both ilmenite and Ti-rich magnetite (on average $(Fe_{80}Ti_{20})_3O_4$) were identified in sample GRWY6, while only Ti-rich magnetite was analyzed in samples GRWY1 and GRWY7P (on average $(Fe_{85}Ti_{15})_3O_4$) (Tables C.14 through C.16, Appendix C). Poor electron microprobe analyses (analyses with measured elemental totals less than 98%) indicate that a secondary alteration of the magnetite to ulvöspinel has occurred in all three samples. The eruption temperature of each flow is needed to estimate the activity of TiO_2 within the Gibbon River samples (Wark and Watson, 2006; Hayden and Watson, 2007). This creates a circuitous issue. Wark and Watson (2006), Wark and others (2007), and Hayden and Watson (2007) suggested that generally silicic melts will have TiO_2 activities of 0.6 or higher. Wark and Watson (2006) also calculated a TiO_2 activity for the Bishop Tuff, part of the voluminous, rhyolitic Long Valley Volcanic Field, as $a_{TiO_2} = 0.63 \pm 0.03$. For the Gibbon River rhyolites, an estimated TiO_2 activity of $a_{TiO_2} = 0.6$ was used for all TitaniQ calculations. This estimate is further justified by an estimate for the activity of TiO_2 for the Yellowstone Volcanic Field of $a_{TiO_2} = 0.58 \pm 0.38$ (Hayden and Watson, 2007).

Seven quartz phenocrysts were analyzed from rim to rim for TiO_2: three from GRWY7P (7P-QA, 7P-QB, and 7P-QC), two from GRWY1 (1-QA and 1-QB), and two

from GRWY6 (6-QA and 6-QB) (Figures 8.1, 8.2, 8.3 & 8.4). Analyses with measured elemental totals less than 98% were omitted from the geothermometry calculations. These TiO_2 analyses were then converted to quartz crystallization temperatures using the TitaniQ geothermometry method (Wark and Watson, 2006). The uncertainty of these TiO_2 analyses is 30 ppm. The uncertainty of the calculated TitaniQ temperatures is logarithmic (Wark and Watson, 2006) and, based on the uncertainty of the Ti-analyses, is calculated for the range of Gibbon River rhyolite quartz temperatures in Table 8.1.

Table 8.1. Calculated uncertainties of calculated TitaniQ temperatures

TiO_2 Concentration (ppm)	TitaniQ Temperature	Calculated Uncertainty (°C) [a]	
		+	-
428	1050°C	14	14
329	1000°C	16	17
247.5	950°C	20	21
181.5	900°C	24	27
129.5	850°C	30	36
89.5	800°C	39	50
59.5	750°C	50	76
38.5	700°C	66	138

[a] Uncertainty was calculated by adding and subtracting 30 ppm from each respective TiO_2 concentration and calculating the TitaniQ temperature of the $TiO_2 \pm 30$ concentrations. The calculated uncertainty is the difference between the TitaniQ temperature and the $TiO_2 \pm 30$ temperature.

Cathodoluminescence (CL) images of all seven analyzed quartz grains were taken to help determine if the grains are chemically zoned (Figures 8.5, 8.6 & 8.7).

Gibbon River Flow – Main Rhyolite

Of the three of the quartz phenocrysts analyzed from sample GRWY7P, two, quartz 7P-QB and 7P-QC, exhibit a relatively constant TiO_2 composition and temperature (Figure 8.2). Quartz 7P-QB has an average temperature of 932°C and ranges in

temperature from 898.8°C to 965.0°C (Figure 8.2). Quartz 7P-QC has an average temperature of 894°C and ranges in temperature from 839.3°C to 937.9°C (Figure 8.2). The TiO_2 content of quartz 7P-QA decreases from the core to the rim and ranges in temperature from 890.0°C to 995.0°C (Figure 8.2). The average temperature of quartz 7P-QA is 956°C (Figure 8.2).

All three CL images of the quartz phenocrysts from sample GRWY7P are euhedral grains with a light grey luminescence (Figure 8.5). The CL image of quartz 7P-QA shows multiple, indistinct growth zones (thin white, concentric lines) but does not exhibit distinct chemical zonation throughout the phenocryst. The CL image of quartz 7P-QB shows a single, darker oblong core (lower left of 7P-QB in Figure 8.2) that was not crossed during the Ti-analysis traverse. The rest of quartz 7P-QB exhibits no distinct chemical zonation across the phenocryst (Figure 8.5). The CL image of quartz 7P-QC shows a slightly darker core with a single light rim along the grain edge (most visible along the middle right of 7P-QC in Figure 8.5).

Gibbon River Flow – Southwestern Rhyolite

Two GRWY1 quartz phenocrysts were analyzed for TiO_2 composition. The temperatures calculated for quartz 1-QA vary between 750°C and 850°C (Figure 8.3). A single edge of quartz 1-QA (left-side of analysis traverse) rises to 907.2°C (Figure 8.3). The average temperature of quartz 1-QA (without the high temperature edge) is 794°C and ranges in temperature from 729.4°C to 850.5°C (Figure 8.3). Quartz 1-QB has at least two temperature zones, a core zone that varies across the 700°C temperature range, and at least one rim zone with temperatures of greater than 900°C (Figure 8.3). The core of quartz 1-QB has an average temperature of 787°C and ranges in temperature from

704.8°C to 839.3°C (Figure 8.3). The rim of quartz 1-QB has an average temperature of 921°C and ranges in temperature from 861.2°C to 971.3°C (Figure 8.3).

The high temperature rim of quartz 1-QB could represent two separate high temperature zones. The temperatures at the edge of the grain are constant (rim 1), whereas between the low temperature core and the constant high temperatures, the high temperatures drop from a maximum temperature and then, consistently rise to second maximum temperature (rim 2) (Figure 8.3). On the right-side of the analysis traverse, the variable high temperature rim (rim 2) consistently drops after reaching the second maximum temperature (Figure 8.3). The average temperature of "rim 1" is 926°C and its temperatures range from 880.8°C to 951.8°C (Figure 8.3). The average temperature of "rim 2" is 915°C and it ranges in temperature from 861.2°C to 971.3°C (Figure 8.3). The average temperature and temperature range of "rim 2" are within the uncertainty of the average temperature and temperature range of "rim 1" (Table 8.3).

Both quartz phenocrysts from sample GRWY1 are anhedral, broken or shattered grains (Figure 8.6). A CL image of quartz phenocryst 1-QA shows strong zonation with a dark core and a distinct light-colored rim (Figure 8.6). The CL image of 1-QB shows strong zonation with several distinct light rims around a dark core (Figure 8.6). A broken edge that exposes the dark core of 1-QB has a light-colored rim along the break (Figure 8.6).

Gibbon River Flow – Sample GRWY6

The calculated temperatures for quartz 6-QA consistently increase and decrease across the grain between 900°C and 975°C (Figure 8.4). The average temperature of 6-QA is 936.3°C and ranges in temperature from 890.0°C and 971.3°C (Figure 8.4).

Quartz 6-QB exhibits a relatively constant TiO_2 composition and temperature (Figure 8.4). The average temperature of quartz 6-QB is 964.6°C and the calculated temperatures range from 930.6°C to 1006.1°C (Figure 8.4).

The two quartz phenocrysts analyzed from sample GRWY6 are subhedral, shattered grains (Figure 8.7). The CL image of quartz 6-QA shows moderate zoning with some lighter rims around a dark core (Figure 8.7). The CL image of quartz 6-QB shows only a slight color variation between the light core and the nearly white rim (Figure 8.7).

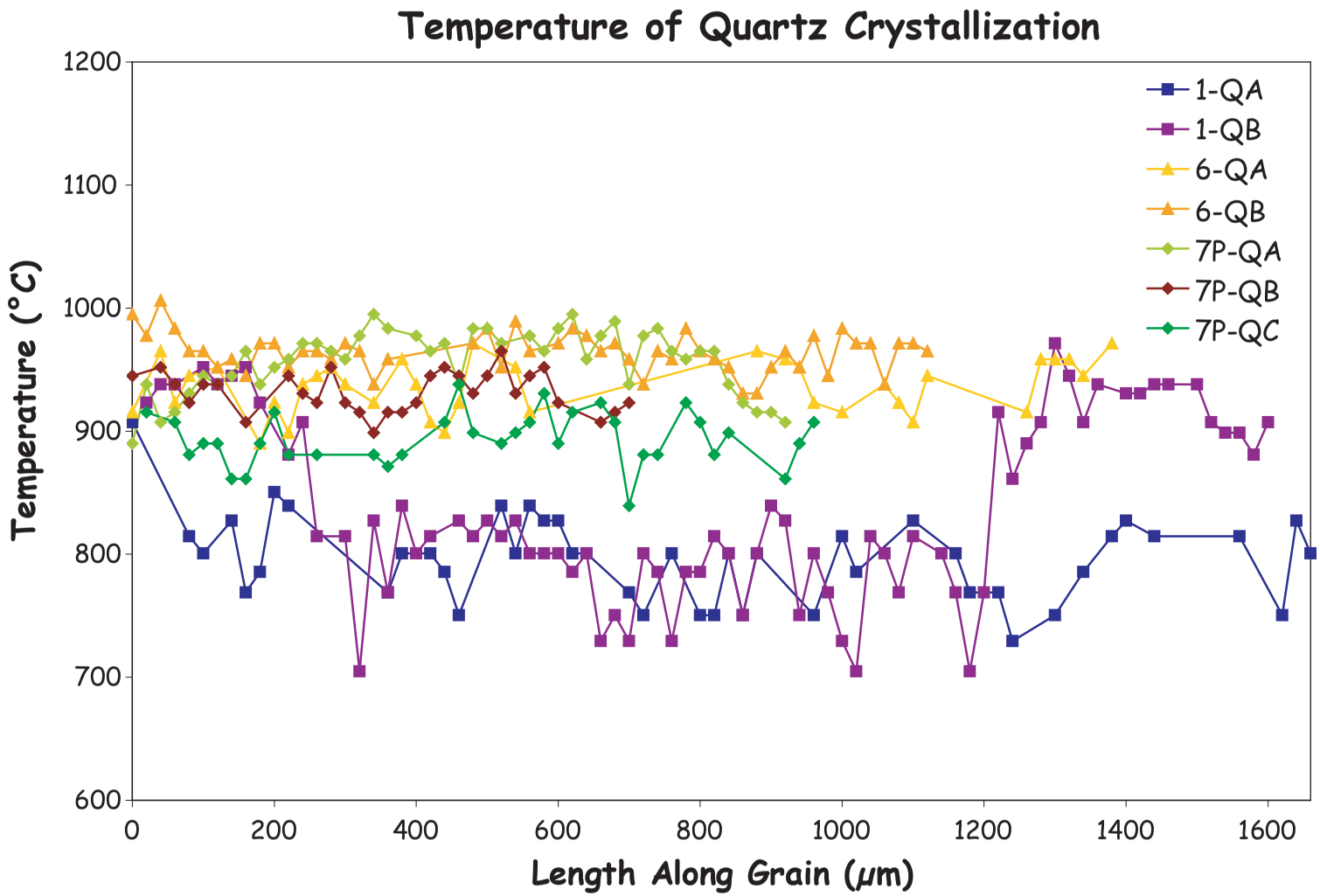

Figure 8.1. Titanium-in-Quartz crystallization temperatures calculated from electron microprobe traverse analyses of TiO (Wark & Watson, 2006) in 3 quartz phenocrysts from GRWY7P (7P-QA, 7P-QB and 7P-QC), 2 quartz phenocrysts from GRWY1 (1-QA and 1-QB), and 2 quartz phenocrysts from GRWY6 (6-QA and 6-QB). Original traverses are from rim to rim.

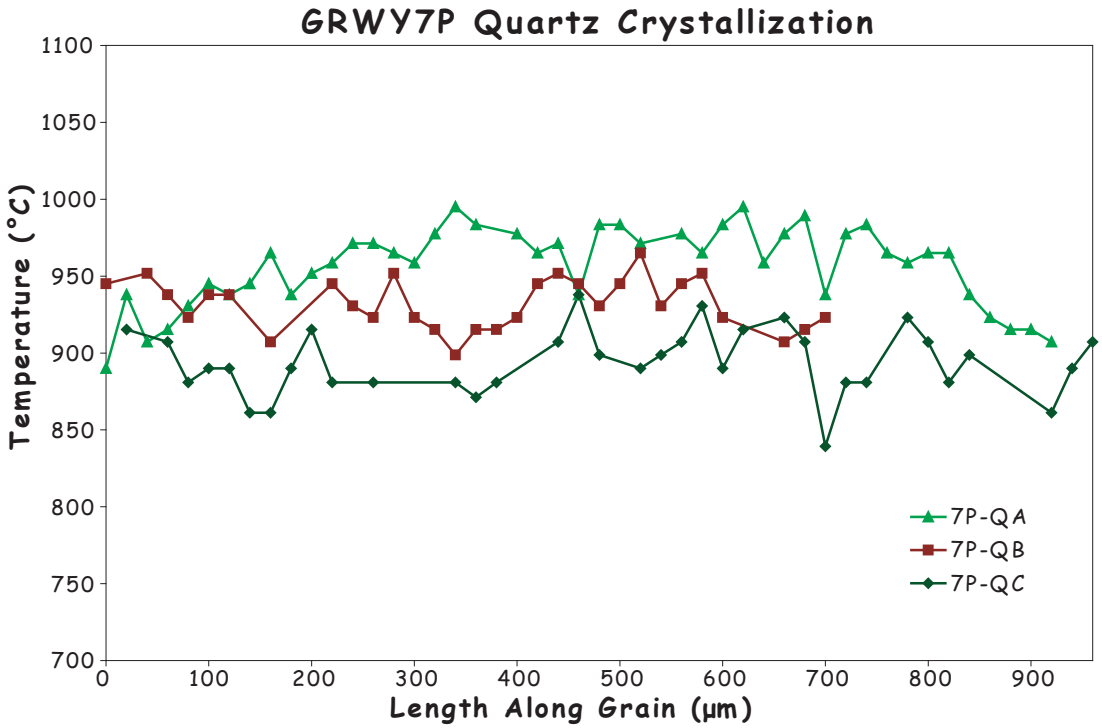

Figure 8.2. Titanium-in-Quartz crystallization temperatures calculated from electron microprobe traverse analyses of TiO (Wark & Watson, 2006) in 3 quartz phenocrysts from GRWY7P (7P-QA, 7P-QB and 7P-QC). Original traverses are from rim to rim.

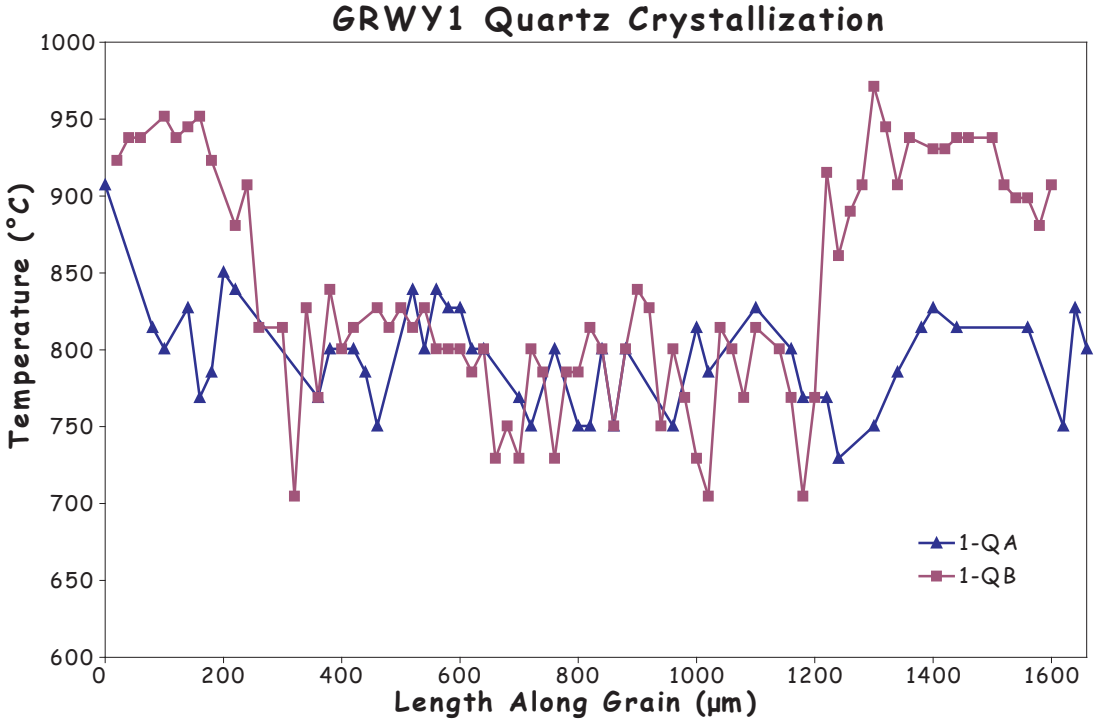

Figure 8.3. Titanium-in-Quartz crystallization temperatures calculated from electron microprobe traverse analyses of TiO (Wark & Watson, 2006) in 2 quartz phenocrysts from GRWY1 (1-QA and 1-QB). Original traverses are from rim to rim.

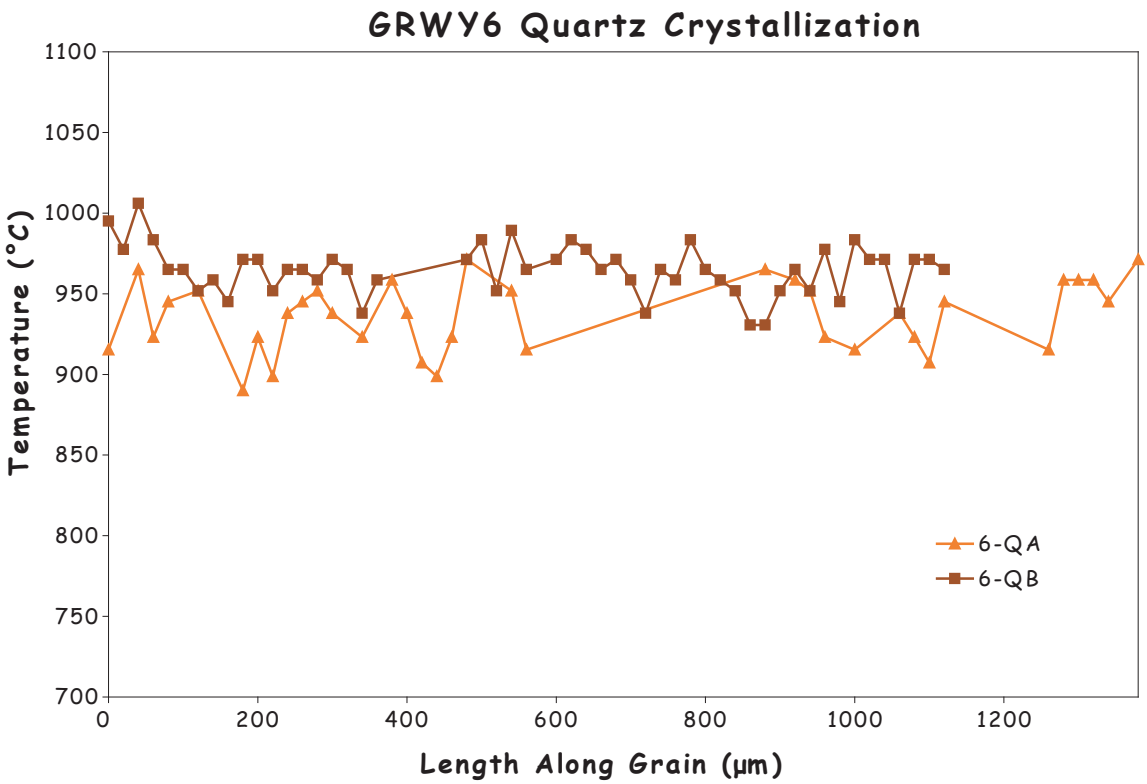

Figure 8.4. Titanium-in-Quartz crystallization temperatures calculated from electron microprobe traverse analyses of TiO (Wark & Watson, 2006) in 2 quartz phenocrysts from GRWY6 (6-QA and 6-QB). Original traverses are from rim to rim.

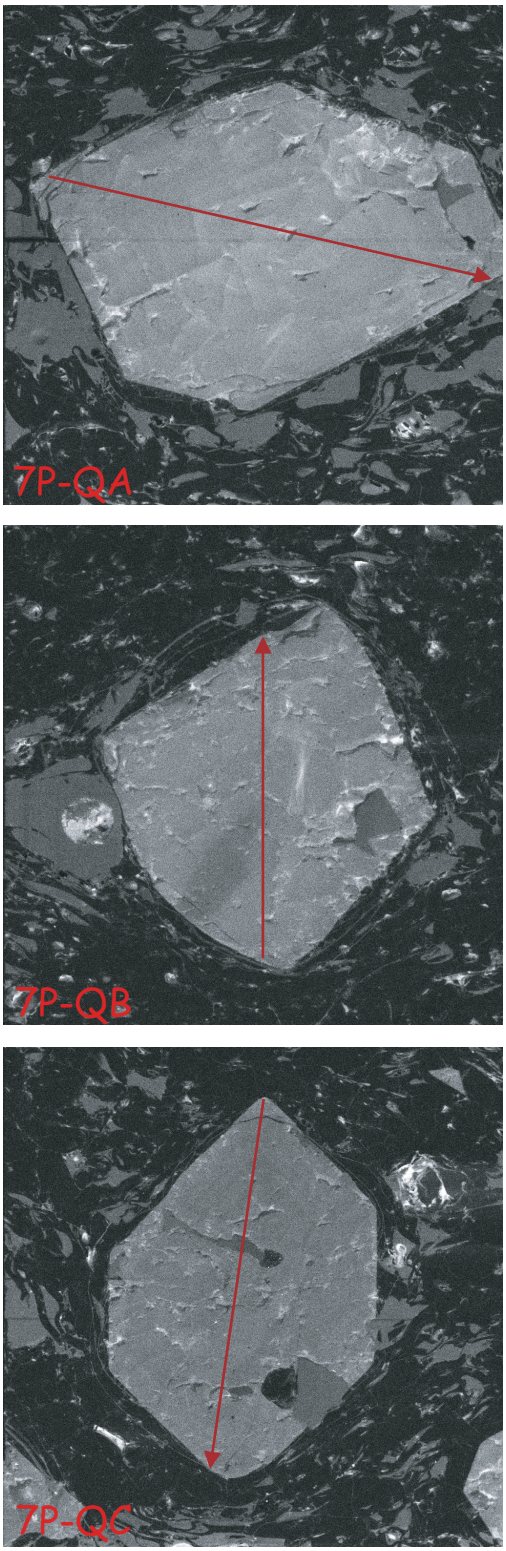

Figure 8.5. CL images of the three GRWY7P quartz phenocrysts analyzed for TiO_2. From top to bottom, 7P-QA, 7P-QB, and 7P-QC. Red line indicates microprobe traverse and direction. TitaniQ quartz crystallization temperatures for these three phenocrysts are presented in Figure 8.1 and Appendix H.

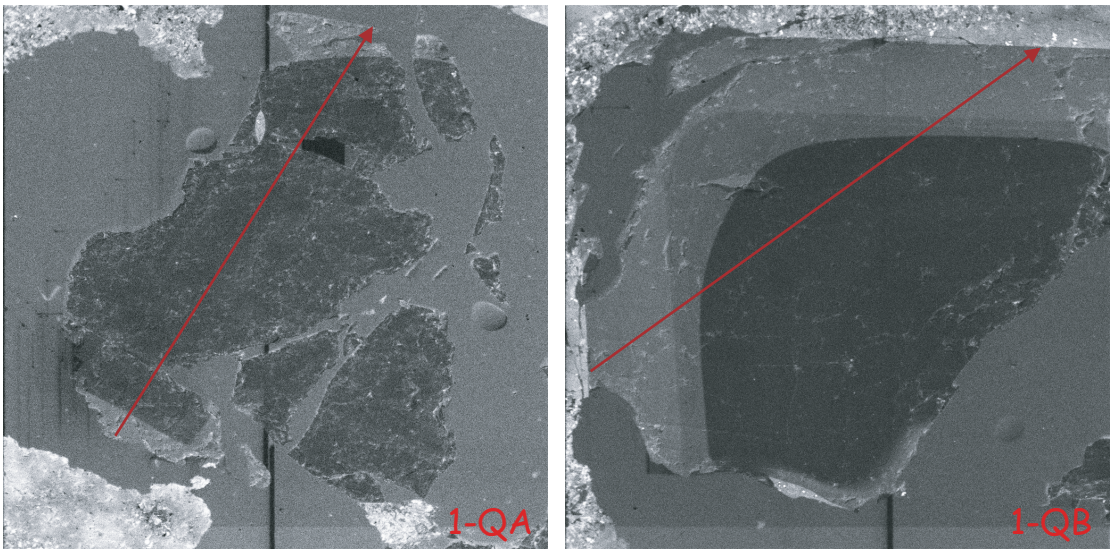

Figure 8.6. CL images of the two GRWY1 quartz phenocrysts analyzed for TiO_2. Notice the distinct compositional zoning. From left to right, 1-QA and 1-QB. Red line indicates microprobe traverse and direction. TitaniQ quartz crystallization temperatures from these two phenocrysts are presented in Figure 8.1 and Appendix H.

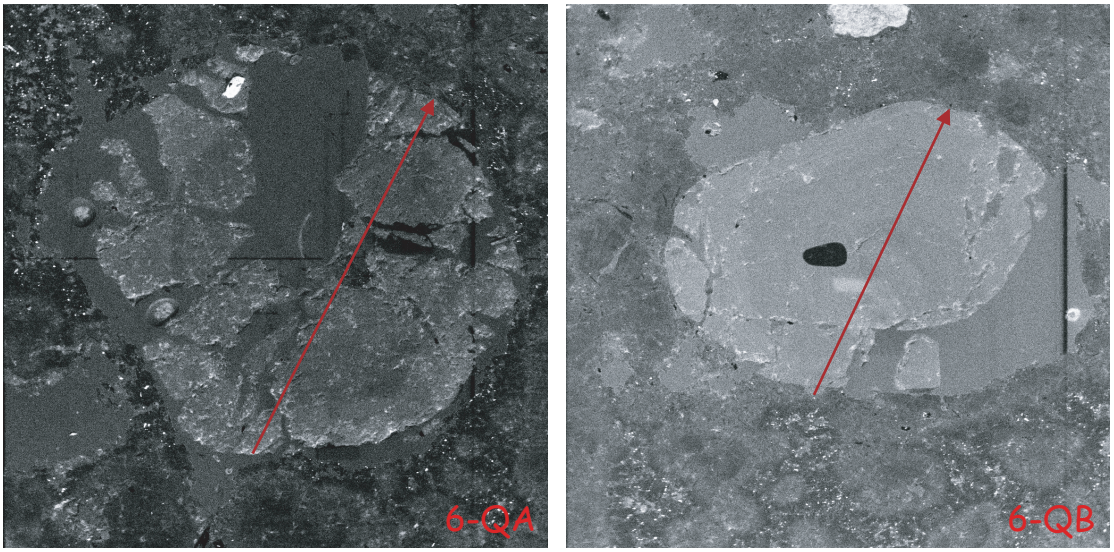

Figure 8.7. CL images of the two GRWY6 quartz phenocrysts analyzed for TiO_2. Notice slightly brighter rim around each phenocryst. From left to right, 6-QA and 6-QB. Red line indicates microprobe traverse and direction. TitaniQ quartz crystallization temperatures from these two phenocrysts are presented in Figure 8.1 and Appendix H.

CHAPTER 9

$^{230}TH/^{238}U$ GEOCHRONOLOGY

Twenty spots on eleven zircon grains from sample GRWY6 were analyzed for $^{230}Th/^{238}U$ ages by ion microprobe. The full data set is contained in Appendix I. Analysis 16 ablated through the grain and into the epoxy (Figure 9.1b), and was excluded from the $^{230}Th/^{238}U$ data set (Schmitt *et al.*, 2006). The zircons range from 72 to 487 ppm in U concentration with an average of 190 ppm (Table 9.1).

CL images of the analyzed grains indicate two populations of zircons within sample GRWY6. The main zircon population (Grains 1, 3, 5-7, 9 & 10) is euhedral to subhedral with multiple, subtle growth zones (Figure 9.1a&b). Many grains contain a euhedral, light-colored CL core, often truncated by the grain's edge (Figure 9.1b). The zircon grains are commonly moderately resorbed (Figure 9.1a&b). The second zircon population (Grains 2, 4, 8 & 11) is subhedral to anhedral with a subhedral, dark-colored CL core surrounded by several subhedral growth zones (Figure 9.2a&b). The growth zones generally grade from the dark-colored CL core to a lighter CL rim (Figure 9.2a&b). A few grains contain very distinct growth zones (Figure 9.2b). The zircon grains typically have slightly to moderately resorbed edges (Figure 9.2a&b).

All spots analyzed were not in secular equilibrium and fall below the $^{230}Th/^{238}U$ equiline (Figure 9.3) (Schmitt *et al.*, 2006). Disequilibrium ages for individual zircon analyses were determined by calculating the slope of two-point isochrons through each zircon composition (Appendix I) and the approximate whole-rock U/Th composition (Table 9.1). The measured U and Th compositions for sample GRWY6 (U = 4.26 ppm, Th = 19.57 ppm; Appendix B, Table B.1) were used for the approximate whole-rock

U/Th composition (U/Th = 0.218). Generally all the analyses have large uncertainties (> ±10 ka) (Table 9.1). A York regression (York, 1969) of all the analyses yielded a disequilibrium age of 105^{+36}_{-27} ka with an MSWD of 0.73 (Figure 9.3).

Table 9.1. U-Th Ages Calculated for GRWY6 Zircon Analyses

Zircon Grain	Spot Location	Spot No.	U (ppm)	Age (ka) [a]	1 σ (ka)
1	rim	1	72	131	34
1	core	2	129	120	29
1	core	3	105	211	64
2	core	4	275	138	17
3	core	5	191	126	19
3	core	6	188	133	21
4	core	7	379	160	20
5	core	8	135	162	33
6	rim	9	142	130	21
6	core	10	153	116	18
6	rim	11	139	139	24
7	core	12	127	138	25
7	core	13	167	148	27
8	core	14	125	132	26
8	rim	15	137	166	36
9	core	17	108	156	35
10	core	18	487	184	24
11	rim	19	126	132	23
11	rim	20	418	137	13
			Isochron Age:	105	+36/-27

[a] Ages calculated from two-point isochrons through the zircon data and approximate whole-rock U/Th composition.

Generally, the dark-colored areas in a zircon CL image indicate a higher U concentration. The second zircon population (see above) has higher U concentrations than the main zircon population. There does not appear to be a significant age difference between analyses located on the core verses the rim of a zircon. Many core analyses are slightly older than the analysis from the adjacent rim, however, the majority of analyses

on the same zircon are within uncertainty of each other (Appendix I). The mean of the two-point isochron ages (Table 9.1) of both zircon populations produces indistinguishable average ages, 146 ± 29 ka (Grains 1, 3, 5-7, 9 & 10) and 144 ± 23 ka (Grains 2, 4, 8 & 11). Isochrons through the two zircon populations also produced indistinguishable disequilibrium ages, 104^{+54}_{-36} ka (Grains 1, 3, 5-7, 9 & 10) and 107^{+58}_{-38} ka (Grains 2, 4, 8 & 11). There does not appear to be an observable age difference between the two zircon populations. An overall, single zircon population is supported by the age probability density plot (Figure 9.4), which indicates a single age distribution.

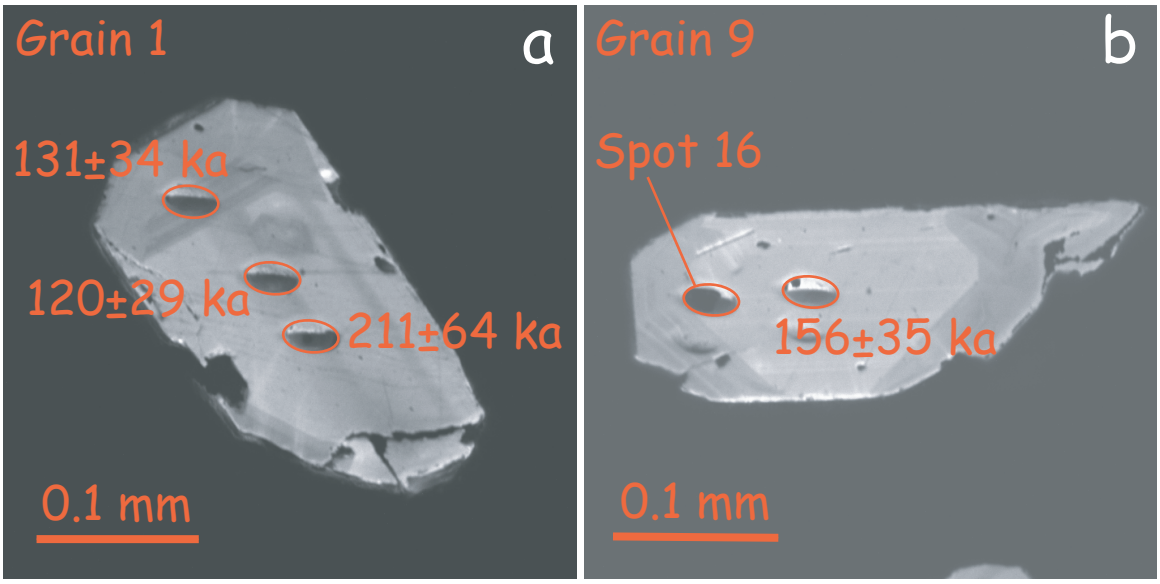

Figure 9.1. CL images of zircons from GRWY6 analyzed for $^{230}Th/^{238}U$ ages. These are representative of the main population: a) Grain 1 (analyses 1, 2, & 3) exhibits multiple, subtle growth zones; and b) Grain 9 (analyses 16 & 17) exhibits a euhedral, light-colored CL core that is truncated by the grain edge. All grains are moderately resorbed. $^{230}Th/^{238}U$ dates correspond to closest analysis spot.

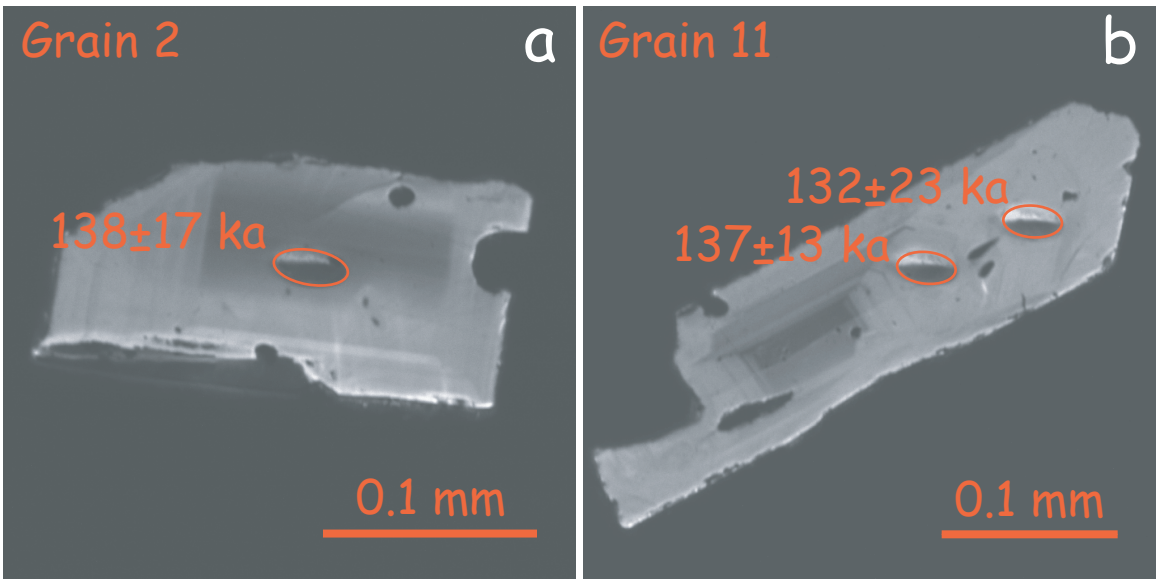

Figure 9.2. CL images of zircons from GRWY6 analyzed for $^{230}Th/^{238}U$ ages. These are representative of the second population: a) Grain 2 (analysis 4) exhibits a subhedral, dark-colored CL core with several subtle growth zones; and b) Grain 11 (analyses 19 & 20) exhibits distinct subhedral growth zones that grade from a dark-colored CL core. All grains are slightly resorbed. $^{230}Th/^{238}U$ dates correspond to closest analysis spot.

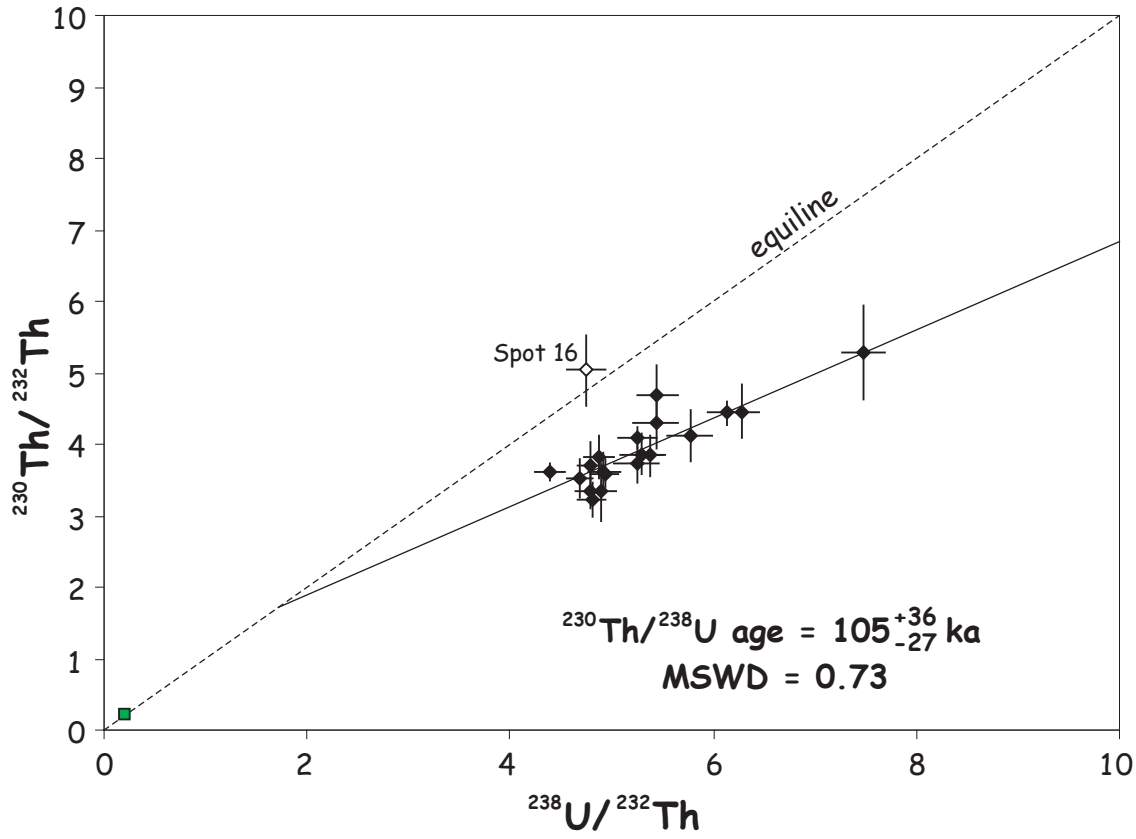

Figure 9.3. $^{230}Th/^{232}Th$ vs. $^{238}U/^{232}Th$ isochron diagram for zircons from the Gibbon River rhyolite GRWY6. A free-fit York regression line through 19 analyses gives a $^{230}Th/^{238}U$ disequilibrium age of 105^{+36}_{-27} ka (1 σ uncertainty; MSWD = 0.73). The analysis above the equiline is spot 16, which included epoxy in the analysis, and is excluded from the calculated isochron age. Uncertainties are 1 σ. The approximate whole-rock U/Th is indicated by (▪).

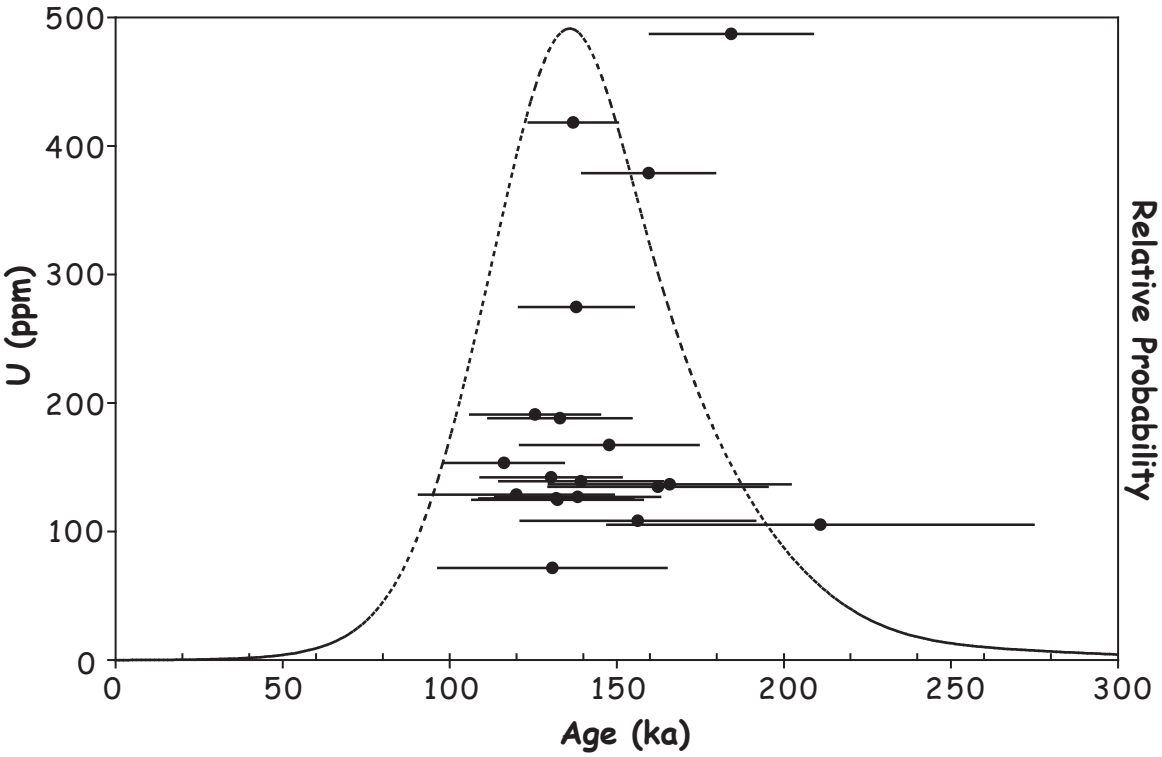

Figure 9.4. U concentrations vs. two-point isochron ages for individual zircon analyses with a probability density curve (dotted line) overlain. Analysis 16 is excluded from the graph. Uncertainties are 1 σ.

CHAPTER 10

$^{40}AR/^{39}AR$ GEOCHRONOLOGY

Crystal Spring Mafic Enclaves

Three 200 mg aliquots of basalt from the enclaves of sample CSWY1E were analyzed by furnace step-heating. CSWY1E #1 yielded a total gas age of 2.32 ± 0.11 Ma (Appendix J). The age spectrum (Figure 10.1) begins with negative ages, rising to a discordant spectrum with a minimum of 383 ka and maximum of 78.19 Ma. A plateau was calculated, yielding an age of 420.1 ± 53.9 ka (steps 3 to 6, of 8 steps). The plateau contained 50.6% of the ^{39}Ar released from the sample. An isochron (Figure 10.2) calculated from steps 3 to 7 yielded an age of 212.0 ± 4.25 ka (52.5% of ^{39}Ar released, MSWD = 1.7). The $^{40}Ar/^{36}Ar$ intercept was 299.4 and the analyses clustered near the y-axis, yielding the sample contained mostly atmospheric argon, causing a poorly constrained isochron age. CSWY1E #2 yielded a total gas age of 547.6 ± 78.7 ka (Appendix J). The age spectrum (Figure 10.3) is similar in shape to CSWY1E #1, with negative ages at the beginning and increasing in age to a maximum age of 16.41 Ma. No plateau or isochron was calculated for this analysis. CSWY1E #3 yielded a total gas age of 1.18 ± 0.10 Ma (Appendix J). The age spectrum (Figure 10.4) rises from negative ages at the beginning to a maximum of 9.87 Ma. No plateau or isochron was calculated for this analysis.

While, the plateau age from CSWY1E #1 is valid statistically, the 2σ uncertainty the plateau age is more than 25% of the calculated age. The plateau age is highly imprecise, making the age unreliable. Both the poorly constrained isochron and the discordant age spectrum of CSWY1E #1 indicate excess Ar in the sample. The assumption that the

sample's initial $^{40}Ar/^{36}Ar$ equals the atmospheric $^{40}Ar/^{36}Ar$ (295.5) is not valid when excess argon is present. This means that the sample contains less $^{40}Ar^{*}$ (radiogenic ^{40}Ar) than calculated, overestimating the $^{40}Ar/^{39}Ar$ age. All of the CSWY1E analyses are poor and the ages calculated for CSWY1E #1 are unreliable, however, the isochron age of CSWY1E #1 provides a maximum age for the CSWY1E enclaves (Table 10.1).

Table 10.1. Ar-Ar Ages Calculated for CSWY1E Basalt Groundmass Analyses

Analysis No. [a]	Total Gas Age [b]	Plateau Age (ka) [b]	Isochron Age (ka) [b]
CSWY1E #1	2.32 ± 0.11 Ma	420.1 ± 53.9	212.0 ± 4.25 [†]
CSWY1E #2	547.6 ± 78.7 ka	none	none
CSWY1E #3	1.18 ± 0.10 Ma	none	none

[a] Analysis data presented in Tables J.1 through J.3, Appendix J.
[b] Uncertainties reported to 1σ.
[†] Maximum age for sample CSWY1E.

Obsidian Cliff Rhyolite

Three aliquots of OCWY2 glass were analyzed by furnace step-heating runs and individual glass grains were analyzed by laser fusion. Furnace step-heat OCWY2 #1 yielded a total gas age of 71.1 ± 5.9 ka (Appendix J). The age spectrum (Figure 10.5) begins with two old ages and then flattens to a plateau consisting of 92.6% of the ^{39}Ar released by the sample (steps 3 to 13, of 13 steps). The plateau age is 59.2 ± 6.0 ka. Two isochron ages were calculated for OCWY2 #1. The first isochron (Figure 10.6), calculated from steps 1 through 9, yielded an age of 56.0 ± 0.7 ka (64.4% of ^{39}Ar released, MSWD = 1.0) with a $^{40}Ar/^{36}Ar$ intercept of 300.4. The second isochron (Figure 10.7), calculated from steps 3 though 12, yielded an age of 62.5 ± 1.6 ka (78.7% of ^{39}Ar released, MSWD = 1.8) with a $^{40}Ar/^{36}Ar$ intercept of 284. Both isochrons had a good spread in radiogenic yield to constrain the calculated ages (Figures 10.6 & 10.7).

Furnace step-heat OCWY2 #2 yielded a total gas age of 69.9 ± 5.9 ka (Appendix J). The age spectrum (Figure 10.8) begins with an old age, then drops to a slightly discordant plateau yielding a plateau age of 58.4 ± 3.0 ka and consisting of 93.1% of the ^{39}Ar released (steps 2 to 13, of 13 steps). No isochron was calculated from the analysis of OCWY2 #2. Analysis OCWY2 #3 yielded a total gas age of 60.6 ± 5.7 ka (Appendix J). The age spectrum (Figure 10.9) is slightly U-shaped and yields a plateau age of 59.9 ± 3.0 ka (96.4% of the ^{39}Ar released; steps 1 to 12, of 13 steps). No isochron was calculated from the analysis of OCWY2 #3. All three OCWY2 furnace step-heat plateau ages overlap at ± 2σ uncertainty and a weighted mean age of 59.2 ± 2.0 ka was calculated for OCWY2.

Obsidian grains from sample OCWY2 were analyzed by single crystal laser fusion (analysis OCWY2 #4). The ^{36}Ar blank measurement was ~50% of the total measured ^{36}Ar and the ^{40}Ar blank measurement was ~20% of the total measured ^{40}Ar. Since the blank corrections were so high compared to the Ar measured from each grain, only 5 obsidian fragments were analyzed. The five samples yielded a mean age of 71.6 ± 20.8 ka (Appendix J). No isochrons were calculated from the analyses.

The first isochron for analysis OCWY2 #1 gives the youngest age of all the OCWY2 #1 $^{40}Ar/^{39}Ar$ ages. However, this isochron contains the first two furnace step-heat steps of the glass analysis. These two steps are very low in neutron induced $^{39}Ar_K$ and it is likely that these steps represent ^{39}Ar recoil during irradiation, giving anomalously high $^{40}Ar/^{39}Ar$ calculated ages (Morgan *et al.*, 2007) (Figure 10.5). This reduces confidence in the first OCWY2 #1 isochron age. However, the second isochron age overlaps with the OCWY2 #1 plateau age at ± 2σ uncertainty, further validating these two ages. Thus the

preferred age for OCWY2 #1 is the second isochron age of 62.5 ± 1.6 ka (Table 10.2). The preferred age of OCWY2 #2 is the plateau age of 58.4 ± 3.0 ka (Table 10.2). The preferred age for OCWY2 #3 is the plateau age of 59.9 ± 3.0 ka (Table 10.2). Since all three OCWY2 furnace step-heat analyses produced excellent plateau ages and the preferred age for OCWY2 #1, the second isochron age, agrees within uncertainty of OCWY2 #1's plateau age, the preferred age for all the analyses of OCWY2 is 59.2 ± 2.0 ka, the weighted mean age of the three plateau ages (Table 10.2).

In the single grain laser fusion analyses of glass fragments from sample OCWY2, the low inferred $^{36}Ar/^{40}Ar$ from the five analyses suggests incomplete degassing during fusion. Since the mean age of the analyses is greater than the furnace step-heat plateau ages, ^{39}Ar recoil and loss is likely to have occurred during irradiation causing anomalously old $^{40}Ar/^{39}Ar$ dates (Morgan *et al.*, 2007). Also, the high blank to total measured Ar ratio suggests these analyses are poorly constrained. These analyses were considered unreliable and were disregarded with respect to any age interpretations.

Table 10.2. Ar-Ar Ages Calculated for OCWY2 Volcanic Glass Analyses

Analysis No. [a]	Total Gas Age (ka) [b]	Plateau Age (ka) [b]	Isochron Age (ka) [b]
OCWY2 #1	71.1 ± 5.9	59.2 ± 6.0	56.0 ± 0.7 & 62.5 ± 1.6 [†]
OCWY2 #2	69.9 ± 5.9	58.4 ± 3.0 [†]	none
OCWY2 #3	60.6 ± 5.7	59.9 ± 3.0 [†]	none
OCWY2 #4	71.6 ± 20.8 [c]	-	none
Weighted Mean Age (Plateau Ages) =		59.2 ± 2.0*	-

[a] Analysis data presented in Tables J.4 through J.7, Appendix J.
[b] Uncertainties reported to 1σ.
[c] Mean age of single laser fusion analyses.
[†] Preferred age for individual analyses.
*Preferred age for sample OCWY2.

Gibbon River Rhyolites

Three aliquots of GRWY6 sanidines were analyzed by furnace step-heat runs and two different sizes of sanidine grains were analyzed by single crystal laser fusion. Furnace step-heat GRWY6 #1 yielded a total gas age of 79.4 ± 6.6 ka (Appendix J). The age spectrum GRWY6 #1 (Figure 10.10) begins with old ages, then drops to a slightly discordant plateau. The plateau age was calculated at 78.0 ± 3.5 ka (steps 4 to 12, of 13 steps) and contains 93.9% of the ^{39}Ar released. No isochron was calculated for analyses GRWY6 #1. Furnace step-heat GRWY6 #2 yielded a total gas age of 114.1 ± 6.2 ka (Appendix J). The age spectrum (Figure 10.11) starts with old ages, then quickly drops to younger ages that progressively increase to 233 ka. Finally, the spectrum drops to a pseudo-plateau which continues the lowering age trend (Figure 10.11). A pseudo-plateau was calculated from the last three steps of the age spectrum, yielding an age of 71.7 ± 5.8 ka (45.3% of the ^{39}Ar released; steps 11 through 13, of 13 steps). No isochron ages were calculated for GRWY2 #2. Furnace step-heat GRWY6 #3 yielded a total gas age of 85.2 ± 6.0 ka (Appendix J). The age spectrum (Figure 10.12) alternated between old and young ages at the beginning and then stabilizes to a slightly hump-shaped plateau. The plateau age is 82.4 ± 7.6 ka and contains 82.6% of the ^{39}Ar released (steps 6 through 12, of 13 steps). No isochron was calculated from GRWY6 #3.

The first set of single crystal laser fusions were preformed on a 850 μm sanidine size fraction from GRWY6 (GRWY6 #4). 12 crystals were fused (Appendix J). A single xenocryst (crystal 11) was analyzed in the data set, yielding an age of 6.15 ± 0.12 Ma (Appendix J). The mean age of all analyzed crystals, excluding the obvious xenocryst (crystal 11), is 95.4 ± 36.9 ka (MSWD = 11; Appendix J). Outliers of the analyzed

population were determined by iteratively calculating the mean age and standard deviation of the population and removing analyses with ages outside 2σ of the mean age. Once an analysis was determined to be an outlier, it was removed from the population, and the mean age and standard deviation was recalculated until all analyses in the population were within 2σ of the calculated mean age. Using this method, crystals 1, 6, and 11 were rejected as being outliers to the data set. The weighted mean age (Figure 10.13) of the remaining crystals (crystals 2-5, 7-10 & 12) is 80.2 ± 3.7 ka (MSWD = 2.0; Appendix J). An isochron (Figure 10.14) yielded an age of 52 ± 8.5 ka from 7 crystals (crystals 2-5, 7-8 & 10, MSWD = 1.9) and had a $^{40}Ar/^{36}Ar$ intercept of 323 ± 11.

The second set of single crystal laser fusions was preformed on a 1400 μm sanidine size fraction (GRWY6 #5). 23 crystals were fused and the mean age of all analyzed crystals is 147.6 ± 50.5 ka (MSWD = 24; Appendix J). Following the method described above, no analyses were determined to be outliers of this population. A cumulative probability plot (Figure 10.15) of the analyses formed three peaks: 80.4 ± 4.6 ka (crystals 14, 16, 20 & 22-23; MSWD = 0.87), 144.4 ± 2.9 ka (crystals 1-2, 5-6, 8-11, 13, 15, 18-19 & 21; MSWD = 3.7), and 221.0 ± 4.6 ka (crystals 3-4, 7, 12 & 17; MSWD = 2.4) from left to right.

It was noticed that the average ages from the beginning of the 1400 μm sanidine analyses to the end decrease (crystals 1-7: 179.3 ± 38.5 ka, crystals 8-15: 151.5 ± 44.2 ka, crystals 16-23: 115.9 ± 51.2 ka). This trend could be caused by incomplete fusion and degassing of the earliest analyses and then, improvement in complete crystal fusion overtime, resulting in anomalously old ages due to incomplete degassing of the crystal. However, volcanic sanidines have a homogeneous internal ^{40}Ar and, using the $^{40}Ar/^{39}Ar$

geochronologic method, the diffusion and release of Ar from a mineral will be the same for all Ar isotopes (Hall and Farrell, 1995). Therefore, incomplete fusion of the sanidine crystals should produce the same age as complete fusion. It appears that this decrease in the average age of the analyses over time is coincidental.

Both populations of sanidine single crystal laser fusion analyses produced trimodal age probability plots (Figures 10.13 & 10.15). The weighted mean ages of the youngest population of each sanidine analysis overlap within 1σ. Along with the 6.15 Ma xenocryst, the analyses of GRWY6 #4 also contained two crystals with ages older than the main sanidine population (Appendix J). These two analyses, crystals 1 and 6, fall with the ages of the middle sanidine population of the GRWY6 #5 analyses (weighted mean age = 144.4 ± 2.9 ka). Finally, GRWY6 #5 has an older sanidine population unrepresented in GRWY6 #4 analyses. Given the presence of xenocrystic sanidines within sample GRWY6, it is likely that the two older sanidine populations represent partially reset sanidine xenocrysts.

For GRWY6 #1, the preferred age is the plateau age of 78.0 ± 3.5 ka (Table 10.3). While GRWY6 #2's pseudo-plateau does not contain 50% of the ^{39}Ar released, it is probably the most reliable age. During a step-heat run, the higher temperatures release gas from the center of the grain, the region of the grain most likely to be protected from Ar contamination and loss. The steps that make up the pseudo-plateau are the three highest temperature steps of analysis GRWY6 #2 (Figure 10.11). The preferred age for GRWY6 #2 is the pseudo-plateau age of 71.7 ± 5.8 ka (Table 10.3). The plateau age of 82.4 ± 7.6 ka is the preferred age for GRWY6 #3 (Table 10.3). The preferred age for GRWY6 #4 is the isochron age of 52 ± 8.5 ka (Table 10.3). Both GRWY6 #4 and

GRWY6 #5 likely contain partially reset xenocrysts (along with the obvious 6.15 Ma xenocryst of GRWY6 #4) within their populations. So, the preferred age for GRWY6 #5 is the youngest population age of 80.4 ± 4.6 ka (Table 10.3). The preferred age for the GRWY6 analyses is the GRWY6 #4 isochron age of 52 ± 8.5 ka (Table 10.3).

Table 10.3. Ar-Ar Ages Calculated for GRWY6 Sanidine Analyses

Analysis No. [a]	Total Gas Age (ka) [b]	Plateau Age (ka) [b]	Isochron Age (ka) [b]
GRWY6 #1	79.4 ± 6.6	78.0 ± 3.5 [†]	none
GRWY6 #2	114.1 ± 6.2	71.7 ± 5.8 [†]	none
GRWY6 #3	85.2 ± 6.0	82.4 ± 7.6 [†]	none
GRWY6 #4	95.4 ± 36.9 [c]	-	52 ± 8.5 [†]*
	Weighted Mean Age =	80.2 ± 3.7	-
GRWY6 #5	147.6 ± 50.5 [c]	-	none
Weighted Mean Age (Population 1) =		80.4 ± 4.6 [†]	-
Weighted Mean Age (Population 2) =		144.4 ± 2.9	-
Weighted Mean Age (Population 3) =		221.0 ± 4.6	-

[a] Analysis data presented in Tables J.8 through J.12, Appendix J.
[b] Uncertainties reported to 1σ.
[c] Mean age of single laser fusion analyses.
[†] Preferred age for individual analyses.
*Preferred age for sample GRWY6.

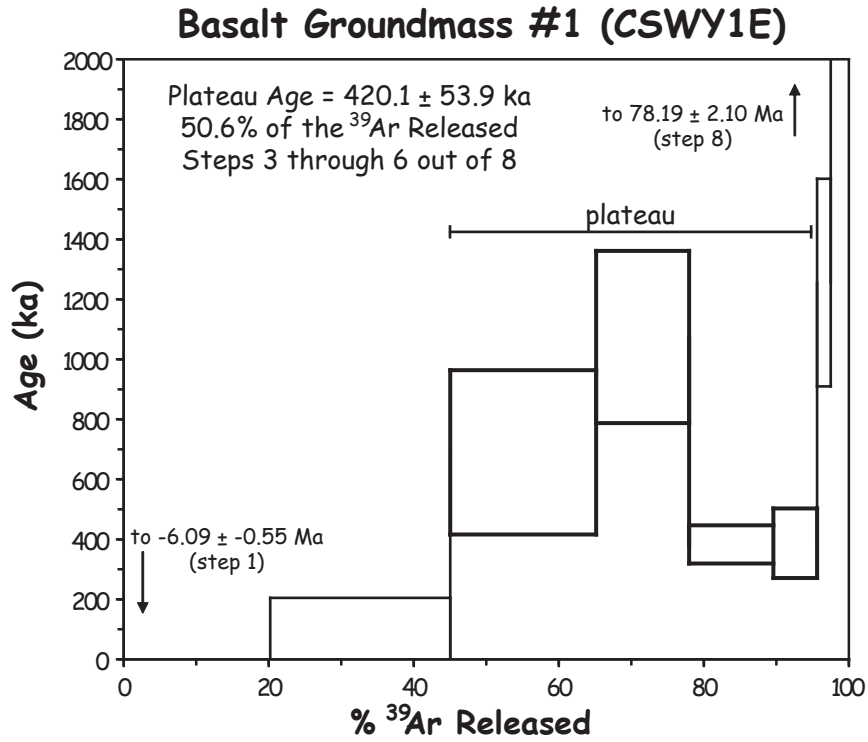

Figure 10.1. Furnace step-heat $^{40}Ar/^{39}Ar$ age spectrum for CSWY1E #1, basalt groundmass. Bold lines mark steps included in plateau age. Errors are reported at 1σ. Error boxes are shown at 1σ.

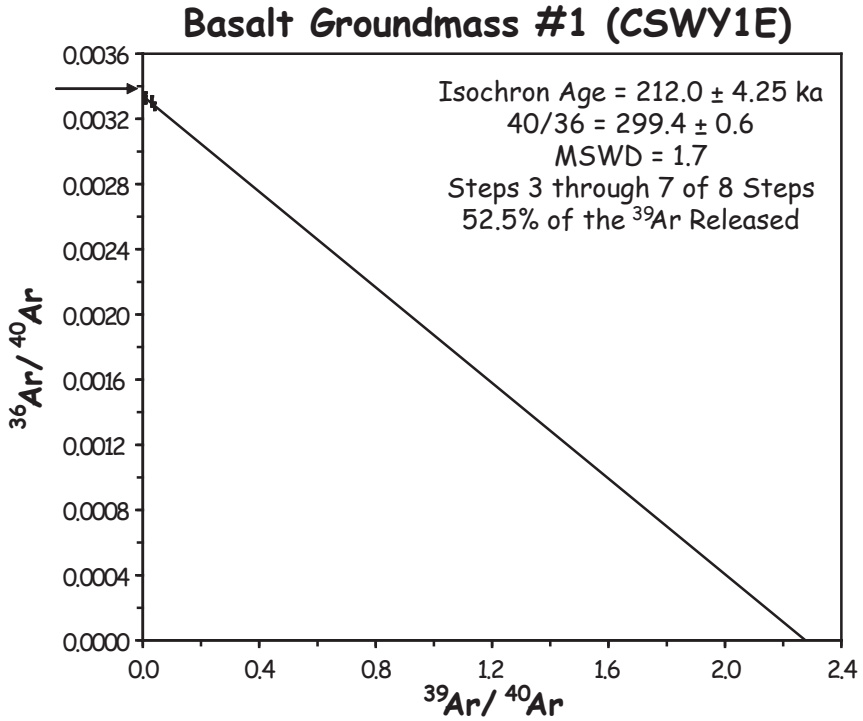

Figure 10.2. $^{40}Ar/^{39}Ar$ inverse isochron for CSWY1E #1, basalt groundmass. Errors are reported at 1σ. Error ellipses are shown at 2σ. Arrow on the y-axis indicates location of atmospheric argon composition.

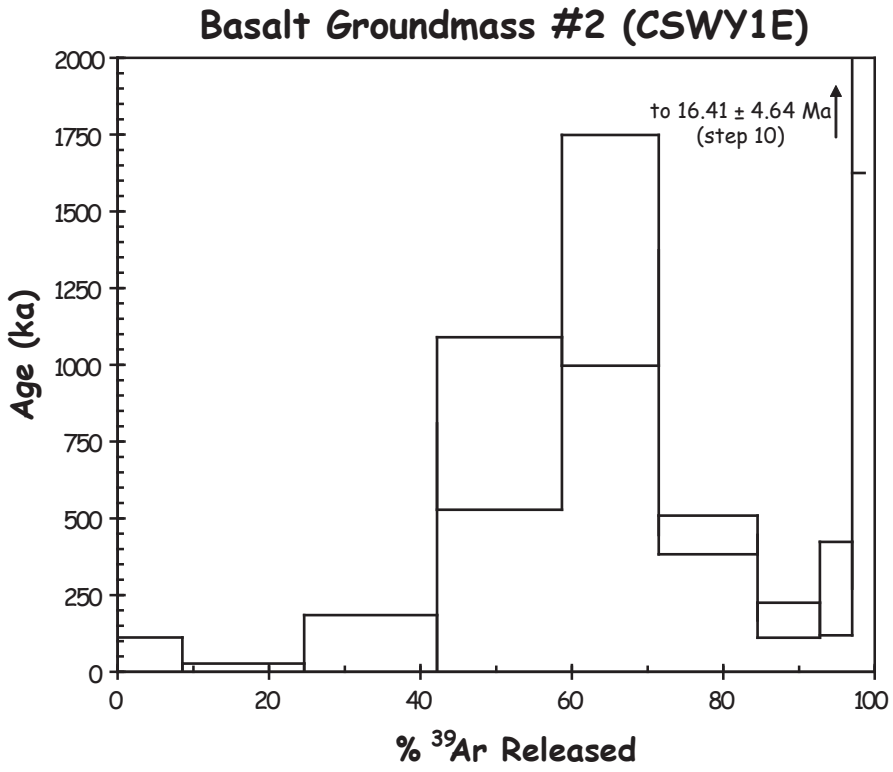

Figure 10.3. Furnace step-heat $^{40}Ar/^{39}Ar$ age spectrum for CSWY1E #2, basalt groundmass. Errors are reported at 1σ. Error boxes are shown at 1σ.

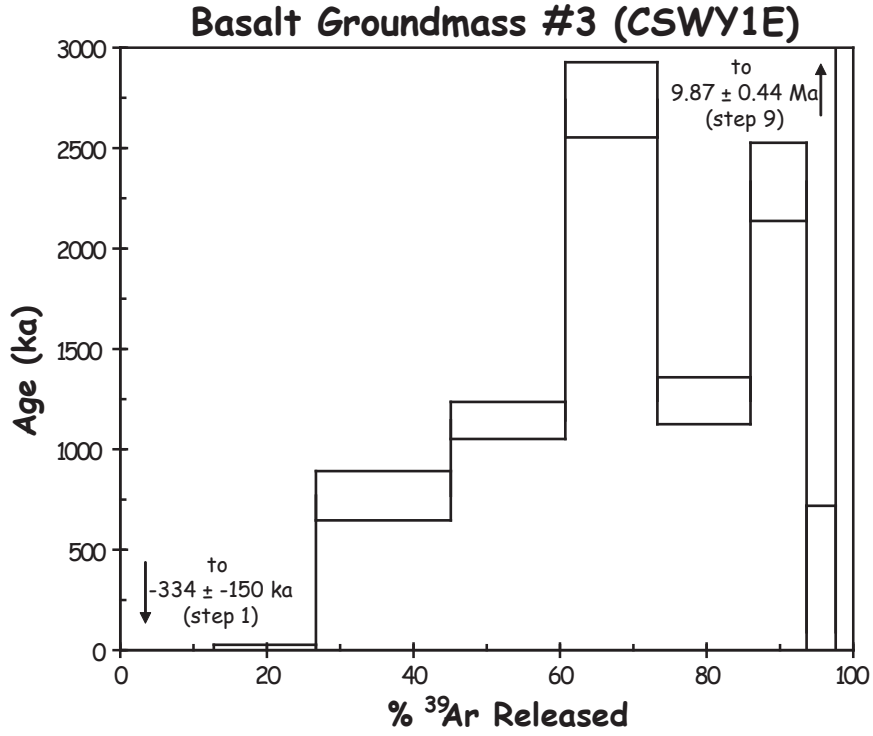

Figure 10.4. Furnace step-heat $^{40}Ar/^{39}Ar$ age spectrum for CSWY1E #3, basalt groundmass. Errors are reported at 1σ. Error boxes are shown at 1σ.

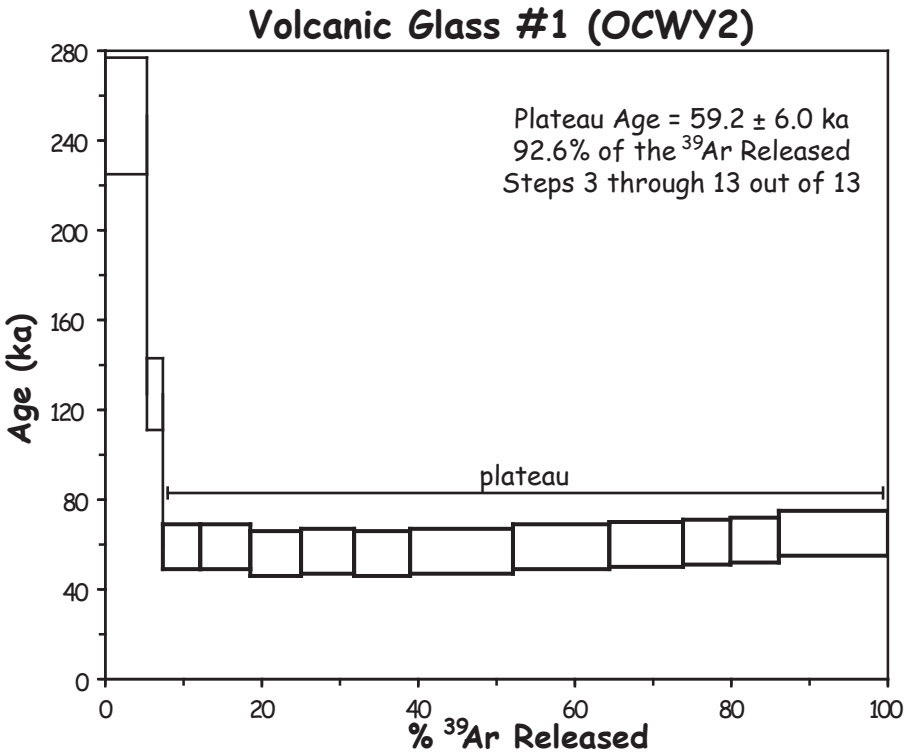

Figure 10.5. Furnace step-heat $^{40}Ar/^{39}Ar$ age spectrum for OCWY2 #1, volcanic glass. Bold lines mark steps included in plateau age. Errors are reported at 1σ. Error boxes are shown at 1σ.

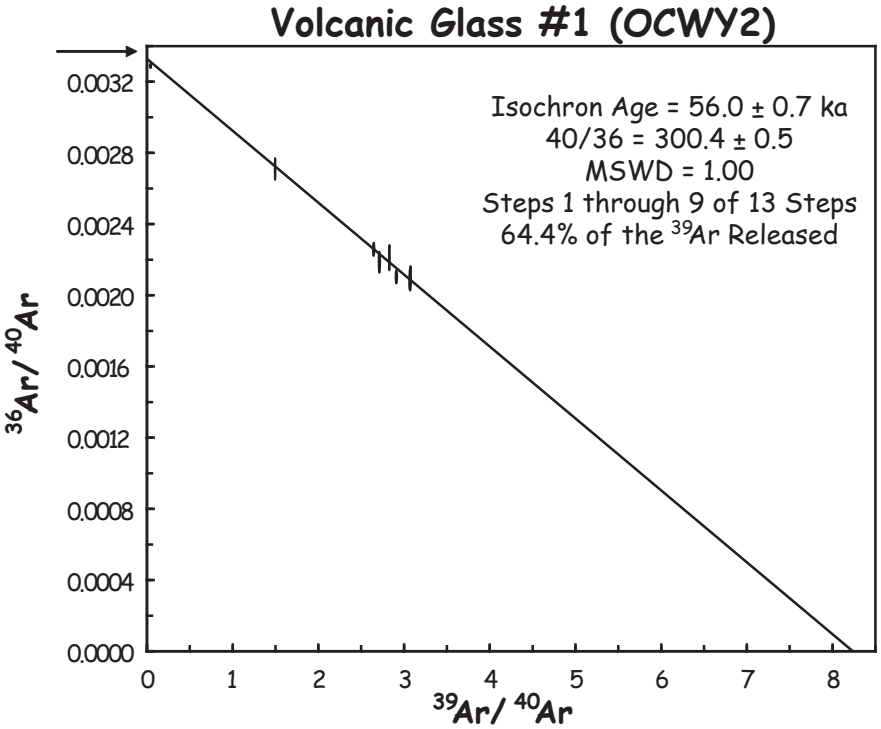

Figure 10.6. $^{40}Ar/^{39}Ar$ inverse isochron #1 for OCWY2 #1, volcanic glass. Errors are reported at 1σ. Error ellipses are shown at 2σ. Arrow on the y-axis indicates location of atmospheric argon composition.

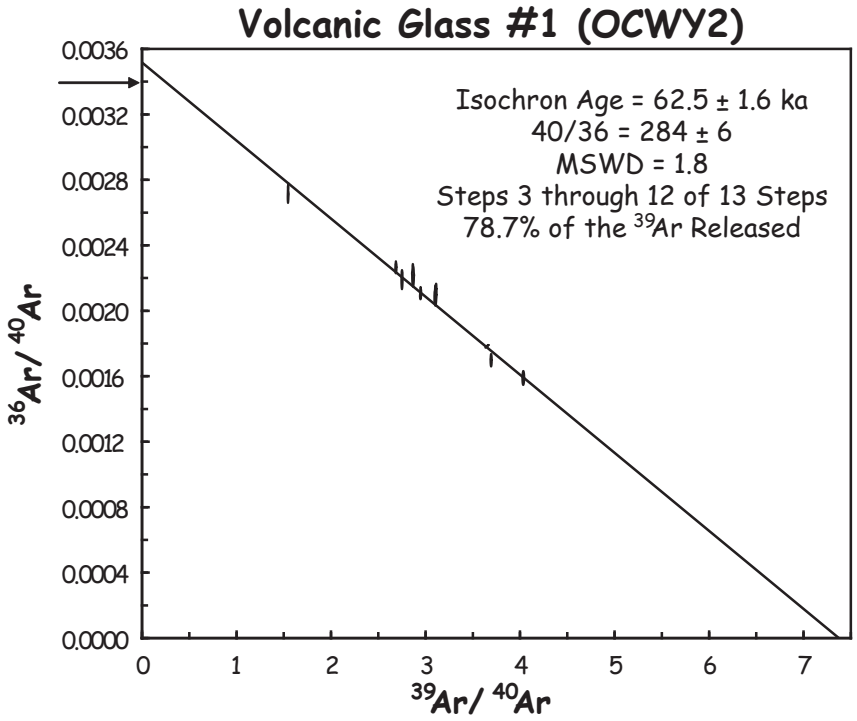

Figure 10.7. $^{40}Ar/^{39}Ar$ inverse isochron #2 for OCWY2 #1, volcanic glass. Errors are reported at 1σ. Error ellipses are shown at 2σ. Arrow on the y-axis indicates location of atmospheric argon composition.

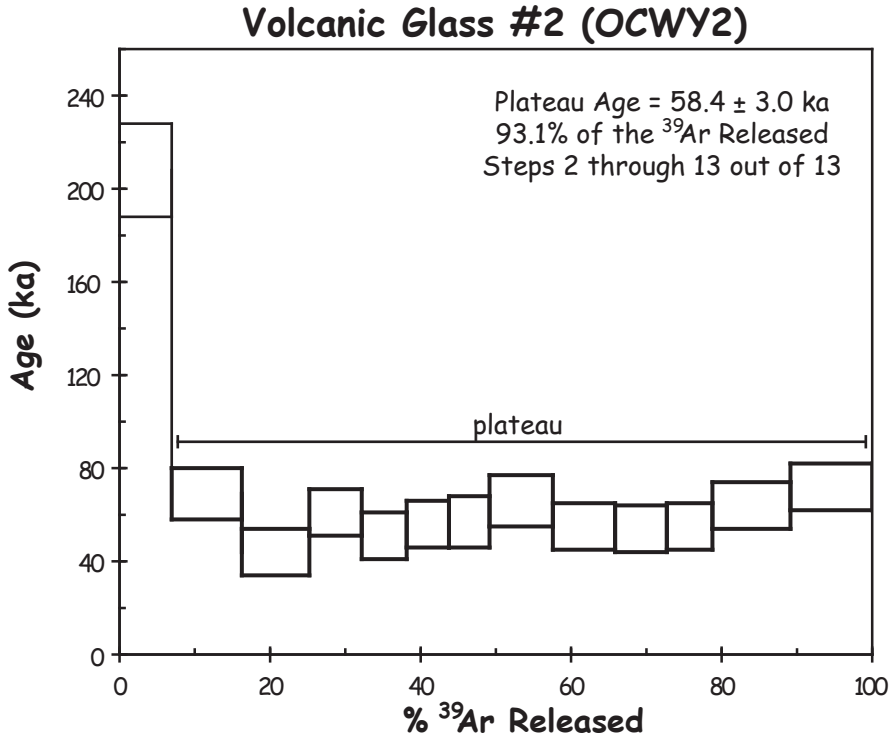

Figure 10.8. Furnace step-heat $^{40}Ar/^{39}Ar$ age spectrum for OCWY2 #2, volcanic glass. Bold lines mark steps included in plateau age. Errors are reported at 1σ. Error boxes are shown at 1σ.

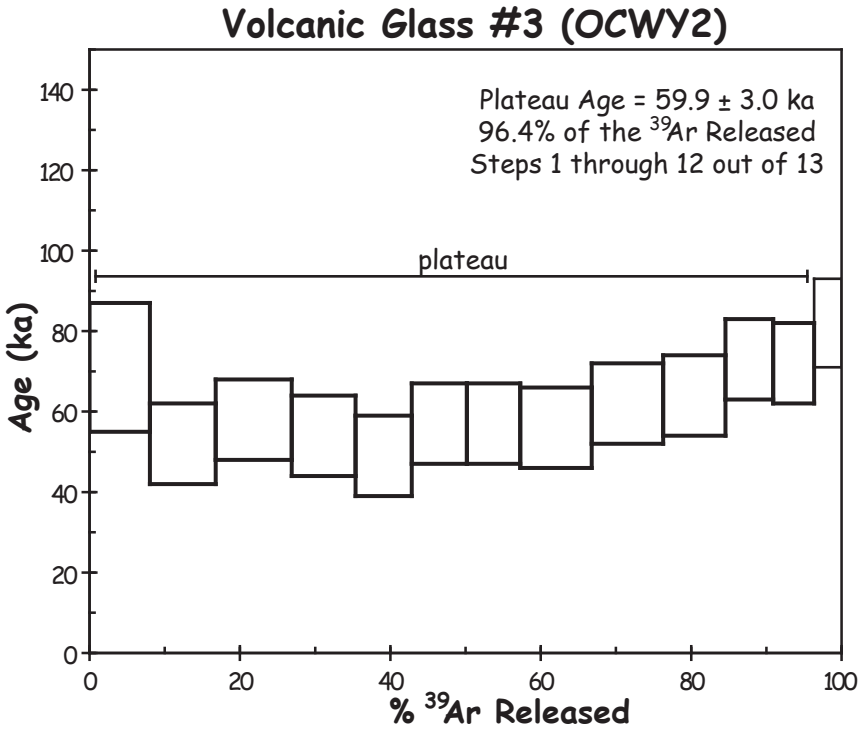

Figure 10.9. Furnace step-heat $^{40}Ar/^{39}Ar$ age spectrum for OCWY2 #3, volcanic glass. Bold lines mark steps included in plateau age. Errors are reported at 1σ. Error boxes are shown at 1σ.

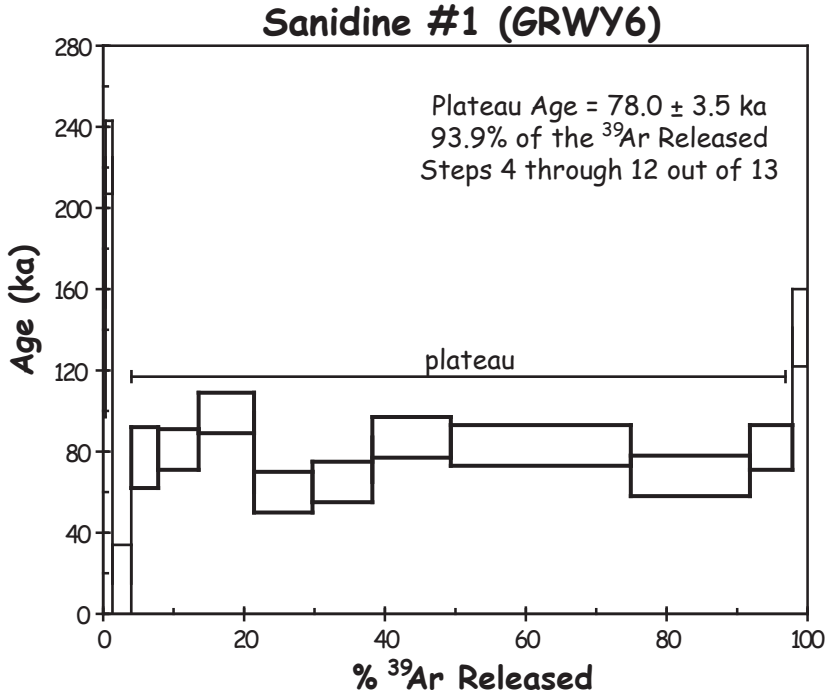

Figure 10.10. Furnace step-heat $^{40}Ar/^{39}Ar$ age spectrum for GRWY6 #1, sanidine. Bold lines mark steps included in plateau age. Errors are reported at 1σ. Error boxes are shown at 1σ.

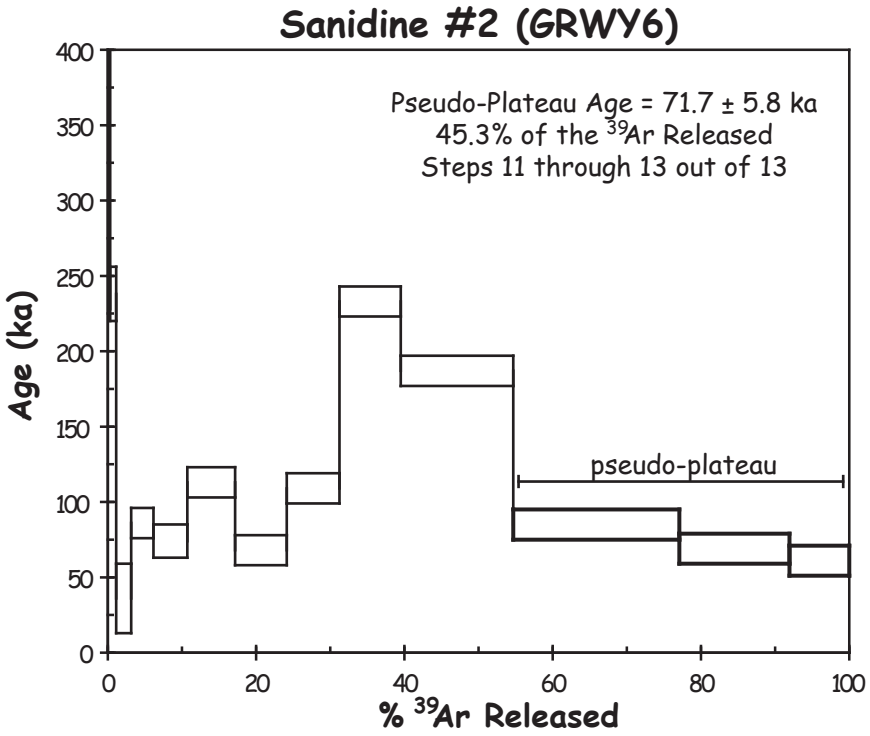

Figure 10.11. Furnace step-heat $^{40}Ar/^{39}Ar$ age spectrum for GRWY6 #2, sanidine. Bold lines mark steps included in pseudo-plateau age. Errors are reported at 1σ. Error boxes are shown at 1σ.

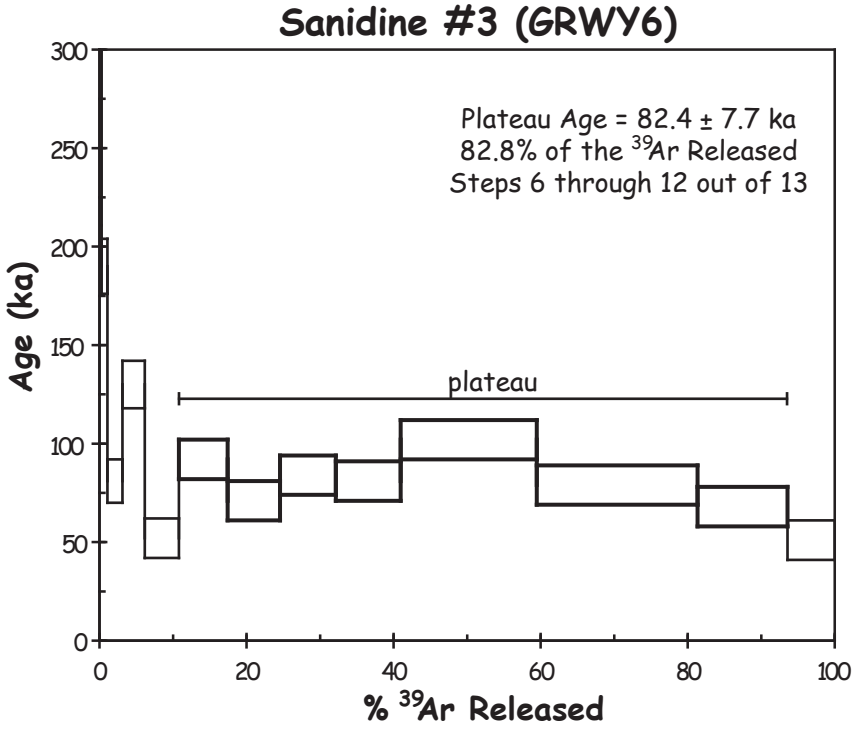

Figure 10.12. Furnace step-heat $^{40}Ar/^{39}Ar$ age spectrum for GRWY6 #3, sanidine. Bold lines mark steps included in plateau age. Errors are reported at 1σ. Error boxes are shown at 1σ.

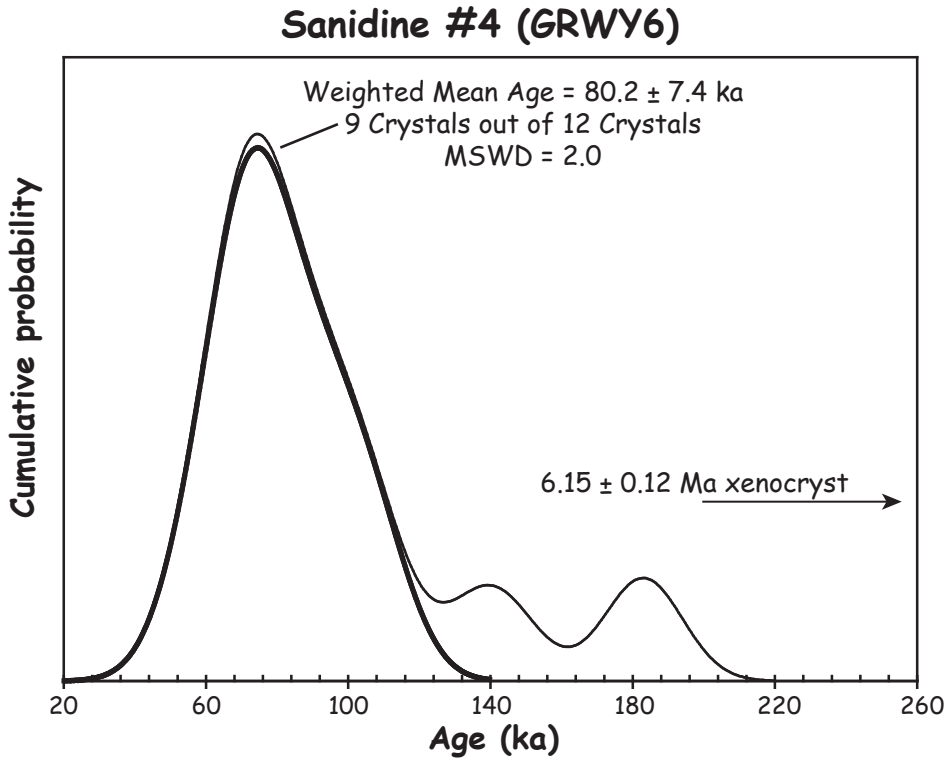

Figure 10.13. Cumulative age probability plot of sanidine crystals 1 through 12 (except xenocryst 11), thin line, and of the crystals used for the weighted mean age (crystals 2-5, 7-10, & 12), bold line.

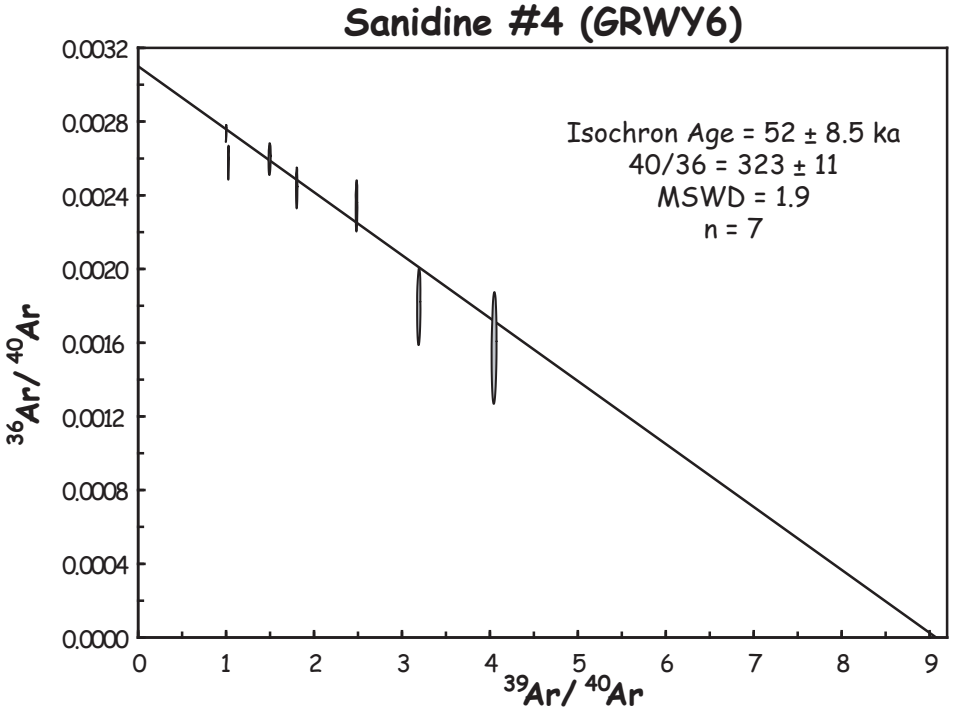

Figure 10.14. $^{40}Ar/^{39}Ar$ inverse isochron for 7 sanidine crystals of GRWY6 #4. Errors are reported at 1σ. Error ellipses are shown at 2σ. Atmospheric argon composition would be located at 0.00338 on the y-axis.

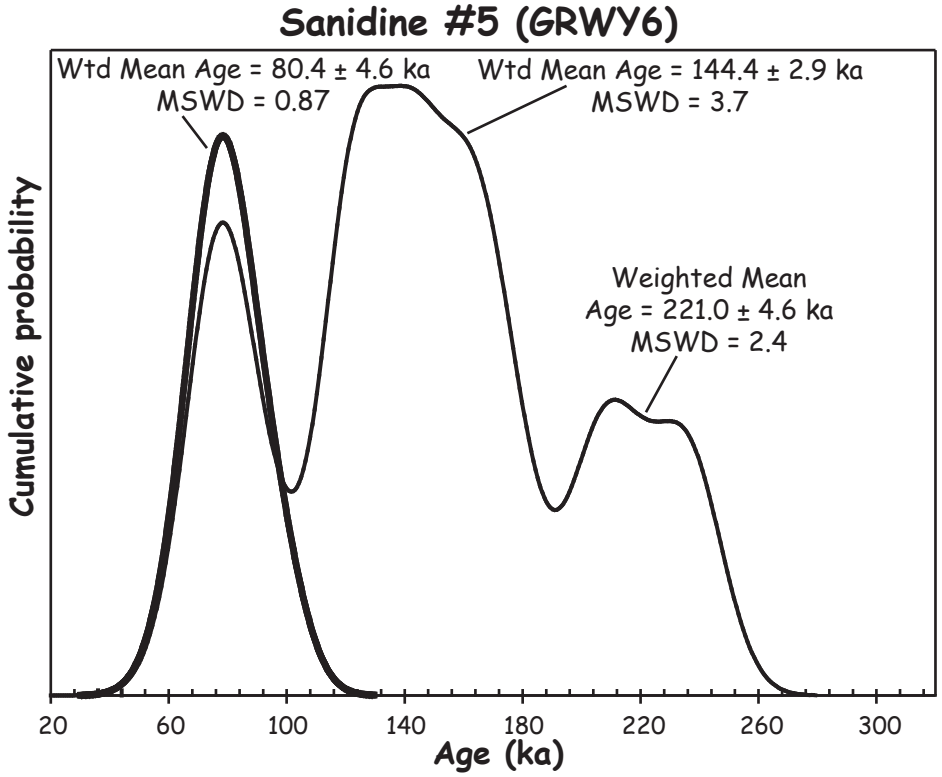

Figure 10.15. Cumulative age probability plot of all 23 sanidine crystals of GRWY6 #5, thin line, and of the 5 sanidine crystals that make up the first peak (crystals 14, 16, 20, 22 & 23), bold line.

CHAPTER 11

DISCUSSION

$^{40}Ar/^{39}Ar$ Geochronology

Crystal Spring Flow

The $^{40}Ar/^{39}Ar$ ages calculated from three analyses of basalt from mafic enclaves within the Crystal Spring mingled lavas are all anomalously old (Chapter 10; Appendix J). These ages are probably a result of excess argon trapped within the enclaves, which probably partly crystallized at depth upon interaction with the cooler silicic magma prior to eruption of the mingled lava. This excess Ar is likely the initial Ar composition of the magmatic (i.e. mantle) source of the basaltic magma (Funkhouser *et al.*, 1968). It indicates the basaltic enclaves did not have time for their argon isotopes to equilibrate with the surrounding silicic magma, which as a crustal magma should reflect atmospheric argon compositions. Excess Ar within basaltic magmas is not uncommon (McDougall and Harrison, 1999), and inverse isochrons calculated for these analyses would provide both accurate $^{40}Ar/^{39}Ar$ ages and the initial Ar composition (McDougall and Harrison, 1999). The only isochron for the Crystal Spring mingled lavas was from analysis CSWY1E #1, which yielded an age of 212.0 ± 4.25 ka (Figure 10.2). However, the four steps that form this isochron cluster near the $^{36}Ar/^{40}Ar$ axis (Figure 10.2) and the isochron is poorly constrained, and is thus considered unreliable (Chapter 10). No useful ages were obtained from the $^{40}Ar/^{39}Ar$ analyses of the Crystal Spring mafic enclaves.

The Crystal Spring and the Obsidian Cliff flows are separated by a wash less than a kilometer wide (Figure 4.1). Both flows are oriented along the dominant strike (north-south) of the East Gallatin-Washburn Fault Zone (Christiansen *et al.*, 2007). Based on

this geographical and structural link, and the geochemical relationship (discussed below) between the Crystal Spring mingled lavas and the Obsidian Cliff flow (Figure 11.1), both flows are considered to have erupted within a brief time interval. The $^{40}Ar/^{39}Ar$ eruption age of the Obsidian Cliff flow would thus be the most likely eruption age of the Crystal Spring mingled lavas.

Obsidian Cliff Flow

Three $^{40}Ar/^{39}Ar$ step-heating analyses and a set of laser fusion analyses of glass fragments from the Obsidian Cliff flow (Chapter 10; Appendix J) produced plateau ages, inverse isochron ages, and a mean age all within uncertainty of each other (Figures 10.5 to 10.9). However, several of the individual step analyses that form the first inverse isochron have low gas yields and give unreliable ages (Chapter 10). The second isochron age is an acceptable eruption age, however, it is the older end of the age range of the plateau ages, isochron ages, and mean age (Figure 10.7; Chapter 10). Additionally, although the first isochron suggests some excess argon in the Obsidian Cliff samples (Figure 10.6), the second isochron yields a $^{40}Ar/^{36}Ar$ ratio that is indistinguishable (within 2σ uncertainty) from the atmospheric argon ratio (Figure 10.7). These observations suggest excess argon is not present and lends support to the reliability of the three plateau ages. Finally, the three separate step-heating analyses yield tightly clustered plateau ages (Figures 10.5, 10.8 & 10.9). Thus, the preferred age for the eruption of the Obsidian Cliff rhyolites is 59.1 ± 2.0 ka, the weighted mean age of the three step-heating plateau ages (Chapter 10).

Gibbon River Flow

Three $^{40}Ar/^{39}Ar$ step-heating and two sets of single-grain laser fusion analyses of sanidine from sample GRWY6 of the Gibbon River rhyolites (Chapter 10; Appendix J) produced ages ranging from 82 ka to 52 ka (Figures 10.10 to 10.15). The plateau ages and pseudo-plateau age calculated from the three step-heating analyses all overlap within uncertainty (Figures 10.10, 10.11 & 10.12). The two youngest weighted mean ages also overlap within uncertainty of the plateau ages (Figures 10.13 & 10.15; Chapter 10). However, a well-constrained inverse isochron indicates there is some excess Ar within sample GRWY6 ($^{40}Ar/^{36}Ar > 295.5$, Figure 10.14). This suggests that the plateau and weighted mean ages may all be anomalously old (McDougall and Harrison, 1999). Thus, the preferred eruption age for sample GRWY6 is considered to be 52.0 ± 8.5 ka, the inverse isochron age calculated for sanidine analysis #4 (Figure 10.14; Chapter 10).

The three flows within the Gibbon River rhyolites are spatially intermingled. The main flow rhyolite surrounds the lava represented by sample GRWY6, with main flow rhyolite outcropping at elevations both above and below the sample location of GRWY6 (Figure 4.2). The southwestern flow of the Gibbon River rhyolites is abutted against and beneath the main Gibbon River flow (Figure 4.2). There is no apparent stratigraphic sequence between the three units (Figure 4.2). The entirety of the Gibbon River rhyolites appear to have erupted concurrently, with the southwestern flow and the lava represented by GRWY6 being included within the main flow of the Gibbon River. Thus, the $^{40}Ar/^{39}Ar$ eruption age obtained for the lava represented by sample GRWY6, 52.0 ± 8.5 ka is also interpreted as the eruption age of the entire Gibbon River flow.

Geochemistry

Crystal Spring Flow

The Crystal Spring lava flow is a mingled rhyolite with tholeiitic basalt enclaves in glassy rhyolite (Figures 5.7, 5.8 & 5.9). The rhyolite samples appear to lie along a mixing line between the basalt enclaves and the majority of the Gibbon River rhyolite flow (Figure 11.1). Geographically, the degree of mingling decreases from north to south along the Crystal Spring lava flow (Figure 4.1; Appendix A). The mingled rhyolites at the northern end of the Crystal Spring flow contain up to 20% basalt enclaves, while rhyolitic glass with <5% small enclaves and mafic glomerocrysts make up the southern end (Chapter 5).

The phenocryst assemblage within the rhyolitic glass of the Crystal Spring mingled lava is the same crystal assemblage that composes the basalt groundmass of the mafic enclaves (Chapter 5). The analyzed plagioclase phenocrysts from the rhyolitic glass (bytownite cores, An_{72} with labradorite rims, An_{70}, average of core and rim point analyses, respectively; Figure 7.19) overlap in composition with the plagioclase of the mafic enclave groundmass (bytownite cores, An_{72} with labradorite rims, An_{65}, average of core and rim point analyses, respectively; Figure 7.19), and are too calcic to have precipitated within a rhyolite magma. In fact, nearly all of the phenocrysts within the mingled lava appear to be derived from the mafic enclaves, including the Mg-rich pyroxenes analyzed in sample CSWY2 (Figure 7.20). A single large, embayed, resorbed quartz grain within sample CSWY2 (Figure 5.10) suggests that the original rhyolitic end-member of the Crystal Spring mingled rhyolite contained large juvenile phenocrysts prior

to mingling with a mafic magma. Mingling with the mafic magma may have heated the rhyolitic magma sufficiently to resorb nearly all of the original rhyolitic phenocrysts.

Throughout the rhyolitic glass of the Crystal Spring mingled lava are mafic phenocrysts that are not juvenile to a silicic magma. Additionally, the rhyolitic glass contains glomerocrysts and small basaltic enclaves of the same composition as the Crystal Spring mafic enclave assemblage (Chapter 5). These "phenocrysts" are thus interpreted to have been derived from the mafic enclaves. This suggests that the rhyolitic portion of the Crystal Spring mingled lava became aphyric upon mingling, resorbing all silicic phenocrysts and incorporating disaggregated mafic crystals, since virtually no juvenile rhyolitic phenocrysts are present.

The holocrystalline enclaves are surrounded by a glass matrix that is denser than the surrounding rhyolitic glass (Chapter 5). Combined with the crenulate margins of the enclaves (Figure 5.7), this glass matrix indicates that a portion of the mafic magma was quenched upon mingling with the rhyolitic magma. However, detailed electron microprobe traverse analyses of plagioclase within rhyolitic glass indicate that compositions become more sodic at the edge of the grains (from An_{72} to An_{64}, averages of all interior and all rim analyses, respectively; Appendix F), just prior to eruption and quenching of the magma (Figures 7.21 & 7.22). This compositional change indicates that after exchange from the mafic magma, the plagioclase phenocrysts continued to grow, with the more sodic plagioclase rims reflecting the new chemistry of the surrounding silicic magma. In addition, modeling of an andesitic enclave (presented below) indicates mixing between the mafic and silicic magmas occurred locally.

The mafic end-member of the Crystal Spring mingled lavas are tholeiitic basalts that are chemically similar to the Swan Lake Flat and Osprey basalts (Figures 6.8 through 6.11). The last of the Swan Lake Flat basalts erupted at 209 ka (Spell *et al.*, 2004; Smith and Bennett, 2006) immediately north of the Crystal Spring lava. Therefore, the Swan Lake Flat basalt is the most likely mafic mingling/mixing component.

Obsidian Cliff Flow

The majority of the Obsidian Cliff rhyolite is a chemically homogeneous, black obsidian (Figure 5.4) with a pumiceous carapace (Figure 5.5). All of the Obsidian Cliff samples cluster near the most evolved end of a mixing line between the Crystal Spring basaltic enclaves and the Gibbon River rhyolites (Figure 11.1). The deviation of Na and K from this mixing line for Obsidian Cliff lavas (Figure 6.2) is likely the result of weathering and the mobilization and transport of these elements during hydration (Lipman, 1965; Noble, 1967). This chemical homogeneity indicates the magma system that produced the Obsidian Cliff rhyolites was well-mixed.

Obsidian Cliff rhyolite is an aphyric obsidian generally containing only unidentifiable microcrysts (Chapter 7). Several samples also contain small glomerocrysts (not analyzed by electron microprobe) of plagioclase, clinopyroxene, and olivine (Chapter 5). A few samples contain small phenocrysts of fayalite (Figures 5.6 & 7.18). No mafic enclaves were observed within the Obsidian Cliff flow. The microcrysts are typically less than 10 μm wide and while they were not quantitatively identified, poor electron microprobe analyses suggest they are feldspar, pyroxene, and olivine (Chapter 7). The generally aphyric nature of the Obsidian Cliff rhyolite suggests the magma was heated sufficiently to resorb all rhyolitic crystals prior to eruption. The only rhyolitic phenocrysts erupted

within the Obsidian Cliff flow, fayalite, are characteristic of high temperature (> 850°C) rhyolitic melts (Hildreth, 1981; Honjo *et al*., 1992; Cathey and Nash, 2004). The presence of glomerocrysts with a mafic crystalline assemblage and the mafic assemblage of the microcrysts within the obsidians suggest the heating of the Obsidian Cliff magma was driven by the injection of a mafic component into the magma. Alternatively, the Obsidian Cliff magma could have been aphyric prior to interaction with a mafic magma represented by the Crystal Spring enclaves. An aphyric silicic magma could have separated from an immobile crystal mush by hindered settling, compaction, and possibly gas-driven filter pressing (Bachmann and Bergantz, 2004). The mafic injection recorded in the Crystal Spring flow could have triggered the eruption of this aphyric magma as the Obsidian Cliff flow. However, the presence of a high-temperature phase, fayalite, and the mafic assemblage of the microcrysts within the Obsidian Cliff flow suggest heating produced the aphyric Obsidian Cliff rhyolite.

Interestingly, the crystal assemblage of glomerocrysts within the Obsidian Cliff lavas is the same assemblage as that of the basalt enclaves within the Crystal Spring mingled lavas (Chapters 5 & 7). The geographical proximity and geochemical link between these flows suggests they could represent the eruption of a single magma batch through two separate vents. The vents may be connected along a single fault running between both flows. Alternatively, these lavas may have been a single flow that was later separated by erosion, producing the wash.

The microcrysts and mafic glomerocrysts within the Obsidian Cliff rhyolite are interpreted as crystals disaggregated from mafic enclaves derived from the basaltic component of the Crystal Spring magma. The Obsidian Cliff rhyolite is apparently the

rhyolitic end-member of the Crystal Spring mingled lavas (Figure 11.1). This is supported spatially by the continual decrease in mafic component within the Crystal Spring/Obsidian Cliff lava from north to south along the two flows. The northern edge of the Crystal Spring flow contains nearly 20% mafic component and large mafic enclaves, whereas the Obsidian Cliff flow contains only a minor mafic component (Figure 11.1). No mafic enclaves were observed within the Obsidian Cliff flow, only mafic glomerocrysts and microcrysts. This geochemical link to the Crystal Spring lavas also provides a mechanism for superheating the Obsidian Cliff magma. The mafic injection, preserved as the mafic enclaves within the Crystal Spring lava, would have rapidly heated the silicic Crystal Spring/Obsidian Cliff rhyolite magma, resorbing all the rhyolitic phenocrysts that may have been present within the magma just prior to eruption. The injection of a hotter mafic magma into the silicic Crystal Spring/Obsidian Cliff magma system would also produce rapid convection within the system, mixing and chemically homogenizing the Obsidian Cliff rhyolite prior to eruption (Couch *et al*., 2001; Huber *et al*., 2009).

Geochemical Modeling of Obsidian Cliff and Crystal Spring Flows

IgPet (Carr, 2000) was used in conjunction with the whole-rock major and trace element data (Appendix B) to quantitatively model magma mixing within the Obsidian Cliff rhyolite and the Crystal Spring mingled rhyolite. The Obsidian Cliff rhyolites were selected as the best representation of the Roaring Mountain rhyolites silicic end-member. While the main flow of the Gibbon River rhyolites appears to fall at the most evolved end of a linear trend with the Crystal Spring mafic enclaves (Figure 11.1), modeling discussed below indicates the main Gibbon River flow records continued evolution after

a mixing event. Additionally, if the main Gibbon River flow was the silicic end-member of the Crystal Spring and Obsidian Cliff flows, as much as 48% mafic component would be required to produce the trace elements of rhyolite sample CSWY1 (Figure 11.1). Such a high mafic contribution would not create a rhyolitic melt (Figure 6.1), but rather a dacitic melt (~64 wt.% SiO_2). Sample OCWY2 was selected to represent the Obsidian Cliff rhyolites as the silicic end-member and sample CSWY1E was selected to represent the composition of the mafic end-member for the mixing models.

Mixing between the Obsidian Cliff rhyolites and the Crystal Spring basaltic enclaves successfully reproduces nearly all the analyzed major and trace elements of the Crystal Spring mingled rhyolite and andesitic enclave samples (Figures 11.1 through 11.5). Mingling, not mixing, with a mafic component appears to be the dominant magma interaction within the Crystal Spring mingled rhyolite. Since the XRF and ICP-MS analyses provide the whole rock element concentrations of each sample, mingling would be analytically modeled by chemical mixing. Thus, the degree of mixing should be practically viewed as the degree of mingling. All of the Crystal Spring mingled rhyolites compositionally lie along a mixing line from the Obsidian Cliff rhyolites to the Crystal Spring basaltic enclaves (Figure 11.1). Based on this modeling, silicic to mafic melt mixture proportions were determined for each of the Crystal Spring samples (Table 11.1).

Table 11.1. Mixing models for the Crystal Spring mingled rhyolite samples

	OCWY2 (%)	CSWY1E (%)	Mixing Model
CSWY1	78	22	Figure 11.2
CSWY1GE	25	75	Figure 11.5
CSWY2	88	12	Figure 11.2
CSWY3	97	3	Figure 11.3
CSWY3V	82	18	Figure 11.3
CSWY4	98	2	Figure 11.4

Gibbon River Rhyolites

Three distinct rhyolites appear to be present within the Gibbon River flow: the main flow, the southwestern flow, and a third composition represented by sample GRWY6 (Figures 6.2 through 6.7). The main flow comprises most of the Gibbon River Rhyolite. The southwestern flow forms the cliff at the southwestern corner of the Gibbon River flow (represented by samples GRWY1 and GRWY3, Figure 4.2). Sample GRWY6 was collected at the surficial top of the northeastern Gibbon River flow, the location of the third Gibbon River unit (Figure 4.2). The main flow and the southwestern flow of the Gibbon River rhyolites have the same mineral assemblage of sanidine, quartz, plagioclase, sparse magnetite, rare pyroxene, fayalite, amphibole, and zircon (Chapters 5 & 7). Sample GRWY6 contains a similar mineral assemblage (sanidine, sparse quartz, fayalite, pyroxene, magnetite, ilmenite, rare amphibole, and zircon), but is generally chemically less evolved than the other Gibbon River rhyolites (Chapters 5 & 7).

Gibbon River Rhyolites – The Main Flow

The main Gibbon River flow is a sparsely porphyritic to porphyritic rhyolite (Figure 5.1). The main flow appears to be the most evolved of the Roaring Mountain rhyolites with the highest Rb, Y, and Ta concentrations, and lowest Fe, Ba, and Ca concentrations. Trace element chemistry suggests the main flow may represent the most evolved end-member of a mixing line between the main flow of the Gibbon River rhyolites and the mafic enclaves of the Crystal Spring mingled lavas (Figure 11.6). However, several of the analyzed elements do not fall directly on this mixing line (Figures 6.1 & 6.2). The elements that fall off trend are compatible in sanidine, plagioclase, magnetite, fayalite, and clinopyroxene. This assemblage corresponds to the phenocryst assemblage of the

main flow of the Gibbon River rhyolites (Chapters 5 & 7). Thus, the magma that produced the main Gibbon River flow may represent residual Crystal Spring/Obsidian Cliff magma that continued to evolve and crystallize. Fractional crystallization appears to account for the compositional difference between the main flow and the Obsidian Cliff rhyolites.

The crystal assemblage of the main Gibbon River flow consists of unzoned, euhedral to subhedral sanidine (Or_{58}) and quartz, with rare oligoclase (An_{21}), olivine (likely fayalite based on olivine compositions analyzed within the other Gibbon River rhyolites), ferroan augite, ferro-actinolite, magnetite, and zircon (Chapters 5 & 7). The quartz population is very homogeneous with similarly sized phenocrysts and no visible or compositional zoning (Figure 8.5), and the sanidine and augite compositions are tightly clustered (Figures 7.1 & 7.2, respectively). Although major elements are generally constant, the sanidine phenocrysts do exhibit generally symmetrical trace element zoning from rim to rim (Figure 7.7). Overall the sanidines have a small range of BaO (<0.5 wt.%, Figure 7.6), excepting sanidine S2, which has a higher Ba concentration than the other sanidines and exhibits the most extensive BaO zonation of the GRWY7P sanidines. The Ba zoning within the sanidine phenocrysts may record minor changes in local magma chemistry during phenocryst precipitation. The general lack of phenocryst zoning and the general chemical homogeneity of phenocryst populations suggests that the main flow of the Gibbon River rhyolites may have been "reset" by heating and crystal resorption, removing previously crystallized phenocrysts and preventing the preservation of their chemistries within "new" phenocrysts as cores or inclusions. Thus, only a single homogeneous magma environment is recorded within the main flow's phenocrysts.

Lending evidence for this model includes the observation that quartz began precipitating in the magma of the main flow of the Gibbon River rhyolites at ~975°C (based on analyses at the center of quartz 7P-QA) (Figure 8.2). The quartz phenocrysts indicate a overall thermally stable system (averaging ~930°C) with slight cooling to just below 900°C prior to eruption and cessation of quartz growth (based on the lowest temperature analyzed at the edge of the 3 quartz crystals, 7P-QA on Figure 8.2).

Eruption temperatures from two-feldspar geothermometry (Fuhrman and Lindsley, 1988) analyses indicate that the main flow of the Gibbon River rhyolites erupted at a lower temperature than indicated by TitaniQ geothermometry (Wark and Watson, 2006). Analyses of coexisting sanidine and plagioclase indicate the main flow was between ~795°C and ~830°C (±30°C) when it erupted and the feldspar phenocrysts stopped precipitating (Chapter 8). Within uncertainties, the TitaniQ and two-feldspar eruption temperatures overlap, albeit at opposite ends of their respective uncertainties. There are several possibilities as to why these temperatures do not match more closely, including that the incorrect α_{Ti} was selected to calculate the TitaniQ temperatures within the main Gibbon River flow (Chapter 8) or that the analyzed feldspar pairs used to calculate the two-feldspar temperatures were not in chemical equilibrium. If the selected α_{Ti} was incorrect and the temperatures calculated by TitaniQ are too high, a higher α_{Ti} would calculate lower temperatures (Wark and Watson, 2006). A higher α_{Ti} also produces a lower range of calculated temperatures (e.g. with α_{Ti}=0.6, the temperature range is 105°C and with α_{Ti}=0.8, the temperature range is 97°C for quartz GRWY7P-QA). Based on the main flow's relation to the Crystal Spring and Obsidian Cliff lavas, the phenocrysts of the main flow likely began precipitating at relatively high, post-superheating temperatures.

If the main flow erupted at ~800°C, as indicated by two-feldspar geothermometry, the quartz phenocrysts should record a continual drop of possibly up to 200°C, from those high initial temperatures to the low two-feldspar eruption temperature. However, the Ti concentrations of the quartz phenocrysts within the main flow record a maximum cooling of 105°C (range of quartz GRWY7P-QA). So, the higher TitaniQ eruption temperatures are favored for the main flow of the Gibbon River rhyolites.

Geochemical Modeling of the Main Gibbon River Flow

The main flow of the Gibbon River rhyolites appears to be the silicic end-member of a mixing trend with the Crystal Spring mafic enclaves (Figure 11.6). Mixing was modeled between the main flow of the Gibbon River rhyolites (with sample GRWY7O representing the silicic end-member) and the Crystal Spring mafic enclaves (represented by CSWY1E). For major elements, mixing models using GRWY7O require ~1% CSWY1E to produce Obsidian Cliff sample OCWY2 (Figure 11.6). However, modeling mixing of trace elements with GRWY7O requires ~25% mafic content (CSWY1E) to produce the composition of OCWY2 (Figure 11.6). There is a similar discrepancy between the mafic content required to produce the major elements versus trace elements the Crystal Spring mingled rhyolite (Figure 11.6). Also, many trace elements (e.g. La, Ce, Pr, Nd, Ba, Sr & Eu) and K and Na (Figure 6.2) do not fit well along a mixing line between the main Gibbon River flow and the Crystal Spring mafic enclaves. Therefore, mixing cannot relate the main flow of the Gibbon River rhyolites to the Crystal Spring and Obsidian Cliff flows.

Since mixing does not relate the Crystal Spring and Obsidian Cliff rhyolites to the main flow of the Gibbon River rhyolites, a Rayleigh fractionation model was calculated

to predict the evolution of residual Obsidian Cliff magma by fractional crystallization. A model was calculated using the Rayleigh fractionation equation,

$$C_l/C_o = F^{(Do-1)}$$

where C_o is the composition of the parent liquid, C_l is the composition of the daughter liquid, D_o is the bulk distribution coefficient, and F is the portion of melt remaining after fractional crystallization. Rayleigh fractionation assumes that crystals formed within a liquid are immediately removed from that liquid. Mineral partition coefficients for high-silica rhyolites were averaged from several sources (Mahood and Hildreth, 1983; Stix and Gorton, 1990; Ewart and Griffin, 1994; Streck and Grunder, 1997) to estimate the partition coefficients within the Roaring Mountain rhyolites. The partition coefficients that were used to calculate the bulk distribution coefficients are presented in Table 11.2. For this model, the fractionating crystal assemblage was based on the point count data for the main flow of the Gibbon River (sample GRWY7O, Table 5.1): 78% sanidine, 9-10% plagioclase, 7-9% quartz, 3% magnetite, 0.5-1% olivine, 0.5% zircon, 0.0-0.5% pyroxene, and 0.0-0.5% amphibole. The assemblage was modified to include observed phenocrysts within the main flow that were not represented in the point count of GRWY7O.

Using the Obsidian Cliff rhyolite (sample OCWY2) as the composition of the parent magma, a fractional crystallization model does successfully reproduce many of the main Gibbon River flow trace elements (Figure 11.7). When compared to Nb, trace elements Sc, Rb, Sr, Y, Ta, Eu, Yb, and Lu indicate ~25% crystal fractionation of Obsidian Cliff composition magma will produce the main flow of the Gibbon River rhyolites (Figure 11.7). The main flow composition of Ba, Tb, Th, and U are nearly matched by this

fractionation model, but do not fall upon the modeled fractionation line. The major elements were not modeled since at high SiO_2 contents, their composition is expected to approach a eutectic composition and not change with further evolution.

Table 11.2. Partition coefficients used in Gibbon River rhyolite models

	Sanidine	Plagioclase	Fayalite	Magnetite	Pyroxene	Zircon	Amphibole
Sc	0.037	0.014	6.40	8.057	111.033	68.65	0
Mn	0.028	0.130	65.333	24.173	31.363	1.52	13.9
Rb	0.417	0.075	0	0.032	0.052	0	0.137
Sr	3.847	10.835	0	0.148	0.165	0	3.356
Y	0.067	0.206	0	1.104	0.81	0	17.832
Nb	0.077	0.242	0	2.264	0.4	0	2.57
Ba	8.173	3.271	0	0	0.614	0	1.064
Hf	0.021	0.057	0.727	2.739	1.31	3193.5	0
Ta	0.026	0.046	0.098	1.927	0.933	47.5	0
La	0.072	0.135	8.803	8.081	6.453	16.9	0
Ce	0.044	0.070	7.703	7.174	6.16	16.75	0
Nd	0.038	0.033	5.423	5.650	7.412	13.3	0
Sm	0.018	0.015	3.319	3.963	7.973	14.4	0
Eu	3.342	5.163	2.103	1.294	5.025	16	0
Tb	0.027	0.027	1.233	2.650	6.255	37	0
Yb	0.017	0.018	1.287	0.693	4.942	527	0
Lu	0.028	0.013	1.587	0.748	5.472	641.5	0
Th	0.014	0	1.295	3.697	5.985	76.8	0
U	0.021	0	0.313	0.855	0.21	340.5	0

The light rare-earth elements of the main Gibbon River flow, however, are still much lower than can be accounted for by the fractional crystallization model presented above. Of the possible crustal contaminants near the Gibbon River rhyolites, the Gibbon Hill and Paintpot Hill rhyolites have very low light REE values (Hildreth *et al.*, 1991; Christiansen, 2001). However, trace elements other than La, Ce, Pr, and Nd would also be affected by crustal assimilation within the magma system. Preliminary assimilation and fractional crystallization modeling suggests that the low light REE composition of the main Gibbon River flow can only be reproduced at the expense of the other trace

elements. Thus, assimilation is not considered a significant factor within the main Gibbon River flow. Instead, the compatibility of the light REEs (Figure 6.3) probably indicates allanite (Mahood and Hildreth, 1983), while not identified within the main flow samples, may have been crystallizing within the main flow of the Gibbon River magma.

Gibbon River Rhyolites – The Southwestern Flow

The southwestern flow of the Gibbon River rhyolite is a porphyritic black and mahogany obsidian. For the major elements, the southwestern flow is nearly identical to the main flow of the Gibbon River rhyolites (Figure 6.2). In the southwestern flow, the K increases and Na decreases relative to the main flow (Figure 6.2), consistent with K and Na mobilization due to hydration (Lipman, 1965; Noble, 1967). However, the southwestern flow trace elements fall between the main Gibbon River flow and the basaltic enclaves of the Crystal Spring (Figures 6.5, 6.6 & 6.7). It thus appears as if the rhyolites of the southwestern flow are a mixture between the main Gibbon River flow and the Crystal Spring basaltic enclaves (Figure 6.6). A mixing model between the main flow of the Gibbon River rhyolites (sample GRWY7O) and the basaltic enclaves of the Crystal Spring rhyolites (sample CSWY1E) was therefore calculated. This model indicates that at least 65% mafic component is required to produce the trace element composition of southwestern flow (Figure 11.8). This percentage mafic contribution would result in an andesitic magma (~59 wt.% SiO_2), not a rhyolitic one (Figure 6.1). Additionally, the complex chemical history detailed in the phenocrysts of the southwestern Gibbon River flow does not record the significant mixing with a mafic component that would be required if the southwestern magma was a hybrid magma of the main Gibbon River flow and the mafic enclaves of the Crystal Spring flow.

Both the main flow and the southwestern flow of the Gibbon River rhyolites contain the same phenocryst assemblage: sanidine, oligoclase, quartz, fayalite, magnetite, ferroan augite, amphibole (ferro-actinolite in the main Gibbon River flow), and zircon. The chemical composition of analyzed feldspar and pyroxene phenocrysts overlap for both flows, with the phenocrysts from the main Gibbon River flow being slightly more evolved in composition (Or_{53}, An_{27} & $Wo_{40}En_{26}Fs_{34}$ vs. Or_{58}, An_{21} & $Wo_{39}En_{24}Fs_{36}$, southwestern vs. main, respectively) (Figures 7.1 & 7.2). The average core composition of plagioclase within the main flow (An_{25}) is similar to the average core and rim composition of plagioclase within the southwestern flow (An_{26} & An_{27}, averages of core and rim point analyses, respectively) (Chapter 7). Thus, the southwestern flow and the main Gibbon River flow may be derived from the same source magma. However, whereas the main flow generally contains unzoned, homogeneous phenocrysts (Figure 7.4), the southwestern flow phenocrysts are zoned and record a more chemically complex magma history prior to eruption (Figure 7.8).

Generally, the southwestern Gibbon River flow contains two populations of sanidines. The first population consists of sanidines (sanidines S1 & S2 of sample GRWY1) with relatively constant Or_{52} composition (Or_{50} & Or_{53}, average composition of S1 and S2, respectively) surrounding anorthoclase (Or_{32} & Or_{34}, S1 & S2, respectively) inclusions (Figures 7.8 & 7.9). The second population consists of strongly zoned sanidines (S5 & S6 of sample GRWY1) with an average interior zone composition (Or_{58} & Or_{57}, average composition of S5 and S6, respectively) that is chemically similar to the main Gibbon River flow's homogeneous sanidine composition (Or_{60}) and an outer compositional rim that is distinctly more sodic (Or_{43} & Or_{44}, most sodic analysis at edge

of S5 and S6, respectively) (Figures 7.8 & 7.9). Sanidine S6 also contains an oligoclase (An_{20}) inclusion that is chemically similar to the rim composition of plagioclase within the main flow (An_{21}, most sodic analysis at edge of sample GRWY7P plagioclase). Though the chemistries are slightly different, sanidine S4 is similar to the second sanidine population exhibiting a sanidine interior (Or_{55}) that becomes more sodic towards the edge of the grain (Or_{40}) (Figures 7.8 & 7.9). The BaO composition of S6 is zero along the plagioclase inclusion, but shows oscillatory zoning throughout the center of the sanidine until a sudden Ba increase at the crystal edges, corresponding to the decrease in Or (Figure 7.13).

Several processes could explain the chemical heterogeneity within the sanidines of the southwestern flow. The oscillatory zoning within sanidine S6 may record periodic destabilizations of the magma system as the local chemical and physical environment changes with time and evolution. Similar oscillatory zoning was described in sanidine phenocrysts from the Laacher See volcanic tephra (Ginibre *et al.*, 2004). These sanidines were interpreted as evolving within a thermally stratified, convecting magma system that had temperatures up to 1000°C (Ginibre *et al.*, 2004). A chemically or thermally stratified magma system could produce multiple sanidine populations and phenocryst movement between these magma zones could form the complex chemical zonation seen within southwestern flow sanidines. Phenocrysts may have been exchanged between magmas that produced the main and the southwestern flows. For example, plagioclase originating within the magma that produced the southwestern flow may have exchanged into the magma that produced the main flow, where rims of more evolved plagioclase precipitated, erupting with the main Gibbon River flow. Additionally, the exchange and

continued growth of phenocrysts within a less evolved magma would create compositional zoning similar to observed zoning within the sanidines of sample GRWY1, where K-rich sanidines are surrounded by Na-rich sanidine rims (e.g. sanidine S6). In a silicic system without basaltic interaction, local or system-wide chemical stratification could form with time through crystal settling (Hildreth, 1979). Mafic underplating probably at least contributed to southwestern flow magma system by providing the heat to maintain the system. It also could have promoted the chemical stratification of the magma system by indirectly providing heat and volatiles to the silicic magma (Hildreth, 1979; Hildreth, 1981).

The quartz phenocrysts within the southwestern flow are strongly zoned and typically broken and shattered (Figure 8.6). From TitaniQ geothermometry (Wark and Watson, 2006), the compositional zones within the quartz of the southwestern flow correspond to low temperature cores (700-800°C) and high temperature rims (900-1000°C) (Figure 8.3). These quartz phenocrysts could record cooling and crystallizing of the silicic magma system (core temperatures) that was then remobilized and heated by a mafic component (producing the higher rim temperatures), possibly the basaltic injection recorded in the Crystal Spring mingled rhyolite. Alternatively, it has been suggested that the magma that produced the main Gibbon River flow reached temperatures high enough to completely resorb all rhyolitic phenocrysts that may have formed prior to the Crystal Spring/Obsidian Cliff eruption. If this also applies to the magma of the southwestern flow and all the rhyolitic phenocrysts within the southwestern flow magma formed after the eruption of the Crystal Spring/Obsidian Cliff flow, then several models could explain the temperature zoning within the quartz phenocrysts. The magma that produced the

southwestern flow could have undergone a low temperature crystallization period wherein new quartz grains precipitated, followed by a high temperature growth period, possibly triggered by continued mafic injection beneath the Roaring Mountain Member area. However, the quartz within the main flow do not record a period of low-temperature quartz crystallization (Figure 8.2) and it seems likely that the heat that maintained a hot main flow magma would also sufficiently heat a neighboring or subjacent magma. Based on the close spatial proximity of the main and the southwestern flows of the Gibbon River rhyolites, it seems unlikely that the southwestern flow magma would have undergone a low-temperature crystallization that was not also recorded within the main flow. One possibility is that the heat that produced the main flow of the Gibbon River remobilized a silicic crystal mush (Bachmann and Bergantz, 2004; Bachmann and Bergantz, 2008) in the Gibbon River magma system vicinity, creating the magma of the southwestern flow and incorporating older phenocrysts into the melt. Another possibility is that the cores of the quartz phenocrysts of the southwestern flow are xenocrysts harvested from the wall rock surrounding the magma of the southwestern flow. If either is the case, the low core temperatures are relict to the crystallization of the crystal mush or the surrounding country rock and the high rim temperatures reflect the temperature within the magma of the southwestern flow. Since Ti diffusion within quartz is very slow (Cherniak *et al.*, 2007), the high temperature rims are probably overgrowths native to the southwestern flow magma.

Given the models suggested above, the quartz rim temperatures should reflect the magma temperature prior to eruption of the southwestern Gibbon River flow. Based on the rim temperatures from quartz 1-QB, the southwestern flow magma was ~900°C at the

time of eruption (Figure 8.3). Two-feldspar geothermometry (Fuhrman and Lindsley, 1988) analyses indicate that the southwestern flow of the Gibbon River rhyolites was ~820°C (±40°C) when it erupted and crystallization of feldspar phenocrysts halted (Chapter 8). The discrepancy between the TitaniQ and two-feldspar eruption temperatures is discussed above, however, the higher eruption temperature is favored based on the presence of fayalite, a high-temperature mineral (> 850°C) (Hildreth, 1981; Honjo *et al*., 1992; Cathey and Nash, 2004), within the southwestern flow and the interpreted close proximity of the southwestern Gibbon River flow magma to the hot magma of the main flow of the Gibbon River rhyolites. It should be noted that both the TitaniQ and two-feldspar temperatures for the southwestern flow overlap with the eruption temperatures of the main flow of the Gibbon River.

Geochemical Modeling of the Southwestern Gibbon River Flow

Several mixing, fractional crystallization, and assimilation and fractional crystallization models were attempted for the southwestern flow of the Gibbon River rhyolites. Since the $^{40}Ar/^{39}Ar$ eruption ages do not preclude the Gibbon River rhyolites from erupting before the Obsidian Cliff rhyolites, the Obsidian Cliff flow (sample OCWY2) was modeled along with the main Gibbon River flow (sample GRWY7O) as a parent magma for the southwestern flow of the Gibbon River rhyolites. Along with the other Roaring Mountain lavas, nearby units such as the Lava Creek Tuff, the Paintpot Hill and Gibbon Hill rhyolites were also modeled as possible assimilants. None of the attempted models successfully reproduced the trace elements of the southwestern Gibbon River flow.

Preliminary work by Nastanski (2005) interpreted the magmas of the Obsidian Cliff and Crystal Spring flow as being the product of a fractionally crystallized residual Gibbon River flow. Her modeling was based on preliminary $^{40}Ar/^{39}Ar$ ages that indicated the Gibbon River flow was erupted prior to the Obsidian Cliff and Crystal Spring flows (Nastanski, 2005). The trace elements of the Gibbon River sample (sample GR-2) collected by Nastanski (2005) indicate it is a southwestern Gibbon River rhyolite (Figure 11.9). This is consistent with the sampling location (east of sample GRWY3) for GR-2 (Nastanski, 2005). Based on the fractional crystallization model presented in Nastanski (2005), the southwestern flow of the Gibbon River rhyolites (the average composition of GRWY1 and GRWY3) was modeled again in this study as the parent magma for the Obsidian Cliff rhyolites (OCWY2). This study's model used the partition coefficients listed in Table 11.1 and the fractionating crystal assemblage from the point count data for the southwestern Gibbon River flow (sample GRWY3, Table 5.1). The fractionating assemblage was modified to include observed phenocrysts that were not represented in the point count: 54% sanidine, 27.5% quartz, 3-5% plagioclase, 12% magnetite, 0.0-1% olivine, 0-0.5% zircon, 0.0-0.5% pyroxene, and 1-3% amphibole. Using these inputs, the Obsidian Cliff rhyolite composition was successfully reproduced for Nb versus La, Eu, and Tb with ~65% fractional crystallization. However, the majority of Obsidian Cliff trace elements are not explained by modeling the southwestern Gibbon River flow. In addition, while the $^{40}Ar/^{39}Ar$ eruption ages allow for the Gibbon River rhyolites to have erupted before the Obsidian Cliff rhyolites, geochemical modeling (above) clearly suggests that the Gibbon River rhyolites erupted after the Obsidian Cliff lavas.

Gibbon River Rhyolites – Sample GRWY6

Sample GRWY6 of the Gibbon River flow is a relatively coarsely porphyritic rhyolite (Figure 5.3) and is the least evolved of the Gibbon River samples (Figures 6.2 & 6.3). The major elements of sample GRWY6 do not overlap within uncertainties with the main Gibbon River flow or the southwestern flow, however, many of GRWY6's trace elements overlap with the trace elements of the main flow, the southwestern flow, and Obsidian Cliff flow (Figure 6.3 & 6.4). This chemical similarity suggests that GRWY6 may be related to the main Gibbon River flow, the southwestern Gibbon River flow, and the Obsidian Cliff flow. However, many of the trace elements are very distinct, for example, Fe, Mn and Ti are the highest of the Gibbon River rhyolite samples (Figure 6.2) and the light REEs are the highest of all the Roaring Mountain Member samples (Figure 6.3). Like the southwestern flow, the major and trace element chemistry of GRWY6 generally appears consistent with mixing of main Gibbon River rhyolite with a mafic component such as the Crystal Spring basaltic enclaves (Figures 6.5 & 6.6). However, mixing with other Roaring Mountain Member compositions does not account for the composition of GRWY6 since the elements that do fall along a mixing line between the main Gibbon River flow and the Crystal Spring basaltic enclaves require a mafic contribution ranging from ~5% (CaO, Figure 11.6) to ~55% (Th & Rb, Figure 11.6).

The phenocryst assemblage of sample GRWY6 is similar to the assemblage of the main Gibbon River flow and the southwestern flow, with one major difference – no plagioclase phenocrysts were identified within sample GRWY6 (Chapter 7). Additionally, the sanidine chemistry of GRWY6 (Or_{44}) is distinctly less evolved than the sanidines of both the main Gibbon River flow and the southwestern flow (Or_{58} & Or_{53},

respectively) (Figure 7.1). The pyroxene and amphibole phenocrysts of GRWY6 are also higher in Fe composition than those of GRWY7P and GRWY1 ($Wo_{41}En_{10}Fs_{48}Ac_1$ & $Wo_3En_{27}Fs_{70}$ vs. $Wo_{39}En_{24}Fs_{36}Ac_1$ & $Wo_{40}En_{26}Fs_{34}Ac_1$, GRWY6 vs. GRWY7P & GRWY1, respectively) (Figure 7.2).

All three sanidines analyzed from GRWY6 are compositionally similar. Sanidine S2 and S4 are unzoned with chemically indistinguishable average compositions (Or_{46} & Or_{47}, average composition of S2 and S4, respectively) (Figures 7.14 & 7.15). The third sanidine, S1 is distinctly zoned (Figures 7.14 & 7.15). The core and the rim compositions of S1 are compositionally indistinguishable (Or_{43} & Or_{42}, core and rim composition, respectively) and overlap with the rim compositions of GRWY1 sanidines S4, S5, and S6 (Or_{40-44}). The inner, high-K compositional zone within sanidine S1 is compositionally similar to that of S2 and S4 (Or_{48}) (Figure 7.14). The compositional overlap of GRWY6 sanidine S1 and GRWY1 sanidines S4, S5, and S6 suggests phenocrysts may have been exchanged between the magmas that produced sample GRWY6 and the southwestern flow.

The quartz phenocrysts within GRWY6 are moderately to weakly zoned and often shattered (Figure 8.7). However, TitaniQ geothermometry (Wark and Watson, 2006) does not show large temperature variations that might correlate with the compositional zones visible in CL images (Figure 8.4). TitaniQ geothermometry indicates the temperatures within the magma of sample GRWY6 averaged around 950°C (Figure 8.4). The temperatures ranged from ~890°C up to ~1010°C.

Geochemical Modeling of GRWY6

In an attempt to reconcile the distinct chemistry of sample GRWY6 with the other two Gibbon River flows, several magma evolution models were calculated including fractional crystallization of different parent magmas including the main Gibbon River flow and the Obsidian Cliff rhyolites, and assimilation and fractional crystallization models with different assimilants such as the Lava Creek Tuff. Of these models, only an assimilation and fractional crystallization model could successfully reproduce trace element compositions of GRWY6. A model was calculated using DePaolo's (1981) equation,

$$C_l = C_o\,(F^{-Z}) + \frac{R}{R - 1 + D_o} C_a\,(1 - F^{-Z})$$

where C_o is the composition of the parent liquid, C_l is the composition of the daughter liquid, C_a is the composition of the assimilant, D_o is the bulk distribution coefficient, R is the ratio of the mass of the mixed component to the mass of the fractionating component, F is the portion of melt remaining after fractional crystallization, and $Z = \frac{R + D_o - 1}{R - 1}$.

The partition coefficients used to calculate the bulk distribution coefficients are presented in Table 11.2. The fractionating assemblage was based on the point count data for sample GRWY6 (Table 5.1): 63% sanidine, 7-9% quartz, 23-25% magnetite, 2-3% olivine, 0.5-2% zircon, 0.0-0.5% pyroxene, and 0.5-2% amphibole. The point count assemblage was modified to include minerals that were observed in sample GRWY6 that were not represented in the point count data.

To model sample GRWY6, the main Gibbon River flow (sample GRWY7O) was used as the parent magma and the Crystal Spring mafic enclave (sample CSWY1E) was

used as the assimilant. R was set at 0.1, meaning the portion of assimilated mafic material was a tenth of the portion of fractionating silicic magma. When compared against Ta, about ~35% crystal fractionation is required to produce trace elements Sr, Sc, and Th (Figure 11.10). None of the other trace elements modeled were successfully reproduced. Additionally, with the assimilation of ~10% mafic component, the major element concentration of GRWY6 should be closer to sample CSWY2 (~12% mafic contribution, Table 11.1) than observed. Also, the most unique trace elements of GRWY6 (very high Eu and light REE concentrations) were not replicated by this model, so it is unlikely that assimilation and fractional crystallization of the Obsidian Cliff, main Gibbon River, and southwestern Gibbon River flows produced the magma represented by GRWY6.

$^{230}Th/^{238}U$ Geochronology

Gibbon River Flow

Zircons separated from Gibbon River rhyolite sample GRWY6 were analyzed by ion microprobe for $^{230}Th/^{238}U$ geochronology (Chapter 9; Appendix I). Individual model ages range from 116 ± 18 ka to 211 ± 64 ka (Table 9.1). The disequilibrium age calculated for these analyses is 105^{+36}_{-27} ka (Figure 9.3). This $^{230}Th/^{238}U$ age indicates the average age of zircon precipitation within the magma of GRWY6 (Reid *et al.*, 1997; Simon and Reid, 2005; Schmitt *et al.*, 2006).

While studying the adjacent intracaldera Central Plateau Member rhyolites of the Yellowstone Caldera, Vazquez and Reid (2002) also preformed $^{230}Th/^{238}U$ analyses on a zircon population from the Gibbon River flow. The two-point isochron ages ("model

ages") of their individual zircon analyses range from 94 ka to 269 ka and the disequilibrium age calculated for all the Gibbon River zircon analyses is 136^{+16}_{-14} ka (MSWD = 1.1; Vazquez and Reid, 2002). These ages agree with the range of individual isochron ages from sample GRWY6 (Table 9.1). Additionally, the disequilibrium ages overlap within uncertainty of each other. The consistency of these two data sets suggests the Gibbon River rhyolites record a single zircon crystallization episode (Figure 9.4; Vazquez and Reid, 2002).

Combining the $^{230}Th/^{238}U$ disequilibrium age (105^{+36}_{-27} ka) with the preferred eruption age of sample GRWY6 (52.0 ± 8.5 ka) indicates the magma that sample GRWY6 originated from evolved for at least 50 ka before eruption. The individual model ages obtained from GRWY6 zircons allow for magma evolution beginning at 211 ± 64 ka. Since geochemistry indicates the Gibbon River rhyolites were the last of the Roaring Mountain rhyolites to erupt, this suggests a maximum time of magma storage and evolution beneath the southeastern Norris-Mammoth Corridor of ~160 ka.

Roaring Mountain Rhyolites Model

The $^{40}Ar/^{39}Ar$ eruption age of the Crystal Spring/Obsidian Cliff flow, 59.1 ± 2.0 ka, and the Gibbon River flow, 52.0 ± 8.5 ka, overlap within uncertainty, and either eruption could have occurred first. However, geochemical modeling indicates that the main flow of the Gibbon River rhyolites evolved from the residual magma of the Crystal Spring/Obsidian Cliff rhyolites after their eruption. Therefore, the Gibbon River rhyolites are interpreted to have erupted after the Crystal Spring/Obsidian Cliff lavas.

Prior to eruption of the Crystal Spring/Obsidian Cliff lavas, a mafic injection, chemically similar to the Swan Lake Flat basalts, superheated the silicic magma system of the Roaring Mountain rhyolites, resorbing nearly all silicic phenocrysts that had precipitated within the system. This mafic magma mingled and mixed with the Roaring Mountain silicic magma, exchanging disaggregated mafic phenocrysts into the silicic magma, quenching into holocrystalline mafic enclaves, and completely hybridizing into local andesitic melts. Produced by mingling of the silicic Roaring Mountain magma and Swan Lake Flat basaltic magma, the Crystal Spring mingled rhyolites contain between 2-22% mafic component (Table 11.1) in the form of basaltic phenocrysts, basaltic glomerocrysts, and quenched basaltic to andesitic enclaves. The Obsidian Cliff rhyolite is the most evolved, silicic end-member of these mingled lavas and probably best represents the composition of the Roaring Mountain silicic magma before basaltic interaction. The Crystal Spring mingled lavas and the Obsidian Cliff rhyolite erupted at 59.1 ± 2.0 ka. Based on their geographical proximity and geochemistry, the Crystal Spring mingled lavas and the Obsidian Cliff rhyolite erupted either as a single flow that was later separated by erosion, or as a single magma batch via two separate vents. Since magmas typically erupt the uppermost material first, drawing down to deeper magmas with continued eruption (Hildreth, 1979), the Crystal Spring lavas probably erupted after the Obsidian Cliff rhyolites. If the flows erupted from a single vent, the Crystal Spring mingled lavas would likely be closest to the vent as the last magma erupted, suggesting that for a single vent model, the Obsidian Cliff/Crystal Spring rhyolites erupted from the mapped Crystal Spring vent.

After eruption of the Crystal Spring mingled lavas and the Obsidian Cliff rhyolites, the Roaring Mountain silicic magma system began cooling, though generally high temperatures (840-995°C) were maintained prior to eruption of the Gibbon River flow. The residual Crystal Spring/Obsidian Cliff magma began evolving by fractional crystallization and from this hot, stable silicic system, the main flow of the Gibbon River rhyolites erupted.

The adjacent, intracaldera Central Plateau Member rhyolites of the Yellowstone Volcanic Field are interpreted as evolving within a fractionating silicic magma system maintained by periodic mafic injection (Vazquez *et al.*, 2009). The interpreted magma evolution of the Crystal Spring mingled rhyolites, the Obsidian Cliff rhyolites, and the main flow of the Gibbon River rhyolite reflects a similar magmatic environment. Mafic injection into silicic magma systems appears to be common within the postcollapse Yellowstone Volcanic Field lavas. TitaniQ geothermometry indicates the Central Plateau Member lavas evolved over progressively cooling temperatures that range from 900°C to 750°C (Vazquez *et al.*, 2009). Similar magma evolution temperatures were observed by TitaniQ geothermometry within the main flow of the Gibbon River rhyolite. However, the Gibbon River rhyolites recorded slightly higher temperatures than those within the Central Plateau lavas. Since the main Gibbon River flow evolved over significantly less time than that of the Central Plateau lavas (~50 ka for the Gibbon River flow vs. >100 ka for the Central Plateau lavas) (Vazquez *et al.*, 2009), the main flow temperatures should reasonably reflect the residual heat of the superheating event that accompanied the mafic injection into the Roaring Mountain magma system.

Though a temporal and spatial relationship appears to exist, the geochemical relation between the southwestern Gibbon River flow, the Gibbon River flow represented by sample GRWY6, and the rest of the Roaring Mountain rhyolites (Crystal Spring, Obsidian Cliff, and main Gibbon River flows), if any, is still unclear. Similar phenocryst assemblages could suggest a shared heritage, and overlapping sanidine and plagioclase compositions between the three Gibbon River rhyolites suggests these magmas may have exchanged phenocrysts. However, these similarities could also be explained simply because all three of these units are high-Si rhyolites. Two models are suggested to produce the southwestern flow of the Gibbon River rhyolites and the lava flow represented by GRWY6: 1) a chemically and thermally stratified magma system (Figure 11.11), and 2) small, independent batches of locally remobilized crystalline mushes (Figure 11.12).

Continued mafic underplating may have chemically and thermally stratified (Hildreth, 1979; Hildreth, 1981) the post-Crystal Spring/Obsidian Cliff flow silicic magma system. A stable, homogeneous magma zone could have formed at the top of the magma system with compositionally different magma zones separating below (Figure 11.11). Based on the overall evolution of the three Gibbon River rhyolites and the chemical gradients between them (i.e. Ba and FeO increase with interpreted magma depth; Figures 6.2 & 6.4), in a stratified Gibbon River magma system, the shallowest magma would be the main flow, followed by the southwestern flow, and the rhyolite represented by GRWY6 would be the deepest magma (Figure 11.11). Similar chemical gradients within the Bishop Tuff were interpreted to represent magma depth within a stratified magma system (Hildreth, 1979). Communication between these magma zones including phenocryst

exchange would produce zoned phenocrysts like those within the southwestern and sample GRWY6 rhyolite flows. Additionally, fractional crystallization and localized crustal contamination could have influenced the heterogeneous chemistries of individual magma zones. This model also provides the best explanation for the intermingled nature of the Gibbon River flows. During eruption of the homogeneous main flow magma, the eruption probably also tapped deeper magma zones, erupting a heterogeneous Gibbon River flow, dominantly composed of homogeneous main Gibbon River flow.

Alternatively, the heat maintaining the hot, homogeneous magma body could also have locally remobilized cooler crystalline mushes (Bachmann and Bergantz, 2004; Bachmann and Bergantz, 2008) within the Roaring Mountain silicic magma system (Figure 11.12). A similar model was proposed for the adjacent Yellowstone Caldera post-collapse, intracaldera rhyolites of the Upper Basin Member, which are interpreted as being individually produced as remobilized crystal mush magma batches (Girard and Stix, 2009). The magma batches of the Upper Basin Member are interpreted as being generally unrelated to the other post-collapse rhyolites within the member (Girard and Stix, 2009). This remobilized crystal mush model would allow for the creation of small, crystal-rich magma batches in the proximity of the silicic magma of the main Gibbon River flow that are unrelated to each other and the main flow of the Gibbon River (Figure 11.12). The remobilization of these mushes' cold phenocrysts and their incorporation into a hot magma batch could account for the cold core, hot rim temperature pattern seen within the quartz of the southwestern flow. Additionally, these remobilized crystals may exhibit relict complex compositional zoning produced during initial crystallization that is retained within the phenocrysts erupted from these mush melts. The inclusions within

phenocrysts of the southwestern flow and the lava represented by sample GRWY6 could have been remobilized crystals that continued to precipitate within their remobilized magmas. The eruption of any of the Gibbon River rhyolite magmas may have intersected the main Gibbon River magma system or the melt pockets of the southwestern flow and the GRWY6 magma, causing the concurrent eruption of all three lavas.

If the Gibbon River rhyolites evolved within a chemically stratified magma system, the zircons analyzed from sample GRWY6 should be representative of the entire Gibbon River eruption. The individual model ages (116 to 211 ka) and the $^{230}Th/^{238}U$ disequilibrium age of 105 ka calculated for these zircons indicates the magma system that produced the Gibbon River rhyolites was evolving up to 160 ka before eruption. Since the Crystal Spring and Obsidian Cliff rhyolites erupted <18 ka before the eruption of the Gibbon River rhyolites, the zircons within the Roaring Mountain magma system apparently survived superheating and the apparent resorption of nearly all silicic phenocrysts. Thus, the time period of magma storage and evolution for the entire Roaring Mountain magma system is interpreted as ~160 ka.

If the magma represented by GRWY6 was a remobilized crystal mush, independent from the Crystal Spring/Obsidian Cliff and main Gibbon River flows, then the zircons analyzed for $^{230}Th/^{238}U$ could have been incorporated into the GRWY6 magma from the remobilized crystal mush. Alternatively, the zircons could have crystallized within the magma represented by GRWY6, suggesting that magma was evolving up to 106 ka before eruption. Thus, the time period of magma storage and evolution recorded within the zircons would not represent the Crystal Spring/Obsidian Cliff and main Gibbon River flow magma system.

Interestingly, the zircons analyzed for $^{230}Th/^{238}U$ (136 ka disequilibrium age with individual model ages ranging from 94 to 269 ka) by Vazquez and Reid (2002) were sampled from the "cliff on [the] east side of Gibbon Canyon." This cliff is composed of both the main flow and the southwestern flow of the Gibbon River rhyolites (Figure 4.2). If the southwestern flow was sampled, this suggests that the for a remobilized crystal mush model, the southwestern mush evolved and crystallized during the same time period as the remobilized crystal mush of the magma represented by GRWY6. If the main flow was sampled by Vazquez and Reid (2002), for either model, the Roaring Mountain magma system was established and evolving ~217 ka before eruption of the Gibbon River rhyolites.

The Gibbon River rhyolites erupted from the Roaring Mountain magma system at 52.0 ± 8.5 ka as a heterogeneous flow consisting of at least three magma compositions. Based on the uncertain geochemical relationship between the three Gibbon River rhyolite flow samples, the remobilization of a silicic crystal mush by heat generated from the mafic underplating beneath Norris Mammoth Corridor and the mafic injection into the Roaring Mountain silicic magma system is favored as the model describing the generation of the southwestern Gibbon River flow and the lava represented by sample GRWY6. This model requires a more complex eruption situation however, without geochemical evidence linking the three Gibbon River units, a model with three independent magma batches best describes the production of the Gibbon River rhyolites.

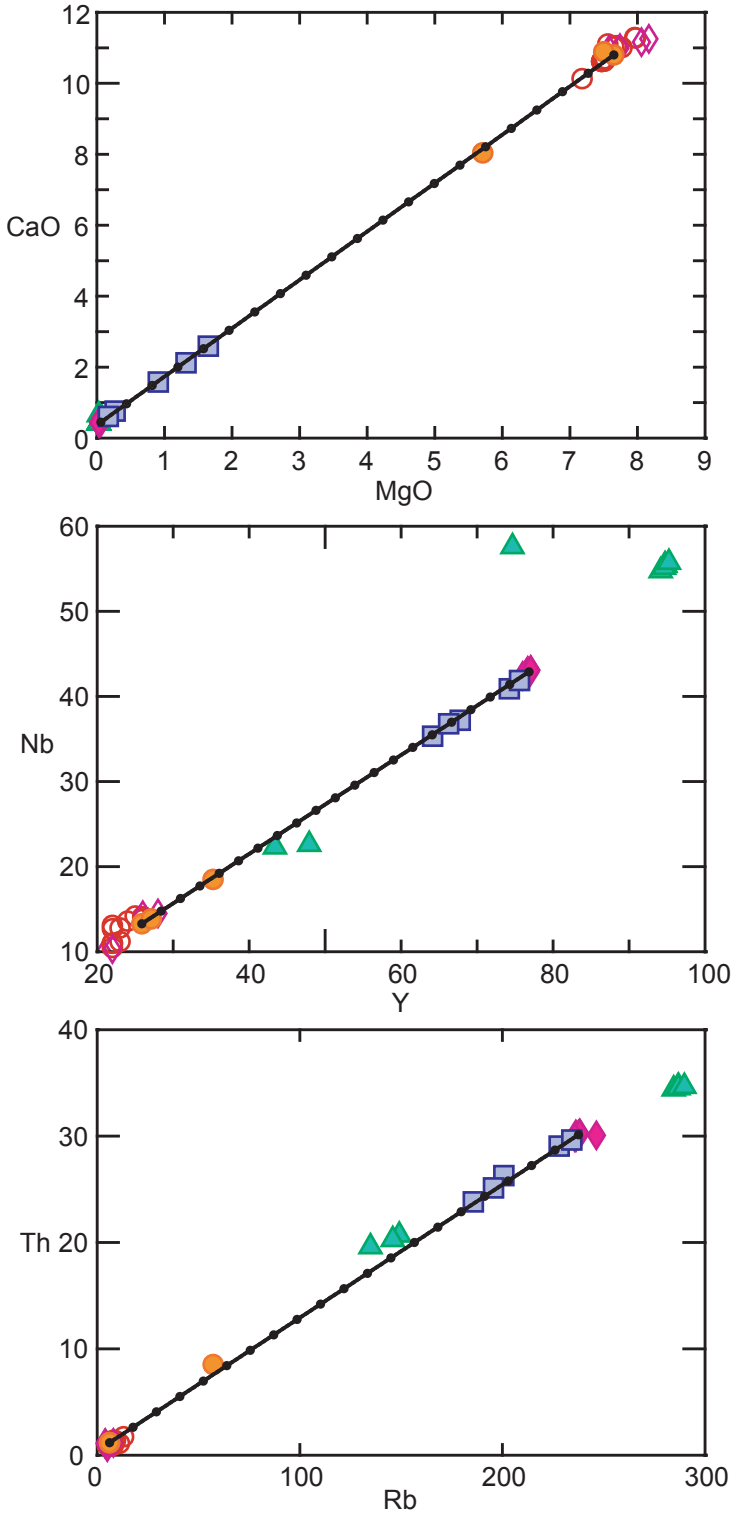

Figure 11.1. Major and trace element diagrams for the Gibbon River lavas (▲), Obsidian Cliff lavas (♦), Crystal Spring mingled rhyolites (■), and mafic enclaves (●) shown with a mixing line modeled between Obsidian Cliff rhyolite OCWY2 and Crystal Spring mafic enclave CSWY1E. Mixing lines are marked at 5% intervals. Swan Lake Flat Basalt (○) and Osprey Basalt (◇) samples are shown for comparison (Bennett, 2006).

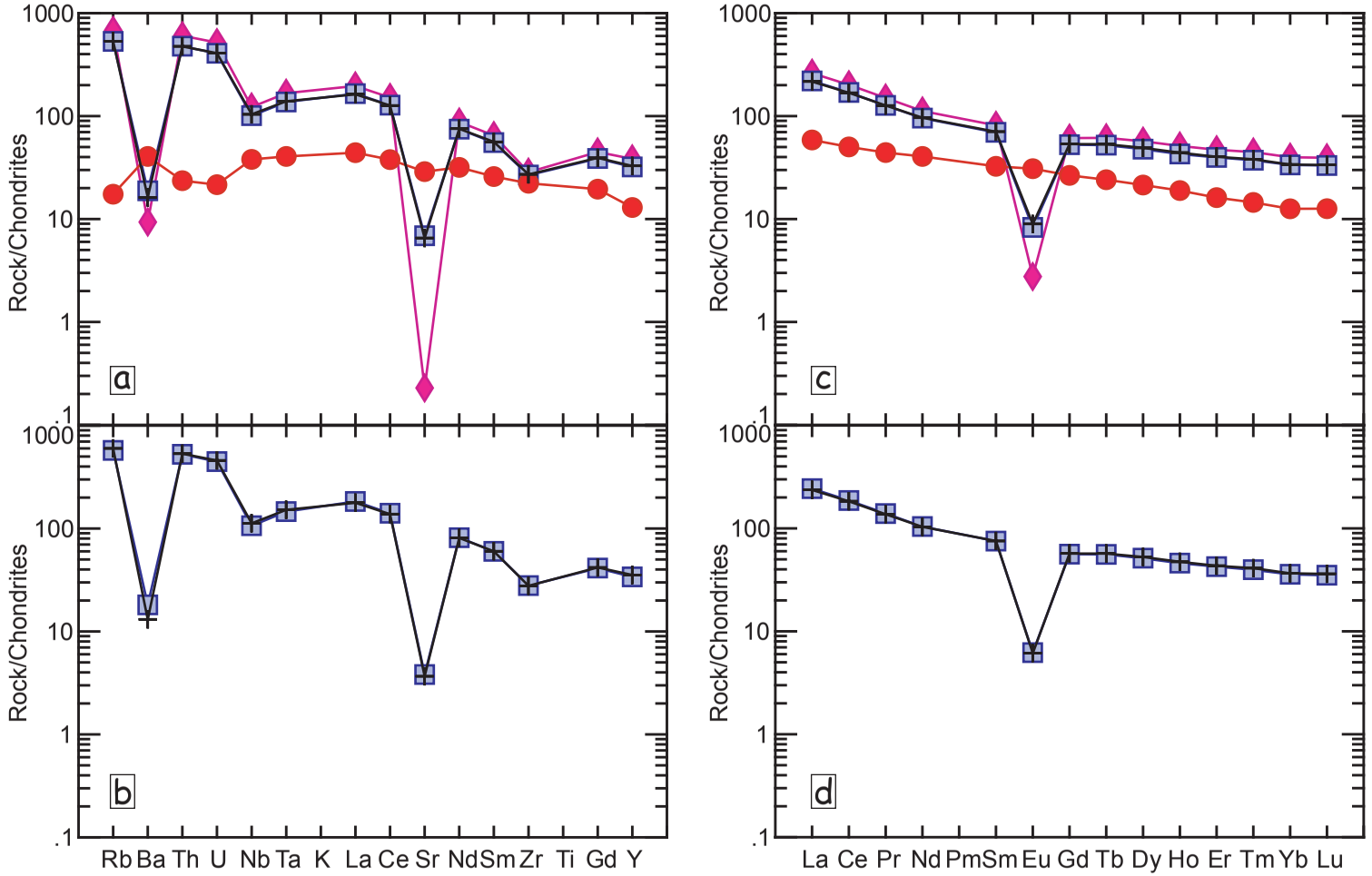

Figure 11.2. Trace element diagrams of Crystal Spring mingled rhyolite (▢) samples CSWY1 (a & c) and CSWY2 (b & d) overlain with best-fit, mixing models (+). CSWY1 can be produced by mixing 78% OCWY2 with 22% CSWY1E. CSWY2 can be produced by mixing 88% OCWY2 with 12% CSWY1E. Parent magmas Obsidian Cliff rhyolite OCWY2 (♦) and Crystal Spring mafic enclave CSWY1E (●) are shown in (a) and (c) for reference. Diagrams (a) & (b) formatted after Sun (1980); (c) & (d) formatted after Sun & McDonough (1989).

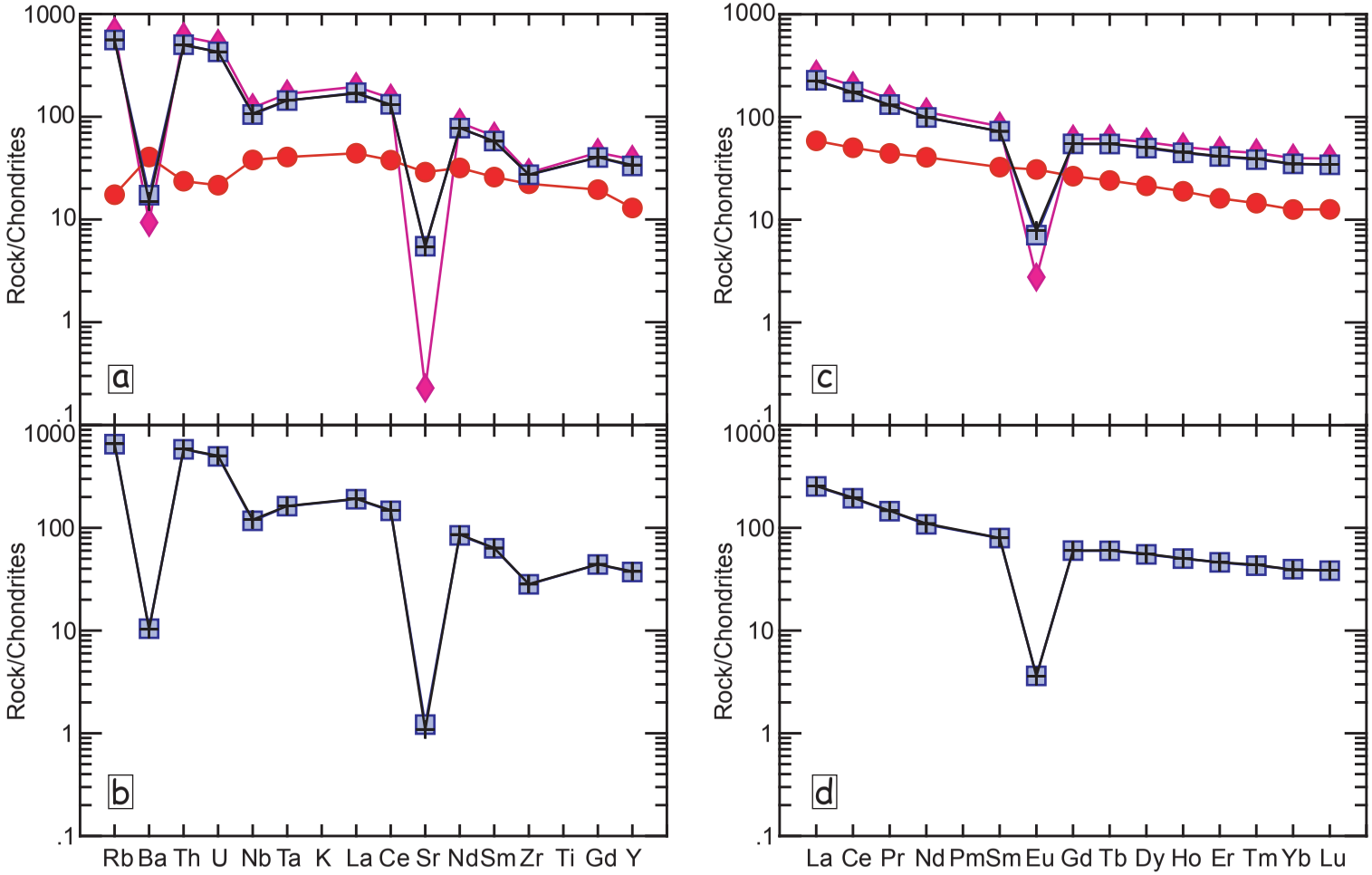

Figure 11.3. Trace element diagrams of Crystal Spring mingled rhyolite (▣) samples CSWY3V (a & c) and CSWY3 (b & d) overlain with best-fit, mixing models (+). CSWY3V can be produced by mixing 82% OCWY2 with 18% CSWY1E. CSWY3 can be produced by mixing 97% OCWY2 with 3% CSWY1E. Parent magmas Obsidian Cliff rhyolite OCWY2 (♦) and Crystal Spring mafic enclave CSWY1E (●) are shown in (a) and (c) for reference. Diagrams (a) & (b) formatted after Sun (1980); (c) & (d) formatted after Sun & McDonough (1989).

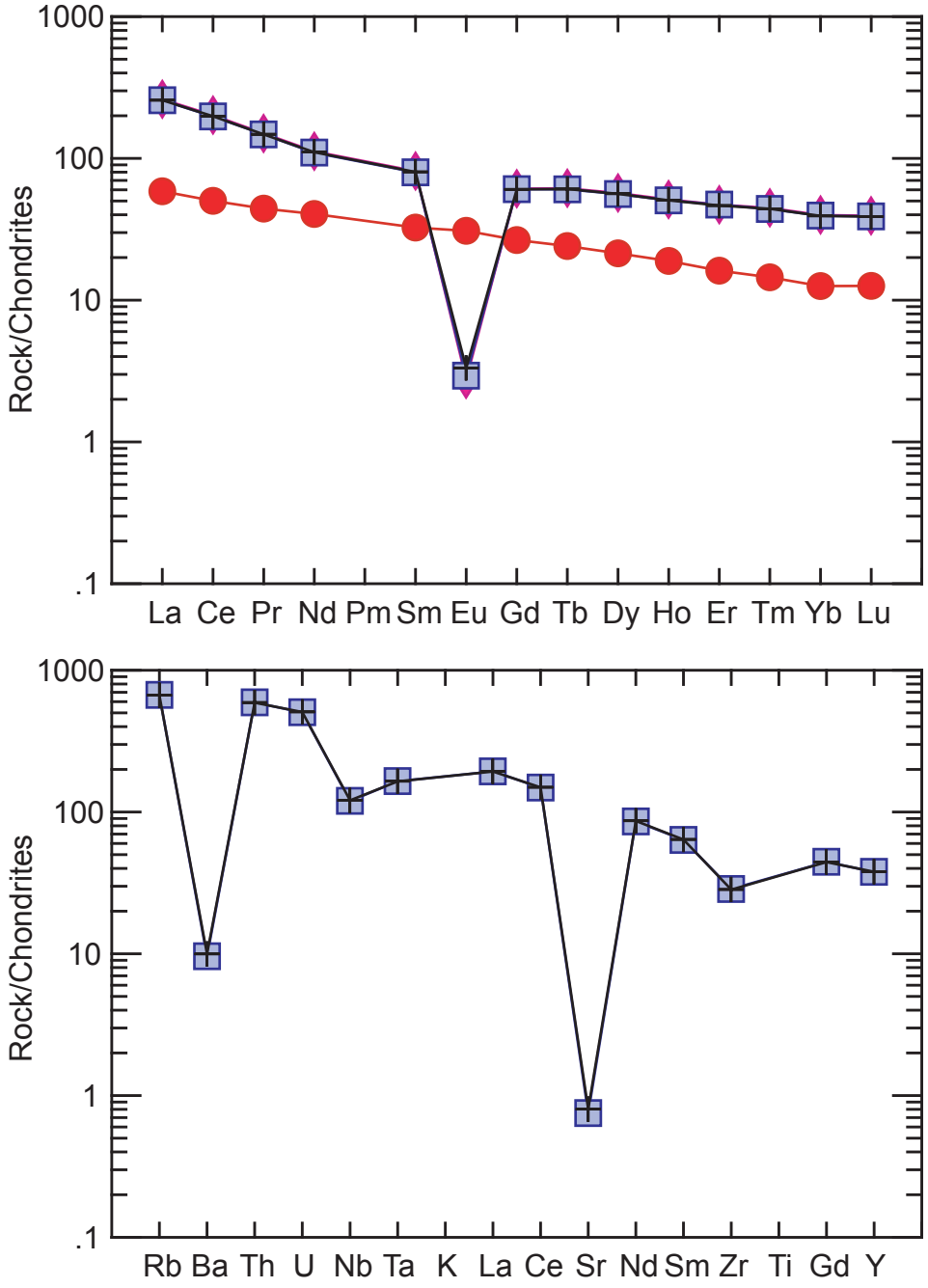

Figure 11.4. Trace element diagrams of Crystal Spring mingled rhyolite CSWY4 (▢) overlain with a best-fit, mixing model (+). CSWY4 can be produced by mixing 98% OCWY2 with 2% CSWY1E. Parent magmas Obsidian Cliff rhyolite OCWY2 (◆) and Crystal Spring mafic enclave CSWY1E (●) are shown in (a) for reference. Diagram (a) formatted after Sun & McDonough (1989); (b) formatted after Sun (1980).

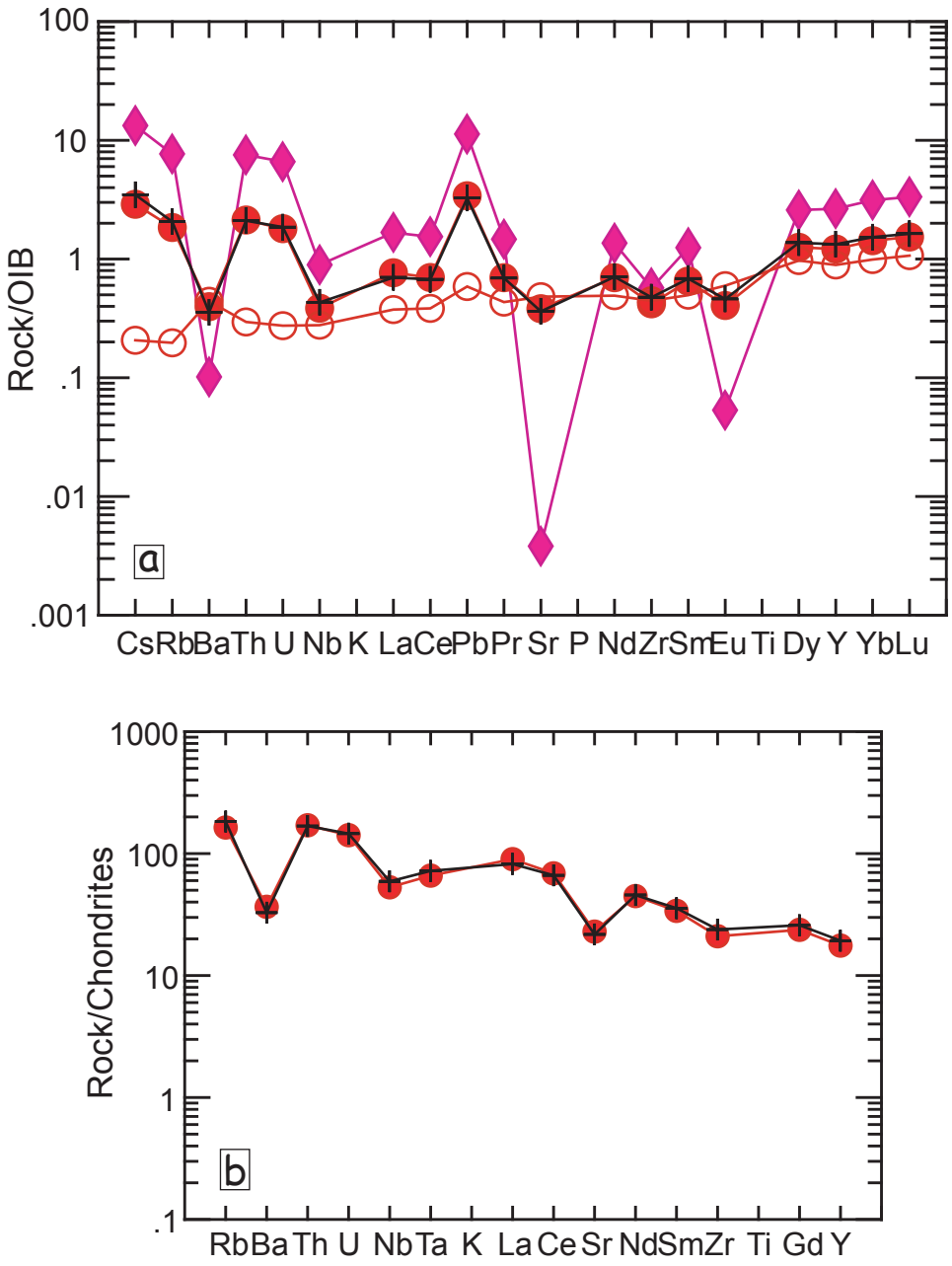

Figure 11.5. Trace element diagrams of Crystal Spring andesitic enclave sample CSYW1GE (●) overlain with a best-fit, mixing model (+). CSWY1GE can be produced by mixing ~75% CSWY1E with ~25% OCWY2. Parent magmas Obsidian Cliff rhyolite OCWY2 (♦) and Crystal Spring mafic enclave CSWY1E (○) are shown in (a) for reference. Diagram (a) formatted after Sun & McDonough (1989); (b) formatted after Sun (1980). OIB is Ocean Island Basalt.

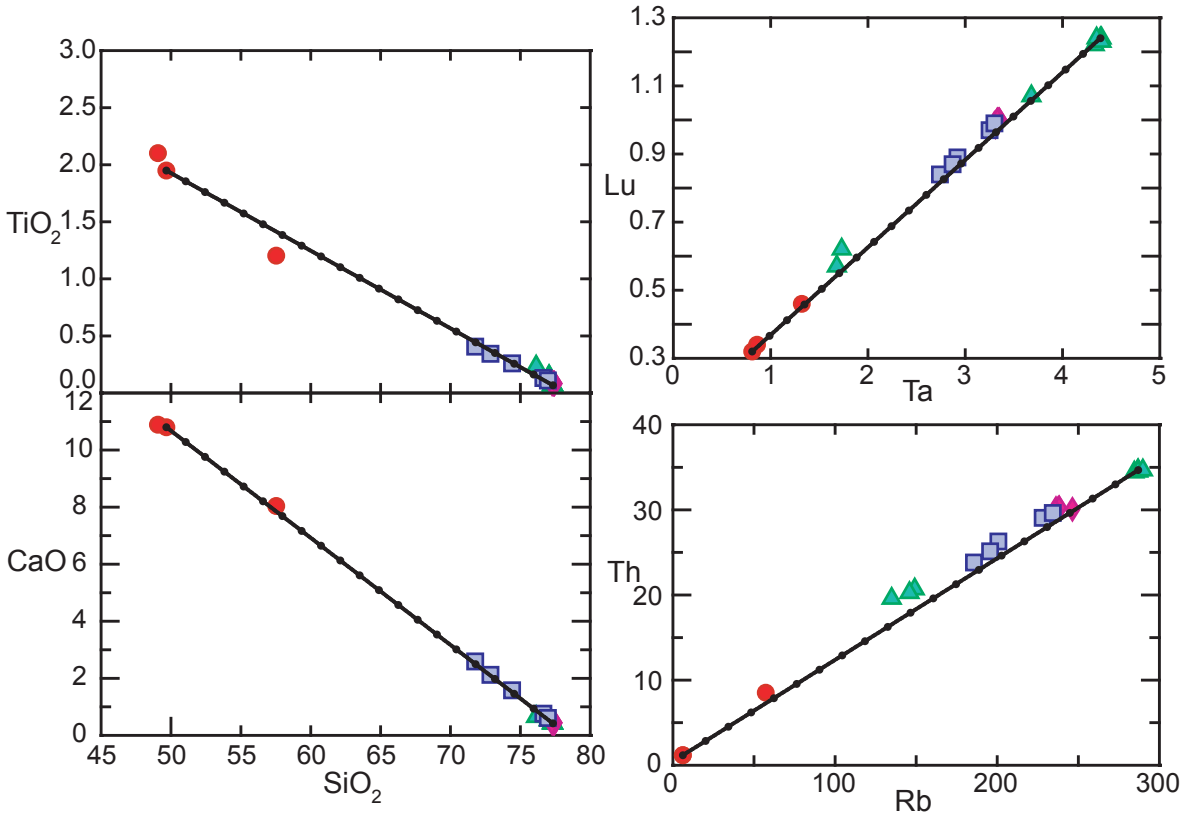

Figure 11.6. Major and trace element diagrams for the Gibbon River lavas (▲), Obsidian Cliff lavas (♦), Crystal Spring mingled rhyolites (■), and mafic enclaves (●) shown with a mixing line modeled between main flow of the Gibbon River rhyolite GRWY7O and Crystal Spring mafic enclave CSWY1E. Mixing lines are marked at 5% intervals.

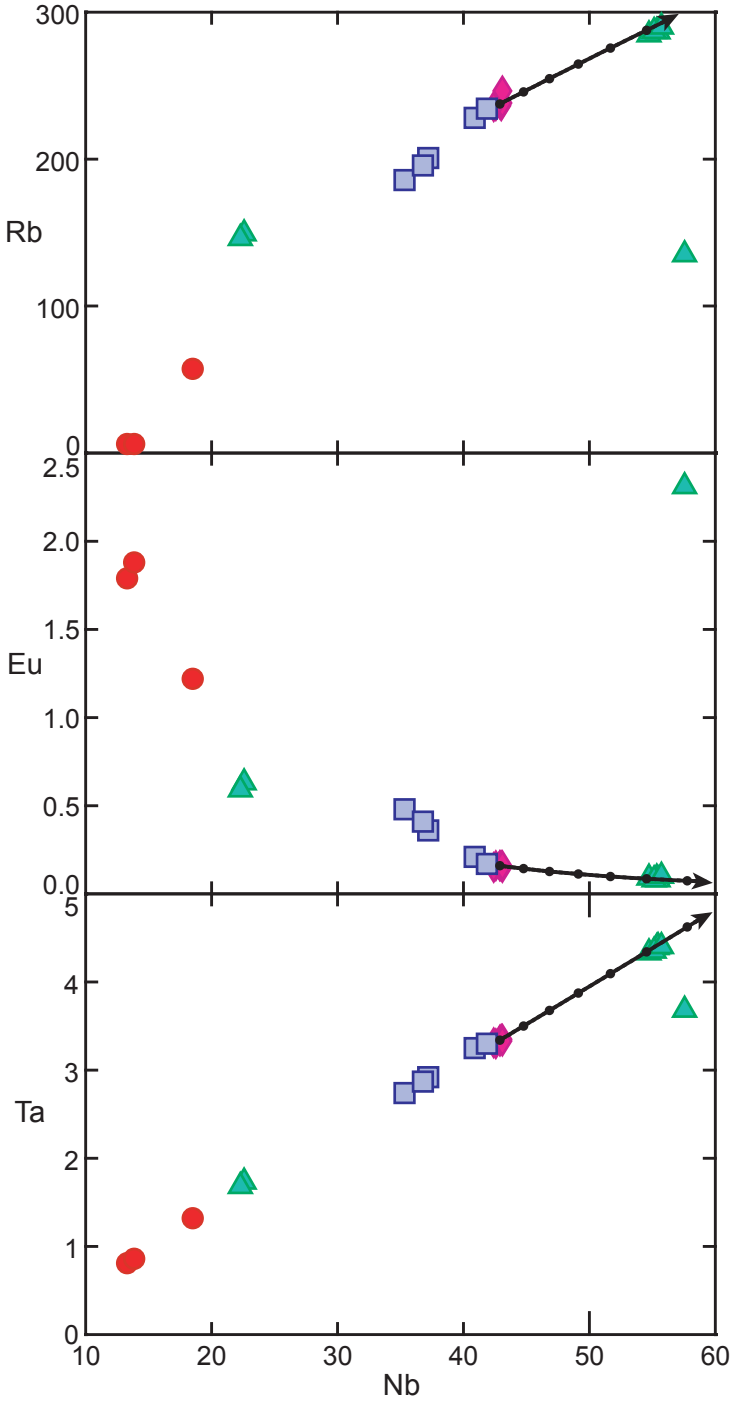

Figure 11.7. Trace element diagrams for the Gibbon River lavas (▲), Obsidian Cliff lavas (♦), Crystal Spring mingled rhyolites (□), and mafic enclaves (●) shown with a fractional crystallization model of Obsidian Cliff rhyolite OCWY2. Arrow indicates direction of increasing crystallization. Fractional crystallization lines are marked at 5% intervals.

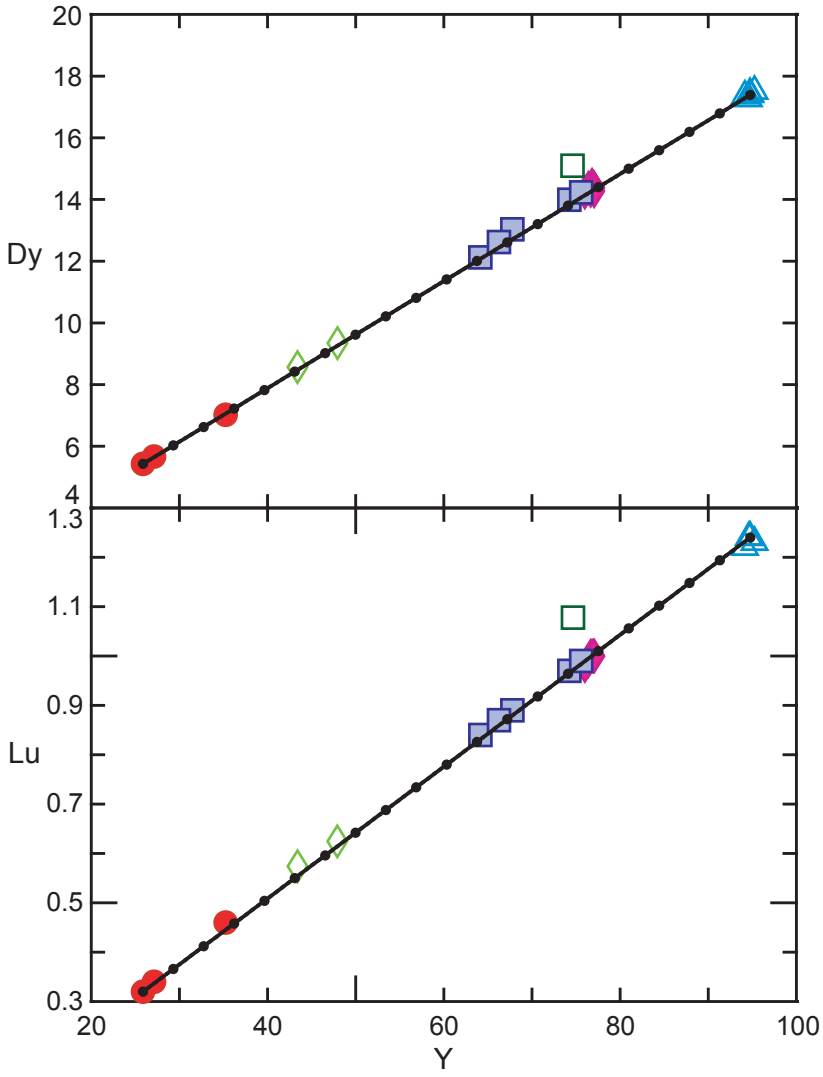

Figure 11.8. Trace element diagrams for the Gibbon River rhyolite main flow (△), southwestern flow (◊), and sample GRWY6 (□), and the Obsidian Cliff lavas (♦), Crystal Spring mingled rhyolites (▩), and mafic enclaves (●) shown with a mixing line modeled between main flow of the Gibbon River rhyolite GRWY7O and Crystal Spring mafic enclave CSWY1E. Mixing lines are marked at 5% intervals.

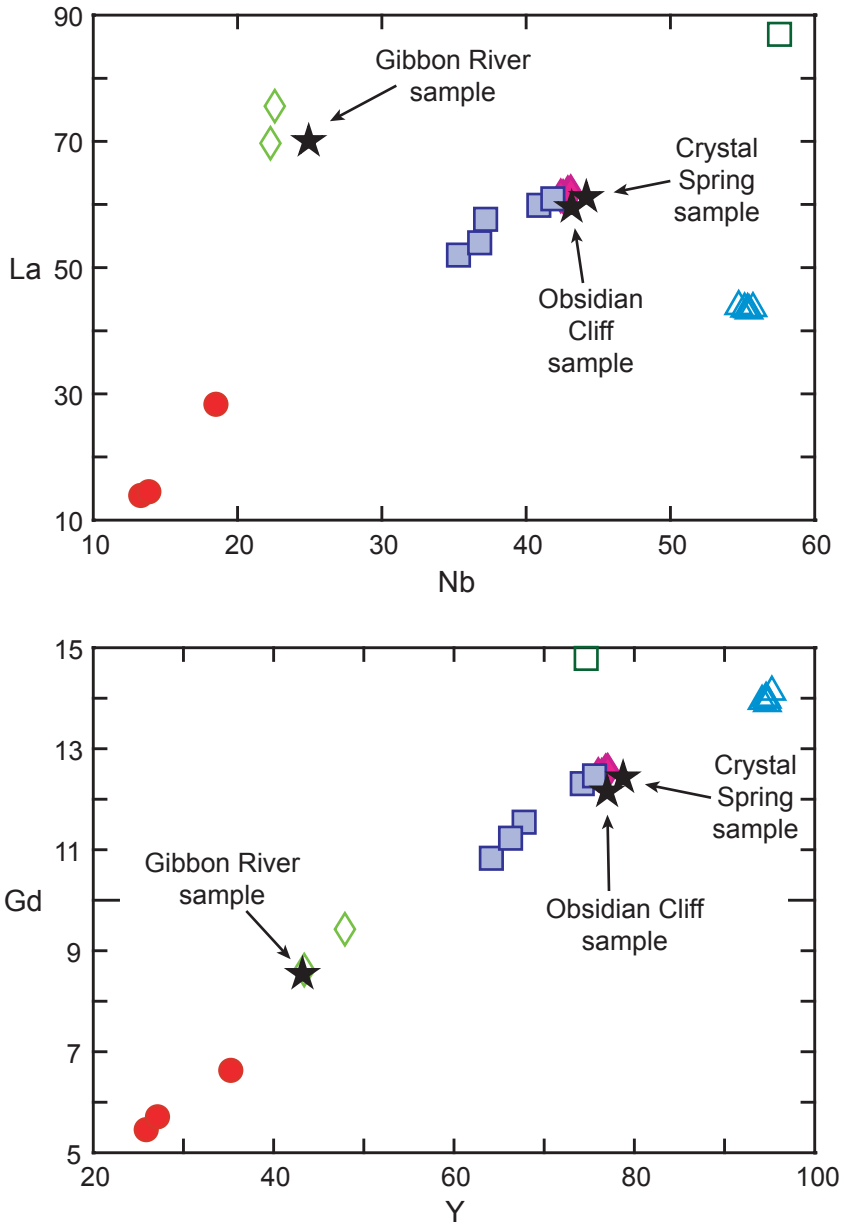

Figure 11.9. Trace element diagrams comparing the Gibbon River main flow (△), southwestern flow (◇), and sample GRWY6 (□), Obsidian Cliff rhyolite (◆), Crystal Spring rhyolite (■), and the Crystal Spring mingled rhyolite mafic enclave (●) samples of this study to the Roaring Mountain Member samples (★) collected by Nastanski (2005).

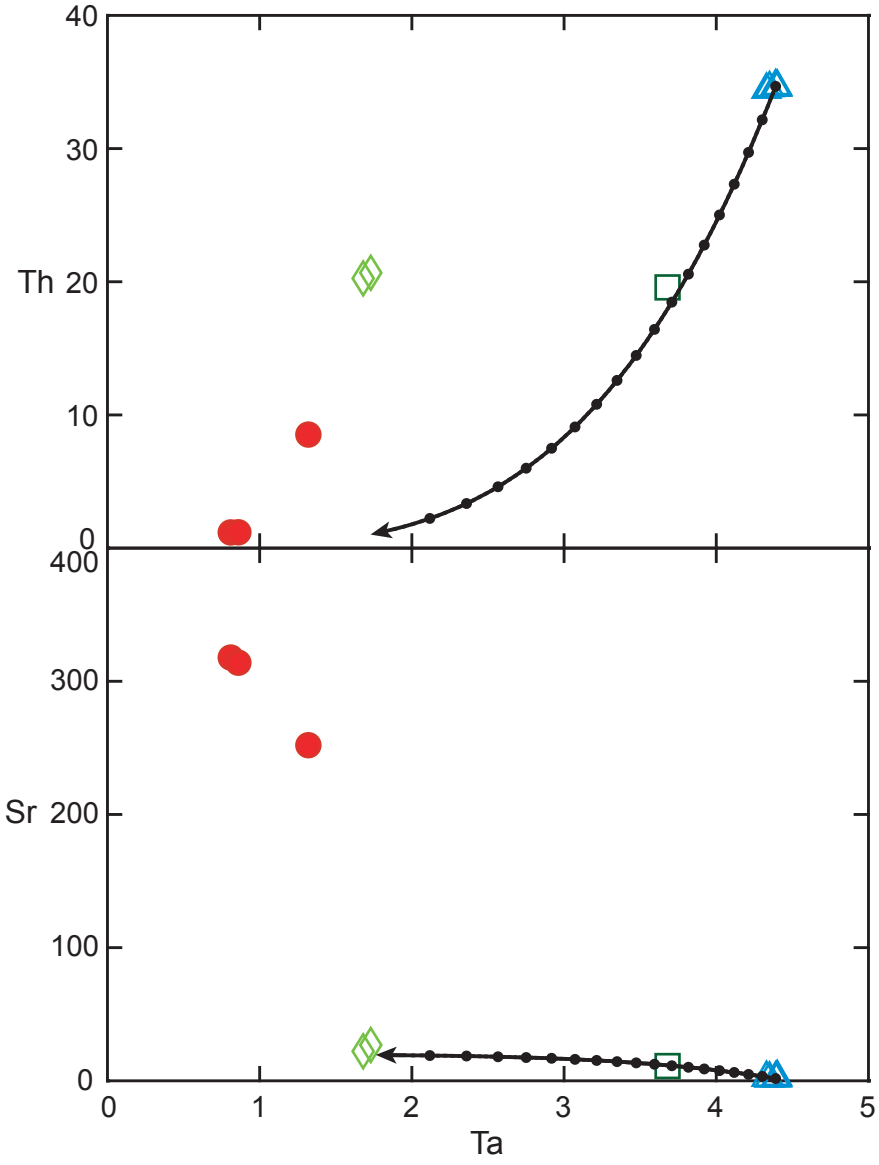

Figure 11.10. Trace element diagrams for the Gibbon River rhyolite main flow (△), southwestern flow (◇), and sample GRWY6 (□), and the Crystal Spring mingled rhyolite mafic enclaves (●) shown with an assimilation and fractional crystallization model of the main flow of the Gibbon River rhyolite GRWY7O, assimilated with the Crystal Spring mafic enclave CSWY1E. $R = 0.1$. Fractional crystallization lines are marked at 5% intervals.

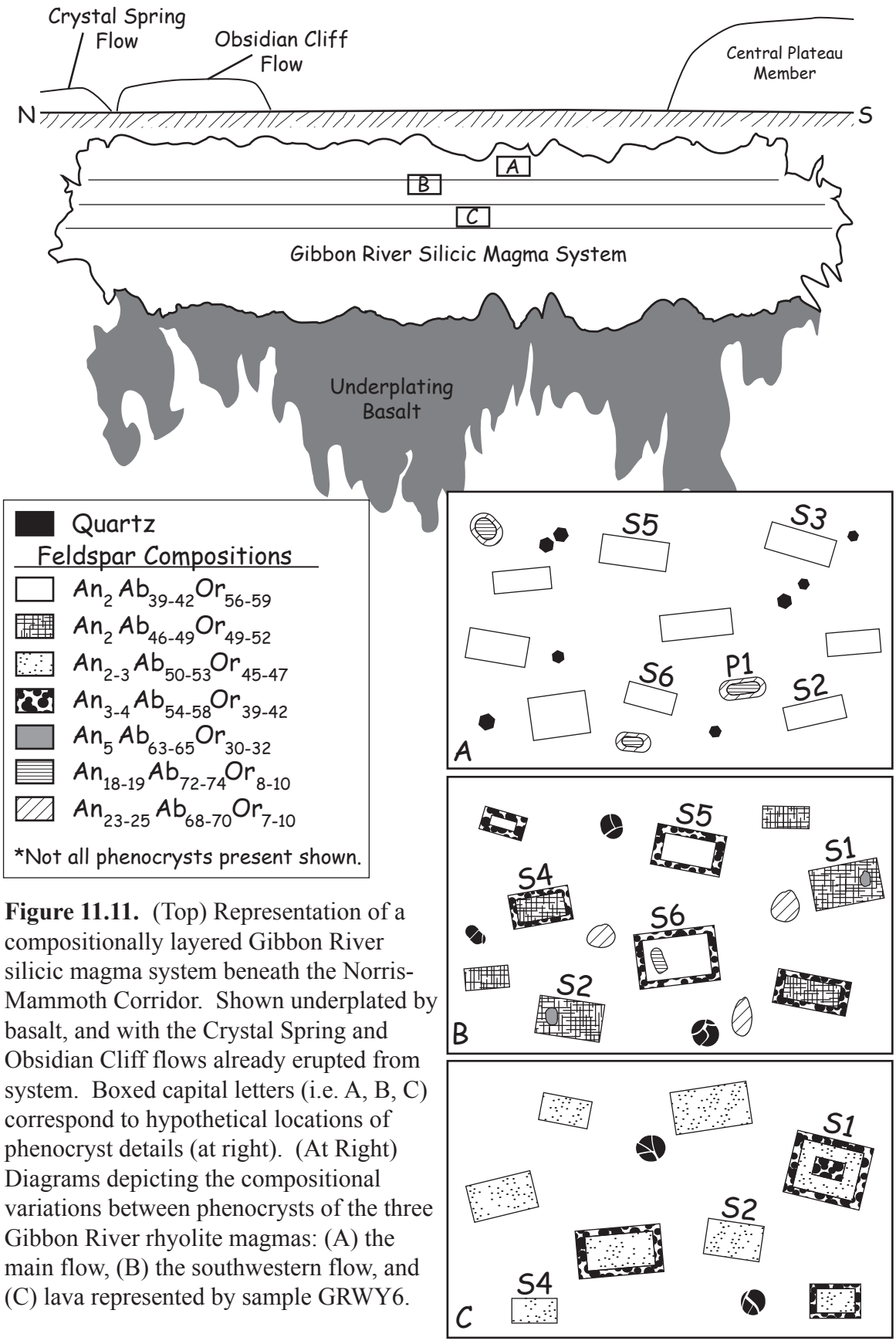

Figure 11.11. (Top) Representation of a compositionally layered Gibbon River silicic magma system beneath the Norris-Mammoth Corridor. Shown underplated by basalt, and with the Crystal Spring and Obsidian Cliff flows already erupted from system. Boxed capital letters (i.e. A, B, C) correspond to hypothetical locations of phenocryst details (at right). (At Right) Diagrams depicting the compositional variations between phenocrysts of the three Gibbon River rhyolite magmas: (A) the main flow, (B) the southwestern flow, and (C) lava represented by sample GRWY6.

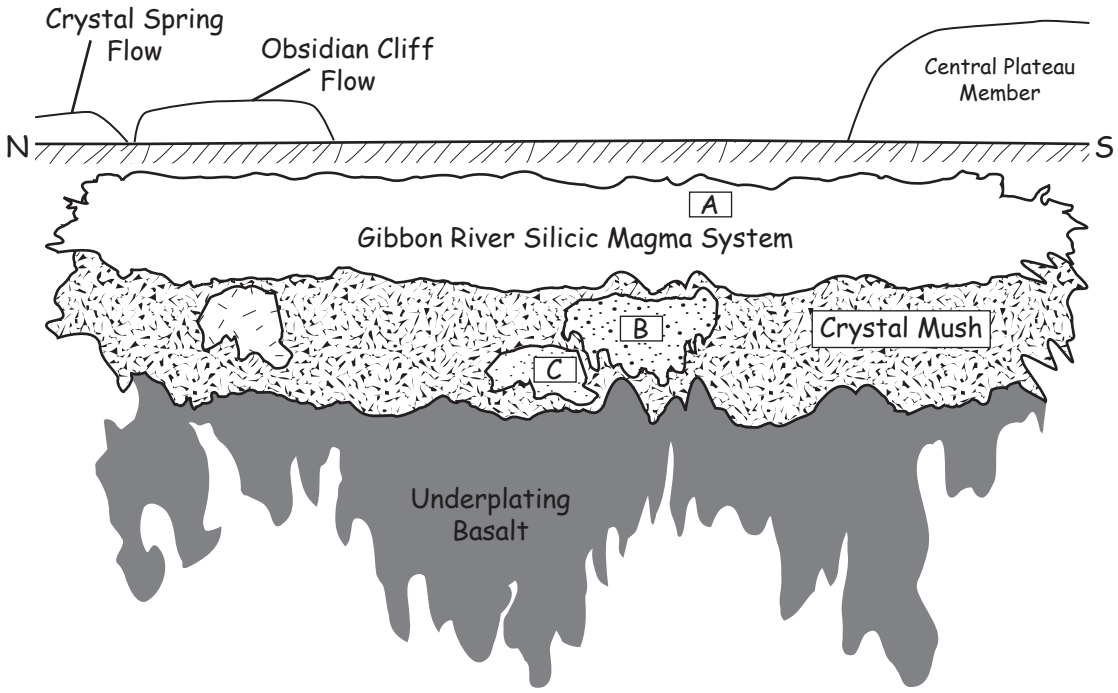

Figure 11.12. A representation of the GIbbon River silicic magma system with a main magma system separated from several remobilized crystal mush melts. Boxed captial letters (i.e. A, B, C) correspond to the phenocryst diagrams depicted in Figure 11.11 and correspond to hypothetical locations of the three Gibbon River rhyolite magmas: (A) the main flow, (B) the southwestern flow, and (C) lava represented by sample GRWY6.

CHAPTER 12

CONCLUSIONS

Petrography, geochemistry, and electron microprobe analyses suggest that the Crystal Spring mingled rhyolites, Obsidian Cliff rhyolite, and the main flow of the Gibbon River rhyolites were all generated within a single, large-scale, coherent silicic magma system beneath the Norris-Mammoth Corridor in the Yellowstone Volcanic Field. The Gibbon River flow consists of three rhyolite units: the main flow, the southwestern flow, and a flow represented by sample GRWY6. The relationship of the southwestern Gibbon River flow and the lava represented by GRWY6 to the Crystal Spring/Obsidian Cliff and main Gibbon River flow magma system is still unclear. They may have developed as small, independent melts or have evolved within a zoned main Gibbon River flow magma system.

Prior to eruption of the Crystal Spring and Obsidian Cliff lavas, the Roaring Mountain silicic magma system was superheated by basaltic magma injection. This mafic magma was a tholeiitic basalt similar in composition to the Swan Lake Flat basalts (Hildreth *et al.*, 1991; Christiansen, 2001). This mafic injection superheated the silicic magma, rapidly convecting and homogenizing the silicic magma and likely resorbing all rhyolitic phenocrysts. This mafic injection also mingled and locally mixed with the silicic magma. The homogeneous, unmingled portion of the silicic magma erupted as the Obsidian Cliff lava flow, and the mixed and mingled magma of the system erupted as the Crystal Spring mingled lavas. The Obsidian Cliff lava is an aphyric, homogeneous obsidian with local outcrops of a pumiceous carapace. The Obsidian Cliff rhyolite contains fayalite and, rarely, mafic glomerocrysts, though no mafic enclaves were

observed within the flow. The Crystal Spring mingled lavas are glassy rhyolites containing mafic crystals and glomerocrysts, and variously sized basaltic to andesitic enclaves. The Crystal Spring mingled rhyolite contains up to ~25% mafic material. The Crystal Spring mingled rhyolite and the Obsidian Cliff rhyolite erupted concurrently in 59.1 ± 2.0 ka, probably from two separate vents that are connected along one of the area's numerous faults.

After eruption of the Crystal Spring and Obsidian Cliff lavas, the residual magma continued evolving by fractional crystallization. The fractionating system began cooling, but maintained high temperatures (840-995°C, as determined by Ti-quartz geothermometry), before erupting as the main flow of the Gibbon River rhyolites at 52.0 ± 8.5 ka. Two-feldspar geothermometry indicates the main flow erupted at lower temperatures (between 796°C and 827°C) than calculated by Ti-quartz geothermometry. The main flow of the Gibbon River rhyolites is a sparsely porphyritic to porphyritic rhyolite containing homogeneous, unzoned sanidine, quartz, plagioclase, pyroxene, amphibole, magnetite, and zircon.

The southwestern Gibbon River flow and the lava represented by GRWY6 may have evolved independently of the Crystal Spring, Obsidian Cliff and main Gibbon River flow magmas. The heat from the mafic magma injected into the Crystal Spring/Obsidian Cliff magma may have remobilized adjacent crystal mushes, generating small, independently evolving magma batches. These melts intersected the magma of the main flow of the Gibbon River rhyolites at some point prior to eruption and were concurrently erupted together with the main Gibbon River flow.

Alternatively, the magma system of the main flow of the Gibbon River rhyolites could have become chemically and/or thermally stratified by heat and volatiles from an underlying mafic component. At the top of this zoned system, the magma of the main Gibbon River flow evolved with the magmas of the southwestern flow and the lava represented by GRWY6 developing at increasingly lower depths, respectively, within the system. When the Gibbon River rhyolites erupted concurrently at 52.0 ± 8.5 ka, the eruption tapped multiple levels of the magma system, creating a heterogeneous lava flow.

Titanium-in-Quartz geothermometry indicates that during the period just prior to eruption, the southwestern flow of the Gibbon River rhyolites evolved at high temperatures (between 860°C and 970°C, high temperature rims). The cores of the southwestern flow quartz indicate this was preceded by a low temperature growth period, though it is unclear if these cores crystallized within the magma of the southwestern flow or are relict to a remobilized crystal mush. Like the main Gibbon River flow, two-feldspar geothermometry suggests the southwestern flow erupted at ~820°C. The southwestern flow is a porphyritic rhyolite containing zoned sanidine and quartz, and plagioclase, pyroxene, fayalite, magnetite, and zircon, with local outcrops of mahogany obsidian. The third Gibbon River rhyolite, represented by GRWY6, also evolved at high magma temperatures (between 890°C and 1006°C, as determined by Ti-quartz geothermometry). Sample GRWY6 is a porphyritic rhyolite containing zoned sanidine and quartz, and fayalite, pyroxene, amphibole, magnetite, ilmenite, and zircon.

$^{230}Th/^{238}U$ zircon geochronology agrees with work by Vazquez and Reid (2002) indicating the presence of a population of zircons that record a single crystallization episode, which crystallized beneath the Gibbon River flow. The zircon began

crystallizing ~160 ka before they were erupted within the Gibbon River rhyolites. The individual zircon model ages also (116 ± 18 to 211 ± 64 ka) overlap with the eruption ages of the last Obsidian Creek Member rhyolites (Gibbon Hill rhyolite at 134.3 ± 2.6 ka and Paintpot Hill rhyolite at 208.1 ± 4.9 ka) (Nastanski, 2005). This supports isotopic evidence linking the Obsidian Creek Member rhyolites and the Roaring Mountain Member rhyolites (Nastanski and Spell, 2004a; Nastanski and Spell, 2004b; Nastanski, 2005). Whether the southwestern Gibbon River flow and the lava represented by GRWY6 evolved within the magma system of the main Gibbon River flow or were rejuvenated crystal mushes, these data suggest that zircons from residual Obsidian Creek Member magma were erupted within the Gibbon River rhyolites.

The Obsidian Creek magma system developed at ~450 ka (Spell and Nastanski, 2004) with continued rhyolite and mingled rhyolite eruptions until 134 ka (Nastanski, 2005). The Obsidian Creek silicic magma system likely became the Roaring Mountain silicic system with the injection of a basaltic magma. Mingling and mixing with the mafic injection reverted the silicic magma system to a more primitive chemistry. From this mingled system the Crystal Spring and Obsidian Cliff lavas erupted at 59 ka. The latest Roaring Mountain eruption was at 52 ka with the Gibbon River rhyolite flow.

The presence of this young, long-lived, large-scale silicic magma system beneath the Norris-Mammoth Corridor, combined with the area's high geothermal flux (Kharaka et al., 2000) and high earthquake and geophysical activity (Wicks et al., 2006; Christiansen et al., 2007), presents this area as the most geologically active site within the Yellowstone Volcanic Field. While there is also significant geothermal and geophysical activity within the Yellowstone Caldera (Kharaka et al., 2000; Wicks et al., 2006; Christiansen et

al., 2007), the site of a large-scale, caldera-forming silicic eruption would be expected to remain geologically active for a significant time period, even after its final volcanic eruption. In contrast, the extracaldera eruptions of the Obsidian Creek and Roaring Mountain rhyolites may represent the initial stages of development of a new large-scale, possibly caldera-forming silicic magma system. So, while the Yellowstone Caldera is the site of the last large-scale, caldera-forming eruption, the next caldera-forming eruption could be developing beneath the Norris-Mammoth Corridor within the young Obsidian Creek/Roaring Mountain magma system.

APPENDIX A

SAMPLE LOCATION DATA

Table A.1. Gibbon River flow sample locations in UTM coordinates

Sample	Latitude	Longitude	Elevation (ft)	Sample Location
Gibbon River flow				
GRWY1	N 4944540	E 520315	7300	Southwest flow lobe of Gibbon River flow
GRWY2	N 4944630	E 520470	7400	Southern edge of southwest lobe of Gibbon River flow
GRWY3	N 4944915	E 520620	7700	Southwest flow lobe of Gibbon River flow along powerline road
GRWY4	N 4950930	E 527030	7660	Along flow front of northeastern Gibbon River flow, northeast of Virginia Cascade
GRWY5	N 4950830	E 527140	7720	Along flow front of northeastern Gibbon River flow, northeast of Virginia Cascade
GRWY6	N 4950750	E 527190	7840	Along flow front of northeastern Gibbon River flow, northeast of Virginia Cascade
GRWY7O [a]	N 4949970	E 525750	8020	Northern edge of northern upper Gibbon River flow lobe near Gibbon Hill
GRWY7P [a]	N 4949970	E 525750	8020	Northern edge of northern upper Gibbon River flow lobe near Gibbon Hill
GRWY8	N 4951030	E 525350	7650	Northern edge of northern lower Gibbon River flow lobe near Gibbon Hill
GRWY9	N 4951400	E 524850	7640	North side of Gibbon River flow near bend in fire road, south of water tower site
GRWY10	N 4951290	E 523280	7760	Cliff of obsidian at northern edge of lower Gibbon River flow lobe
GRWY11	N 4944930	E 521270	7760	Along south-central region of southern flow lobe
GRWY12	N 4945360	E 521860	7750	Along central region of southern flow lobe
GRWY13	N 4944830	E 520765	7700	Along south end of Hwy 89 telephone lines, on cliff of most-western flow
GRWY14	N 4945730	E 520560	7800	Along south end of Hwy 89 telephone lines, on cliff of most-western flow
GRWY15	N 4946500	E 520810	7850	Along south end of Hwy 89 telephone lines, on cliff of most-western flow

[a] Samples GRWY7O and GRWY7P are from the same site; GRWY7O is obsidian and GRWY7P is pumiceous rhyolite.

Table A.2. Obsidian Cliff flow sample locations in UTM coordinates

Sample	Latitude	Longitude	Elevation (ft)	Sample Location
Obsidian Cliff flow				
OCWY1	N 4959415	E 523640	7740	Southwestern edge of southern Obsidian Cliff flow lobe
OCWY2	N 4959370	E 523695	7765	Southwestern edge of southern Obsidian Cliff flow lobe
OCWY3 [a]	N 4959150	E 524240	7770	Middle edge of southern Obsidian Cliff flow lobe
OCWY4 [a]	N 4959360	E 524570	7815	East side of Obsidian Cliff southern lobe
OCWY5 [a]	N 4959805	E 524765	7830	Northern side of stream on southern Obsidian Cliff flow lobe
OCWY6	N 4960665	E 525070	7865	Northeastern corner of Obsidian Cliff southern flow lobe
OCWY7	N 4960490	E 524000	7935	East of Lake of the Woods
OCWY8	N 4960410	E 523745	7890	Southeast of Lake of the Woods
OCWY9	N 4964550	E 522750	7800	Northwest side of northern Obsidian Cliff flow lobe; southeast of Obsidian Lake
OCWY10	N 4964300	E 524150	8100	North end of Obsidian Cliff northern flow lobe
OCWY11 [a]	N 4964130	E 524390	8110	North edge of Obsidian Cliff northern flow lobe
OCWY12	N 4964450	E 523590	8050	North edge of Obsidian Cliff northern flow lobe
OCWY13	N 4964355	E 521595	7400	Northwestern edge of northern Obsidian Cliff flow lobe along Hwy 89
OCWY14	N 4963010	E 521550	7400	Obsidian Cliff Overlook on Hwy 89

[a] Samples OCWY3, OCWY4, OCWY5, and OCWY11 are pumiceous rhyolite samples. All other samples are obsidian.

Table A.3. Crystal Spring flow sample locations in UTM coordinates

Sample	Latitude	Longitude	Elevation (ft)	Sample Location
Crystal Spring flow				
CSWY1	N 4966920	E 522820	7720	Large rock outcrop along hillside of northwest edge of Crystal Spring flow
CSWY1P	N 4966920	E 522820	7720	Large rock outcrop along hillside of northwest edge of Crystal Spring flow
CSWY1E	N 4966920	E 522820	7720	Large rock outcrop along hillside of northwest edge of Crystal Spring flow
CSWY1ME	N 4966920	E 522820	7720	Large rock outcrop along hillside of northwest edge of Crystal Spring flow
CSWY2	N 4966860	E 522900	7740	Small rock outcrop north of mapped Crystal Spring vent
CSWY2E	N 4966860	E 522900	7740	Small rock outcrop north of mapped Crystal Spring vent
CSWY3	N 4967235	E 523420	7730	Northeastern edge of Crystal Spring flow
CSWY3E	N 4967235	E 523420	7730	Northeastern edge of Crystal Spring flow
CSWY3V	N 4967235	E 523420	7730	Northeastern edge of Crystal Spring flow
CSWY4	N 4965250	E 523620	7920	Talus slope on southern-most edge of Crystal Spring flow
CSWY4E	N 4965250	E 523620	7920	Talus slope on southern-most edge of Crystal Spring flow

Notes: Samples with the same numeral in the sample ID are from the same site.
Samples with no letter at the end of the sample ID are mingled rhyolite.
Samples with an “E” at the end of the sample ID are mafic enclaves.
Sample CSWY1P is more sample of CSWY1.
Sample CSWY1ME is a darker, more vesicular portion of the mafic enclaves at this site.
Sample CSWY3V is a vesicular obsidian.
Analyses of CSWY1GE are taken from a small mafic enclave within sample CSWY1.

APPENDIX B

XRF AND ICP-MS MAJOR AND TRACE ELEMENT GEOCHEMISTRY DATA

Table B.1. Major and trace element analyses of samples

Sample	GRWY1	GRWY3	GRWY6	GRWY7O	GRWY9	GRWY10
SiO_2	77.47	75.90	75.51	76.91	76.57	76.71
Al_2O_3	12.31	12.04	11.92	12.12	12.10	12.10
TiO_2	0.15	0.14	0.23	0.07	0.07	0.07
FeO	1.29	1.25	2.06	1.11	1.11	1.11
MnO	0.02	0.02	0.05	0.02	0.02	0.02
CaO	0.54	0.52	0.65	0.42	0.43	0.42
MgO	0.08	0.07	0.03	0.03	0.03	0.03
K_2O	5.21	5.12	5.08	4.82	4.81	4.80
Na_2O	3.44	3.41	3.63	3.96	3.94	3.93
P_2O_5	0.03	0.01	0.01	0.01	0.01	0.01
LOI (%)	0.23	1.18	0.18	0.36	0.30	0.36
Total	100.55	98.49	99.18	99.46	99.09	99.20
La	75.57	69.69	86.94	43.33	43.83	43.14
Ce	131.01	129.85	176.49	93.76	94.19	93.55
Pr	15.04	14.16	19.90	11.59	11.59	11.58
Nd	54.26	49.78	74.82	44.66	44.75	44.89
Sm	10.72	9.85	15.93	12.65	12.63	12.64
Eu	0.63	0.59	2.31	0.09	0.09	0.08
Gd	9.42	8.62	14.79	13.89	13.94	13.96
Tb	1.55	1.44	2.46	2.72	2.69	2.71
Dy	9.31	8.51	14.95	17.39	17.35	17.43
Ho	1.82	1.68	2.98	3.54	3.52	3.55
Er	4.85	4.44	7.96	9.57	9.68	9.70
Tm	0.69	0.64	1.14	1.42	1.42	1.42
Yb	4.20	3.82	7.07	8.47	8.43	8.50
Lu	0.62	0.57	1.07	1.24	1.22	1.24
Ba	419.33	440.48	878.32	19.22	23.13	22.65
Th	20.67	20.25	19.57	34.67	34.40	34.55
Nb	22.58	22.28	57.56	55.35	54.73	55.45
Y	47.91	43.40	74.67	94.76	94.16	94.74
Hf	6.38	6.33	13.98	8.57	8.53	8.48
Ta	1.73	1.68	3.68	4.39	4.33	4.40
U	3.80	3.78	4.26	8.35	8.31	8.38
Pb	24.68	28.53	29.26	42.23	41.88	42.00
Rb	149.12	145.90	134.91	286.91	284.54	286.57
Cs	1.72	2.52	1.90	6.65	6.65	6.67
Sr	26.81	22.06	11.07	1.69	2.08	1.82
Sc	1.85	1.89	1.86	1.11	1.17	1.18
Zr	173.10	172.07	470.05	152.72	153.46	152.78
Ni	3.30	2.71	3.17	4.61	4.09	4.09
Cr	1.60	0.00	0.00	0.00	1.10	0.80
V	2.20	2.40	0.00	0.90	0.00	0.40
Ga	20.10	19.90	25.20	28.10	26.70	25.90
Cu	3.50	2.10	1.80	2.90	1.70	2.20
Zn	46.10	59.70	115.70	87.30	85.60	88.10

Major elements are unnormalized (wt. %). Total = the sum of the major element analyses including LOI values. Trace elements are ppm. Major elements and Ni, Cr, V, Ga, Cu, & Zn analyzed by XRF; all other trace elements analyzed by ICP-MS.

Table B.1. Major and trace element analyses of samples (continued)

Sample	GRWY12	GRWY15	OCWY2	OCWY5	OCWY6	OCWY8
SiO_2	77.11	76.34	76.68	75.59	76.87	76.80
Al_2O_3	12.17	12.04	11.99	11.92	12.01	12.00
TiO_2	0.07	0.07	0.08	0.08	0.08	0.08
FeO	1.10	1.09	1.13	1.10	1.12	1.13
MnO	0.02	0.02	0.02	0.02	0.02	0.02
CaO	0.42	0.41	0.44	0.43	0.43	0.43
MgO	0.03	0.03	0.06	0.03	0.04	0.04
K_2O	4.89	4.80	4.92	4.89	4.93	4.95
Na_2O	3.92	3.92	3.78	3.64	3.75	3.74
P_2O_5	0.01	0.01	0.01	0.01	0.01	0.01
LOI (%)	0.33	0.31	0.22	1.93	0.33	0.25
Total	99.74	98.73	99.11	97.72	99.26	99.19
La	43.44	43.51	61.85	61.43	61.52	61.26
Ce	93.75	93.75	123.29	123.42	122.83	122.48
Pr	11.57	11.59	14.23	14.15	14.16	14.09
Nd	44.62	45.12	52.33	51.84	52.00	51.47
Sm	12.70	12.76	12.43	12.35	12.34	12.25
Eu	0.08	0.10	0.16	0.16	0.16	0.16
Gd	14.00	14.12	12.56	12.50	12.56	12.47
Tb	2.72	2.73	2.30	2.28	2.29	2.29
Dy	17.26	17.50	14.47	14.29	14.40	14.37
Ho	3.52	3.51	2.90	2.90	2.89	2.87
Er	9.58	9.68	7.79	7.79	7.80	7.71
Tm	1.40	1.42	1.14	1.12	1.13	1.12
Yb	8.54	8.59	6.77	6.79	6.84	6.79
Lu	1.24	1.23	1.00	1.00	1.00	0.99
Ba	21.66	19.68	35.48	41.73	35.33	35.10
Th	34.52	34.65	30.13	30.15	30.20	29.89
Nb	55.14	55.72	42.89	43.00	42.90	42.57
Y	94.62	95.25	76.83	76.67	77.00	76.40
Hf	8.50	8.54	7.80	7.77	7.68	7.69
Ta	4.35	4.40	3.34	3.35	3.33	3.30
U	8.36	8.40	6.73	6.69	6.74	6.68
Pb	42.01	41.83	36.07	36.19	35.92	35.75
Rb	286.87	289.84	237.52	236.27	238.20	236.33
Cs	6.61	6.68	5.14	5.09	5.05	5.05
Sr	1.60	2.67	2.51	2.52	2.54	2.46
Sc	1.20	1.26	1.44	1.53	1.50	1.47
Zr	153.39	153.86	159.62	160.08	159.32	159.60
Ni	3.37	3.89	2.37	2.85	2.68	3.35
Cr	0.20	0.30	0.00	1.10	0.60	0.00
V	0.00	0.00	0.00	0.00	0.00	0.00
Ga	26.60	26.70	25.40	24.40	24.90	23.90
Cu	2.50	2.30	4.20	3.00	2.50	1.70
Zn	85.10	85.60	71.90	73.20	69.90	71.80

Major elements are unnormalized (wt. %). Total = the sum of the major element analyses including LOI values. Trace elements are ppm. Major elements and Ni, Cr, V, Ga, Cu, & Zn analyzed by XRF; all other trace elements analyzed by ICP-MS.

Table B.1. Major and trace element analyses of samples (continued)

Sample	OCWY11	OCWY12	OCWY14	CSWY1	CSWY1GE [a]	CSWY1E
SiO_2	76.01	76.98	76.24	71.11	57.25	49.70
Al_2O_3	11.96	12.04	11.92	12.74	14.74	15.53
TiO_2	0.08	0.08	0.08	0.40	1.20	1.95
FeO	1.11	1.11	1.10	3.01	7.84	10.98
MnO	0.02	0.02	0.02	0.05	0.13	0.17
CaO	0.43	0.44	0.43	2.57	8.01	10.81
MgO	0.04	0.03	0.03	1.64	5.69	7.66
K_2O	4.91	4.94	5.51	3.97	1.46	0.36
Na_2O	3.70	3.77	3.33	3.53	3.01	2.66
P_2O_5	0.01	0.01	0.01	0.05	0.19	0.24
LOI (%)	1.12	0.28	0.21	0.07	0.18	-0.31
Total	98.27	99.41	98.67	99.08	99.52	100.06
La	62.02	61.35	61.79	51.99	28.36	13.90
Ce	123.44	121.95	123.08	103.80	55.98	30.74
Pr	14.24	14.09	14.21	12.04	6.75	4.20
Nd	52.44	51.46	52.04	44.56	26.78	18.93
Sm	12.48	12.32	12.38	10.62	6.51	4.97
Eu	0.15	0.15	0.16	0.48	1.22	1.79
Gd	12.57	12.49	12.53	10.83	6.63	5.46
Tb	2.30	2.28	2.30	1.95	1.15	0.90
Dy	14.37	14.23	14.27	12.12	7.02	5.43
Ho	2.89	2.85	2.89	2.42	1.38	1.07
Er	7.86	7.69	7.84	6.57	3.65	2.67
Tm	1.14	1.13	1.14	0.95	0.51	0.37
Yb	6.87	6.79	6.85	5.70	3.08	2.14
Lu	1.00	0.98	1.00	0.84	0.46	0.32
Ba	36.28	35.13	35.06	71.38	138.94	154.16
Th	30.26	29.89	30.06	23.81	8.52	1.18
Nb	43.09	42.40	43.09	35.32	18.50	13.29
Y	77.06	76.00	77.07	64.15	35.25	25.87
Hf	7.73	7.62	7.67	6.75	4.02	3.29
Ta	3.35	3.31	3.33	2.74	1.32	0.81
U	6.71	6.66	6.74	5.29	1.84	0.28
Pb	36.02	35.62	35.74	28.14	10.92	1.88
Rb	238.18	235.71	246.39	185.69	57.22	6.10
Cs	5.06	5.06	5.06	3.90	1.12	0.08
Sr	2.60	2.52	2.33	75.66	251.95	317.80
Sc	1.50	1.47	1.53	8.14	24.43	31.81
Zr	160.63	157.68	159.61	149.59	117.60	124.54
Ni	2.68	3.44	3.28	17.47	52.52	96.76
Cr	0.70	0.90	0.50	26.80	96.30	252.90
V	0.00	0.00	0.20	48.80	180.90	242.40
Ga	24.30	23.40	23.50	22.80	19.60	18.20
Cu	2.50	2.60	1.10	8.80	30.70	52.00
Zn	71.00	70.20	71.20	75.00	93.00	97.90

[a] Analyses of CSWY1GE are taken from a small mafic enclave within sample CSWY1.
Major elements are unnormalized (wt. %). Total = the sum of the major element analyses including LOI values. Trace elements are ppm. Major elements and Ni, Cr, V, Ga, Cu, & Zn analyzed by XRF; all other trace elements analyzed by ICP-MS.

Table B.1. Major and trace element analyses of samples (continued)

Sample	CSWY1ME	CSWY2	CSWY3	CSWY3V	CSWY4
SiO_2	49.04	74.63	76.35	72.55	76.34
Al_2O_3	15.16	12.52	12.14	12.72	12.07
TiO_2	2.10	0.26	0.13	0.34	0.11
FeO	11.70	2.19	1.41	2.71	1.27
MnO	0.18	0.04	0.03	0.05	0.03
CaO	10.88	1.58	0.75	2.11	0.60
MgO	7.49	0.91	0.27	1.31	0.17
K_2O	0.38	4.48	4.79	4.18	4.85
Na_2O	2.75	3.64	3.72	3.56	3.73
P_2O_5	0.25	0.03	0.01	0.04	0.01
LOI (%)	-0.01	0.19	0.26	0.29	0.22
Total	99.94	100.28	99.62	99.58	99.17
La	14.50	57.65	59.85	53.93	60.89
Ce	32.13	114.18	118.77	107.25	120.81
Pr	4.41	13.23	13.79	12.55	14.02
Nd	19.74	48.59	50.44	46.15	51.24
Sm	5.15	11.51	12.14	11.11	12.20
Eu	1.88	0.36	0.21	0.41	0.17
Gd	5.71	11.54	12.31	11.23	12.46
Tb	0.95	2.09	2.23	2.04	2.26
Dy	5.67	13.03	13.99	12.62	14.23
Ho	1.10	2.60	2.84	2.53	2.86
Er	2.83	7.03	7.63	6.82	7.80
Tm	0.39	1.01	1.09	0.98	1.12
Yb	2.29	6.08	6.72	5.94	6.70
Lu	0.34	0.89	0.97	0.87	0.99
Ba	154.86	68.79	39.63	65.43	36.48
Th	1.19	26.28	29.06	25.13	29.63
Nb	13.85	37.20	40.89	36.78	41.86
Y	27.12	67.78	74.24	66.27	75.59
Hf	3.44	7.15	7.50	6.92	7.61
Ta	0.86	2.92	3.25	2.87	3.30
U	0.29	5.81	6.45	5.56	6.56
Pb	2.13	31.15	34.58	29.92	35.28
Rb	6.07	200.71	228.05	195.65	234.26
Cs	0.08	4.25	4.90	4.18	5.01
Sr	313.91	41.98	13.35	60.37	8.26
Sc	32.79	4.56	2.33	6.52	1.94
Zr	129.90	156.11	157.63	152.35	160.41
Ni	89.98	10.00	4.78	15.07	4.55
Cr	234.80	15.20	4.50	21.80	1.20
V	263.70	26.00	7.60	40.00	2.70
Ga	19.70	23.50	24.00	24.40	22.60
Cu	61.00	6.50	4.90	10.10	2.50
Zn	104.90	75.00	72.70	75.60	73.50

Major elements are unnormalized (wt. %). Total = the sum of the major element analyses including LOI values. Trace elements are ppm. Major elements and Ni, Cr, V, Ga, Cu, & Zn analyzed by XRF; all other trace elements analyzed by ICP-MS.

Table B.2. XRF instrumental precision for major and trace element analyses

Unnormalized Major Element Results (wt.%)		
	Result	Standard Deviation
SiO_2	68.45	0.18
Al_2O_3	15.35	0.11
TiO_2	0.667	0.004
FeO	3.86	0.04
MnO	0.038	0.001
CaO	2.02	0.01
MgO	1.10	0.10
K_2O	5.56	0.09
Na_2O	2.91	0.05
P_2O_5	0.287	0.003
Total	100.24	0.36
Normalized Major Element Results (wt.%)		
SiO_2	68.29	0.09
Al_2O_3	15.31	0.07
TiO_2	0.666	0.004
FeO	3.85	0.01
MnO	0.037	0.001
CaO	2.01	0.01
MgO	1.09	0.10
K_2O	5.55	0.07
Na_2O	2.90	0.05
P_2O_5	0.286	0.002
Trace Element Results (ppm)		
Ni	16	1
Cr	16	2
Sc	4	2
V	54	5
Ba	1294	9
Rb	253	1
Sr	233	1
Zr	527	1
Y	30	1
Nb	27.4	0.5
Ga	23	1
Cu	31	2
Zn	103	2
Pb	53	2
La	184	10
Ce	399	10
Th	106	2

Precision measured over an eight month period on Washington State University standard GSP-1 (Johnson *et al.*, 1999).

Table B.3. ICP-MS instrumental precision for trace element analyses

	± 2 σ (ppm)
La	0.98
Ce	1.24
Nd	0.96
Sm	0.3
Eu	0.08
Gd	0.16
Tb	0.02
Dy	0.2
Ho	0.04
Er	0.12
Tm	0.02
Yb	0.06
Lu	0.02
Ba	25.36
Th	0.98
Y	0.58
Hf	0.14
Ta	0.04
U	0.22
Pb	0.58
Rb	1.34
Cs	0.06
Sr	n.d
Sc	n.d
Zr	n.d

Precision measured over a four month period on Washington State University standard BCS-P (Knaack *et al.*, 1994).
No data (n.d.) were reported for Sr, Sc, and Zr.

APPENDIX C

ELECTRON MICROPROBE POINT ANALYSES

OF GIBBON RIVER RHYOLITE SAMPLES

Table C.1. Electron Microprobe Core and Rim Point Analyses of Sanidine from Gibbon River Sample GRWY1

Analysis No.	SiO_2	FeO	K_2O	Na_2O	Al_2O_3	TiO_2	CaO	MgO	Total	An	Ab	Or
S1C1	64.578	0.118	9.511	4.627	18.928	0.000	0.383	0.000	98.145	1.91	41.70	56.39
S1C2	64.998	0.076	8.570	5.259	19.356	0.000	0.501	0.000	98.760	2.48	47.06	50.46
S1C3	64.775	0.130	9.166	4.646	19.208	0.013	0.426	0.000	98.364	2.16	42.58	55.27
S1C4	64.997	0.137	9.479	4.760	18.807	0.000	0.435	0.000	98.615	2.14	42.36	55.50
S2C1	65.083	0.147	9.122	4.984	18.767	0.022	0.488	0.000	98.613	2.40	44.28	53.32
S2C2	65.863	0.091	8.809	4.921	19.134	0.000	0.430	0.000	99.248	2.17	44.92	52.91
S2C3	66.143	0.119	9.157	5.262	19.290	0.019	0.455	0.000	100.445	2.18	45.60	52.22
S2C4	65.357	0.131	8.313	5.322	18.569	0.000	0.566	0.000	98.258	2.82	47.93	49.26
S3C2	64.618	0.102	8.970	4.923	19.323	0.000	0.546	0.000	98.482	2.71	44.25	53.04
S4C1	65.541	0.066	8.914	5.008	19.148	0.000	0.512	0.000	99.189	2.54	44.89	52.57
S5C1	65.032	0.115	8.966	5.045	19.423	0.000	0.483	0.000	99.064	2.38	45.00	52.62
S5C2	66.029	0.126	8.840	5.070	19.429	0.017	0.509	0.000	100.020	2.52	45.40	52.08
S5C3	64.693	0.085	8.900	5.044	19.071	0.000	0.527	0.000	98.320	2.60	45.07	52.33
S5C4	65.360	0.083	8.442	5.309	18.839	0.003	0.532	0.000	98.568	2.63	47.58	49.78
S6C1	64.777	0.102	9.779	4.634	19.037	0.000	0.383	0.000	98.712	1.88	41.08	57.04
S6C2	65.487	0.094	8.885	5.192	18.898	0.000	0.515	0.000	99.071	2.51	45.86	51.63
S6C3	65.570	0.135	9.074	4.929	19.227	0.006	0.495	0.000	99.436	2.45	44.12	53.44
Core Ave.	65.229	0.109	8.994	4.996	19.086	0.005	0.482	0.000		2.38	44.69	52.93
S1R1	65.214	0.137	9.013	4.614	19.255	0.000	0.459	0.000	98.692	2.35	42.73	54.92
S2R1	77.608	0.163	5.317	3.123	11.554	0.027	0.274	0.000	98.066	2.24	46.11	51.65
S4R1	65.503	0.111	7.322	5.815	19.602	0.008	0.678	0.000	99.039	3.40	52.83	43.77
S6R1	65.052	0.126	9.135	5.027	18.618	0.027	0.455	0.000	98.440	2.23	44.53	53.24
Rim Ave.	68.344	0.134	7.697	4.645	17.257	0.016	0.467	0.000		2.55	46.55	50.90

Table C.2. Electron Microprobe Core and Rim Point Analyses of Sanidine from Gibbon River Sample GRWY6

Analysis No.	SiO_2	FeO	K_2O	Na_2O	Al_2O_3	TiO_2	CaO	MgO	Total	An	Ab	Or
S1C1	65.680	0.136	6.599	6.175	19.837	0.000	0.873	0.000	99.300	4.39	56.14	39.47
S1C2	65.083	0.148	6.484	6.395	19.716	0.021	1.040	0.000	98.887	5.11	56.92	37.97
S1C3	65.245	0.184	6.434	6.239	19.733	0.048	0.987	0.000	98.870	4.95	56.63	38.42
S1C4	64.908	0.173	6.899	5.822	19.583	0.019	0.844	0.000	98.248	4.31	53.77	41.92
S2C1	66.015	0.146	7.192	5.462	19.408	0.000	0.677	0.000	98.900	3.54	51.68	44.78
S2C2	65.834	0.167	7.610	5.885	19.302	0.000	0.610	0.000	99.408	3.00	52.41	44.59
S2C3	65.951	0.072	7.206	6.056	19.417	0.000	0.697	0.000	99.399	3.44	54.16	42.40
S2C4	66.089	0.143	7.120	5.791	19.403	0.000	0.628	0.000	99.174	3.21	53.51	43.29
S3C1	64.563	0.144	6.621	6.100	19.641	0.016	0.960	0.000	98.045	4.83	55.52	39.65
S3C2	65.068	0.157	6.651	6.224	19.726	0.028	0.885	0.000	98.739	4.41	56.13	39.46
S3C3	65.095	0.163	6.935	6.114	19.551	0.008	0.848	0.000	98.714	4.20	54.86	40.94
S4C1	66.247	0.129	7.575	5.675	19.415	0.001	0.641	0.000	99.683	3.22	51.53	45.26
S4C2	66.472	0.116	7.475	5.894	19.453	0.000	0.644	0.000	100.054	3.19	52.78	44.04
S4C3	66.612	0.111	7.566	5.593	19.333	0.000	0.601	0.000	99.816	3.05	51.30	45.66
S4C4	66.047	0.119	7.491	5.759	19.158	0.020	0.640	0.000	99.234	3.20	52.16	44.64
Core Ave.	65.661	0.141	7.057	5.946	19.512	0.011	0.772	0.000		3.87	53.96	42.17
S1R1	65.198	0.174	6.018	6.498	19.663	0.024	1.090	0.000	98.665	5.45	58.75	35.80
S1R2	65.135	0.221	7.411	5.729	19.819	0.005	0.862	0.000	99.182	4.30	51.70	44.00
S2R1	65.938	0.111	7.486	5.778	19.304	0.003	0.526	0.000	99.146	2.64	52.56	44.80
S2R2	66.056	0.135	7.578	5.819	19.197	0.014	0.553	0.000	99.352	2.75	52.37	44.88
S3R1	65.013	0.192	7.147	5.975	19.714	0.017	0.792	0.000	98.850	3.94	53.76	42.31
S3R2	65.119	0.170	6.634	6.164	19.596	0.020	0.844	0.000	98.547	4.24	56.06	39.70
S4R1	65.785	0.078	7.416	6.157	18.903	0.001	0.639	0.000	98.979	3.10	54.06	42.84
S4R2	65.321	0.127	7.133	5.858	19.099	0.001	0.688	0.000	98.227	3.48	53.59	42.93
Rim Ave.	65.446	0.151	7.103	5.997	19.412	0.011	0.749	0.000		3.74	54.11	42.16

Table C.3. Electron Microprobe Core Point Analyses of Sanidine from Gibbon River Sample GRWY7P

Analysis No.	SiO_2	FeO	K_2O	Na_2O	Al_2O_3	TiO_2	CaO	MgO	Total	An	Ab	Or
S1C1	64.160	0.134	9.340	4.426	19.512	0.039	0.521	0.000	98.132	2.65	40.76	56.59
S1C2	65.431	0.168	9.589	4.508	19.655	0.008	0.504	0.000	99.863	2.51	40.63	56.86
S1C3	64.779	0.087	9.485	4.452	19.253	0.041	0.418	0.000	98.515	2.11	40.76	57.13
S1C4	64.202	0.125	9.419	4.663	19.535	0.053	0.494	0.000	98.491	2.45	41.88	55.66
S2C1	64.232	0.145	9.499	4.471	19.379	0.019	0.482	0.000	98.227	2.42	40.69	56.88
S2C2	64.698	0.135	9.657	4.397	19.270	0.000	0.402	0.000	98.559	2.02	40.07	57.90
S2C3	64.534	0.097	9.492	4.505	19.495	0.043	0.448	0.000	98.614	2.25	40.96	56.79
S2C4	64.203	0.099	9.567	4.500	19.342	0.000	0.429	0.000	98.140	2.15	40.79	57.06
S3C1	64.784	0.093	9.759	4.442	19.214	0.008	0.447	0.000	98.747	2.22	39.98	57.79
S3C2	65.803	0.093	9.827	4.591	18.814	0.016	0.410	0.000	99.554	2.01	40.69	57.30
S3C3	65.336	0.150	9.743	4.523	18.777	0.000	0.407	0.000	98.936	2.02	40.53	57.45
S3C4	65.773	0.080	9.751	4.683	19.343	0.000	0.414	0.000	100.044	2.02	41.34	56.64
S4C1	63.902	0.130	9.682	4.536	19.401	0.006	0.415	0.000	98.072	2.06	40.73	57.21
S4C2	64.790	0.110	9.784	4.281	19.216	0.020	0.406	0.000	98.607	2.05	39.12	58.83
S4C3	64.709	0.116	9.784	4.329	19.194	0.022	0.403	0.000	98.557	2.03	39.39	58.58
S4C4	64.977	0.133	9.591	4.393	19.148	0.000	0.394	0.000	98.636	1.99	40.22	57.78
S5C1	64.354	0.124	9.643	4.566	19.088	0.009	0.408	0.000	98.192	2.02	41.00	56.97
S5C2	64.962	0.115	9.427	4.670	19.104	0.000	0.466	0.000	98.744	2.31	41.96	55.73
S5C3	65.269	0.085	9.802	4.529	18.989	0.000	0.399	0.000	99.073	1.97	40.44	57.59
S5C4	65.686	0.101	9.775	4.544	19.251	0.011	0.441	0.000	99.809	2.17	40.50	57.33
S6C1	64.670	0.126	9.660	4.391	19.109	0.018	0.456	0.000	98.430	2.29	39.92	57.79
S6C2	66.362	0.144	9.877	4.726	19.514	0.000	0.469	0.000	101.092	2.26	41.15	56.59
S6C3	65.271	0.111	9.652	4.618	19.237	0.000	0.442	0.000	99.331	2.18	41.18	56.64
S6C4	65.219	0.095	9.651	4.536	19.058	0.005	0.439	0.000	99.003	2.18	40.76	57.06
Core Ave.	64.921	0.117	9.644	4.512	19.246	0.013	0.438	0.000		2.18	40.65	57.17

Table C.4. Electron Microprobe Rim Point Analyses of Sanidine from Gibbon River Sample GRWY7P

Analysis No.	SiO_2	FeO	K_2O	Na_2O	Al_2O_3	TiO_2	CaO	MgO	Total	An	Ab	Or
S1R1	64.470	0.101	9.523	4.412	19.569	0.006	0.454	0.000	98.535	2.30	40.37	57.33
S1R2	65.321	0.099	9.629	4.472	19.224	0.033	0.433	0.000	99.211	2.17	40.48	57.35
S2R1	64.533	0.165	9.430	4.629	19.377	0.042	0.476	0.000	98.652	2.37	41.72	55.91
S3R1	65.569	0.052	9.920	4.535	19.012	0.000	0.411	0.000	99.499	2.01	40.17	57.82
S3R2	66.029	0.115	9.923	4.622	19.528	0.020	0.441	0.000	100.678	2.14	40.56	57.30
S4R1	64.710	0.085	9.758	4.522	19.071	0.017	0.459	0.000	98.622	2.27	40.39	57.35
S5R1	66.069	0.099	9.900	4.391	19.437	0.038	0.406	0.000	100.340	2.02	39.45	58.53
S5R2	65.270	0.082	9.334	4.525	19.100	0.000	0.433	0.000	98.744	2.19	41.49	56.31
S6R1	65.438	0.170	9.668	4.516	18.998	0.001	0.426	0.000	99.217	2.12	40.64	57.24
Rim Ave.	65.268	0.108	9.676	4.514	19.257	0.017	0.438	0.000		2.18	40.59	57.24

Table C.5. Electron Microprobe Core and Rim Point Analyses of Plagioclase from Gibbon River Sample GRWY1

Analysis No.	SiO_2	FeO	K_2O	Na_2O	Al_2O_3	TiO_2	CaO	MgO	Total	An	Ab	Or
P1C1	61.775	0.190	1.196	7.597	23.015	0.000	5.027	0.000	98.800	24.89	68.06	7.05
P1C2	62.058	0.194	1.275	7.928	23.456	0.008	4.868	0.000	99.787	23.48	69.20	7.32
P1C3	60.836	0.207	1.203	7.634	23.515	0.008	4.805	0.010	98.218	23.96	68.89	7.14
P1C4	61.520	0.168	1.119	7.886	23.423	0.012	5.136	0.002	99.266	24.76	68.81	6.42
Core Ave.	61.547	0.190	1.198	7.761	23.352	0.007	4.959	0.003		24.27	68.74	6.98
Rim Analy.:												
P1R1	61.892	0.179	1.230	7.714	23.694	0.002	5.026	0.000	99.737	24.58	68.26	7.16

Table C.6. Electron Microprobe Core and Rim Point Analyses of Plagioclase from Gibbon River Sample GRWY7P

Analysis No.	SiO_2	FeO	K_2O	Na_2O	Al_2O_3	TiO_2	CaO	MgO	Total	An	Ab	Or
P1C1	62.397	0.200	1.142	8.034	23.515	0.000	4.957	0.004	100.249	23.77	69.71	6.52
P1C2	63.706	0.218	1.286	8.121	23.796	0.000	4.728	0.011	101.866	22.56	70.13	7.31
Core Ave.	63.052	0.209	1.214	8.078	23.656	0.000	4.843	0.008		23.17	69.92	6.91
Rim Analy.:												
P1R1	63.312	0.201	1.583	7.863	22.666	0.000	3.819	0.000	99.444	19.16	71.38	9.46

Table C.7. Electron Microprobe Analyses of Pyroxene from Gibbon River Sample GRWY1

Analysis No.	SiO_2	MnO	CaO	Na_2O	Al_2O_3	FeO	TiO_2	MgO	Total	Wo	En	Fs	Ac
Pyrx1	49.722	0.618	18.586	0.260	0.532	19.739	0.135	8.675	98.267	39.57	25.70	33.73	1.00

Table C.8. Electron Microprobe Analyses of Pyroxene from Gibbon River Sample GRWY6

Analysis No.	SiO_2	MnO	CaO	Na_2O	Al_2O_3	FeO	TiO_2	MgO	Total	Wo	En	Fs	Ac
Ol5	47.447	1.626	1.474	0.014	0.581	39.422	0.339	8.949	99.852	3.22	27.17	69.56	0.06
Ol6	48.606	0.970	18.798	0.293	0.759	25.059	0.360	4.793	99.638	40.66	14.43	43.77	1.15
Pyrx1	46.769	1.161	18.629	0.340	0.545	30.134	0.316	1.561	99.455	40.83	4.76	53.06	1.35
Average [a]	47.688	1.066	18.714	0.317	0.652	27.597	0.338	3.177		40.74	9.59	48.42	1.25

[a] Average is of analyses Ol6 and Pyrx1.

Table C.9. Electron Microprobe Analyses of Pyroxene from Gibbon River Sample GRWY7P

Analysis No.	SiO_2	MnO	CaO	Na_2O	Al_2O_3	FeO	TiO_2	MgO	Total	Wo	En	Fs	Ac
Pyrx1	49.395	0.704	18.542	0.258	0.499	22.270	0.139	7.717	99.524	38.98	22.58	37.46	0.98
Pyrx2	49.549	0.706	18.762	0.234	0.518	20.838	0.171	7.836	98.614	40.04	23.27	35.78	0.90
Pyrx3	49.354	0.647	18.848	0.296	0.520	20.904	0.159	8.394	99.122	39.46	24.46	34.96	1.12
Pyrx4	49.213	0.633	18.526	0.284	0.557	20.187	0.150	8.655	98.205	39.22	25.50	34.20	1.09
Average	49.378	0.673	18.670	0.268	0.524	21.050	0.155	8.151		39.43	23.95	35.60	1.02

Table C.10. Electron Microprobe Analyses of Amphibole from Gibbon River Sample GRWY6

Analysis No.	SiO_2	MnO	CaO	Na_2O	Al_2O_3	FeO	TiO_2	MgO	Total
Amphib1	49.297	1.104	18.265	0.322	0.538	27.673	0.219	4.169	101.587
Amphib2	49.092	1.006	18.393	0.376	0.576	27.612	0.239	4.082	101.376
Amphib3	49.279	1.018	18.447	0.296	0.545	27.008	0.218	4.197	101.008
Amphib4	49.324	1.035	18.339	0.306	0.544	27.276	0.226	4.183	101.233
Amphib5	48.391	1.019	18.766	0.319	0.501	30.633	0.366	1.864	101.859
Amphib6	48.282	1.149	18.544	0.298	0.544	31.253	0.355	1.338	101.763
Amphib7	49.159	1.043	18.453	0.368	0.489	28.221	0.222	3.393	101.348
Amphib8	47.798	1.040	18.548	0.342	0.543	29.934	0.322	1.689	100.216
Amphib9	47.984	1.040	17.998	0.301	0.602	30.231	0.371	1.375	99.902
Amphib10	47.648	1.031	18.428	0.370	0.557	30.531	0.387	1.313	100.265
Average	48.625	1.049	18.418	0.330	0.544	29.037	0.293	2.760	

Table C.11. Electron Microprobe Analyses of Amphibole from Gibbon River Sample GRWY7P

Analysis No.	SiO_2	MnO	CaO	Na_2O	Al_2O_3	FeO	TiO_2	MgO	Total
Amphib1	50.979	0.547	18.829	0.328	0.648	19.079	0.177	9.876	100.463
Amphib2	50.505	0.596	18.931	0.323	0.640	21.716	0.158	8.234	101.103
Amphib3	50.642	0.670	18.866	0.270	0.559	21.842	0.139	8.201	101.189
Amphib4	51.153	0.550	19.293	0.319	0.645	18.849	0.127	9.056	99.992
Amphib5	50.882	0.634	19.005	0.274	0.585	21.277	0.154	8.325	101.136
Amphib6	51.547	0.601	19.255	0.326	0.681	19.332	0.194	9.916	101.852
Amphib7	50.779	0.654	18.798	0.278	0.593	22.844	0.158	7.576	101.680
Average	50.927	0.607	18.997	0.303	0.622	20.706	0.158	8.741	

Table C.12. Electron Microprobe Analyses of Olivine from Gibbon River Sample GRWY1

Analysis No.	SiO_2	MnO	CaO	Na_2O	Al_2O_3	FeO	TiO_2	MgO	Total	Fo	Fa	Tp
Ol1	28.106	1.924	0.000	0.006	0.001	68.708	0.000	1.566	100.311	3.80	93.55	2.65
Ol2	27.702	1.782	0.000	0.018	0.000	69.688	0.000	0.737	99.927	1.80	95.72	2.48
Ol3	28.454	2.186	0.051	0.000	0.021	68.103	0.000	1.421	100.236	3.48	93.48	3.04
Ol4	28.318	2.433	0.103	0.019	0.000	69.141	0.030	1.419	101.463	3.41	93.26	3.32
Ol5	27.983	2.345	0.000	0.000	0.000	68.849	0.023	1.379	100.579	3.34	93.44	3.22
Ol6	28.297	2.079	0.000	0.004	0.018	69.024	0.005	0.960	100.387	2.35	94.76	2.89
Ol7	27.953	2.173	0.007	0.009	0.014	69.095	0.023	1.088	100.362	2.65	94.35	3.01
Ol8	28.525	1.825	0.006	0.000	0.021	70.526	0.000	0.877	101.780	2.11	95.39	2.50
Ol9	28.541	1.873	0.000	0.002	0.000	69.362	0.003	1.317	101.098	3.19	94.23	2.58
Average	28.209	2.069	0.019	0.006	0.008	69.166	0.009	1.196		2.90	94.24	2.85

Table C.13. Electron Microprobe Analyses of Olivine from Gibbon River Sample GRWY6

Analysis No.	SiO_2	MnO	CaO	Na_2O	Al_2O_3	FeO	TiO_2	MgO	Total	Fo	Fa	Tp
Ol1	28.676	2.662	0.376	0.049	0.000	68.208	0.046	1.106	101.123	2.71	93.59	3.70
Ol3	28.569	2.650	0.345	0.038	0.000	68.419	0.031	1.081	101.133	2.64	93.69	3.68
Ol4	28.149	2.576	0.353	0.049	0.016	66.387	0.043	1.042	98.615	2.62	93.70	3.68
Average	28.465	2.629	0.358	0.045	0.005	67.671	0.040	1.076		2.66	93.66	3.69

Table C.14. Electron Microprobe Analyses of Fe-Oxide from Gibbon River Sample GRWY1

Analysis No.	SiO_2	MnO	CaO	Na_2O	Al_2O_3	FeO	TiO_2	MgO	Total
FeR4	0.125	0.580	0.000	0.000	1.134	79.696	16.420	0.190	98.145
FeR8	0.129	0.585	0.000	0.004	1.259	79.414	17.214	0.185	98.790
FeR11	0.146	0.426	0.000	0.017	1.077	83.234	13.784	0.113	98.797
Average	0.133	0.530	0.000	0.007	1.157	80.781	15.806	0.163	

Table C.15. Electron Microprobe Analyses of Fe-Oxide from Gibbon River Sample GRWY6

Analysis No.	SiO_2	MnO	CaO	Na_2O	Al_2O_3	FeO	TiO_2	MgO	Total
FeR1	0.149	0.963	0.000	0.000	0.860	75.335	21.134	0.087	98.528
FeR2	0.114	0.978	0.000	0.036	0.872	75.526	21.524	0.084	99.134
FeR4	0.032	1.111	0.000	0.014	0.057	46.215	50.860	0.070	98.359
Average [a]	0.132	0.971	0.000	0.018	0.866	75.431	21.329	0.086	

[a] Average is of analyses FeR1 and FeR2.

Table C.16. Electron Microprobe Analyses of Fe-Oxide from Gibbon River Sample GRWY7P

Analysis No.	SiO_2	MnO	CaO	Na_2O	Al_2O_3	FeO	TiO_2	MgO	Total
FeR1	0.092	0.551	0.000	0.000	1.178	80.165	16.293	0.377	98.656
FeR3	0.087	0.482	0.000	0.013	1.120	79.485	16.583	0.356	98.126
FeR5	0.097	0.454	0.000	0.000	1.130	79.866	17.160	0.415	99.122
FeR6	0.104	0.270	0.000	0.000	1.245	85.683	10.898	0.172	98.372
FeR8	0.143	0.563	0.000	0.014	1.154	80.036	16.604	0.431	98.945
FeR9	0.097	0.575	0.000	0.039	1.135	79.221	17.026	0.396	98.489
FeR10	0.135	0.476	0.000	0.021	1.156	79.174	16.925	0.409	98.296
Average	0.108	0.482	0.000	0.012	1.160	80.519	15.927	0.365	

APPENDIX D

ELECTRON MICROPROBE TRAVERSE ANALYSES

OF GIBBON RIVER RHYOLITE SAMPLES

Table D.1. Electron Microprobe Traverse Analyses of Sanidine S1 from Gibbon River Sample GRWY1

Length (μm)	SiO_2	BaO	K_2O	Na_2O	Al_2O_3	SrO	CaO	MgO	Total	An	Ab	Or
30	65.419	0.377	9.373	5.656	18.982	0.000	0.496	0.000	100.435	2.27	46.75	50.98
40	65.085	0.443	9.362	5.526	19.501	0.000	0.472	0.000	100.521	2.18	46.26	51.56
50	65.578	0.396	9.557	5.775	19.483	0.000	0.488	0.000	101.409	2.19	46.83	50.99
60	64.954	0.426	9.490	5.831	19.784	0.000	0.430	0.000	101.047	1.93	47.36	50.71
90	65.478	0.427	9.489	5.602	19.674	0.000	0.463	0.000	101.265	2.11	46.29	51.59
100	65.061	0.490	9.699	5.659	19.550	0.000	0.477	0.000	101.068	2.14	45.99	51.87
140	65.324	0.541	9.733	5.644	19.595	0.000	0.498	0.000	101.467	2.23	45.80	51.97
170	65.279	0.564	9.548	5.744	19.283	0.000	0.438	0.000	100.988	1.97	46.82	51.21
200	64.052	0.567	9.298	5.607	20.971	0.000	0.561	0.008	101.196	2.58	46.59	50.83
210	65.402	0.617	9.561	5.846	19.162	0.000	0.444	0.000	101.164	1.98	47.21	50.81
300	64.002	0.567	9.644	5.700	19.342	0.000	0.488	0.000	99.875	2.19	46.28	51.53
340	63.031	0.585	9.470	5.300	19.547	0.000	0.453	0.000	98.518	2.12	44.99	52.89
350	65.009	0.535	9.221	5.500	19.144	0.000	0.415	0.000	99.956	1.94	46.62	51.43
370	64.406	0.557	9.749	5.546	18.323	0.000	0.460	0.000	99.173	2.08	45.40	52.51
410	65.528	0.539	9.780	5.633	19.689	0.000	0.448	0.000	101.749	2.01	45.74	52.25
420	65.700	0.553	9.786	5.671	19.434	0.000	0.463	0.000	101.739	2.07	45.86	52.07
460	65.510	0.507	9.758	5.551	19.618	0.000	0.394	0.000	101.470	1.79	45.54	52.67
480	64.886	0.472	9.462	5.279	20.230	0.000	0.474	0.000	100.935	2.23	44.86	52.91
500	65.369	0.504	9.485	5.728	19.619	0.000	0.396	0.000	101.233	1.80	47.00	51.21
510	65.229	0.489	9.632	5.562	19.506	0.000	0.407	0.000	100.957	1.86	45.87	52.27
520	65.023	0.456	9.576	5.692	19.512	0.000	0.391	0.000	100.782	1.77	46.62	51.61
530	65.645	0.490	9.801	5.829	19.649	0.000	0.432	0.000	101.978	1.91	46.57	51.52
540	65.763	0.453	9.756	5.701	19.721	0.000	0.428	0.000	101.954	1.91	46.14	51.95
580	62.829	0.449	9.285	5.286	21.292	0.000	0.499	0.000	99.772	2.36	45.29	52.35
680	65.387	0.380	9.522	5.409	19.497	0.000	0.440	0.000	100.767	2.04	45.39	52.57
690	64.935	0.379	9.073	5.389	19.513	0.000	0.510	0.000	99.931	2.42	46.30	51.28
740	66.057	0.307	8.739	6.052	19.422	0.000	0.555	0.000	101.264	2.53	49.98	47.49
750	66.153	0.310	9.222	5.848	19.422	0.000	0.555	0.000	101.642	2.51	47.85	49.64
760	65.625	0.290	8.663	5.852	19.350	0.000	0.550	0.000	100.462	2.56	49.36	48.08
770	65.550	0.314	8.646	6.088	19.738	0.000	0.608	0.004	101.080	2.77	50.26	46.96

For the analyses, FeO was set at 0.122 and TiO_2 was set at 0.01.

Table D.1. Electron Microprobe Traverse Analyses of Sanidine S1 from Gibbon River Sample GRWY1 (continued)

Length (μm)	SiO_2	BaO	K_2O	Na_2O	Al_2O_3	SrO	CaO	MgO	Total	An	Ab	Or
790	65.153	0.322	8.654	6.554	19.288	0.000	0.541	0.000	100.644	2.38	52.24	45.38
840	72.256	0.301	6.216	5.977	16.059	0.000	0.656	0.000	101.597	3.48	57.31	39.22
850	80.343	0.000	3.385	4.375	11.501	0.000	0.634	0.000	100.370	5.04	62.93	32.03
860	75.017	0.000	4.881	4.520	13.131	0.000	0.653	0.000	98.334	4.46	55.86	39.69
880	76.364	0.000	4.268	4.507	12.769	0.000	0.612	0.000	98.652	4.42	58.89	36.69
890	78.772	0.000	4.373	4.320	11.991	0.000	0.551	0.000	100.139	4.06	57.59	38.35
930	77.781	0.000	5.524	3.410	11.708	0.000	0.291	0.000	98.846	2.23	47.33	50.44
970	77.509	0.000	5.902	3.738	12.301	0.000	0.243	0.000	99.825	1.73	48.20	50.07
980	72.476	0.000	6.851	4.548	14.988	0.000	0.373	0.000	99.368	2.23	49.10	48.67
990	77.562	0.000	5.676	3.416	11.621	0.000	0.182	0.000	98.589	1.39	47.11	51.50
1010	76.557	0.000	6.023	3.819	12.870	0.000	0.234	0.000	99.635	1.63	48.27	50.09

For the analyses, FeO was set at 0.122 and TiO_2 was set at 0.01.

Table D.2. Electron Microprobe Traverse Analyses of Sanidine S2 from Gibbon River Sample GRWY1

Length (μm)	SiO_2	BaO	K_2O	Na_2O	Al_2O_3	SrO	CaO	MgO	Total	An	Ab	Or
0	64.229	0.036	8.740	5.483	19.929	0.000	0.717	0.006	99.272	3.41	47.15	49.45
70	65.962	0.068	8.907	6.028	19.260	0.000	0.518	0.000	100.875	2.35	49.51	48.14
160	65.994	0.090	9.517	6.083	19.524	0.000	0.486	0.000	101.826	2.13	48.23	49.64
170	65.189	0.092	9.509	5.762	19.556	0.000	0.531	0.000	100.771	2.38	46.80	50.82
250	65.933	0.092	9.265	5.880	19.777	0.000	0.467	0.000	101.546	2.11	48.06	49.83
260	66.107	0.042	9.632	6.005	19.478	0.000	0.512	0.000	101.908	2.24	47.56	50.20
270	66.109	0.021	9.580	5.845	19.421	0.000	0.510	0.000	101.618	2.27	47.02	50.71
440	66.448	0.053	9.399	5.783	19.600	0.000	0.452	0.000	101.867	2.04	47.34	50.62
470	65.475	0.053	9.342	5.010	19.519	0.000	0.438	0.000	99.969	2.12	43.95	53.92
500	64.582	0.056	9.567	5.888	19.735	0.000	0.468	0.000	100.428	2.08	47.33	50.60
700	77.062	0.000	5.898	4.231	12.631	0.000	0.381	0.000	100.335	2.53	50.84	46.63
710	81.225	0.000	5.031	3.503	11.373	0.000	0.354	0.000	101.618	2.79	49.98	47.23
720	78.573	0.000	5.597	4.065	12.406	0.000	0.444	0.000	101.217	3.07	50.86	46.07
730	74.901	0.000	3.918	5.577	13.988	0.000	0.863	0.000	99.379	5.52	64.61	29.87
740	76.914	0.000	5.587	3.960	12.590	0.000	0.385	0.000	99.568	2.71	50.45	46.84
750	77.129	0.000	6.129	4.085	12.896	0.000	0.304	0.000	100.675	2.03	49.30	48.67
760	76.902	0.000	6.262	4.107	12.584	0.000	0.275	0.000	100.262	1.81	49.01	49.17
770	77.003	0.000	5.656	3.662	12.087	0.000	0.287	0.015	98.842	2.10	48.55	49.34
800	78.191	0.000	5.435	3.942	12.559	0.000	0.441	0.000	100.700	3.14	50.79	46.07
810	77.473	0.000	5.533	3.674	11.839	0.000	0.289	0.000	98.940	2.14	49.16	48.71
820	73.893	0.000	6.394	4.181	13.295	0.000	0.287	0.000	98.182	1.86	48.92	49.22
840	78.812	0.000	4.893	3.550	10.967	0.000	0.314	0.000	98.668	2.50	51.13	46.37
850	75.692	0.000	6.428	4.043	13.976	0.000	0.360	0.000	100.631	2.35	47.73	49.93
860	78.005	0.000	5.550	3.820	11.928	0.000	0.292	0.000	99.727	2.11	50.05	47.84
870	76.590	0.000	6.103	4.170	12.818	0.000	0.316	0.000	100.129	2.09	49.88	48.03
880	74.866	0.000	6.530	4.928	14.530	0.000	0.393	0.000	101.379	2.30	52.19	45.51
890	76.653	0.000	6.184	3.722	12.751	0.000	0.316	0.010	99.768	2.19	46.73	51.08
895	77.402	0.000	6.149	3.927	12.962	0.000	0.335	0.005	100.912	2.27	48.14	49.59

For the analyses, FeO was set at 0.122 and TiO_2 was set at 0.01.

Table D.3. Electron Microprobe Traverse Analyses of Sanidine S4 from Gibbon River Sample GRWY1

Length (μm)	SiO_2	BaO	K_2O	Na_2O	Al_2O_3	SrO	CaO	MgO	Total	An	Ab	Or
0	66.151	0.394	7.477	7.343	19.583	0.000	0.713	0.000	101.793	3.11	58.02	38.87
20	65.795	0.564	8.272	6.418	19.829	0.000	0.637	0.000	101.647	2.88	52.55	44.57
60	65.861	0.506	8.909	5.868	19.125	0.000	0.597	0.000	100.998	2.74	48.66	48.61
70	64.545	0.493	9.352	5.711	19.384	0.000	0.608	0.000	100.225	2.75	46.81	50.44
80	65.707	0.542	8.937	5.437	19.800	0.000	0.593	0.000	101.148	2.81	46.69	50.50
90	65.521	0.540	9.456	5.560	19.650	0.000	0.572	0.000	101.431	2.61	45.96	51.43
100	65.209	0.500	8.859	5.545	19.610	0.000	0.511	0.000	100.366	2.42	47.57	50.01
120	64.992	0.470	9.177	4.914	19.667	0.000	0.589	0.000	99.941	2.89	43.57	53.54
130	64.884	0.473	9.419	5.850	19.618	0.000	0.538	0.000	100.914	2.41	47.39	50.20
140	65.179	0.455	8.836	5.658	19.207	0.000	0.533	0.000	100.000	2.50	48.09	49.41
150	65.266	0.452	9.482	5.762	19.425	0.000	0.493	0.000	101.012	2.22	46.95	50.83
160	65.405	0.440	9.467	5.486	19.441	0.000	0.512	0.000	100.883	2.36	45.72	51.92
170	65.212	0.471	9.358	5.842	19.454	0.000	0.527	0.000	100.996	2.37	47.53	50.10
180	65.562	0.437	9.315	5.660	19.518	0.000	0.447	0.000	101.071	2.05	47.03	50.92
190	65.077	0.440	9.372	5.614	19.601	0.000	0.497	0.000	100.733	2.28	46.57	51.15
200	65.339	0.426	9.549	5.604	19.388	0.000	0.505	0.000	100.943	2.29	46.06	51.64
210	64.701	0.425	9.664	5.600	19.074	0.000	0.515	0.000	100.111	2.32	45.74	51.94
220	65.650	0.442	9.302	5.665	19.622	0.000	0.523	0.000	101.336	2.39	46.92	50.69
230	66.085	0.461	9.332	5.664	19.675	0.000	0.584	0.000	101.933	2.66	46.71	50.63
240	65.597	0.397	9.161	5.795	19.443	0.000	0.491	0.000	101.016	2.24	47.92	49.84
250	65.875	0.455	9.180	6.111	18.666	0.000	0.558	0.000	100.977	2.47	49.05	48.48
260	65.638	0.450	9.094	6.106	19.094	0.000	0.513	0.000	101.027	2.29	49.35	48.36
270	66.003	0.448	8.767	6.303	19.694	0.000	0.546	0.000	101.893	2.44	50.94	46.62
280	65.797	0.447	8.572	6.336	19.668	0.000	0.583	0.000	101.535	2.62	51.52	45.86
290	64.929	0.504	8.435	6.185	19.417	0.000	0.635	0.000	100.237	2.90	51.18	45.92
300	65.800	0.505	7.715	6.928	19.639	0.000	0.695	0.000	101.414	3.10	55.92	40.98

For the analyses, FeO was set at 0.122 and TiO_2 was set at 0.01.

Table D.4. Electron Microprobe Traverse Analyses of Sanidine S5 from Gibbon River Sample GRWY1

Length (μm)	SiO_2	BaO	K_2O	Na_2O	Al_2O_3	SrO	CaO	MgO	Total	An	Ab	Or
0	64.964	1.861	7.403	6.388	19.981	0.000	0.662	0.000	101.391	3.15	54.95	41.90
20	64.630	1.780	7.668	5.674	19.900	0.000	0.624	0.000	100.408	3.12	51.28	45.60
30	64.890	1.723	8.697	6.473	19.439	0.000	0.594	0.000	101.948	2.62	51.69	45.69
50	64.257	1.794	8.786	5.908	19.935	0.000	0.587	0.000	101.399	2.70	49.18	48.12
80	65.236	1.688	9.425	4.828	19.993	0.053	0.539	0.000	101.894	2.63	42.62	54.75
90	65.205	1.885	10.164	4.157	19.970	0.000	0.437	0.000	101.950	2.18	37.50	60.32
100	64.842	1.673	9.686	4.208	19.852	0.000	0.498	0.000	100.891	2.53	38.76	58.70
110	63.473	1.706	9.505	4.295	19.720	0.000	0.477	0.000	99.308	2.44	39.72	57.84
120	65.312	1.643	9.319	4.523	20.116	0.037	0.527	0.000	101.609	2.66	41.32	56.02
130	65.243	1.647	9.311	4.557	19.973	0.042	0.526	0.000	101.431	2.65	41.53	55.83
140	65.327	1.594	9.349	4.305	20.066	0.024	0.500	0.000	101.297	2.57	40.11	57.31
150	65.081	1.549	9.103	4.450	19.819	0.003	0.535	0.000	100.672	2.75	41.45	55.79
160	64.255	1.543	9.456	4.449	19.096	0.000	0.492	0.000	99.423	2.48	40.66	56.86
170	64.759	1.490	9.432	4.292	19.322	0.043	0.461	0.000	99.931	2.37	39.92	57.72
180	64.634	1.443	9.429	4.473	19.703	0.000	0.446	0.000	100.260	2.26	40.95	56.79
210	63.882	1.420	9.340	4.162	19.788	0.062	0.527	0.000	99.313	2.75	39.27	57.98
220	64.556	1.435	9.462	4.540	19.910	0.068	0.525	0.000	100.628	2.62	41.06	56.31
230	65.230	1.322	9.521	4.564	20.155	0.062	0.513	0.000	101.499	2.55	41.07	56.38
240	64.658	1.270	9.485	4.531	19.561	0.000	0.527	0.000	100.164	2.63	40.96	56.41
250	64.355	1.168	9.063	4.614	19.496	0.000	0.490	0.000	99.318	2.50	42.53	54.97
260	64.285	1.165	9.425	4.395	19.105	0.000	0.533	0.000	99.040	2.70	40.36	56.94
270	65.596	0.974	9.619	4.576	19.268	0.000	0.433	0.000	100.598	2.15	41.06	56.79
280	65.217	0.889	9.505	4.488	19.752	0.032	0.441	0.000	100.456	2.22	40.85	56.93
290	65.304	0.853	9.570	4.593	19.557	0.088	0.372	0.000	100.469	1.85	41.40	56.75
300	65.206	0.824	9.440	4.449	19.553	0.066	0.420	0.000	100.090	2.13	40.85	57.02
310	64.680	0.712	9.434	4.328	19.371	0.000	0.415	0.000	99.072	2.13	40.21	57.66
330	65.594	0.677	9.447	4.302	19.671	0.019	0.362	0.000	100.204	1.87	40.14	57.99
340	65.311	0.657	9.499	4.534	19.577	0.003	0.429	0.000	100.142	2.15	41.14	56.71
350	65.143	0.598	9.563	4.620	19.591	0.000	0.419	0.000	100.066	2.08	41.46	56.46
360	64.552	0.579	9.567	4.311	19.327	0.191	0.445	0.000	99.104	2.27	39.73	58.01

For the analyses, FeO was set at 0.122 and TiO_2 was set at 0.01.

Table D.4. Electron Microprobe Traverse Analyses of Sanidine S5 from Gibbon River Sample GRWY1 (continued)

Length (μm)	SiO_2	BaO	K_2O	Na_2O	Al_2O_3	SrO	CaO	MgO	Total	An	Ab	Or
370	65.188	0.558	9.511	4.667	19.085	0.057	0.468	0.000	99.666	2.31	41.73	55.96
380	65.321	0.503	9.393	4.514	19.577	0.003	0.463	0.000	99.906	2.34	41.22	56.44
390	65.088	0.468	9.364	4.667	19.476	0.000	0.473	0.000	99.668	2.36	42.08	55.56
400	66.096	0.428	9.273	4.631	19.711	0.036	0.461	0.000	100.768	2.32	42.15	55.53
410	65.139	0.442	8.798	4.501	19.454	0.032	0.523	0.000	99.021	2.73	42.55	54.72
420	65.025	0.386	9.262	4.832	19.351	0.033	0.504	0.000	99.525	2.49	43.13	54.39
430	65.476	0.375	9.314	4.834	19.501	0.000	0.535	0.000	100.167	2.63	42.94	54.44
440	65.611	0.323	9.196	4.889	19.468	0.000	0.524	0.000	100.143	2.58	43.54	53.88
450	65.639	0.275	9.300	4.840	19.363	0.041	0.507	0.000	100.097	2.49	43.06	54.44
460	65.788	0.242	9.338	4.796	19.438	0.013	0.508	0.000	100.255	2.50	42.74	54.76
470	65.052	0.241	9.303	4.790	19.382	0.000	0.470	0.000	99.370	2.33	42.88	54.80
480	66.995	0.215	9.558	4.705	19.477	0.000	0.498	0.000	101.580	2.44	41.75	55.81
490	65.005	0.289	8.897	5.041	19.301	0.000	0.509	0.006	99.180	2.52	45.10	52.38
500	65.478	0.290	8.694	5.230	19.319	0.006	0.557	0.000	99.706	2.73	46.46	50.81
510	64.637	0.372	9.393	4.296	19.576	0.009	0.680	0.000	99.095	3.46	39.59	56.95
530	65.319	0.350	8.970	4.905	19.339	0.077	0.518	0.000	99.610	2.58	44.22	53.20
550	65.353	0.257	8.308	5.451	19.505	0.052	0.568	0.000	99.626	2.79	48.53	48.67

For the analyses, FeO was set at 0.122 and TiO_2 was set at 0.01.

Table D.5. Electron Microprobe Traverse Analyses of Sanidine S6 from Gibbon River Sample GRWY1

Length (μm)	SiO_2	BaO	K_2O	Na_2O	Al_2O_3	SrO	CaO	MgO	Total	An	Ab	Or
0	65.450	0.316	7.648	5.564	19.606	0.000	0.628	0.000	99.344	3.17	50.84	45.98
40	65.756	0.190	8.988	4.783	19.437	0.000	0.503	0.000	99.789	2.53	43.58	53.89
60	66.232	0.093	8.937	5.089	19.480	0.000	0.566	0.000	100.529	2.77	45.11	52.12
70	65.411	0.038	8.809	4.998	19.376	0.000	0.582	0.000	99.346	2.89	44.96	52.14
80	65.960	0.011	8.929	4.770	19.406	0.000	0.548	0.000	99.756	2.77	43.57	53.66
90	65.365	0.042	9.017	5.048	19.372	0.000	0.548	0.000	99.524	2.68	44.74	52.58
100	65.641	0.003	9.096	5.024	19.255	0.000	0.529	0.000	99.680	2.59	44.46	52.96
110	65.654	0.000	9.134	4.481	19.380	0.039	0.552	0.000	99.372	2.83	41.51	55.67
120	65.797	0.059	9.279	4.811	19.185	0.120	0.536	0.000	99.919	2.64	42.91	54.45
130	65.556	0.041	9.272	4.626	19.284	0.000	0.500	0.000	99.411	2.51	42.04	55.45
140	65.444	0.000	9.384	4.732	19.267	0.066	0.451	0.000	99.476	2.23	42.42	55.35
150	65.739	0.013	9.360	4.628	19.336	0.014	0.498	0.000	99.720	2.49	41.84	55.67
160	65.002	0.048	9.336	4.829	19.399	0.000	0.491	0.000	99.237	2.41	42.95	54.64
170	66.197	0.033	9.435	4.784	19.492	0.000	0.477	0.000	100.550	2.34	42.50	55.15
180	65.727	0.061	9.659	4.831	19.235	0.032	0.465	0.000	100.142	2.25	42.22	55.54
190	65.824	0.034	9.751	4.746	19.302	0.000	0.477	0.000	100.266	2.31	41.54	56.15
200	65.994	0.000	9.877	4.566	19.518	0.057	0.429	0.000	100.573	2.10	40.40	57.50
210	65.981	0.042	9.763	4.652	19.357	0.000	0.427	0.000	100.354	2.09	41.13	56.79
220	65.243	0.050	9.762	4.546	19.249	0.000	0.456	0.000	99.438	2.25	40.51	57.24
230	65.509	0.050	9.769	4.603	19.400	0.008	0.466	0.000	99.937	2.28	40.78	56.94
240	63.647	0.084	9.510	4.442	20.210	0.084	0.484	0.000	98.593	2.44	40.50	57.06
250	65.635	0.067	9.790	4.700	19.380	0.000	0.452	0.000	100.156	2.19	41.26	56.55
260	66.134	0.069	9.699	4.485	19.573	0.000	0.480	0.000	100.572	2.38	40.29	57.33
270	65.769	0.019	9.849	4.477	19.555	0.000	0.458	0.000	100.259	2.26	39.94	57.81
280	66.030	0.077	9.651	4.354	19.351	0.000	0.458	0.000	100.053	2.31	39.74	57.95
300	65.440	0.101	9.639	4.681	19.612	0.094	0.461	0.000	100.160	2.26	41.51	56.23
310	65.966	0.093	9.746	4.571	19.395	0.013	0.434	0.000	100.350	2.14	40.73	57.14
320	64.613	0.069	9.502	4.620	19.463	0.059	0.495	0.000	98.953	2.45	41.45	56.09
330	65.585	0.108	9.632	4.621	19.553	0.013	0.474	0.000	100.118	2.33	41.18	56.48
340	65.434	0.133	9.664	4.681	19.412	0.000	0.461	0.000	99.917	2.26	41.45	56.30

For the analyses, FeO was set at 0.122 and TiO_2 was set at 0.01.

Table D.5. Electron Microprobe Traverse Analyses of Sanidine S6 from Gibbon River Sample GRWY1 (continued)

Length (μm)	SiO_2	BaO	K_2O	Na_2O	Al_2O_3	SrO	CaO	MgO	Total	An	Ab	Or
350	65.176	0.092	9.502	4.579	19.281	0.000	0.483	0.000	99.245	2.41	41.26	56.33
360	65.003	0.088	9.318	4.322	19.398	0.000	0.483	0.000	98.744	2.49	40.32	57.19
370	65.434	0.054	9.816	4.489	19.156	0.129	0.473	0.000	99.683	2.33	40.05	57.62
380	65.126	0.075	9.465	4.456	19.305	0.000	0.467	0.000	99.026	2.36	40.73	56.92
390	64.475	0.081	9.847	4.358	19.233	0.109	0.412	0.000	98.647	2.06	39.39	58.56
400	65.384	0.070	9.834	4.358	19.429	0.000	0.449	0.000	99.656	2.24	39.34	58.42
410	64.159	0.073	9.772	4.512	19.301	0.000	0.443	0.000	98.392	2.19	40.33	57.48
420	66.838	0.164	9.301	4.661	19.451	0.040	0.464	0.000	101.051	2.32	42.23	55.45
430	65.020	0.234	9.387	4.513	19.227	0.000	0.438	0.000	98.951	2.21	41.29	56.50
440	65.670	0.197	9.681	4.565	19.173	0.035	0.450	0.000	99.903	2.22	40.82	56.96
450	65.094	0.154	9.592	4.749	19.553	0.132	0.516	0.000	99.922	2.51	41.86	55.63
460	65.786	0.046	9.484	4.641	19.180	0.000	0.573	0.000	99.842	2.83	41.45	55.73
470	65.870	0.093	9.339	4.779	19.610	0.000	0.504	0.000	100.327	2.49	42.66	54.85
480	65.778	0.056	9.481	4.817	19.521	0.011	0.567	0.000	100.363	2.76	42.37	54.87
490	65.904	0.109	9.538	4.584	19.528	0.024	0.510	0.000	100.329	2.53	41.14	56.33
500	65.680	0.138	9.467	4.602	19.631	0.000	0.514	0.000	100.164	2.56	41.40	56.04
510	65.878	0.097	9.438	4.825	19.535	0.000	0.540	0.000	100.445	2.63	42.57	54.79
520	66.030	0.064	9.119	4.675	19.286	0.022	0.499	0.000	99.827	2.52	42.69	54.79
530	65.841	0.106	9.204	4.747	19.542	0.000	0.559	0.000	100.131	2.78	42.72	54.50
540	63.526	0.149	8.900	4.413	21.049	0.000	0.612	0.000	98.781	3.19	41.60	55.21
550	65.654	0.108	9.377	4.816	19.383	0.073	0.542	0.000	100.085	2.65	42.68	54.67
560	65.241	0.119	9.505	4.801	19.561	0.000	0.523	0.000	99.882	2.55	42.32	55.13
570	66.401	0.136	9.346	4.674	19.511	0.000	0.554	0.000	100.754	2.75	42.00	55.25
580	66.202	0.132	9.318	4.442	19.660	0.000	0.550	0.000	100.436	2.79	40.84	56.37
610	65.921	0.061	9.474	4.783	19.181	0.000	0.517	0.000	100.069	2.53	42.32	55.15
620	64.304	0.133	9.270	4.510	19.619	0.000	0.558	0.004	98.530	2.82	41.31	55.87
630	65.853	0.130	9.654	4.622	19.442	0.000	0.482	0.000	100.315	2.37	41.12	56.51
640	65.857	0.141	9.517	4.680	19.200	0.043	0.511	0.000	100.081	2.52	41.70	55.79
650	65.381	0.120	9.444	4.877	19.463	0.000	0.503	0.000	99.920	2.44	42.90	54.66
660	65.378	0.089	9.198	4.513	19.267	0.057	0.503	0.000	99.137	2.56	41.62	55.81

For the analyses, FeO was set at 0.122 and TiO_2 was set at 0.01.

Table D.5. Electron Microprobe Traverse Analyses of Sanidine S6 from Gibbon River Sample GRWY1 (continued)

Length (μm)	SiO_2	BaO	K_2O	Na_2O	Al_2O_3	SrO	CaO	MgO	Total	An	Ab	Or
670	63.920	0.081	9.412	4.817	19.105	0.000	0.557	0.000	98.024	2.72	42.56	54.72
680	63.979	0.137	9.028	5.469	19.006	0.000	0.577	0.000	98.328	2.72	46.63	50.65
700	65.319	0.120	9.354	4.814	19.433	0.000	0.506	0.000	99.678	2.49	42.80	54.72
710	65.109	0.118	8.967	4.684	20.985	0.000	0.557	0.000	100.552	2.83	43.01	54.17
720	65.912	0.109	9.452	4.744	19.518	0.000	0.492	0.000	100.359	2.42	42.23	55.35
730	65.204	0.104	9.411	4.790	19.227	0.046	0.510	0.000	99.424	2.50	42.53	54.97
750	65.630	0.082	9.424	4.712	19.724	0.000	0.459	0.000	100.163	2.27	42.20	55.53
760	65.898	0.084	9.461	4.620	19.432	0.054	0.502	0.000	100.183	2.49	41.54	55.97
770	65.513	0.135	9.527	4.611	19.043	0.071	0.490	0.000	99.522	2.43	41.35	56.22
780	64.965	0.051	9.557	4.600	19.467	0.000	0.496	0.000	99.268	2.46	41.21	56.33
790	65.913	0.079	9.335	4.711	19.367	0.022	0.495	0.000	100.054	2.46	42.34	55.20
800	66.230	0.091	9.539	4.616	19.246	0.112	0.468	0.000	100.434	2.32	41.40	56.29
810	66.443	0.106	9.521	4.743	19.440	0.000	0.476	0.000	100.861	2.33	42.08	55.58
820	66.294	0.112	9.670	4.784	19.634	0.035	0.496	0.000	101.157	2.40	41.89	55.71
830	66.269	0.094	9.394	4.888	19.688	0.000	0.547	0.000	101.012	2.66	42.99	54.36
850	65.058	0.105	9.384	4.573	19.386	0.000	0.492	0.000	99.130	2.47	41.50	56.03
860	65.924	0.104	9.315	4.749	19.237	0.041	0.518	0.000	100.020	2.56	42.54	54.90
870	65.678	0.123	9.372	4.762	19.461	0.103	0.491	0.000	100.122	2.42	42.52	55.06
880	65.967	0.060	9.349	4.854	19.617	0.000	0.532	0.000	100.511	2.60	42.96	54.44
890	65.494	0.125	9.369	4.762	19.311	0.048	0.498	0.000	99.739	2.46	42.51	55.03
900	65.389	0.138	9.418	4.779	19.587	0.000	0.494	0.000	99.937	2.43	42.49	55.09
910	65.282	0.132	9.216	4.642	19.326	0.000	0.470	0.000	99.200	2.37	42.33	55.30
920	65.497	0.144	9.390	4.742	19.458	0.000	0.486	0.000	99.849	2.40	42.38	55.22
930	66.183	0.160	9.520	4.840	19.446	0.068	0.497	0.000	100.846	2.41	42.54	55.05
950	65.938	0.120	9.767	4.447	19.434	0.000	0.438	0.000	100.276	2.18	40.01	57.81
960	67.099	0.046	9.690	4.830	19.251	0.135	0.482	0.000	101.665	2.32	42.10	55.58
970	67.564	0.071	8.789	4.540	18.061	0.059	0.548	0.000	99.764	2.85	42.73	54.42
990	69.912	0.000	6.031	4.908	17.802	0.000	0.894	0.000	99.679	5.27	52.38	42.35
1000	66.039	0.000	8.823	4.971	19.371	0.032	0.616	0.000	99.984	3.06	44.72	52.22
1010	65.349	0.000	5.512	6.561	20.541	0.000	1.714	0.000	99.809	8.51	58.92	32.57

For the analyses, FeO was set at 0.122 and TiO_2 was set at 0.01.

Table D.5. Electron Microprobe Traverse Analyses of Sanidine S6 from Gibbon River Sample GRWY1 (continued)

Length (μm)	SiO_2	BaO	K_2O	Na_2O	Al_2O_3	SrO	CaO	MgO	Total	An	Ab	Or
1020	63.249	0.000	1.328	8.219	22.712	0.049	3.570	0.002	99.261	17.83	74.28	7.90
1030	63.302	0.000	1.683	7.924	22.179	0.112	3.641	0.004	98.977	18.22	71.75	10.03
1040	63.747	0.000	2.107	7.881	21.983	0.028	3.231	0.000	99.109	16.15	71.30	12.54
1060	63.444	0.000	2.151	7.738	21.987	0.000	3.200	0.000	98.652	16.19	70.85	12.96
1070	65.256	0.000	9.012	4.548	18.864	0.000	0.414	0.004	98.230	2.14	42.48	55.38
1080	64.296	0.096	9.636	4.532	19.365	0.000	0.455	0.000	98.512	2.26	40.74	57.00
1090	66.566	0.089	9.867	4.639	19.251	0.085	0.459	0.000	101.088	2.23	40.75	57.02
1100	65.111	0.054	9.812	4.331	18.937	0.129	0.407	0.000	98.913	2.04	39.33	58.63
1110	65.420	0.051	9.711	4.512	19.145	0.000	0.408	0.000	99.379	2.03	40.55	57.42
1120	65.073	0.095	9.756	4.348	19.404	0.030	0.437	0.000	99.275	2.19	39.50	58.31
1140	65.595	0.083	9.928	4.323	19.440	0.119	0.443	0.000	100.063	2.21	38.95	58.85
1150	65.900	0.090	9.836	4.526	19.490	0.018	0.458	0.000	100.450	2.25	40.23	57.52
1160	65.860	0.141	9.790	4.535	19.355	0.030	0.486	0.000	100.329	2.39	40.33	57.28
1170	65.683	0.100	9.731	4.669	18.989	0.005	0.471	0.000	99.780	2.30	41.20	56.50
1200	65.323	0.103	8.631	5.349	19.932	0.122	0.648	0.000	100.240	3.14	46.98	49.88
1210	65.606	0.102	9.425	4.719	19.647	0.000	0.559	0.000	100.190	2.75	42.02	55.22
1220	63.984	0.095	9.011	5.160	19.357	0.000	0.602	0.000	98.341	2.91	45.18	51.91
1250	65.041	0.058	9.182	4.806	19.367	0.159	0.604	0.000	99.349	2.99	42.98	54.03
1260	64.511	0.084	9.760	4.374	19.274	0.087	0.585	0.007	98.814	2.91	39.34	57.75
1270	64.265	0.099	10.042	4.341	19.331	0.081	0.444	0.000	98.735	2.19	38.78	59.03
1280	65.454	0.083	10.163	4.074	19.430	0.000	0.438	0.000	99.774	2.20	37.03	60.77
1290	66.337	0.049	8.952	3.773	18.472	0.055	0.505	0.000	98.275	2.81	37.95	59.24
1300	65.698	0.023	10.120	4.430	19.512	0.048	0.397	0.000	100.360	1.94	39.18	58.88
1310	65.505	0.037	10.049	4.459	19.529	0.038	0.414	0.000	100.163	2.02	39.46	58.51
1320	65.318	0.104	9.864	4.439	19.426	0.082	0.433	0.000	99.798	2.14	39.75	58.11
1330	65.216	0.052	10.043	4.281	19.221	0.000	0.403	0.000	99.348	2.00	38.53	59.47
1340	65.632	0.065	10.164	4.422	19.232	0.000	0.433	0.000	100.080	2.11	38.96	58.93
1350	64.975	0.072	9.612	4.552	19.703	0.000	0.462	0.000	99.508	2.29	40.89	56.81
1360	65.006	0.062	9.592	4.666	19.586	0.035	0.497	0.000	99.576	2.44	41.47	56.09
1370	65.319	0.047	9.573	4.810	19.269	0.034	0.493	0.000	99.677	2.39	42.26	55.34

For the analyses, FeO was set at 0.122 and TiO_2 was set at 0.01.

Table D.5. Electron Microprobe Traverse Analyses of Sanidine S6 from Gibbon River Sample GRWY1 (continued)

Length (μm)	SiO_2	BaO	K_2O	Na_2O	Al_2O_3	SrO	CaO	MgO	Total	An	Ab	Or
1390	65.386	0.058	9.405	4.887	19.434	0.000	0.499	0.000	99.801	2.43	43.05	54.52
1410	64.739	0.051	9.658	4.616	19.358	0.037	0.483	0.000	99.074	2.38	41.08	56.55
1420	65.699	0.059	9.167	4.969	19.560	0.000	0.542	0.000	100.128	2.65	43.97	53.38
1560	65.761	0.281	8.749	5.033	19.311	0.024	0.670	0.000	99.961	3.32	45.10	51.58
1570	66.229	0.347	7.970	5.645	20.095	0.026	0.746	0.005	101.195	3.65	49.95	46.40
1590	66.175	0.396	7.563	5.696	19.814	0.037	0.761	0.000	100.574	3.79	51.35	44.86
1600	66.731	0.249	6.882	5.862	20.298	0.000	0.808	0.000	100.962	4.12	54.09	41.79
1610	65.869	0.294	6.754	5.531	19.860	0.029	0.882	0.000	99.351	4.66	52.87	42.48

For the analyses, FeO was set at 0.122 and TiO_2 was set at 0.01.

Table D.6. Electron Microprobe Traverse Analyses of Sanidine S1 from Gibbon River Sample GRWY6

Length (μm)	SiO_2	BaO	K_2O	Na_2O	Al_2O_3	SrO	CaO	MgO	Total	An	Ab	Or
0	64.869	0.984	6.879	5.591	20.028	0.113	0.871	0.001	99.468	4.541	52.753	42.706
10	64.080	0.969	6.897	5.647	20.569	0.000	0.884	0.006	99.184	4.577	52.907	42.516
20	65.892	0.868	7.991	5.551	19.288	0.000	0.558	0.000	100.280	2.774	49.932	47.294
30	64.929	0.847	7.803	5.408	19.312	0.000	0.539	0.000	98.970	2.748	49.890	47.363
40	65.368	0.785	7.871	5.294	19.939	0.008	0.544	0.011	99.952	2.790	49.139	48.070
50	66.229	0.813	7.846	5.518	19.820	0.065	0.546	0.000	100.969	2.747	50.245	47.007
60	66.403	0.832	7.970	5.484	19.686	0.000	0.534	0.000	101.041	2.677	49.750	47.573
70	66.473	0.810	7.855	5.601	19.953	0.000	0.508	0.000	101.332	2.540	50.688	46.772
80	65.271	0.836	7.865	5.472	19.425	0.073	0.486	0.000	99.560	2.460	50.131	47.409
90	65.850	0.762	7.889	5.343	19.660	0.000	0.505	0.000	100.141	2.581	49.414	48.005
110	64.798	0.754	7.766	5.209	19.204	0.000	0.487	0.000	98.350	2.542	49.198	48.260
120	66.537	0.782	7.810	5.523	19.795	0.000	0.492	0.000	101.071	2.487	50.514	46.999
130	65.686	0.845	7.917	5.467	19.526	0.000	0.509	0.000	100.082	2.567	49.893	47.540
140	65.667	0.772	7.631	5.117	19.636	0.000	0.534	0.000	99.489	2.828	49.046	48.125
150	65.715	0.820	7.761	5.629	19.445	0.114	0.512	0.000	100.128	2.568	51.087	46.345
160	65.390	0.826	7.747	5.429	19.525	0.003	0.514	0.000	99.566	2.627	50.221	47.152
170	65.227	0.845	7.697	5.354	19.108	0.000	0.519	0.000	98.882	2.679	50.013	47.308
200	65.524	0.875	7.805	5.384	19.571	0.000	0.563	0.000	99.854	2.873	49.711	47.416
210	65.717	0.896	7.579	5.333	19.583	0.000	0.515	0.000	99.755	2.684	50.291	47.025
220	66.971	0.863	7.563	5.226	20.026	0.000	0.537	0.000	101.318	2.826	49.777	47.397
260	65.969	0.768	6.463	6.195	20.043	0.039	0.817	0.000	100.426	4.142	56.841	39.017
280	64.973	0.815	6.473	5.910	20.128	0.000	0.918	0.000	99.349	4.752	55.356	39.892
300	61.396	0.843	6.122	5.451	23.257	0.046	0.893	0.022	98.162	4.948	54.660	40.391
310	64.486	0.740	6.361	6.076	19.214	0.178	0.826	0.000	98.013	4.259	56.691	39.050
370	65.077	0.875	6.741	5.640	19.876	0.106	0.867	0.000	99.314	4.539	53.437	42.023
390	65.196	0.835	6.664	6.038	19.915	0.064	0.917	0.000	99.761	4.636	55.246	40.118
400	65.031	0.853	6.739	5.972	19.771	0.000	0.824	0.000	99.322	4.192	54.984	40.824
410	64.878	0.875	7.018	5.032	19.482	0.000	0.803	0.000	98.220	4.396	49.855	45.749
420	64.767	0.888	7.049	5.744	19.810	0.069	0.875	0.000	99.334	4.450	52.865	42.685
430	65.018	0.792	5.818	6.575	20.461	0.011	1.192	0.000	99.999	5.955	59.439	34.606

For the analyses, FeO was set at 0.122 and TiO_2 was set at 0.01.

Table D.6. Electron Microprobe Traverse Analyses of Sanidine S1 from Gibbon River Sample GRWY6 (continued)

Length (μm)	SiO_2	BaO	K_2O	Na_2O	Al_2O_3	SrO	CaO	MgO	Total	An	Ab	Or
440	65.171	0.812	5.825	6.511	19.970	0.000	1.217	0.000	99.638	6.105	59.104	34.791
460	65.184	0.923	6.469	6.120	20.352	0.000	1.040	0.000	100.220	5.248	55.885	38.867
470	64.692	0.795	6.361	6.190	19.550	0.163	1.093	0.000	98.976	5.501	56.379	38.120
480	65.286	0.827	6.395	6.112	20.289	0.000	1.084	0.000	100.125	5.486	55.977	38.536
490	64.885	0.804	6.366	5.803	20.136	0.060	1.098	0.000	99.284	5.725	54.754	39.521
500	65.485	0.885	6.384	6.127	20.399	0.000	1.132	0.003	100.547	5.711	55.939	38.350
510	64.164	0.862	6.318	6.074	20.001	0.143	1.104	0.000	98.798	5.627	56.028	38.345
540	63.867	0.826	6.465	6.142	19.843	0.000	0.994	0.000	98.269	5.019	56.117	38.864
550	64.793	0.832	6.595	6.078	19.571	0.000	0.941	0.000	98.942	4.754	55.572	39.674
560	64.399	0.809	6.200	6.369	20.276	0.089	1.014	0.000	99.288	5.090	57.854	37.056
570	65.236	0.835	8.372	5.122	19.624	0.000	0.533	0.000	99.854	2.696	46.883	50.421
580	65.136	0.811	6.306	5.891	20.219	0.000	1.073	0.000	99.568	5.576	55.403	39.021
590	65.208	0.871	6.425	5.989	20.182	0.005	1.075	0.000	99.887	5.495	55.400	39.105
600	64.967	0.865	6.388	6.085	19.775	0.089	1.077	0.000	99.378	5.469	55.912	38.620
610	64.674	0.889	7.483	5.507	19.925	0.039	0.750	0.000	99.399	3.822	50.779	45.399
620	64.959	0.861	6.464	6.040	19.980	0.024	0.930	0.000	99.390	4.755	55.890	39.355
630	65.532	0.726	5.686	6.581	20.398	0.074	1.059	0.000	100.188	5.365	60.335	34.299
640	65.037	0.931	7.656	5.307	19.573	0.010	0.654	0.000	99.300	3.376	49.571	47.053
650	65.200	0.807	6.778	5.825	19.697	0.000	0.796	0.000	99.235	4.102	54.315	41.584
660	64.495	0.870	6.503	5.801	19.935	0.178	0.941	0.000	98.855	4.906	54.728	40.366
670	65.322	0.725	6.224	6.358	19.994	0.036	0.892	0.000	99.683	4.503	58.085	37.412
740	64.516	0.857	6.799	5.996	20.151	0.000	0.735	0.000	99.186	3.735	55.132	41.133
750	65.129	0.824	6.331	6.254	19.905	0.008	0.840	0.000	99.423	4.265	57.462	38.273
760	64.961	0.828	6.827	5.472	20.005	0.073	0.701	0.001	99.000	3.742	52.863	43.395
770	65.054	0.830	6.252	6.234	20.174	0.096	0.850	0.000	99.622	4.342	57.630	38.028
790	65.173	0.879	6.763	6.079	20.248	0.023	0.708	0.000	100.005	3.583	55.668	40.749
800	65.107	0.869	6.879	5.819	20.132	0.107	0.711	0.000	99.756	3.659	54.191	42.150
810	65.252	0.936	7.014	5.379	20.096	0.073	0.639	0.000	99.521	3.413	51.986	44.602
820	65.285	0.897	6.592	6.001	20.112	0.113	0.722	0.000	99.854	3.716	55.889	40.395
830	65.772	0.848	6.947	5.875	20.003	0.000	0.654	0.006	100.237	3.344	54.362	42.294

For the analyses, FeO was set at 0.122 and TiO_2 was set at 0.01.

Table D.6. Electron Microprobe Traverse Analyses of Sanidine S1 from Gibbon River Sample GRWY6 (continued)

Length (μm)	SiO_2	BaO	K_2O	Na_2O	Al_2O_3	SrO	CaO	MgO	Total	An	Ab	Or
840	65.724	0.797	6.986	5.865	20.128	0.000	0.654	0.000	100.286	3.339	54.191	42.470
850	66.532	0.762	6.898	5.319	20.497	0.000	0.601	0.000	100.741	3.259	52.200	44.541
870	65.812	0.809	6.626	5.730	20.294	0.000	0.710	0.003	100.116	3.743	54.665	41.592
890	65.127	0.853	7.013	5.668	19.693	0.000	0.624	0.000	99.110	3.245	53.335	43.420
900	64.975	0.853	6.682	5.709	19.878	0.016	0.621	0.000	98.866	3.284	54.639	42.077
910	65.113	0.828	6.253	6.041	20.001	0.000	0.741	0.000	99.109	3.876	57.181	38.943
920	65.012	0.839	6.816	5.918	19.945	0.093	0.651	0.000	99.406	3.343	54.988	41.670
930	64.692	0.864	6.778	5.833	19.787	0.029	0.703	0.000	98.818	3.637	54.610	41.753
940	65.391	0.830	6.537	5.918	20.020	0.150	0.670	0.000	99.648	3.496	55.886	40.617
950	65.204	0.798	6.447	6.117	20.021	0.018	0.779	0.000	99.516	3.990	56.695	39.315
960	64.673	0.910	6.620	5.746	20.244	0.000	0.773	0.000	99.098	4.057	54.574	41.369
970	64.733	0.840	6.373	5.892	19.961	0.000	0.767	0.000	98.698	4.033	56.066	39.901
990	64.203	0.878	6.609	5.534	19.935	0.015	0.889	0.000	98.195	4.736	53.346	41.918
1000	64.248	0.800	6.110	5.702	20.326	0.000	0.904	0.006	98.228	4.887	55.783	39.330
1010	64.882	0.858	6.563	5.906	20.128	0.000	0.795	0.000	99.264	4.120	55.385	40.495
1020	62.826	0.858	6.311	5.741	22.095	0.161	0.815	0.000	98.939	4.354	55.502	40.144
1080	65.346	0.902	7.297	5.697	20.152	0.154	0.587	0.000	100.267	2.997	52.640	44.363
1090	65.445	0.880	7.171	5.587	20.168	0.000	0.626	0.000	100.009	3.248	52.454	44.298
1100	65.403	0.902	7.031	5.776	20.092	0.081	0.677	0.000	100.094	3.472	53.599	42.929
1110	65.733	0.849	6.499	6.200	20.281	0.000	0.756	0.000	100.450	3.835	56.913	39.252
1120	64.906	0.900	6.713	6.035	20.374	0.011	0.786	0.001	99.858	3.990	55.437	40.573
1150	65.494	0.821	6.710	6.008	20.115	0.000	0.736	0.000	100.016	3.756	55.477	40.767
1160	65.295	0.784	6.527	5.664	20.143	0.000	0.794	0.000	99.339	4.220	54.476	41.304
1170	65.167	0.788	6.188	6.173	20.126	0.044	0.869	0.000	99.487	4.478	57.559	37.964
1190	65.786	0.809	6.059	6.386	20.557	0.024	0.806	0.000	100.559	4.117	59.031	36.851
1200	65.562	0.846	6.482	6.142	20.401	0.005	0.789	0.000	100.359	4.021	56.645	39.334
1210	65.759	0.847	6.608	6.112	20.367	0.000	0.775	0.000	100.600	3.933	56.135	39.932
1220	65.234	0.855	6.567	5.890	20.118	0.000	0.785	0.000	99.581	4.075	55.333	40.592
1230	64.954	0.848	6.572	5.941	20.196	0.000	0.774	0.000	99.417	4.000	55.561	40.439
1240	64.392	0.827	6.648	5.909	19.791	0.000	0.697	0.000	98.396	3.610	55.388	41.001

For the analyses, FeO was set at 0.122 and TiO_2 was set at 0.01.

Table D.6. Electron Microprobe Traverse Analyses of Sanidine S1 from Gibbon River Sample GRWY6 (continued)

Length (μm)	SiO_2	BaO	K_2O	Na_2O	Al_2O_3	SrO	CaO	MgO	Total	An	Ab	Or
1250	65.385	0.865	7.022	5.858	19.974	0.000	0.668	0.000	99.904	3.403	54.004	42.593
1260	65.257	0.918	6.928	5.807	20.126	0.029	0.661	0.000	99.858	3.404	54.116	42.480
1270	64.826	0.858	6.296	6.012	20.169	0.031	0.798	0.000	99.122	4.162	56.741	39.097
1280	65.318	0.820	6.406	6.207	20.442	0.000	0.832	0.003	100.160	4.225	57.041	38.734
1290	65.472	0.781	6.597	5.895	20.325	0.000	0.708	0.000	99.910	3.682	55.473	40.845
1320	65.858	0.867	6.740	5.910	20.320	0.000	0.718	0.000	100.545	3.694	55.021	41.286
1330	65.518	0.916	6.747	5.980	19.918	0.000	0.669	0.000	99.880	3.427	55.427	41.146
1340	64.876	0.858	6.676	5.923	20.032	0.034	0.645	0.000	99.176	3.340	55.500	41.160
1420	65.356	0.398	7.980	5.450	18.795	0.000	0.283	0.000	98.394	1.440	50.198	48.361
1450	65.114	0.690	7.891	5.509	19.372	0.000	0.427	0.000	99.135	2.157	50.371	47.472
1460	65.966	0.697	7.870	5.274	19.242	0.108	0.431	0.000	99.720	2.228	49.334	48.438
1480	66.078	0.628	7.795	5.359	19.721	0.019	0.435	0.000	100.167	2.241	49.952	47.807
1490	64.244	0.599	7.753	5.518	19.805	0.000	0.492	0.000	98.543	2.496	50.665	46.838
1500	65.507	0.639	7.859	5.610	19.782	0.000	0.458	0.000	99.987	2.294	50.843	46.863
1510	65.796	0.617	7.756	5.549	19.981	0.118	0.513	0.000	100.462	2.592	50.742	46.665
1540	63.941	0.583	7.465	5.301	20.002	0.063	0.515	0.000	98.002	2.711	50.499	46.790
1570	64.714	0.617	7.613	5.458	19.780	0.000	0.531	0.000	98.845	2.727	50.723	46.550
1600	65.766	0.652	7.664	5.494	20.050	0.000	0.484	0.000	100.242	2.476	50.851	46.673
1630	65.345	0.643	7.713	5.321	19.784	0.000	0.487	0.000	99.425	2.523	49.892	47.584
1640	66.108	0.614	7.659	5.529	19.782	0.000	0.516	0.000	100.340	2.627	50.942	46.431
1660	65.527	0.623	7.469	4.703	19.630	0.000	0.509	0.000	98.593	2.842	47.512	49.647
1670	65.743	0.638	7.639	5.679	19.628	0.036	0.475	0.000	99.970	2.393	51.780	45.827
1690	66.170	0.652	7.665	5.344	19.833	0.000	0.452	0.000	100.248	2.348	50.239	47.412
1700	65.859	0.679	7.702	4.855	19.869	0.000	0.500	0.000	99.596	2.709	47.603	49.688
1710	65.529	0.703	7.540	5.584	19.233	0.034	0.527	0.000	99.282	2.687	51.531	45.782
1720	66.156	0.746	7.476	5.419	19.892	0.115	0.497	0.000	100.433	2.588	51.062	46.350
1740	66.113	0.727	7.433	5.637	19.660	0.113	0.535	0.000	100.350	2.732	52.082	45.186
1750	65.122	0.959	6.889	5.822	20.326	0.066	0.753	0.000	100.069	3.863	54.054	42.083
1760	64.663	0.972	6.471	5.886	19.975	0.027	0.739	0.000	98.865	3.870	55.781	40.349

For the analyses, FeO was set at 0.122 and TiO_2 was set at 0.01.

Table D.7. Electron Microprobe Traverse Analyses of Sanidine S2 from Gibbon River Sample GRWY6

Length (μm)	SiO_2	BaO	K_2O	Na_2O	Al_2O_3	SrO	CaO	MgO	Total	An	Ab	Or
0	65.512	0.360	7.419	5.675	19.726	0.024	0.492	0.000	99.340	2.511	52.409	45.080
10	65.140	0.366	7.302	5.678	19.684	0.013	0.521	0.000	98.836	2.673	52.719	44.608
80	65.993	0.465	7.526	5.478	19.691	0.000	0.433	0.002	99.720	2.243	51.345	46.413
90	64.906	0.459	7.515	5.633	19.887	0.000	0.440	0.000	98.972	2.247	52.057	45.695
110	65.551	0.343	7.317	5.643	19.649	0.045	0.415	0.000	99.095	2.146	52.804	45.050
120	65.698	0.322	7.363	5.576	19.738	0.069	0.426	0.000	99.324	2.209	52.327	45.463
130	65.712	0.360	7.369	5.618	19.502	0.000	0.423	0.000	99.116	2.185	52.503	45.312
140	65.560	0.316	7.545	5.690	19.615	0.119	0.459	0.000	99.436	2.325	52.164	45.511
150	66.065	0.300	7.537	5.607	19.708	0.040	0.434	0.000	99.823	2.219	51.888	45.892
160	66.160	0.345	7.434	5.650	19.332	0.000	0.464	0.000	99.517	2.375	52.326	45.299
170	65.326	0.259	7.481	5.474	19.503	0.070	0.459	0.000	98.704	2.382	51.400	46.219
180	65.411	0.290	7.555	5.508	19.601	0.091	0.422	0.000	99.010	2.177	51.418	46.405
190	66.067	0.296	7.536	5.714	19.183	0.058	0.394	0.000	99.380	1.999	52.470	45.531
200	65.370	0.256	7.514	5.614	19.483	0.013	0.409	0.000	98.791	2.096	52.059	45.845
210	66.383	0.255	7.609	5.660	19.675	0.013	0.407	0.003	100.137	2.065	51.968	45.967
220	66.426	0.214	7.513	5.581	19.709	0.055	0.461	0.000	100.091	2.363	51.777	45.860
230	66.083	0.282	7.549	5.513	19.837	0.000	0.433	0.000	99.829	2.232	51.431	46.337
250	65.704	0.247	7.446	5.476	19.454	0.000	0.440	0.000	98.899	2.290	51.571	46.139
300	64.922	0.261	7.492	5.770	19.508	0.010	0.555	0.023	98.673	2.787	52.425	44.788
320	66.614	0.262	7.620	5.690	19.876	0.021	0.474	0.000	100.689	2.389	51.890	45.722
330	66.480	0.249	7.230	5.823	19.601	0.087	0.522	0.000	100.124	2.654	53.577	43.769
340	64.921	0.260	7.392	5.852	19.902	0.047	0.502	0.004	99.012	2.523	53.234	44.243
360	64.854	0.277	7.330	5.823	19.513	0.000	0.448	0.015	98.392	2.273	53.454	44.273
380	64.829	0.298	7.624	5.966	19.349	0.000	0.459	0.000	98.657	2.257	53.097	44.645
410	65.025	0.305	7.529	5.552	19.661	0.087	0.483	0.000	98.774	2.478	51.538	45.985
420	65.915	0.270	7.606	5.507	19.478	0.000	0.466	0.000	99.374	2.391	51.138	46.471
430	66.098	0.346	7.143	5.536	19.402	0.000	0.422	0.000	99.079	2.228	52.880	44.893
440	66.380	0.340	7.508	5.680	19.817	0.000	0.436	0.000	100.293	2.218	52.298	45.484
450	66.519	0.370	7.253	5.836	19.692	0.000	0.453	0.000	100.255	2.305	53.746	43.949
460	64.657	0.349	7.523	5.728	19.564	0.000	0.511	0.000	98.464	2.576	52.262	45.162

For the analyses, FeO was set at 0.122 and TiO_2 was set at 0.01.

Table D.7. Electron Microprobe Traverse Analyses of Sanidine S2 from Gibbon River Sample GRWY6 (continued)

Length (μm)	SiO_2	BaO	K_2O	Na_2O	Al_2O_3	SrO	CaO	MgO	Total	An	Ab	Or
470	66.645	0.390	7.310	5.861	19.580	0.000	0.479	0.000	100.397	2.421	53.597	43.983
480	65.748	0.390	7.321	5.565	19.616	0.002	0.494	0.000	99.268	2.562	52.229	45.209
490	65.622	0.415	7.447	5.477	19.666	0.019	0.445	0.000	99.223	2.315	51.559	46.126
500	65.626	0.437	7.197	5.828	19.681	0.029	0.449	0.000	99.379	2.295	53.906	43.799
510	65.841	0.500	7.413	5.928	19.439	0.034	0.487	0.000	99.774	2.430	53.528	44.042
550	67.104	0.553	6.957	6.018	20.146	0.000	0.517	0.005	101.432	2.626	55.307	42.068
570	65.661	0.558	7.103	5.645	19.791	0.000	0.474	0.000	99.364	2.476	53.353	44.171
580	65.226	0.588	6.983	5.452	20.588	0.000	0.569	0.019	99.557	3.035	52.621	44.345
590	65.966	0.548	7.159	5.786	19.320	0.000	0.472	0.000	99.383	2.425	53.787	43.788
600	66.355	0.582	7.163	5.650	19.649	0.068	0.484	0.000	100.083	2.516	53.149	44.335
620	65.383	0.538	7.117	5.418	19.695	0.000	0.462	0.000	98.745	2.465	52.317	45.217
630	66.307	0.594	7.105	6.036	19.948	0.132	0.456	0.004	100.714	2.299	55.059	42.643
640	65.972	0.530	7.353	5.771	19.645	0.141	0.430	0.000	99.974	2.191	53.206	44.604
650	65.893	0.604	7.478	5.845	19.159	0.000	0.429	0.000	99.540	2.155	53.125	44.720

For the analyses, FeO was set at 0.122 and TiO_2 was set at 0.01.

Table D.8. Electron Microprobe Traverse Analyses of Sanidine S4 from Gibbon River Sample GRWY6

Length (μm)	SiO_2	BaO	K_2O	Na_2O	Al_2O_3	SrO	CaO	MgO	Total	An	Ab	Or
0	66.705	0.220	7.564	5.331	19.746	0.000	0.408	0.000	100.106	2.140	50.611	47.249
10	66.355	0.242	7.716	5.676	19.560	0.023	0.455	0.000	100.159	2.285	51.580	46.135
20	66.059	0.183	7.817	5.668	19.771	0.040	0.486	0.001	100.157	2.424	51.156	46.420
30	66.083	0.222	7.697	5.726	19.803	0.065	0.495	0.012	100.235	2.472	51.754	45.774
40	65.517	0.215	7.592	5.545	19.479	0.082	0.468	0.000	99.030	2.395	51.348	46.257
50	65.934	0.207	7.693	5.766	19.459	0.000	0.444	0.000	99.635	2.216	52.072	45.712
60	65.876	0.192	7.694	5.693	19.563	0.000	0.472	0.000	99.622	2.368	51.678	45.954
70	66.203	0.200	7.677	5.735	19.530	0.106	0.457	0.001	100.041	2.288	51.954	45.759
80	66.258	0.247	7.618	5.789	19.615	0.000	0.456	0.003	100.118	2.280	52.373	45.347
90	65.997	0.170	7.649	5.655	19.688	0.000	0.460	0.000	99.751	2.323	51.682	45.995
100	66.547	0.203	7.320	5.809	19.665	0.098	0.430	0.000	100.204	2.187	53.476	44.337
110	65.876	0.224	7.621	5.731	19.908	0.002	0.485	0.000	99.979	2.434	52.037	45.530
120	66.024	0.216	7.579	5.682	19.536	0.143	0.494	0.000	99.806	2.495	51.930	45.575
130	66.330	0.222	7.695	5.651	19.695	0.071	0.432	0.000	100.228	2.180	51.594	46.226
140	65.915	0.198	7.606	5.690	19.350	0.000	0.489	0.000	99.380	2.464	51.894	45.642
150	65.988	0.231	7.586	5.581	19.586	0.108	0.520	0.010	99.742	2.646	51.392	45.962
160	66.434	0.192	7.680	5.698	19.777	0.008	0.496	0.000	100.417	2.486	51.681	45.833
170	66.127	0.192	7.627	5.732	19.707	0.000	0.425	0.000	99.942	2.138	52.180	45.682
180	65.949	0.195	7.581	5.447	19.267	0.000	0.480	0.000	99.051	2.479	50.905	46.616
190	66.286	0.144	7.618	5.568	19.767	0.000	0.484	0.000	99.999	2.466	51.328	46.206
200	66.364	0.161	7.698	5.736	19.898	0.000	0.459	0.000	100.448	2.294	51.888	45.818
210	66.089	0.203	7.707	5.569	19.617	0.000	0.454	0.000	99.771	2.304	51.135	46.561
220	65.972	0.201	7.408	5.707	19.591	0.000	0.478	0.000	99.489	2.436	52.622	44.943
230	65.585	0.223	7.576	5.433	19.615	0.000	0.476	0.000	99.040	2.463	50.867	46.670

For the analyses, FeO was set at 0.122 and TiO_2 was set at 0.01.

Table D.9. Electron Microprobe Traverse Analyses of Sanidine S2 from Gibbon River Sample GRWY7P

Length (μm)	SiO_2	BaO	K_2O	Na_2O	Al_2O_3	SrO	CaO	MgO	Total	An	Ab	Or
0	65.175	0.564	9.816	4.318	19.344	0.000	0.402	0.000	99.751	2.020	39.259	58.721
10	65.270	0.549	9.857	4.341	19.343	0.002	0.419	0.000	99.913	2.094	39.256	58.650
20	64.351	0.588	9.872	4.375	19.543	0.000	0.353	0.000	99.214	1.763	39.537	58.700
30	65.265	0.623	9.880	4.389	19.550	0.029	0.417	0.000	100.285	2.072	39.469	58.459
40	64.477	0.796	9.750	4.357	19.711	0.034	0.476	0.000	99.733	2.384	39.483	58.133
60	64.100	0.856	9.625	3.924	19.644	0.000	0.565	0.000	98.846	2.954	37.127	59.919
70	63.601	0.945	9.676	4.397	19.735	0.048	0.548	0.000	99.082	2.736	39.733	57.530
80	64.461	0.921	9.793	4.403	19.602	0.037	0.540	0.000	99.889	2.678	39.507	57.815
90	64.463	0.981	9.395	3.729	19.725	0.051	0.507	0.000	98.983	2.749	36.592	60.659
100	62.110	0.924	9.161	4.145	21.448	0.079	0.604	0.028	98.631	3.177	39.452	57.371
110	63.983	0.950	9.609	4.244	18.524	0.065	0.499	0.000	98.006	2.543	39.144	58.313
120	64.344	1.037	9.623	4.358	19.637	0.000	0.527	0.000	99.658	2.652	39.687	57.660
130	64.582	1.096	9.631	4.400	19.653	0.000	0.494	0.000	99.988	2.479	39.964	57.556
140	64.804	1.046	9.563	4.279	19.538	0.082	0.496	0.000	99.940	2.527	39.455	58.017
150	64.598	1.111	9.688	4.152	19.691	0.000	0.521	0.000	99.893	2.662	38.394	58.944
160	64.392	1.108	9.758	4.174	19.829	0.000	0.493	0.000	99.886	2.507	38.410	59.082
170	64.002	1.137	9.758	4.461	19.474	0.018	0.526	0.000	99.508	2.602	39.930	57.468
180	65.142	1.169	9.510	4.230	20.465	0.000	0.538	0.000	101.186	2.757	39.223	58.020
190	65.393	1.137	9.788	4.381	19.811	0.000	0.454	0.000	101.096	2.266	39.568	58.166
200	64.882	1.118	9.742	4.102	19.955	0.000	0.463	0.000	100.394	2.376	38.095	59.529
220	64.315	1.156	9.675	4.447	19.727	0.036	0.461	0.000	99.949	2.302	40.181	57.518
230	65.386	1.177	9.757	4.436	19.776	0.176	0.495	0.000	101.335	2.458	39.859	57.683
240	65.316	1.238	9.789	4.281	19.865	0.000	0.488	0.000	101.109	2.453	38.948	58.598
250	65.144	1.259	9.726	4.330	19.977	0.058	0.492	0.000	101.118	2.471	39.359	58.169
260	64.709	1.200	9.797	4.178	19.873	0.013	0.487	0.000	100.389	2.471	38.354	59.175
270	65.044	1.209	9.698	4.314	20.095	0.010	0.485	0.000	100.987	2.445	39.351	58.204
280	64.721	1.283	9.644	4.262	19.805	0.084	0.484	0.000	100.415	2.459	39.191	58.349
290	64.008	1.224	9.684	4.219	19.584	0.000	0.474	0.000	99.325	2.414	38.875	58.711
300	64.525	1.189	9.746	3.779	19.499	0.000	0.488	0.006	99.364	2.578	36.124	61.298
310	64.138	1.151	9.684	4.252	19.678	0.117	0.459	0.000	99.611	2.332	39.090	58.578

For the analyses, FeO was set at 0.122 and TiO_2 was set at 0.01.

Table D.9. Electron Microprobe Traverse Analyses of Sanidine S2 from Gibbon River Sample GRWY7P (continued)

Length (μm)	SiO_2	BaO	K_2O	Na_2O	Al_2O_3	SrO	CaO	MgO	Total	An	Ab	Or
320	64.733	1.175	9.759	4.314	19.018	0.121	0.438	0.000	99.690	2.205	39.300	58.495
330	64.140	1.095	9.678	4.160	19.492	0.000	0.449	0.000	99.146	2.303	38.605	59.093
340	64.613	1.081	9.710	4.257	19.633	0.000	0.475	0.000	99.901	2.406	39.025	58.568
350	64.576	1.034	9.730	4.250	19.485	0.000	0.443	0.000	99.650	2.247	39.002	58.751
360	64.300	1.012	9.793	4.366	19.519	0.006	0.439	0.000	99.567	2.195	39.504	58.301
370	64.579	0.932	9.963	4.251	19.058	0.129	0.445	0.000	99.489	2.225	38.463	59.312
380	64.866	0.946	9.654	4.035	19.454	0.075	0.411	0.000	99.573	2.140	38.016	59.845
400	65.815	0.900	9.731	4.171	19.955	0.000	0.439	0.000	101.143	2.243	38.562	59.195
410	64.742	0.941	9.595	4.315	19.606	0.000	0.436	0.000	99.767	2.217	39.700	58.084
420	64.633	0.978	9.832	4.270	19.587	0.000	0.463	0.000	99.895	2.327	38.836	58.837
430	64.655	1.097	9.844	4.275	19.529	0.000	0.408	0.000	99.940	2.054	38.944	59.003
440	64.438	1.210	9.632	4.327	19.468	0.024	0.480	0.000	99.711	2.427	39.589	57.984
450	63.476	1.238	9.779	4.179	18.965	0.000	0.458	0.000	98.227	2.329	38.458	59.213
460	64.435	1.206	9.833	4.403	19.756	0.053	0.459	0.000	100.277	2.280	39.573	58.148
470	64.601	1.247	9.748	4.176	19.753	0.000	0.445	0.000	100.102	2.269	38.539	59.191
480	64.728	1.166	9.761	4.384	19.492	0.070	0.439	0.000	100.172	2.196	39.678	58.126
490	64.514	1.216	9.654	4.334	19.294	0.058	0.448	0.000	99.650	2.264	39.640	58.096
500	64.187	1.211	9.802	4.385	18.715	0.000	0.449	0.005	98.886	2.239	39.567	58.194
510	63.862	1.168	9.630	4.176	19.917	0.014	0.506	0.000	99.405	2.591	38.696	58.713
520	64.367	1.209	9.849	4.215	19.776	0.056	0.457	0.000	100.061	2.307	38.501	59.192
530	64.773	1.217	9.830	4.326	19.634	0.016	0.461	0.000	100.389	2.306	39.155	58.540
540	64.683	1.237	9.618	4.311	19.629	0.000	0.443	0.000	100.053	2.249	39.608	58.143
550	64.049	1.197	9.393	4.099	19.612	0.013	0.482	0.000	98.977	2.526	38.869	58.605
570	64.843	1.130	9.696	4.130	19.517	0.088	0.471	0.000	100.007	2.417	38.348	59.236
580	64.814	1.164	9.545	4.203	19.845	0.005	0.437	0.000	100.145	2.252	39.190	58.559
590	64.416	1.156	9.561	4.299	19.632	0.019	0.444	0.000	99.659	2.264	39.677	58.059
600	64.539	1.201	9.710	4.331	19.483	0.054	0.452	0.000	99.902	2.277	39.482	58.241
610	64.593	1.188	9.750	4.134	19.756	0.067	0.475	0.000	100.095	2.428	38.237	59.336
620	65.061	1.203	9.664	4.314	19.405	0.000	0.436	0.000	100.215	2.208	39.529	58.263
630	65.103	1.159	9.598	4.362	19.879	0.000	0.449	0.000	100.682	2.271	39.926	57.803

For the analyses, FeO was set at 0.122 and TiO_2 was set at 0.01.

Table D.9. Electron Microprobe Traverse Analyses of Sanidine S2 from Gibbon River Sample GRWY7P (continued)

Length (μm)	SiO_2	BaO	K_2O	Na_2O	Al_2O_3	SrO	CaO	MgO	Total	An	Ab	Or
640	63.967	1.150	9.559	4.311	19.597	0.005	0.457	0.000	99.178	2.327	39.722	57.951
650	64.907	1.138	9.580	4.369	19.796	0.000	0.464	0.000	100.386	2.346	39.977	57.676
660	64.400	1.163	9.693	4.408	19.610	0.000	0.493	0.000	99.899	2.464	39.862	57.674
670	64.095	1.175	9.725	4.355	19.304	0.045	0.462	0.000	99.293	2.319	39.559	58.122
680	63.852	1.137	9.480	4.125	19.562	0.034	0.483	0.000	98.805	2.511	38.808	58.681
690	64.119	1.149	9.645	4.321	19.710	0.088	0.477	0.001	99.642	2.411	39.531	58.057
700	63.081	1.084	9.530	3.980	19.789	0.245	0.514	0.000	98.355	2.696	37.781	59.523
740	65.007	0.944	10.144	3.786	19.715	0.000	0.378	0.000	100.106	1.958	35.485	62.557
750	65.499	0.900	10.175	4.048	19.479	0.086	0.350	0.000	100.669	1.769	37.015	61.217
760	65.298	0.893	10.073	4.194	19.611	0.000	0.401	0.010	100.612	2.007	37.978	60.015
770	64.867	0.785	9.931	4.252	19.682	0.000	0.359	0.000	100.008	1.806	38.709	59.485
780	63.112	0.760	9.614	4.114	20.880	0.063	0.426	0.006	99.107	2.205	38.538	59.256
790	63.701	0.732	9.841	4.311	19.570	0.000	0.454	0.000	98.741	2.273	39.060	58.667
800	65.126	0.683	9.854	4.450	19.723	0.000	0.482	0.000	100.450	2.378	39.732	57.889
810	65.283	0.666	9.929	4.337	19.675	0.016	0.454	0.000	100.492	2.256	38.999	58.745
820	65.496	0.629	9.770	4.431	19.823	0.083	0.478	0.000	100.842	2.375	39.835	57.791
830	65.285	0.666	9.780	4.246	19.689	0.000	0.439	0.000	100.237	2.221	38.870	58.909
840	63.616	0.582	9.570	4.344	20.952	0.000	0.446	0.000	99.642	2.264	39.900	57.836

For the analyses, FeO was set at 0.122 and TiO_2 was set at 0.01.

Table D.10. Electron Microprobe Traverse Analyses of Sanidine S3 from Gibbon River Sample GRWY7P

Length (μm)	SiO_2	BaO	K_2O	Na_2O	Al_2O_3	SrO	CaO	MgO	Total	An	Ab	Or
0	65.778	0.467	9.980	4.293	19.730	0.093	0.383	0.000	100.856	1.912	38.777	59.312
10	65.520	0.456	10.065	4.398	19.455	0.000	0.418	0.000	100.444	2.053	39.089	58.858
20	65.660	0.455	10.092	4.302	19.275	0.000	0.403	0.000	100.319	1.995	38.532	59.474
30	65.533	0.400	10.035	4.312	19.649	0.055	0.354	0.000	100.470	1.761	38.811	59.428
40	65.706	0.388	10.054	4.209	19.167	0.000	0.344	0.000	100.000	1.726	38.214	60.060
50	65.712	0.396	9.969	4.346	19.168	0.000	0.393	0.000	100.116	1.953	39.074	58.973
70	64.894	0.325	8.062	4.250	21.139	0.010	0.461	0.012	99.285	2.597	43.327	54.076
80	65.156	0.416	9.785	4.263	19.262	0.025	0.396	0.000	99.435	2.004	39.039	58.958
90	65.335	0.387	9.976	4.245	19.530	0.000	0.406	0.000	100.011	2.033	38.475	59.492
100	64.660	0.436	9.837	4.189	19.555	0.000	0.409	0.000	99.218	2.076	38.476	59.448
110	65.033	0.411	9.936	4.293	19.462	0.000	0.365	0.000	99.632	1.828	38.913	59.258
120	64.440	0.448	9.707	3.800	19.369	0.018	0.377	0.000	98.291	2.004	36.555	61.440
130	64.693	0.435	10.011	4.246	19.435	0.056	0.391	0.000	99.399	1.956	38.429	59.615
140	66.273	0.394	10.160	4.502	19.689	0.000	0.384	0.000	101.534	1.862	39.494	58.644
150	65.677	0.473	10.226	4.245	19.713	0.000	0.381	0.000	100.847	1.883	37.956	60.161
160	65.547	0.430	10.043	4.236	19.377	0.045	0.376	0.000	100.186	1.880	38.329	59.791
170	65.554	0.456	10.031	4.389	19.588	0.000	0.378	0.000	100.528	1.865	39.195	58.940
180	65.098	0.469	10.146	4.292	19.538	0.109	0.353	0.000	100.137	1.747	38.449	59.803
200	66.556	0.462	9.983	4.266	19.766	0.000	0.378	0.000	101.543	1.891	38.630	59.479
210	65.075	0.439	10.071	4.340	19.501	0.000	0.342	0.000	99.900	1.694	38.905	59.401
220	65.514	0.441	10.057	4.045	19.305	0.077	0.386	0.000	99.957	1.961	37.194	60.845
230	64.873	0.449	10.079	4.245	19.479	0.000	0.349	0.000	99.606	1.742	38.349	59.909
240	65.209	0.437	10.116	4.198	18.873	0.000	0.378	0.000	99.343	1.888	37.947	60.165
260	65.539	0.443	10.062	4.104	19.545	0.000	0.364	0.000	100.189	1.841	37.563	60.596
270	65.271	0.475	9.948	4.323	19.491	0.000	0.382	0.000	100.022	1.905	39.018	59.077
280	65.365	0.438	9.973	4.087	19.078	0.014	0.363	0.000	99.450	1.849	37.670	60.481
290	65.382	0.471	9.740	4.096	19.441	0.114	0.360	0.000	99.736	1.859	38.268	59.873
300	65.166	0.463	10.093	4.346	19.531	0.000	0.352	0.000	100.083	1.740	38.868	59.392
310	65.035	0.532	9.852	4.326	19.261	0.000	0.377	0.000	99.515	1.891	39.268	58.841
330	65.370	0.487	9.999	4.239	19.571	0.047	0.366	0.000	100.211	1.835	38.466	59.699
340	64.447	0.477	10.020	3.802	19.322	0.000	0.413	0.000	98.613	2.148	35.790	62.061

For the analyses, FeO was set at 0.122 and TiO_2 was set at 0.01.

Table D.10. Electron Microprobe Traverse Analyses of Sanidine S3 from Gibbon River Sample GRWY7P (continued)

Length (μm)	SiO_2	BaO	K_2O	Na_2O	Al_2O_3	SrO	CaO	MgO	Total	An	Ab	Or
350	66.094	0.484	10.094	4.485	19.746	0.000	0.392	0.000	101.427	1.910	39.540	58.551
360	65.228	0.490	10.018	4.262	19.232	0.011	0.384	0.000	99.757	1.918	38.516	59.567
370	65.004	0.493	9.890	4.231	19.516	0.000	0.381	0.000	99.647	1.923	38.644	59.433
380	65.497	0.487	10.006	4.296	19.580	0.147	0.406	0.000	100.551	2.021	38.689	59.290
390	65.600	0.477	9.781	3.440	19.310	0.010	0.406	0.000	99.156	2.221	34.060	63.719
410	65.252	0.565	10.068	4.418	19.706	0.018	0.426	0.006	100.591	2.087	39.174	58.738
420	65.350	0.557	10.005	4.323	19.679	0.016	0.417	0.000	100.479	2.069	38.819	59.112
430	65.395	0.560	10.019	4.382	19.776	0.010	0.395	0.000	100.669	1.950	39.152	58.898
440	65.617	0.538	9.918	4.381	19.817	0.000	0.412	0.000	100.815	2.045	39.347	58.608
460	65.653	0.506	9.999	4.420	19.441	0.055	0.413	0.000	100.619	2.033	39.369	58.598
470	65.019	0.527	9.847	4.371	19.193	0.000	0.438	0.000	99.527	2.182	39.407	58.411
480	65.226	0.486	9.748	4.425	19.415	0.000	0.419	0.000	99.851	2.092	39.972	57.937
490	65.158	0.497	9.889	4.490	19.693	0.000	0.399	0.000	100.258	1.966	40.028	58.006
500	65.115	0.502	9.700	4.406	19.635	0.063	0.409	0.000	99.962	2.052	40.003	57.945
510	64.851	0.517	9.884	4.344	19.686	0.074	0.391	0.000	99.879	1.953	39.265	58.782
520	65.393	0.492	9.766	4.044	19.274	0.003	0.413	0.000	99.517	2.133	37.802	60.065
530	65.371	0.487	9.681	4.462	19.394	0.000	0.472	0.000	99.999	2.351	40.225	57.423
540	65.750	0.437	9.825	4.334	19.597	0.000	0.407	0.000	100.482	2.040	39.316	58.643
550	64.934	0.474	9.938	4.379	19.533	0.000	0.425	0.000	99.815	2.106	39.264	58.630
560	66.079	0.469	9.827	4.338	19.733	0.000	0.399	0.000	100.977	2.000	39.350	58.650
570	65.592	0.470	9.807	4.350	19.473	0.061	0.439	0.000	100.324	2.196	39.384	58.420
580	65.858	0.503	9.937	4.245	19.739	0.000	0.407	0.000	100.821	2.043	38.563	59.394
630	65.606	0.366	9.800	4.412	19.682	0.061	0.387	0.000	100.446	1.931	39.841	58.227
640	64.789	0.425	9.849	4.365	19.068	0.000	0.403	0.000	99.031	2.012	39.438	58.550
650	65.088	0.408	9.702	4.392	19.314	0.027	0.447	0.003	99.513	2.241	39.846	57.913
660	64.713	0.374	9.713	4.592	19.504	0.113	0.453	0.000	99.594	2.228	40.879	56.892
670	63.568	0.396	9.878	4.473	19.590	0.000	0.391	0.000	98.428	1.931	39.979	58.090
680	65.257	0.355	9.814	4.379	19.371	0.106	0.432	0.000	99.846	2.156	39.540	58.305
690	64.442	0.347	9.760	4.226	19.165	0.126	0.513	0.000	98.711	2.593	38.660	58.747
700	64.566	0.365	9.916	4.345	19.860	0.005	0.507	0.018	99.714	2.513	38.970	58.517
710	63.688	0.347	8.823	3.943	20.555	0.000	0.725	0.072	98.285	3.948	38.852	57.201

For the analyses, FeO was set at 0.122 and TiO_2 was set at 0.01.

Table D.10. Electron Microprobe Traverse Analyses of Sanidine S3 from Gibbon River Sample GRWY7P (continued)

Length (μm)	SiO_2	BaO	K_2O	Na_2O	Al_2O_3	SrO	CaO	MgO	Total	An	Ab	Or
720	65.550	0.321	9.919	4.373	19.757	0.000	0.429	0.000	100.481	2.129	39.268	58.604
730	65.626	0.294	9.343	4.457	19.635	0.037	0.420	0.000	99.944	2.142	41.130	56.728
740	65.869	0.341	9.835	4.419	19.752	0.019	0.421	0.008	100.796	2.092	39.730	58.179
750	65.816	0.333	9.819	4.499	19.807	0.000	0.466	0.000	100.872	2.296	40.109	57.596
770	66.823	0.308	9.910	4.623	19.622	0.033	0.453	0.000	101.904	2.197	40.575	57.228
780	65.312	0.361	9.733	4.512	19.402	0.000	0.451	0.000	99.903	2.232	40.411	57.356
790	65.334	0.295	9.794	4.313	19.627	0.000	0.402	0.000	99.897	2.023	39.283	58.693
800	65.481	0.341	9.608	4.405	19.580	0.096	0.357	0.000	100.000	1.806	40.324	57.870
810	65.144	0.366	9.837	4.332	19.529	0.000	0.421	0.002	99.763	2.108	39.250	58.642
820	65.450	0.395	9.980	4.222	19.578	0.000	0.415	0.000	100.172	2.081	38.320	59.599
830	65.317	0.400	9.632	4.432	19.471	0.021	0.433	0.000	99.838	2.174	40.259	57.568
840	65.062	0.441	9.650	4.344	19.219	0.000	0.441	0.000	99.289	2.228	39.718	58.054
850	64.204	0.453	9.881	3.755	19.473	0.050	0.428	0.000	98.376	2.254	35.786	61.960
860	65.028	0.490	9.771	4.208	19.427	0.181	0.458	0.000	99.695	2.324	38.641	59.035
870	64.956	0.545	9.859	4.337	19.563	0.021	0.440	0.000	99.853	2.197	39.189	58.614
890	64.030	0.485	9.577	4.668	19.467	0.061	0.454	0.008	98.882	2.236	41.604	56.160

For the analyses, FeO was set at 0.122 and TiO_2 was set at 0.01.

Table D.11. Electron Microprobe Traverse Analyses of Sanidine S5 from Gibbon River Sample GRWY7P

Length (μm)	SiO_2	BaO	K_2O	Na_2O	Al_2O_3	SrO	CaO	MgO	Total	An	Ab	Or
0	65.161	0.349	9.616	4.293	19.360	0.000	0.417	0.000	99.328	2.124	39.565	58.311
10	65.400	0.356	9.861	4.329	19.605	0.000	0.427	0.000	100.110	2.135	39.165	58.700
20	64.908	0.318	9.886	4.122	19.203	0.024	0.403	0.000	98.996	2.053	37.993	59.954
30	65.352	0.298	9.807	4.390	19.666	0.000	0.442	0.000	100.087	2.203	39.596	58.201
40	65.387	0.286	9.947	4.311	19.107	0.035	0.370	0.000	99.575	1.849	38.978	59.174
50	65.375	0.266	9.886	4.442	19.487	0.056	0.377	0.000	100.021	1.868	39.821	58.311
60	64.250	0.209	9.951	4.396	19.346	0.000	0.396	0.000	98.680	1.960	39.383	58.657
70	65.019	0.235	9.976	4.412	19.438	0.053	0.382	0.000	99.647	1.887	39.439	58.674
80	65.110	0.211	9.881	4.291	19.457	0.000	0.416	0.000	99.498	2.086	38.931	58.984
90	64.875	0.235	9.716	4.305	19.349	0.043	0.423	0.000	99.078	2.138	39.382	58.480
110	65.135	0.199	9.803	4.264	19.475	0.000	0.433	0.000	99.441	2.185	38.929	58.886
120	65.712	0.215	9.805	4.363	19.459	0.026	0.414	0.004	100.130	2.072	39.509	58.419
130	65.287	0.227	9.889	4.205	19.434	0.000	0.422	0.000	99.596	2.131	38.420	59.449
140	64.864	0.216	9.941	4.270	19.588	0.000	0.441	0.000	99.452	2.205	38.627	59.169
150	65.313	0.260	9.940	4.305	19.399	0.061	0.452	0.000	99.862	2.251	38.802	58.947
160	65.638	0.245	9.917	4.260	19.546	0.129	0.451	0.000	100.318	2.259	38.607	59.134
170	65.056	0.255	9.833	4.393	19.361	0.127	0.440	0.000	99.597	2.189	39.556	58.255
180	65.163	0.245	9.838	4.534	19.279	0.027	0.438	0.000	99.656	2.152	40.306	57.543
190	65.599	0.211	9.670	4.228	19.562	0.040	0.438	0.000	99.880	2.234	39.031	58.735
200	65.881	0.260	9.973	4.399	19.485	0.000	0.468	0.000	100.598	2.305	39.209	58.486
210	65.787	0.249	9.933	4.244	19.622	0.000	0.437	0.008	100.412	2.191	38.508	59.301
220	64.420	0.235	9.772	4.446	19.595	0.000	0.454	0.000	99.054	2.255	39.959	57.786
230	65.514	0.224	9.729	4.486	19.133	0.000	0.477	0.004	99.699	2.364	40.230	57.406
250	65.413	0.314	9.778	4.496	19.462	0.029	0.454	0.006	100.084	2.244	40.213	57.543
260	64.766	0.244	9.878	4.416	19.226	0.000	0.457	0.000	99.119	2.261	39.542	58.197
270	65.558	0.288	9.868	4.476	19.552	0.000	0.416	0.001	100.291	2.053	39.969	57.978
280	65.625	0.298	9.950	4.008	19.568	0.047	0.453	0.000	100.081	2.317	37.094	60.589
290	64.979	0.268	9.839	4.391	19.412	0.063	0.466	0.005	99.555	2.315	39.480	58.205

For the analyses, FeO was set at 0.122 and TiO_2 was set at 0.01.

Table D.11. Electron Microprobe Traverse Analyses of Sanidine S5 from Gibbon River Sample GRWY7P (continued)

Length (μm)	SiO_2	BaO	K_2O	Na_2O	Al_2O_3	SrO	CaO	MgO	Total	An	Ab	Or
300	64.577	0.283	9.830	4.290	19.561	0.000	0.516	0.013	99.202	2.582	38.848	58.569
310	64.925	0.299	9.790	4.314	19.274	0.000	0.448	0.000	99.182	2.250	39.207	58.543
320	64.947	0.306	9.710	4.350	19.193	0.000	0.405	0.002	99.045	2.042	39.680	58.278
330	64.924	0.291	9.611	4.397	19.428	0.182	0.405	0.000	99.370	2.045	40.176	57.780
340	65.013	0.298	9.670	4.369	19.182	0.000	0.431	0.000	99.095	2.171	39.828	58.001
350	65.245	0.316	9.663	4.474	19.570	0.035	0.455	0.000	99.890	2.269	40.367	57.364
360	64.992	0.345	9.740	4.398	19.340	0.000	0.418	0.000	99.365	2.093	39.846	58.061
370	65.091	0.347	9.627	4.106	19.300	0.000	0.447	0.000	99.050	2.311	38.420	59.269
380	64.655	0.294	9.737	4.376	19.306	0.057	0.476	0.016	99.049	2.381	39.618	58.001
390	65.138	0.263	9.651	4.329	19.548	0.000	0.445	0.000	99.506	2.251	39.625	58.124
400	65.564	0.314	9.690	4.246	19.430	0.108	0.413	0.000	99.897	2.103	39.134	58.762
410	64.815	0.275	9.777	4.321	18.998	0.000	0.454	0.000	98.772	2.280	39.265	58.455
420	64.933	0.343	9.544	4.153	19.040	0.000	0.430	0.005	98.580	2.227	38.921	58.852
430	65.369	0.360	9.758	4.375	19.305	0.000	0.381	0.000	99.680	1.913	39.751	58.336
440	64.721	0.317	9.759	4.447	19.592	0.000	0.456	0.000	99.424	2.266	39.991	57.743
450	65.117	0.282	9.809	4.391	19.474	0.067	0.428	0.000	99.700	2.134	39.625	58.241
460	65.294	0.260	9.571	4.392	19.621	0.000	0.439	0.000	99.709	2.219	40.176	57.605
470	64.632	0.281	9.726	4.306	19.300	0.021	0.432	0.000	98.830	2.181	39.346	58.473
480	64.882	0.260	9.936	4.168	19.578	0.000	0.433	0.000	99.389	2.186	38.082	59.732
490	65.179	0.287	9.906	4.347	19.558	0.000	0.449	0.000	99.858	2.233	39.117	58.651
500	64.893	0.276	9.940	3.518	19.512	0.000	0.436	0.000	98.707	2.339	34.158	63.502
510	65.859	0.268	9.972	4.407	19.430	0.000	0.391	0.000	100.459	1.932	39.404	58.665
520	65.241	0.277	9.925	4.428	19.425	0.106	0.434	0.000	99.968	2.142	39.542	58.316
530	65.288	0.272	9.907	4.288	19.548	0.051	0.455	0.000	99.941	2.274	38.778	58.948
540	64.659	0.286	10.027	4.510	19.430	0.000	0.440	0.000	99.484	2.142	39.734	58.124
550	65.233	0.267	9.763	4.383	19.405	0.093	0.430	0.000	99.706	2.152	39.686	58.163
570	64.871	0.258	9.598	4.412	19.509	0.000	0.443	0.000	99.223	2.231	40.212	57.557
580	65.135	0.256	9.734	4.194	19.399	0.089	0.410	0.000	99.349	2.093	38.743	59.164

For the analyses, FeO was set at 0.122 and TiO_2 was set at 0.01.

Table D.11. Electron Microprobe Traverse Analyses of Sanidine S5 from Gibbon River Sample GRWY7P (continued)

Length (μm)	SiO_2	BaO	K_2O	Na_2O	Al_2O_3	SrO	CaO	MgO	Total	An	Ab	Or
590	65.227	0.232	9.832	4.357	19.433	0.002	0.438	0.000	99.653	2.187	39.365	58.448
600	65.130	0.245	10.006	4.342	19.447	0.098	0.393	0.000	99.793	1.949	38.967	59.084
610	64.503	0.249	9.856	4.209	19.411	0.000	0.430	0.000	98.790	2.174	38.503	59.323
620	65.350	0.212	9.798	4.365	19.370	0.019	0.433	0.000	99.679	2.165	39.499	58.336
630	65.094	0.266	9.659	4.369	19.421	0.054	0.400	0.000	99.395	2.020	39.917	58.064
640	65.112	0.222	9.977	4.366	19.330	0.042	0.374	0.000	99.555	1.856	39.202	58.942
660	64.966	0.173	9.723	4.394	19.264	0.000	0.398	0.000	99.050	1.997	39.904	58.098
670	65.098	0.230	9.860	4.074	19.283	0.209	0.406	0.000	99.292	2.080	37.772	60.148
680	64.029	0.202	10.008	4.349	19.313	0.000	0.396	0.000	98.429	1.962	38.995	59.043
690	65.279	0.186	9.568	4.330	18.659	0.069	0.386	0.000	98.609	1.968	39.950	58.083
720	65.124	0.262	9.951	4.393	19.479	0.000	0.406	0.000	99.747	2.010	39.347	58.643
730	64.972	0.313	9.969	3.993	19.563	0.000	0.429	0.000	99.371	2.197	37.009	60.794
740	64.269	0.341	9.885	4.328	18.998	0.030	0.395	0.000	98.378	1.975	39.167	58.858
750	64.807	0.359	9.920	4.109	19.186	0.000	0.392	0.000	98.905	1.996	37.862	60.142
760	65.111	0.460	9.696	4.091	19.319	0.032	0.439	0.000	99.280	2.264	38.187	59.549
770	65.368	0.475	8.224	4.845	18.906	0.000	0.487	0.000	98.437	2.557	46.032	51.411

For the analyses, FeO was set at 0.122 and TiO_2 was set at 0.01.

Table D.12. Electron Microprobe Traverse Analyses of Sanidine S6 from Gibbon River Sample GRWY7P

Length (μm)	SiO_2	BaO	K_2O	Na_2O	Al_2O_3	SrO	CaO	MgO	Total	An	Ab	Or
0	65.391	0.419	9.608	4.560	19.336	0.003	0.501	0.000	99.950	2.481	40.866	56.653
10	65.376	0.421	9.668	4.495	19.611	0.167	0.457	0.000	100.327	2.273	40.464	57.263
20	65.501	0.425	9.832	4.453	19.768	0.063	0.484	0.000	100.658	2.390	39.796	57.814
30	65.973	0.333	9.827	4.569	19.033	0.000	0.400	0.000	100.267	1.964	40.592	57.444
40	65.987	0.340	9.570	4.315	19.499	0.000	0.390	0.000	100.233	1.990	39.853	58.156
50	65.156	0.409	9.901	4.440	19.587	0.000	0.416	0.000	100.041	2.055	39.698	58.246
60	64.959	0.317	9.543	4.564	19.293	0.022	0.422	0.000	99.252	2.105	41.206	56.689
70	65.167	0.332	9.552	4.352	19.440	0.016	0.481	0.000	99.472	2.438	39.917	57.645
80	66.050	0.366	9.806	4.722	20.004	0.080	0.467	0.000	101.627	2.257	41.305	56.438
90	64.922	0.359	9.552	4.500	19.318	0.052	0.468	0.000	99.303	2.342	40.748	56.910
100	65.045	0.322	9.647	4.506	19.658	0.016	0.442	0.000	99.768	2.201	40.603	57.196
110	65.214	0.325	9.580	4.524	19.306	0.000	0.465	0.000	99.546	2.318	40.815	56.867
120	64.495	0.375	9.616	4.502	19.565	0.000	0.468	0.000	99.153	2.333	40.604	57.063
130	65.221	0.347	9.565	4.027	19.151	0.123	0.467	0.000	99.033	2.440	38.068	59.493
140	65.129	0.344	9.441	4.440	19.497	0.070	0.474	0.000	99.527	2.400	40.683	56.917
160	64.698	0.375	9.385	4.287	20.139	0.000	0.498	0.012	99.526	2.563	39.927	57.510
170	65.153	0.383	9.140	4.467	19.408	0.000	0.490	0.000	99.173	2.518	41.548	55.934
190	65.119	0.423	9.702	4.231	19.553	0.010	0.490	0.000	99.660	2.488	38.869	58.644
200	65.233	0.419	9.784	4.328	19.524	0.000	0.452	0.000	99.872	2.268	39.291	58.442
220	65.422	0.468	9.730	4.367	19.541	0.093	0.477	0.000	100.230	2.389	39.583	58.028
230	64.548	0.457	9.704	4.347	19.196	0.000	0.478	0.000	98.862	2.402	39.533	58.065
250	65.380	0.483	9.784	4.421	19.525	0.053	0.472	0.000	100.250	2.346	39.760	57.895
260	64.853	0.555	9.595	4.529	19.493	0.066	0.467	0.000	99.690	2.325	40.801	56.874
270	64.974	0.500	9.360	4.323	19.528	0.026	0.489	0.000	99.332	2.513	40.207	57.279
280	64.926	0.482	9.175	4.245	20.145	0.000	0.581	0.003	99.689	3.028	40.036	56.936
290	63.841	0.537	9.386	4.731	19.108	0.087	0.498	0.000	98.320	2.461	42.310	55.229
300	66.347	0.555	9.619	4.452	20.112	0.027	0.450	0.000	101.694	2.255	40.364	57.381
310	64.365	0.550	9.414	4.678	19.674	0.000	0.539	0.017	99.369	2.667	41.880	55.453
320	65.019	0.554	9.515	4.417	19.854	0.000	0.492	0.002	99.985	2.483	40.340	57.177
330	64.261	0.562	9.619	4.294	19.380	0.000	0.473	0.018	98.739	2.401	39.451	58.147
340	64.467	0.590	9.507	4.276	19.526	0.000	0.495	0.009	99.002	2.532	39.575	57.893

For the analyses, FeO was set at 0.122 and TiO_2 was set at 0.01.

Table D.12. Electron Microprobe Traverse Analyses of Sanidine S6 from Gibbon River Sample GRWY7P (continued)

Length (μm)	SiO_2	BaO	K_2O	Na_2O	Al_2O_3	SrO	CaO	MgO	Total	An	Ab	Or
350	64.869	0.553	9.657	4.306	19.180	0.000	0.437	0.002	99.136	2.215	39.499	58.285
360	65.482	0.584	9.663	4.406	19.603	0.000	0.447	0.000	100.317	2.243	40.015	57.742
370	64.910	0.536	9.817	4.545	19.811	0.011	0.445	0.000	100.207	2.186	40.400	57.415
380	65.378	0.604	9.848	4.451	19.219	0.000	0.431	0.000	100.063	2.132	39.852	58.015
390	65.912	0.612	9.861	4.087	19.689	0.047	0.459	0.000	100.799	2.342	37.742	59.916
400	65.311	0.566	9.865	4.315	19.608	0.094	0.442	0.000	100.333	2.210	39.050	58.740
410	65.106	0.538	9.753	4.330	19.364	0.000	0.467	0.000	99.690	2.345	39.345	58.310
420	65.254	0.560	9.765	4.338	19.517	0.000	0.446	0.000	100.012	2.239	39.402	58.359
430	65.699	0.619	9.836	4.235	19.539	0.000	0.406	0.000	100.466	2.052	38.743	59.205
440	64.578	0.538	9.956	4.268	19.378	0.000	0.456	0.000	99.306	2.276	38.552	59.171
450	66.290	0.592	10.092	4.348	19.860	0.000	0.440	0.006	101.760	2.165	38.713	59.122
460	65.127	0.534	9.390	4.396	19.194	0.045	0.377	0.000	99.195	1.932	40.769	57.298
470	65.443	0.549	10.078	4.356	19.685	0.000	0.377	0.000	100.620	1.861	38.909	59.230
480	64.830	0.554	10.028	4.187	19.391	0.103	0.483	0.000	99.708	2.415	37.885	59.700
490	65.232	0.608	10.084	4.278	18.809	0.125	0.447	0.000	99.715	2.213	38.334	59.453
500	65.560	0.568	10.014	4.259	19.676	0.023	0.381	0.000	100.613	1.904	38.514	59.582
510	65.713	0.567	9.852	4.213	19.222	0.006	0.415	0.000	100.120	2.099	38.564	59.336
520	64.290	0.572	10.127	4.226	19.505	0.098	0.395	0.000	99.345	1.965	38.047	59.988
530	64.622	0.553	9.902	4.234	19.412	0.000	0.392	0.000	99.247	1.975	38.611	59.413
540	65.105	0.562	10.175	4.070	19.510	0.000	0.347	0.000	99.901	1.750	37.147	61.103
560	65.523	0.524	10.213	4.311	19.609	0.135	0.359	0.000	100.806	1.767	38.391	59.842
570	65.485	0.558	10.366	4.269	19.584	0.069	0.327	0.000	100.790	1.603	37.879	60.518
580	65.437	0.542	10.151	4.028	19.526	0.080	0.389	0.000	100.285	1.968	36.880	61.152
590	65.568	0.531	9.963	4.050	19.483	0.160	0.397	0.000	100.284	2.027	37.415	60.559
600	65.755	0.554	9.904	4.396	19.619	0.000	0.372	0.000	100.732	1.849	39.539	58.612
610	65.324	0.562	9.845	4.299	19.600	0.153	0.412	0.000	100.327	2.069	39.067	58.865

For the analyses, FeO was set at 0.122 and TiO_2 was set at 0.01.

Table D.13. Electron Microprobe Traverse Analyses of Plagioclase P1 from Gibbon River Sample GRWY7P

Length (μm)	SiO_2	BaO	K_2O	Na_2O	Al_2O_3	SrO	CaO	MgO	Total	An	Ab	Or
0	62.897	0.000	1.595	7.791	22.432	0.000	3.973	0.006	98.826	19.894	70.597	9.509
10	63.055	0.000	1.533	7.911	23.009	0.039	4.032	0.000	99.711	19.987	70.965	9.048
20	62.597	0.000	1.514	7.620	22.615	0.000	4.065	0.000	98.543	20.680	70.150	9.171
50	63.665	0.000	1.469	7.928	23.191	0.100	3.920	0.000	100.405	19.585	71.677	8.739
60	63.595	0.000	1.487	7.822	23.174	0.000	3.757	0.019	99.986	19.088	71.916	8.995
70	62.803	0.000	1.505	7.914	23.122	0.018	4.054	0.000	99.548	20.102	71.013	8.885
90	63.133	0.000	1.453	7.285	22.849	0.000	3.869	0.013	98.734	20.599	70.190	9.211
100	63.155	0.000	1.543	7.644	23.312	0.000	4.155	0.000	99.941	20.959	69.774	9.267
110	63.404	0.000	1.520	7.831	23.347	0.000	4.120	0.011	100.365	20.497	70.500	9.004
120	63.202	0.011	1.441	6.855	23.581	0.120	4.443	0.000	99.785	23.934	66.824	9.242
130	63.338	0.000	1.447	7.890	23.357	0.025	4.343	0.010	100.542	21.348	70.183	8.469
140	62.319	0.000	1.453	7.899	23.321	0.000	4.438	0.009	99.571	21.689	69.856	8.455
150	62.823	0.000	1.427	7.805	23.099	0.000	4.287	0.000	99.573	21.318	70.234	8.449
160	62.820	0.000	1.407	7.575	23.111	0.042	4.309	0.000	99.396	21.882	69.611	8.507
170	63.058	0.000	1.410	7.769	23.339	0.000	4.533	0.005	100.246	22.362	69.356	8.282
180	62.573	0.026	1.369	7.242	23.198	0.034	4.459	0.002	99.035	23.231	68.277	8.492
190	63.530	0.000	1.548	7.746	22.874	0.000	3.907	0.000	99.737	19.765	70.911	9.324
200	63.694	0.000	1.624	8.142	23.033	0.082	3.933	0.001	100.641	19.092	71.522	9.386
210	63.395	0.000	1.552	8.041	23.109	0.054	4.228	0.014	100.525	20.497	70.544	8.959
220	63.551	0.000	1.520	7.971	23.369	0.013	4.215	0.000	100.771	20.612	70.538	8.850
230	63.423	0.000	1.438	8.003	23.744	0.000	4.561	0.000	101.301	21.975	69.776	8.249
240	63.262	0.000	1.445	7.801	23.444	0.021	4.462	0.000	100.567	21.981	69.543	8.476
250	62.894	0.000	1.479	7.849	23.439	0.000	3.995	0.007	99.795	20.015	71.162	8.823
260	63.355	0.000	1.335	7.790	23.591	0.012	4.494	0.011	100.720	22.269	69.854	7.877
270	63.088	0.000	1.438	7.556	23.505	0.033	4.474	0.000	100.226	22.528	68.851	8.621
280	62.784	0.000	1.461	7.817	23.281	0.089	4.461	0.000	100.025	21.925	69.525	8.550
290	62.699	0.000	1.310	7.762	23.414	0.044	4.641	0.014	100.016	22.922	69.374	7.704
310	63.205	0.000	1.347	7.728	23.956	0.000	4.639	0.011	101.018	22.934	69.137	7.929
320	62.330	0.000	1.270	7.670	23.543	0.011	4.851	0.000	99.807	23.964	68.566	7.470
330	62.452	0.000	1.263	7.723	23.770	0.087	4.695	0.000	100.122	23.272	69.274	7.454
340	62.539	0.000	1.336	7.502	23.177	0.082	4.558	0.006	99.332	23.108	68.827	8.065

Table D.13. Electron Microprobe Traverse Analyses of Plagioclase P1 from Gibbon River Sample GRWY7P (continued)

Length (μm)	SiO_2	BaO	K_2O	Na_2O	Al_2O_3	SrO	CaO	MgO	Total	An	Ab	Or
360	62.513	0.001	1.313	7.607	23.396	0.000	4.677	0.000	99.639	23.378	68.808	7.814
370	62.546	0.000	1.260	7.723	23.725	0.035	4.693	0.000	100.114	23.269	69.293	7.438
380	63.062	0.000	1.349	7.723	23.700	0.000	4.644	0.004	100.614	22.961	69.098	7.941
390	62.686	0.000	1.336	7.658	23.713	0.035	4.525	0.004	100.089	22.655	69.381	7.964
400	62.042	0.000	1.301	7.673	23.670	0.000	4.461	0.001	99.280	22.422	69.792	7.786
410	62.505	0.000	1.314	7.640	23.380	0.015	4.698	0.000	99.684	23.387	68.825	7.788
420	63.158	0.000	1.265	7.309	23.774	0.030	4.705	0.033	100.406	24.206	68.046	7.749
430	62.416	0.000	1.310	7.478	23.732	0.000	4.850	0.010	99.928	24.320	67.858	7.821
440	62.046	0.000	1.236	7.592	23.953	0.000	5.059	0.002	100.020	24.959	67.781	7.261
450	63.730	0.000	1.364	7.915	23.772	0.084	4.689	0.000	101.686	22.722	69.408	7.870
460	62.850	0.000	1.380	7.758	23.385	0.000	4.354	0.000	99.859	21.731	70.068	8.201
470	62.806	0.000	1.267	7.698	23.549	0.000	4.534	0.001	99.987	22.701	69.746	7.553
480	63.172	0.000	1.297	7.830	24.406	0.062	4.965	0.000	101.864	24.010	68.522	7.468
490	62.629	0.000	1.309	7.662	23.571	0.056	4.457	0.001	99.817	22.419	69.742	7.840
530	61.860	0.000	1.259	7.419	22.808	0.070	4.652	0.003	98.203	23.763	68.580	7.657
540	62.214	0.000	1.275	7.479	23.634	0.000	4.588	0.005	99.327	23.360	68.910	7.729
550	61.767	0.000	1.203	7.488	23.620	0.000	4.743	0.015	98.968	24.045	68.694	7.261
560	61.530	0.000	1.199	7.499	23.500	0.000	4.752	0.000	98.612	24.061	68.711	7.228
570	61.413	0.000	1.196	7.647	23.769	0.000	4.610	0.000	98.767	23.198	69.636	7.166
590	62.042	0.000	1.215	7.476	23.745	0.000	5.113	0.014	99.737	25.453	67.346	7.201
600	62.136	0.000	1.100	7.393	23.729	0.000	4.994	0.018	99.502	25.373	67.972	6.654
610	62.467	0.000	1.173	7.625	24.052	0.066	4.948	0.000	100.463	24.564	68.502	6.934
620	62.519	0.000	1.217	7.760	23.689	0.000	4.753	0.000	100.070	23.478	69.365	7.158
630	62.451	0.000	1.230	7.599	23.585	0.000	4.738	0.000	99.735	23.745	68.916	7.340
650	62.487	0.000	1.263	7.831	23.746	0.016	4.983	0.001	100.459	24.122	68.599	7.280
660	62.410	0.000	1.297	7.833	23.672	0.038	4.857	0.000	100.239	23.605	68.890	7.505
670	61.993	0.000	1.371	7.637	23.538	0.033	4.512	0.001	99.217	22.600	69.223	8.177
680	62.592	0.000	1.263	7.817	23.752	0.159	4.657	0.008	100.380	22.933	69.661	7.405
690	62.685	0.000	1.287	7.168	23.975	0.000	4.918	0.021	100.186	25.322	66.788	7.890
700	62.794	0.000	1.310	7.898	23.637	0.050	4.739	0.006	100.566	23.015	69.410	7.575

Table D.13. Electron Microprobe Traverse Analyses of Plagioclase P1 from Gibbon River Sample GRWY7P (continued)

Length (μm)	SiO_2	BaO	K_2O	Na_2O	Al_2O_3	SrO	CaO	MgO	Total	An	Ab	Or
710	61.844	0.000	1.259	7.704	23.787	0.058	4.860	0.000	99.644	23.941	68.675	7.384
720	61.673	0.000	1.318	7.741	23.327	0.000	4.502	0.022	98.715	22.421	69.764	7.815
730	62.710	0.000	1.294	7.640	23.698	0.061	4.646	0.004	100.185	23.216	69.085	7.699
740	62.302	0.000	1.320	7.541	23.582	0.000	4.690	0.013	99.580	23.558	68.547	7.895
750	62.697	0.000	1.363	7.804	23.565	0.000	4.691	0.000	100.252	22.954	69.104	7.941
780	62.102	0.000	1.392	7.774	23.051	0.000	4.360	0.000	98.811	21.707	70.041	8.252
790	62.554	0.000	1.422	7.864	23.223	0.000	4.303	0.000	99.498	21.274	70.356	8.371
800	62.437	0.000	1.340	7.606	23.268	0.024	4.422	0.008	99.237	22.354	69.580	8.066
810	62.185	0.000	1.398	7.775	23.177	0.000	4.456	0.000	99.123	22.070	69.686	8.244
820	62.682	0.002	1.378	7.558	23.429	0.000	4.626	0.000	99.807	23.195	68.578	8.227
830	62.241	0.000	1.353	7.616	23.345	0.000	4.558	0.011	99.256	22.846	69.079	8.075
840	61.526	0.000	1.389	7.727	23.238	0.008	4.483	0.005	98.508	22.282	69.498	8.220
850	62.448	0.000	1.295	7.621	22.897	0.000	4.476	0.000	98.869	22.596	69.620	7.784
860	62.239	0.000	1.324	7.575	23.111	0.132	4.515	0.007	99.035	22.804	69.234	7.962
870	62.013	0.000	1.361	7.659	23.379	0.052	4.279	0.000	98.875	21.656	70.143	8.201
880	62.182	0.023	1.424	7.832	23.180	0.002	4.352	0.000	99.127	21.523	70.092	8.385
890	61.805	0.000	1.412	7.409	23.166	0.026	4.467	0.006	98.423	22.842	68.560	8.597
900	62.531	0.000	1.595	7.864	23.002	0.147	3.977	0.000	99.248	19.779	70.776	9.445
910	62.760	0.002	1.631	7.610	22.797	0.000	3.927	0.007	98.866	19.995	70.118	9.888
920	63.057	0.000	1.520	7.866	22.973	0.000	4.071	0.000	99.619	20.238	70.764	8.997
930	61.476	0.000	1.450	7.617	23.892	0.007	4.218	0.003	98.795	21.380	69.868	8.751
940	63.194	0.000	1.513	7.742	23.102	0.000	4.275	0.000	99.958	21.283	69.749	8.969
950	62.898	0.000	1.565	7.963	23.156	0.061	4.103	0.016	99.894	20.136	70.719	9.145
960	63.338	0.014	1.589	7.656	23.323	0.130	4.100	0.009	100.291	20.659	69.808	9.533
970	61.886	0.000	1.610	7.790	22.981	0.000	4.174	0.018	98.591	20.676	69.829	9.496
980	62.793	0.000	1.629	7.741	22.837	0.000	4.117	0.009	99.258	20.518	69.815	9.667
990	63.013	0.000	1.644	7.809	22.746	0.077	3.906	0.000	99.327	19.535	70.675	9.790
1000	63.028	0.000	1.633	7.931	22.856	0.038	3.957	0.003	99.578	19.537	70.862	9.600
1010	62.983	0.000	1.643	7.904	22.407	0.000	3.741	0.000	98.810	18.705	71.514	9.781
1020	61.895	0.000	1.526	7.867	22.755	0.049	3.815	0.008	98.047	19.202	71.653	9.145

For the analyses, FeO was set at 0.122 and TiO_2 was set at 0.01.

APPENDIX E

ELECTRON MICROPROBE POINT ANALYSES OF CRYSTAL SPRING MINGLED RHYOLITE SAMPLES

Table E.1. Electron Microprobe Core and Rim Point Analyses of Plagioclase from Crystal Spring Sample CSWY1

Analysis No.	SiO_2	FeO	K_2O	Na_2O	Al_2O_3	TiO_2	CaO	MgO	Total	An	Ab	Or
P1C1	50.750	0.337	0.102	3.269	31.261	0.040	14.460	0.201	100.420	70.55	28.86	0.59
P1C2	50.687	0.384	0.136	3.047	30.990	0.041	14.275	0.190	99.750	71.55	27.64	0.81
P1C3	50.612	0.404	0.065	2.812	31.101	0.037	14.453	0.185	99.669	73.67	25.94	0.39
P1C4	49.783	0.367	0.170	3.082	30.554	0.050	14.478	0.190	98.674	71.47	27.53	1.00
P2C1	50.453	0.534	0.064	3.341	30.867	0.025	14.408	0.195	99.887	70.18	29.45	0.37
P2C2	50.362	0.521	0.086	3.171	31.130	0.000	14.588	0.205	100.063	71.41	28.09	0.50
P2C3	51.982	0.539	0.157	3.668	30.445	0.067	13.719	0.219	100.796	66.78	32.31	0.91
P2C4	50.130	0.463	0.124	3.075	31.777	0.027	15.258	0.213	101.067	72.76	26.54	0.70
Core Ave.	50.595	0.444	0.113	3.183	31.016	0.036	14.455	0.200		71.05	28.29	0.66
P1R1	49.524	0.351	0.227	4.262	31.191	0.033	14.654	0.167	100.409	64.74	34.07	1.19
P1R2	50.684	0.389	0.200	3.697	31.287	0.039	14.451	0.201	100.948	67.59	31.29	1.11
P1R3	50.640	0.365	0.092	3.227	31.582	0.027	14.638	0.205	100.776	71.10	28.37	0.53
P1R4	51.082	0.497	0.097	3.212	31.357	0.046	14.719	0.213	101.223	71.29	28.15	0.56
P1R5	50.581	0.358	0.059	3.172	31.579	0.035	14.749	0.193	100.726	71.74	27.92	0.34
P1R6	50.851	0.367	0.078	3.208	31.522	0.030	14.786	0.187	101.029	71.48	28.07	0.45
P1R7	51.879	0.543	0.159	3.833	30.287	0.072	13.723	0.195	100.691	65.82	33.27	0.91
P2R1	50.316	0.488	0.109	3.223	31.361	0.037	14.670	0.197	100.401	71.10	28.27	0.63
P2R2	51.416	0.543	0.175	3.742	29.928	0.051	14.024	0.202	100.081	66.77	32.24	0.99
Rim Ave.	50.775	0.433	0.133	3.508	31.122	0.041	14.490	0.196		69.07	30.18	0.75

Table E.2. Electron Microprobe Core Point Analyses of Plagioclase from Crystal Spring Sample CSWY1E

Analysis No.	SiO_2	FeO	K_2O	Na_2O	Al_2O_3	TiO_2	CaO	MgO	Total	An	Ab	Or
P1C1	49.905	0.374	0.055	3.282	31.036	0.043	14.820	0.180	99.695	71.17	28.52	0.31
P1C2	50.309	0.414	0.068	2.923	31.877	0.023	15.260	0.189	101.063	73.97	25.64	0.39
P1C3	51.516	0.526	0.111	3.574	30.799	0.056	14.471	0.190	101.243	68.68	30.69	0.63
P1C4	51.407	0.482	0.110	3.478	30.927	0.073	14.331	0.183	100.991	69.05	30.32	0.63
P2C2	50.598	0.422	0.060	3.174	31.523	0.049	15.000	0.189	101.015	72.06	27.59	0.34
P2C3	50.661	0.398	0.071	3.310	31.411	0.075	14.520	0.163	100.609	70.50	29.08	0.41
P2C4	50.688	0.371	0.092	3.129	31.790	0.062	15.013	0.180	101.325	72.23	27.24	0.53
P3C1	49.860	0.532	0.101	3.107	32.036	0.054	15.375	0.120	101.185	72.81	26.62	0.57
P3C3	50.986	0.426	0.097	3.297	31.387	0.070	14.963	0.168	101.394	71.10	28.35	0.55
P3C4	51.108	0.476	0.077	3.158	31.684	0.044	14.985	0.160	101.692	72.07	27.49	0.44
P4C1	51.202	0.403	0.064	3.493	31.002	0.047	14.786	0.163	101.160	69.80	29.84	0.36
P4C3	49.913	0.506	0.058	3.322	31.855	0.034	14.801	0.175	100.664	70.88	28.79	0.33
P4C4	50.587	0.450	0.055	3.178	32.158	0.035	15.215	0.172	101.850	72.34	27.34	0.31
Core Ave.	50.672	0.445	0.078	3.263	31.499	0.051	14.888	0.172		71.28	28.27	0.45

Table E.3. Electron Microprobe Rim Point Analyses of Plagioclase from Crystal Spring Sample CSWY1E

Analysis No.	SiO_2	FeO	K_2O	Na_2O	Al_2O_3	TiO_2	CaO	MgO	Total	An	Ab	Or
P1R1	50.584	0.538	0.083	3.356	31.651	0.066	15.019	0.156	101.453	70.87	28.66	0.47
P1R2	53.791	0.834	0.172	4.399	28.727	0.122	11.257	0.092	99.394	57.96	40.99	1.05
P1R3	51.343	0.616	0.100	3.384	31.240	0.041	13.999	0.172	100.895	69.16	30.25	0.59
P1R4	50.651	0.764	0.148	3.751	30.769	0.075	13.903	0.117	100.178	66.63	32.53	0.84
P2R1	51.292	0.704	0.178	3.779	29.851	0.081	13.482	0.189	99.556	65.66	33.31	1.03
P2R2	52.486	0.767	0.164	3.785	30.312	0.055	13.628	0.143	101.340	65.92	33.13	0.94
P2R3	53.245	0.713	0.151	4.195	30.067	0.089	13.121	0.124	101.705	62.80	36.34	0.86
P2R4	52.877	1.074	0.230	4.435	29.387	0.235	12.673	0.101	101.012	60.43	38.27	1.31
P3R1	51.718	0.690	0.120	3.687	31.257	0.090	14.193	0.130	101.885	67.56	31.76	0.68
P3R2	52.538	0.737	0.156	3.729	30.411	0.087	13.409	0.143	101.210	65.92	33.17	0.91
P3R3	54.519	0.912	0.340	4.982	28.981	0.101	11.677	0.080	101.592	55.35	42.73	1.92
P3R4	51.543	2.114	0.181	4.882	25.032	4.720	10.330	0.072	98.874	53.30	45.59	1.11
P4R1	52.960	1.142	0.157	4.443	29.918	0.094	13.066	0.132	101.912	61.36	37.76	0.88
P4R2	52.693	0.795	0.186	4.146	29.676	0.071	12.999	0.144	100.710	62.73	36.20	1.07
ResP1	50.899	0.391	0.054	2.991	31.540	0.058	14.941	0.189	101.063	73.18	26.51	0.31
ResP2	50.982	0.469	0.091	3.215	31.411	0.051	14.887	0.190	101.296	71.53	27.95	0.52
ResP3	52.560	0.830	0.160	4.170	29.535	0.118	12.329	0.180	99.882	61.44	37.61	0.95
ResP4	53.510	0.768	0.266	4.747	29.476	0.029	12.108	0.057	100.961	57.62	40.88	1.51
Rim Ave.	52.233	0.825	0.163	4.004	29.958	0.344	13.168	0.134		63.86	35.20	0.94

Table E.4. Electron Microprobe Core and Rim Point Analyses of Olivine from Crystal Spring Sample CSWY1E

Analysis No.	SiO2	MnO	CaO	Na2O	Al2O3	FeO	TiO2	MgO	Total	Fo	Fa	Tp
Ol11	37.581	0.313	0.249	0.012	0.018	22.687	0.010	39.990	100.860	75.61	24.06	0.34
Ol12	39.106	0.264	0.234	0.002	0.049	19.859	0.013	40.995	100.522	78.41	21.30	0.29
Ol13	38.537	0.245	0.214	0.002	0.036	17.875	0.010	43.714	100.633	81.13	18.61	0.26
Ol14	38.526	0.273	0.251	0.000	0.042	18.089	0.000	43.392	100.573	80.81	18.90	0.29
Ol15	38.299	0.268	0.231	0.000	0.039	19.262	0.033	42.057	100.189	79.33	20.38	0.29
Ol16	37.979	0.323	0.223	0.012	0.019	21.707	0.000	39.751	100.014	76.28	23.36	0.35
Ol17	37.922	0.342	0.194	0.025	0.029	22.729	0.000	38.534	99.775	74.86	24.77	0.38
Ol18	36.294	0.442	0.275	0.054	0.028	31.248	0.007	30.803	99.151	63.41	36.08	0.52
Ol19	38.103	0.301	0.243	0.009	0.039	19.698	0.004	41.904	100.301	78.88	20.80	0.32
Ol2R11	36.104	0.488	0.213	0.007	0.045	31.713	0.039	31.719	100.328	63.71	35.73	0.56
Ol2C12	37.464	0.357	0.218	0.034	0.061	22.936	0.023	39.741	100.834	75.26	24.36	0.38
Ol2C13	37.583	0.324	0.237	0.000	0.032	22.118	0.029	39.785	100.108	75.96	23.69	0.35
Ol2C14	37.484	0.285	0.227	0.002	0.029	21.220	0.008	39.589	98.844	76.64	23.04	0.31
Ol2C15	37.641	0.341	0.218	0.013	0.037	22.089	0.000	39.330	99.669	75.76	23.87	0.37
Ol2C16	36.120	0.487	0.228	0.013	0.033	29.771	0.022	32.601	99.275	65.76	33.68	0.56
Ol2R17	35.640	0.517	0.252	0.019	0.038	32.509	0.064	30.410	99.449	62.14	37.26	0.60
Ol3C18	38.098	0.295	0.210	0.000	0.047	20.879	0.009	40.791	100.329	77.45	22.23	0.32
Ol3C19	37.970	0.268	0.218	0.024	0.050	21.029	0.009	41.035	100.603	77.45	22.26	0.29
Ol3R20	35.514	0.524	0.235	0.000	0.019	33.951	0.046	29.480	99.769	60.38	39.01	0.61
Ol3R21	36.501	0.405	0.254	0.009	0.001	30.085	0.015	32.769	100.039	65.70	33.83	0.46
Ol4C22	37.804	0.289	0.218	0.000	0.026	21.064	0.009	41.103	100.513	77.43	22.26	0.31
Ol4C23	37.943	0.338	0.229	0.015	0.042	21.021	0.011	39.797	99.396	76.86	22.77	0.37
Ol4C24	37.193	0.389	0.219	0.000	0.042	25.301	0.000	36.945	100.089	71.94	27.63	0.43
Ol4R25	35.278	0.528	0.259	0.012	0.000	33.869	0.011	28.306	98.263	59.46	39.91	0.63
Ol4R26	36.075	0.500	0.224	0.000	0.013	30.947	0.030	31.217	99.006	63.89	35.53	0.58

Table E.4. Electron Microprobe Core and Rim Point Analyses of Olivine from Crystal Spring Sample CSWY1E (continued)

Analysis No.	SiO_2	MnO	CaO	Na_2O	Al_2O_3	FeO	TiO_2	MgO	Total	Fo	Fa	Tp
Ol5C27	38.232	0.304	0.259	0.000	0.023	20.309	0.000	41.119	100.246	78.05	21.62	0.33
Ol5C28	38.247	0.282	0.219	0.000	0.026	19.220	0.000	42.034	100.028	79.35	20.35	0.30
Ol5C29	38.183	0.270	0.207	0.017	0.022	20.883	0.000	40.373	99.955	77.28	22.42	0.29
Ol5R30	35.059	0.552	0.280	0.001	0.000	35.790	0.019	28.033	99.734	57.89	41.46	0.65
Ol5R31	35.111	0.523	0.269	0.018	0.015	37.555	0.060	25.749	99.300	54.66	44.71	0.63
Ol5R32	36.986	0.372	0.187	0.026	0.020	27.173	0.019	35.465	100.248	69.65	29.93	0.42
Ol6C33	38.446	0.253	0.238	0.038	0.067	18.904	0.000	42.539	100.485	79.83	19.90	0.27
Ol6C34	38.695	0.253	0.190	0.033	0.026	19.295	0.030	41.820	100.342	79.23	20.50	0.27
Ol6C35	38.334	0.302	0.244	0.014	0.034	21.381	0.016	41.098	101.423	77.16	22.52	0.32
Ol6R36	36.426	0.435	0.208	0.000	0.025	30.926	0.016	32.300	100.336	64.74	34.77	0.50
Ol6R37	36.658	0.438	0.239	0.029	0.036	28.476	0.000	34.345	100.221	67.92	31.59	0.49
Ol6R38	35.367	0.465	0.224	0.030	0.060	32.231	0.076	30.420	98.873	62.38	37.07	0.54
Average	37.257	0.366	0.231	0.013	0.032	25.022	0.017	37.055		71.96	27.63	0.41
Core Ave. [a]	37.954	0.303	0.223	0.013	0.038	21.177	0.010	40.473		77.04	22.63	0.33
Rim Ave. [b]	35.911	0.480	0.236	0.013	0.023	31.923	0.032	30.986		62.95	36.50	0.56

[a] Core Average is samples with a "C" in the analysis ID.
[b] Rim Average is of samples with a "R" in the analysis ID.

Table E.5. Electron Microprobe Analyses of Pyroxene from Crystal Spring Sample CSWY1E

Analysis No.	SiO_2	MnO	CaO	Na_2O	Al_2O_3	FeO	TiO_2	MgO	Total	Wo	En	Fs	Ac
Pyrx1	50.704	0.305	18.290	0.275	0.194	13.630	0.959	15.006	99.363	36.26	41.40	21.35	0.99
Pyrx2	50.734	0.305	18.347	0.264	0.176	12.470	1.129	15.899	99.324	36.10	43.54	19.42	0.94
Pyrx3	51.016	0.227	18.018	0.235	0.188	11.567	0.894	16.638	98.783	35.53	45.65	17.98	0.84
Pyrx5	51.156	0.235	18.754	0.261	0.133	11.172	0.855	16.244	98.810	37.02	44.63	17.42	0.93
Pyrx6	51.028	0.221	18.705	0.259	0.166	10.628	0.876	16.553	98.436	36.97	45.53	16.58	0.93
Pyrx7	50.936	0.261	18.587	0.253	0.185	11.097	0.802	16.524	98.645	36.58	45.25	17.27	0.90
Pyrx8	51.474	0.240	18.864	0.267	0.170	11.044	0.843	16.131	99.033	37.33	44.42	17.29	0.96
Pyrx9	51.969	0.220	16.799	0.173	0.149	11.196	0.730	17.844	99.080	33.07	48.89	17.42	0.62
Pyrx10	51.560	0.244	18.218	0.241	2.387	9.609	0.807	17.048	100.114	36.42	47.42	15.29	0.87
Pyrx11	50.645	0.162	19.962	0.272	3.165	8.758	1.070	15.434	99.468	40.85	43.95	14.19	1.01
Pyrx12	50.832	0.240	19.238	0.266	2.294	10.208	0.903	15.421	99.402	39.03	43.54	16.46	0.98
Pyrx13	52.439	0.244	18.145	0.225	1.756	9.310	0.721	16.760	99.600	36.78	47.28	15.11	0.83
Pyrx14	51.508	0.221	18.527	0.230	1.964	9.838	0.836	16.478	99.602	37.29	46.15	15.73	0.84
Pyrx15	51.094	0.200	19.323	0.272	2.149	9.231	0.814	16.001	99.084	39.11	45.07	14.82	1.00
Pyrx16	51.738	0.247	18.227	0.244	2.007	9.594	0.916	16.743	99.716	36.73	46.95	15.43	0.89
Pyrx17	51.530	0.215	18.412	0.205	2.199	9.407	0.850	15.720	98.538	38.22	45.41	15.60	0.77
Pyrx18	52.991	0.528	3.838	0.065	0.526	21.902	0.361	20.755	100.966	7.63	57.41	34.73	0.23
Pyrx19	50.048	0.217	18.155	0.262	2.279	11.237	1.072	15.218	98.488	37.28	43.49	18.26	0.97
Average [a]	51.201	0.236	18.504	0.247	1.268	10.588	0.887	16.215		37.09	45.21	16.80	0.90

[a] Average does not include analysis Pyrx18.

Table E.6. Electron Microprobe Analyses of Fe-Oxide from Crystal Spring Sample CSWY1E

Analysis No.	SiO_2	MnO	CaO	Na_2O	Al_2O_3	FeO	TiO_2	MgO	Total
Fe1	0.110	0.360	0.000	0.000	1.694	75.166	19.976	1.460	98.766
Fe2	0.090	0.375	0.000	0.005	1.747	78.337	18.359	1.290	100.203
Fe3	0.083	0.419	0.000	0.011	1.685	74.175	21.641	1.834	99.848
Fe4	0.052	0.330	0.000	0.005	2.198	76.912	18.041	1.366	98.904
Fe6	0.077	0.488	0.027	0.000	2.019	67.330	26.613	2.866	99.420
Fe8	0.066	0.332	0.000	0.000	1.869	76.814	18.701	1.167	98.949
Fe11	0.090	0.331	0.021	0.000	1.995	73.246	20.938	1.579	98.200
Fe14	0.055	0.406	0.000	0.010	1.730	75.755	19.835	1.341	99.132
Fe15	0.084	0.426	0.000	0.000	1.747	75.451	20.516	1.486	99.710
Average	0.079	0.385	0.005	0.003	1.854	74.798	20.513	1.599	

APPENDIX F

ELECTRON MICROPROBE TRAVERSE ANALYSES OF CRYSTAL SPRING MINGLED RHYOLITE SAMPLES

Table F.1. Electron Microprobe Traverse Analyses of Plagioclase P1, Traverse A from Crystal Spring Sample CSWY1E

Length (μm)	SiO_2	BaO	K_2O	Na_2O	Al_2O_3	SrO	CaO	MgO	Total	An	Ab	Or
0	52.090	0.000	0.437	4.433	29.055	0.000	12.068	0.085	98.300	58.553	38.922	2.525
20	50.520	0.000	0.161	3.223	30.832	0.044	14.046	0.191	99.149	69.985	29.060	0.955
30	50.335	0.000	0.146	3.013	31.101	0.000	14.455	0.229	99.411	71.983	27.152	0.866
40	49.999	0.000	0.197	3.461	30.690	0.000	13.833	0.222	98.534	68.040	30.806	1.154
50	50.071	0.000	0.421	4.535	29.762	0.000	13.706	0.221	98.848	61.150	36.614	2.236
100	49.732	0.000	0.430	4.251	30.842	0.000	14.170	0.178	99.735	63.331	34.381	2.288
110	49.773	0.000	0.259	4.276	30.560	0.000	14.074	0.187	99.261	63.625	34.981	1.394
120	50.597	0.000	0.132	3.371	31.370	0.017	14.297	0.227	100.143	69.557	29.678	0.765
130	51.223	0.000	0.117	2.962	31.759	0.000	14.537	0.200	100.930	72.553	26.752	0.695
140	51.049	0.000	0.079	3.197	31.813	0.000	14.326	0.213	100.809	70.902	28.633	0.466
150	51.293	0.000	0.075	2.830	31.721	0.000	14.567	0.218	100.836	73.654	25.894	0.452
160	50.397	0.000	0.139	3.037	31.729	0.129	14.570	0.193	100.326	72.017	27.165	0.818
170	50.592	0.000	0.097	3.074	31.504	0.000	14.593	0.186	100.178	71.989	27.442	0.570
180	50.193	0.000	0.086	3.086	31.859	0.000	14.364	0.182	99.902	71.638	27.852	0.511
190	50.439	0.000	0.081	3.021	31.717	0.003	13.768	0.177	99.338	71.221	28.280	0.499
200	50.933	0.000	0.098	3.171	31.612	0.000	14.471	0.188	100.605	71.195	28.231	0.574
210	50.813	0.000	0.079	3.116	31.768	0.107	14.466	0.190	100.671	71.618	27.916	0.466
220	50.607	0.000	0.094	3.294	31.546	0.061	14.399	0.173	100.306	70.336	29.117	0.547
230	50.734	0.000	0.090	3.073	31.248	0.049	14.530	0.197	100.053	71.937	27.532	0.531
240	50.747	0.000	0.085	3.102	31.571	0.020	13.862	0.198	99.717	70.809	28.674	0.517
260	50.524	0.000	0.086	3.163	31.299	0.101	14.304	0.177	99.786	71.057	28.434	0.509
270	50.885	0.000	0.083	3.085	31.294	0.005	14.198	0.218	99.900	71.420	28.083	0.497
280	50.790	0.000	0.091	3.036	31.499	0.030	14.548	0.195	100.321	72.197	27.265	0.538
290	50.765	0.000	0.078	3.180	31.727	0.000	14.539	0.204	100.625	71.317	28.227	0.456
300	50.118	0.000	0.083	3.218	30.964	0.061	14.586	0.187	99.349	71.123	28.395	0.482
320	50.012	0.000	0.105	3.185	31.532	0.089	14.366	0.197	99.618	70.927	28.456	0.617
330	50.577	0.000	0.077	3.228	31.412	0.070	14.507	0.187	100.190	70.973	28.578	0.449
340	50.737	0.000	0.123	3.184	31.068	0.027	14.176	0.176	99.623	70.583	28.688	0.729
360	50.309	0.000	0.105	2.667	31.298	0.049	14.112	0.184	98.856	74.027	25.317	0.656
370	50.682	0.000	0.103	2.653	31.658	0.035	14.397	0.187	99.847	74.517	24.849	0.635

For the analyses, FeO was set at 0.122 and TiO_2 was set at 0.01.

Table F.1. Electron Microprobe Traverse Analyses of Plagioclase P1, Traverse A from Crystal Spring Sample CSWY1E (continued)

Length (μm)	SiO_2	BaO	K_2O	Na_2O	Al_2O_3	SrO	CaO	MgO	Total	An	Ab	Or
380	50.635	0.000	0.099	2.759	31.201	0.227	14.329	0.170	99.552	73.710	25.683	0.606
390	50.866	0.000	0.085	2.776	31.483	0.140	14.259	0.186	99.927	73.562	25.916	0.522
400	50.284	0.000	0.149	3.669	31.010	0.042	14.445	0.201	99.932	67.938	31.227	0.834
410	49.576	0.000	0.348	4.842	30.642	0.010	13.913	0.160	99.623	60.257	37.949	1.795
420	48.974	0.000	0.286	3.819	30.666	0.041	14.261	0.171	98.350	66.292	32.125	1.583
430	51.071	0.000	0.086	2.896	31.412	0.000	14.082	0.194	99.873	72.494	26.979	0.527
440	50.390	0.000	0.099	2.867	31.224	0.041	14.556	0.193	99.502	73.286	26.121	0.593
450	50.331	0.000	0.077	2.820	31.537	0.000	14.026	0.191	99.114	72.973	26.550	0.477
460	50.979	0.000	0.082	3.083	31.529	0.008	14.439	0.168	100.420	71.780	27.735	0.485
470	50.939	0.000	0.081	3.232	31.834	0.000	14.521	0.191	100.930	70.951	28.577	0.471
480	49.663	0.000	0.161	3.567	31.383	0.076	14.016	0.192	99.190	67.833	31.240	0.928
490	50.319	0.000	0.112	3.248	31.575	0.000	14.281	0.191	99.858	70.378	28.965	0.657
500	50.362	0.000	0.099	3.144	31.422	0.030	14.400	0.199	99.788	71.261	28.155	0.583
510	50.350	0.000	0.080	2.985	31.458	0.000	14.460	0.211	99.676	72.456	27.067	0.477
520	50.455	0.000	0.157	3.697	30.457	0.035	14.214	0.187	99.334	67.393	31.720	0.886
530	50.447	0.000	0.089	2.914	30.800	0.000	14.233	0.212	98.827	72.572	26.887	0.540
540	50.022	0.000	0.170	3.719	30.800	0.076	13.990	0.197	99.106	66.866	32.166	0.967
550	49.620	0.000	0.167	3.209	31.298	0.000	14.800	0.198	99.424	71.134	27.911	0.956
560	48.993	0.000	0.075	2.741	31.405	0.005	14.716	0.215	98.282	74.453	25.095	0.452
590	49.820	0.000	0.070	2.749	31.636	0.076	14.497	0.201	99.181	74.135	25.439	0.426
600	49.922	0.000	0.109	2.819	31.511	0.000	13.967	0.201	98.661	72.752	26.572	0.676
610	50.664	0.000	0.164	3.353	30.986	0.066	14.040	0.207	99.612	69.153	29.886	0.962
620	51.168	0.000	0.219	3.695	30.801	0.000	13.645	0.188	99.848	66.263	32.471	1.266
640	51.037	0.000	0.252	3.865	30.871	0.000	13.649	0.151	99.957	65.171	33.396	1.433
650	51.087	0.000	0.319	3.914	30.266	0.161	13.330	0.149	99.358	64.109	34.064	1.827
660	53.230	0.000	0.369	4.370	28.948	0.097	11.536	0.211	98.893	58.018	39.772	2.210
670	54.515	0.000	0.435	5.023	28.490	0.075	10.741	0.049	99.460	52.785	44.670	2.545

For the analyses, FeO was set at 0.122 and TiO_2 was set at 0.01.

Table F.2. Electron Microprobe Traverse Analyses of Plagioclase P1, Traverse B from Crystal Spring Sample CSWY1E

Length (μm)	SiO_2	BaO	K_2O	Na_2O	Al_2O_3	SrO	CaO	MgO	Total	An	Ab	Or
0	51.031	0.000	0.153	3.286	31.018	0.000	14.297	0.173	100.090	69.996	29.113	0.892
5	50.273	0.000	0.126	2.951	31.487	0.000	14.799	0.180	99.948	72.940	26.320	0.739
10	49.909	0.000	0.133	3.174	31.538	0.000	14.271	0.182	99.339	70.743	28.472	0.785
15	50.606	0.000	0.097	3.182	31.911	0.057	14.625	0.189	100.799	71.346	28.091	0.563
20	50.474	0.000	0.075	3.095	31.560	0.034	14.556	0.176	100.102	71.895	27.663	0.441
25	51.100	0.000	0.075	3.225	31.687	0.000	14.601	0.182	101.002	71.133	28.432	0.435
30	51.151	0.000	0.088	3.084	31.746	0.025	14.476	0.220	100.922	71.800	27.681	0.520
35	50.879	0.000	0.078	3.230	31.792	0.000	14.296	0.203	100.610	70.654	28.887	0.459
40	49.990	0.000	0.316	4.128	30.987	0.000	14.174	0.195	99.922	64.368	33.924	1.709
45	50.688	0.000	0.119	3.185	31.767	0.043	14.248	0.197	100.379	70.698	28.599	0.703
50	51.164	0.000	0.107	3.213	31.906	0.020	14.466	0.204	101.212	70.885	28.491	0.624
55	51.304	0.000	0.093	3.119	32.006	0.095	14.613	0.198	101.560	71.745	27.711	0.544
60	50.993	0.000	0.102	3.177	31.871	0.005	14.495	0.188	100.963	71.174	28.230	0.596
65	50.988	0.000	0.076	3.068	31.766	0.080	14.177	0.167	100.454	71.531	28.012	0.457
70	50.896	0.000	0.098	3.107	31.710	0.000	14.050	0.214	100.207	70.998	28.412	0.590
75	50.582	0.000	0.082	3.238	31.600	0.061	14.412	0.180	100.287	70.754	28.767	0.479
80	50.795	0.000	0.079	3.251	31.879	0.000	14.344	0.168	100.648	70.587	28.950	0.463
85	51.125	0.000	0.101	3.210	32.139	0.000	14.635	0.219	101.561	71.168	28.248	0.585
90	50.650	0.000	0.206	3.707	31.710	0.050	13.998	0.226	100.679	66.811	32.018	1.171
130	50.001	0.000	0.330	4.700	31.555	0.106	13.407	0.180	100.411	60.107	38.131	1.762
145	50.277	0.000	0.090	3.142	31.404	0.049	14.132	0.219	99.445	70.926	28.536	0.538
150	50.128	0.000	0.074	2.834	30.835	0.000	14.144	0.191	98.338	73.056	26.489	0.455
155	50.508	0.000	0.086	3.173	31.484	0.020	14.592	0.213	100.208	71.402	28.097	0.501
160	50.808	0.000	0.108	3.160	31.392	0.000	14.505	0.189	100.294	71.271	28.097	0.632
165	50.627	0.000	0.081	3.269	31.845	0.000	14.191	0.177	100.322	70.242	29.281	0.477
170	50.628	0.000	0.093	3.085	31.393	0.000	14.609	0.179	100.119	71.957	27.498	0.545
175	49.830	0.000	0.112	2.639	31.307	0.000	14.423	0.182	98.625	74.607	24.703	0.690
180	51.600	0.000	0.099	2.666	31.920	0.010	14.672	0.209	101.308	74.803	24.597	0.601
185	50.648	0.000	0.074	2.638	31.772	0.109	14.457	0.194	100.024	74.834	24.710	0.456
190	50.888	0.000	0.074	2.608	31.528	0.000	14.408	0.205	99.843	74.981	24.561	0.459
195	50.973	0.000	0.075	2.572	31.576	0.133	14.273	0.179	99.913	75.055	24.475	0.470

For the analyses, FeO was set at 0.122 and TiO_2 was set at 0.01.

Table F.2. Electron Microprobe Traverse Analyses of Plagioclase P1, Traverse B from Crystal Spring Sample CSWY1E (continued)

Length (μm)	SiO_2	BaO	K_2O	Na_2O	Al_2O_3	SrO	CaO	MgO	Total	An	Ab	Or
200	50.416	0.000	0.076	2.418	31.516	0.000	14.460	0.190	99.208	76.402	23.120	0.478
240	49.824	0.000	0.079	2.458	31.241	0.000	14.385	0.201	98.320	76.002	23.501	0.497
245	50.514	0.000	0.088	2.343	31.489	0.000	14.481	0.189	99.236	76.921	22.522	0.557
250	50.533	0.000	0.075	3.239	31.440	0.000	14.401	0.201	100.021	70.761	28.800	0.439
255	50.836	0.000	0.084	3.132	31.675	0.137	14.257	0.218	100.471	71.197	28.304	0.499
260	50.890	0.000	0.070	3.187	31.339	0.061	14.041	0.189	99.909	70.588	28.993	0.419
265	50.540	0.000	0.093	3.157	31.451	0.019	14.371	0.211	99.974	71.162	28.289	0.548
270	50.768	0.000	0.095	2.790	31.368	0.049	14.377	0.209	99.788	73.581	25.840	0.579
280	49.928	0.000	0.083	3.364	31.188	0.000	14.632	0.199	99.526	70.284	29.241	0.475
295	50.624	0.000	0.067	3.197	31.326	0.003	14.200	0.198	99.747	70.770	28.833	0.398
300	50.332	0.000	0.077	3.151	31.545	0.000	14.093	0.200	99.530	70.866	28.673	0.461
305	50.775	0.000	0.083	3.021	31.435	0.103	14.500	0.188	100.237	72.263	27.245	0.493
310	50.531	0.000	0.095	3.081	31.453	0.050	14.377	0.181	99.900	71.650	27.786	0.564
315	50.782	0.000	0.058	3.123	31.669	0.000	14.534	0.196	100.494	71.757	27.902	0.341
320	49.649	0.000	0.083	3.071	31.638	0.057	14.430	0.200	99.260	71.841	27.667	0.492
325	50.351	0.000	0.091	2.943	30.172	0.000	14.407	0.179	98.275	72.612	26.842	0.546
330	50.961	0.000	0.071	3.130	31.541	0.000	14.319	0.189	100.343	71.354	28.225	0.421
335	50.557	0.000	0.089	3.093	31.314	0.000	14.323	0.154	99.662	71.522	27.949	0.529
340	50.546	0.000	0.077	3.065	31.069	0.005	14.475	0.194	99.563	71.968	27.576	0.456
345	50.968	0.000	0.069	3.072	31.587	0.025	14.502	0.177	100.532	71.994	27.598	0.408
360	50.475	0.000	0.071	2.863	31.593	0.000	14.923	0.187	100.244	73.918	25.663	0.419
365	49.955	0.000	0.049	2.735	32.197	0.000	15.290	0.212	100.570	75.329	24.384	0.287
370	49.076	0.000	0.080	2.731	31.913	0.017	15.167	0.198	99.314	75.068	24.460	0.471
375	50.328	0.000	0.094	3.181	31.450	0.000	14.569	0.201	99.955	71.286	28.166	0.548
380	50.645	0.000	0.085	3.108	31.617	0.000	14.681	0.242	100.510	71.943	27.561	0.496
390	50.431	0.000	0.064	2.979	31.607	0.008	14.482	0.221	99.924	72.595	27.023	0.382
395	50.777	0.000	0.092	3.160	31.278	0.074	14.665	0.197	100.375	71.561	27.904	0.535
405	50.716	0.000	0.080	2.974	31.484	0.059	14.528	0.201	100.174	72.622	26.902	0.476
415	51.002	0.000	0.095	3.362	30.630	0.044	14.231	0.221	99.717	69.664	29.782	0.554
430	50.568	0.000	0.137	3.269	31.136	0.000	13.847	0.236	99.325	69.493	29.688	0.819
435	49.939	0.000	0.126	2.993	31.575	0.000	14.608	0.191	99.564	72.409	26.847	0.744

For the analyses, FeO was set at 0.122 and TiO_2 was set at 0.01.

Table F.3. Electron Microprobe Traverse Analyses of Plagioclase P5, Traverse A from Crystal Spring Sample CSWY1E

Length (μm)	SiO_2	BaO	K_2O	Na_2O	Al_2O_3	SrO	CaO	MgO	Total	An	Ab	Or
0	53.684	0.000	0.254	3.946	29.644	0.095	13.001	0.123	100.879	63.593	34.928	1.479
5	53.203	0.000	0.192	3.689	30.128	0.017	13.279	0.165	100.805	65.792	33.075	1.133
10	51.219	0.000	0.151	3.344	30.893	0.019	14.359	0.195	100.312	69.737	29.390	0.873
15	51.528	0.000	0.115	3.384	30.992	0.041	14.766	0.210	101.168	70.225	29.124	0.651
20	51.475	0.000	0.087	3.129	31.136	0.070	14.704	0.201	100.934	71.832	27.662	0.506
25	51.627	0.000	0.069	3.241	30.883	0.000	14.538	0.203	100.693	70.969	28.630	0.401
30	52.235	0.000	0.090	3.423	30.899	0.009	14.511	0.235	101.534	69.723	29.763	0.515
35	52.196	0.000	0.117	3.594	30.206	0.131	13.894	0.250	100.520	67.653	31.668	0.678
40	52.144	0.000	0.112	3.344	30.422	0.000	13.633	0.242	100.029	68.792	30.535	0.673
45	52.112	0.000	0.111	3.429	30.826	0.015	14.485	0.208	101.318	69.565	29.801	0.635
50	51.847	0.000	0.098	3.151	31.126	0.000	14.760	0.222	101.336	71.724	27.709	0.567
55	51.520	0.000	0.080	3.159	31.139	0.000	14.634	0.212	100.876	71.574	27.960	0.466
60	51.525	0.000	0.087	3.052	30.899	0.063	14.525	0.222	100.505	72.079	27.407	0.514
65	51.884	0.000	0.150	3.296	30.995	0.000	14.556	0.189	101.202	70.322	28.815	0.863
75	52.490	0.000	0.174	2.868	30.342	0.000	14.449	0.152	100.607	72.805	26.151	1.044
85	50.898	0.000	0.137	3.085	31.099	0.063	14.939	0.184	100.537	72.222	26.989	0.789
90	52.006	0.000	0.194	3.492	30.042	0.000	13.784	0.145	99.795	67.787	31.077	1.136
95	53.403	0.000	0.256	4.005	29.426	0.118	12.876	0.155	100.371	63.030	35.478	1.492
100	52.811	0.000	0.246	3.779	29.657	0.113	13.122	0.122	99.982	64.789	33.765	1.446
105	53.249	0.000	0.316	4.268	29.060	0.024	12.084	0.126	99.259	59.870	38.266	1.864

For the analyses, FeO was set at 0.122 and TiO_2 was set at 0.01.

Table F.4. Electron Microprobe Traverse Analyses of Plagioclase P5, Traverse B from Crystal Spring Sample CSWY1E

Length (μm)	SiO_2	BaO	K_2O	Na_2O	Al_2O_3	SrO	CaO	MgO	Total	An	Ab	Or
0	53.476	0.000	0.375	3.534	29.314	0.037	12.880	0.114	99.862	65.309	32.427	2.264
5	50.836	0.000	0.168	3.348	30.254	0.000	13.934	0.151	98.823	69.005	30.004	0.991
10	51.692	0.000	0.119	3.459	30.767	0.029	14.074	0.179	100.451	68.737	30.571	0.692
15	51.412	0.000	0.115	3.325	30.724	0.073	14.236	0.204	100.221	69.819	29.510	0.672
20	51.901	0.000	0.111	3.441	30.508	0.000	14.331	0.203	100.627	69.265	30.096	0.639
25	52.233	0.000	0.095	3.426	30.271	0.027	13.444	0.219	99.847	68.047	31.380	0.573
30	52.142	0.000	0.095	3.561	30.176	0.008	13.945	0.241	100.300	68.017	31.431	0.552
35	52.324	0.000	0.102	3.465	30.225	0.029	13.780	0.220	100.277	68.313	31.085	0.602
40	51.364	0.000	0.083	3.442	30.140	0.000	13.872	0.230	99.263	68.675	30.836	0.489
45	51.765	0.000	0.108	3.505	30.128	0.048	13.783	0.260	99.729	68.050	31.315	0.635
55	52.059	0.000	0.124	3.438	30.258	0.068	14.090	0.239	100.408	68.869	30.409	0.722
60	50.883	0.000	0.411	4.225	29.349	0.000	13.694	0.274	98.968	62.733	35.025	2.242
65	52.272	0.000	0.106	3.560	30.565	0.092	13.983	0.211	100.921	68.039	31.347	0.614
70	52.111	0.000	0.090	3.434	30.516	0.051	14.125	0.249	100.708	69.083	30.393	0.524
75	51.660	0.000	0.083	3.143	30.379	0.000	14.247	0.235	99.879	71.116	28.391	0.493
80	52.138	0.000	0.092	3.448	30.586	0.000	14.174	0.220	100.790	69.064	30.403	0.534
85	51.845	0.000	0.109	3.381	29.434	0.000	13.995	0.243	99.139	69.135	30.224	0.641
90	51.468	0.000	0.088	3.024	30.411	0.071	14.226	0.248	99.668	71.837	27.634	0.529
95	51.909	0.000	0.096	3.343	30.346	0.035	14.260	0.228	100.349	69.820	29.620	0.560
100	51.836	0.000	0.086	3.227	30.315	0.000	14.168	0.229	99.993	70.452	29.038	0.509
105	51.707	0.000	0.108	3.428	30.446	0.147	14.191	0.233	100.392	69.147	30.226	0.627
110	52.222	0.000	0.111	3.477	30.758	0.000	14.273	0.252	101.225	68.961	30.400	0.639
115	52.041	0.000	0.093	3.360	30.673	0.118	13.381	0.231	100.029	68.368	31.066	0.566
120	52.143	0.000	0.091	3.421	30.698	0.107	13.981	0.227	100.800	68.940	30.526	0.534
125	52.021	0.000	0.088	3.425	30.581	0.170	13.704	0.227	100.348	68.497	30.979	0.524
130	51.239	0.000	0.097	3.319	30.312	0.180	14.109	0.219	99.607	69.741	29.688	0.571
135	51.880	0.000	0.090	3.163	30.565	0.041	14.269	0.232	100.372	70.990	28.477	0.533
140	52.068	0.000	0.113	3.407	30.448	0.000	14.323	0.252	100.743	69.452	29.896	0.652
145	52.344	0.000	0.098	3.333	30.490	0.003	13.957	0.236	100.593	69.420	30.000	0.580
150	52.262	0.000	0.096	3.318	30.834	0.083	14.321	0.246	101.292	70.065	29.376	0.559

For the analyses, FeO was set at 0.122 and TiO_2 was set at 0.01.

Table F.4. Electron Microprobe Traverse Analyses of Plagioclase P5, Traverse B from Crystal Spring Sample CSWY1E (continued)

Length (μm)	SiO_2	BaO	K_2O	Na_2O	Al_2O_3	SrO	CaO	MgO	Total	An	Ab	Or
155	52.060	0.000	0.090	3.364	30.442	0.216	14.192	0.257	100.753	69.614	29.860	0.526
160	52.101	0.000	0.090	3.422	30.575	0.000	13.836	0.228	100.384	68.714	30.754	0.532
165	51.388	0.000	0.093	3.273	30.503	0.000	14.434	0.223	100.046	70.521	28.938	0.541
170	52.160	0.000	0.104	3.387	30.780	0.054	14.196	0.221	101.034	69.421	29.973	0.606
175	52.050	0.000	0.134	3.297	30.837	0.027	14.320	0.240	101.037	70.039	29.181	0.780
180	52.198	0.000	0.124	3.406	30.960	0.000	14.144	0.213	101.177	69.146	30.132	0.722
185	52.018	0.000	0.110	3.238	30.715	0.002	14.245	0.187	100.647	70.396	28.957	0.647
190	50.148	0.000	0.148	3.394	30.775	0.000	14.356	0.184	99.137	69.440	29.708	0.852
195	51.169	0.000	0.186	3.124	30.752	0.065	13.846	0.175	99.449	70.210	28.667	1.123
200	51.664	0.000	0.132	2.883	30.968	0.005	14.730	0.168	100.682	73.268	25.950	0.782
205	51.997	0.000	0.140	2.937	31.258	0.000	14.580	0.203	101.247	72.676	26.493	0.831
210	52.171	0.000	0.122	3.264	30.866	0.000	14.537	0.215	101.307	70.606	28.688	0.706
215	50.772	0.000	0.087	3.341	30.760	0.176	14.317	0.220	99.805	69.953	29.541	0.506
220	51.560	0.000	0.079	3.330	30.852	0.169	14.108	0.235	100.465	69.745	29.790	0.465
225	51.655	0.000	0.084	3.265	30.865	0.000	14.182	0.222	100.405	70.241	29.263	0.495
230	51.668	0.000	0.087	3.344	30.715	0.000	13.757	0.211	99.914	69.089	30.391	0.520
235	51.874	0.000	0.081	3.341	30.782	0.154	14.335	0.203	100.902	70.004	29.525	0.471
240	50.841	0.000	0.099	2.830	30.434	0.000	14.429	0.216	98.981	73.362	26.038	0.599
245	51.018	0.000	0.078	3.277	31.028	0.000	14.225	0.214	99.972	70.254	29.287	0.459
250	51.463	0.000	0.087	3.304	31.166	0.065	14.673	0.184	101.074	70.694	28.807	0.499
255	51.286	0.000	0.089	3.329	30.971	0.000	14.480	0.187	100.474	70.257	29.229	0.514
260	51.220	0.000	0.070	3.315	30.695	0.020	14.262	0.171	99.885	70.103	29.487	0.410
265	50.916	0.000	0.070	3.162	31.469	0.000	14.982	0.205	100.936	72.073	27.526	0.401
270	51.140	0.000	0.085	3.239	31.467	0.063	15.055	0.172	101.353	71.631	27.888	0.482
275	51.842	0.000	0.083	3.071	30.665	0.000	15.057	0.181	101.031	72.693	26.830	0.477
280	51.513	0.000	0.070	2.937	31.481	0.000	15.061	0.197	101.391	73.615	25.978	0.407
285	51.624	0.000	0.081	3.321	31.552	0.003	14.577	0.226	101.516	70.478	29.056	0.466
290	51.645	0.000	0.092	2.888	30.870	0.000	14.747	0.213	100.587	73.431	26.023	0.545
295	51.585	0.000	0.086	3.200	31.122	0.041	14.816	0.205	101.187	71.543	27.962	0.494
300	51.897	0.000	0.097	3.152	30.968	0.010	14.777	0.168	101.201	71.746	27.694	0.561

For the analyses, FeO was set at 0.122 and TiO_2 was set at 0.01.

Table F.4. Electron Microprobe Traverse Analyses of Plagioclase P5, Traverse B from Crystal Spring Sample CSWY1E (continued)

Length (μm)	SiO_2	BaO	K_2O	Na_2O	Al_2O_3	SrO	CaO	MgO	Total	An	Ab	Or
305	51.662	0.000	0.107	3.075	30.686	0.000	14.549	0.195	100.406	71.879	27.492	0.629
310	51.580	0.000	0.076	3.161	30.913	0.031	14.644	0.218	100.755	71.592	27.965	0.442
315	51.854	0.000	0.076	3.247	30.898	0.000	14.092	0.211	100.510	70.255	29.294	0.451
320	52.248	0.000	0.077	3.186	30.973	0.000	14.294	0.201	101.111	70.934	28.611	0.455
325	51.379	0.000	0.110	3.444	30.222	0.000	13.872	0.222	99.381	68.554	30.799	0.647
330	52.207	0.000	0.095	3.287	30.804	0.061	14.199	0.234	101.019	70.083	29.359	0.558
335	51.894	0.000	0.092	3.092	30.915	0.034	14.174	0.213	100.546	71.302	28.147	0.551
340	51.252	0.000	0.082	3.247	31.562	0.021	14.731	0.184	101.211	71.149	28.380	0.472
345	52.033	0.000	0.084	3.419	31.058	0.000	14.659	0.217	101.602	69.984	29.538	0.477
350	51.977	0.000	0.081	3.089	30.785	0.022	14.623	0.232	100.941	72.001	27.524	0.475
355	51.303	0.000	0.105	3.270	30.728	0.102	14.266	0.206	100.112	70.247	29.138	0.616
360	51.572	0.000	0.091	3.142	31.100	0.032	14.602	0.214	100.885	71.592	27.877	0.531
365	50.824	0.000	0.087	2.996	31.514	0.152	15.005	0.224	100.934	73.087	26.408	0.505
370	50.955	0.000	0.092	3.042	31.645	0.000	15.247	0.201	101.314	73.087	26.388	0.525
375	51.179	0.000	0.124	2.825	31.476	0.058	14.955	0.165	100.914	73.980	25.289	0.730
380	51.917	0.000	0.166	2.941	30.382	0.000	14.387	0.185	100.110	72.272	26.735	0.993
390	52.928	0.000	0.236	3.865	29.890	0.000	13.305	0.155	100.511	64.650	33.985	1.365
395	52.586	0.000	0.236	3.269	30.102	0.017	13.584	0.157	100.083	68.673	29.906	1.421
400	53.147	0.000	0.240	3.940	29.518	0.000	13.071	0.134	100.182	63.803	34.803	1.395
405	52.909	0.000	0.246	3.880	29.572	0.000	13.364	0.126	100.229	64.628	33.955	1.416
410	52.318	0.000	0.251	3.641	28.831	0.000	13.071	0.727	98.971	65.490	33.012	1.497
415	53.273	0.000	0.258	3.535	29.435	0.058	13.542	0.279	100.512	66.887	31.596	1.517

For the analyses, FeO was set at 0.122 and TiO_2 was set at 0.01.

Table F.5. Electron Microprobe Traverse Analyses of Plagioclase P6, Traverse A from Crystal Spring Sample CSWY1E

Length (μm)	SiO_2	BaO	K_2O	Na_2O	Al_2O_3	SrO	CaO	MgO	Total	An	Ab	Or
0	51.291	0.000	0.168	3.373	30.802	0.068	14.155	0.155	100.144	69.188	29.835	0.978
5	50.530	0.000	0.096	2.861	31.445	0.022	14.264	0.169	99.519	72.941	26.475	0.585
10	50.464	0.000	0.077	3.042	31.306	0.073	15.134	0.195	100.423	73.003	26.554	0.442
15	50.834	0.000	0.065	2.983	31.758	0.000	14.865	0.180	100.817	73.081	26.539	0.380
20	50.906	0.000	0.067	2.981	31.820	0.000	15.123	0.217	101.246	73.422	26.190	0.387
25	50.778	0.000	0.069	2.919	31.881	0.055	15.257	0.179	101.270	73.986	25.615	0.398
30	50.802	0.000	0.072	2.940	31.885	0.038	15.161	0.229	101.259	73.715	25.868	0.417
35	51.166	0.000	0.079	3.089	31.421	0.048	15.218	0.209	101.362	72.807	26.743	0.450
40	51.029	0.000	0.073	3.054	31.617	0.000	15.277	0.190	101.372	73.129	26.455	0.416
45	50.903	0.000	0.060	2.936	31.682	0.029	15.301	0.205	101.248	73.970	25.685	0.345
50	50.674	0.000	0.063	2.883	32.029	0.005	15.416	0.202	101.404	74.444	25.194	0.362
55	50.220	0.000	0.065	2.759	31.711	0.036	15.118	0.225	100.266	74.886	24.731	0.383
60	50.346	0.000	0.083	2.741	31.178	0.000	14.758	0.179	99.417	74.471	25.030	0.499
65	50.398	0.000	0.077	2.682	31.732	0.000	15.222	0.182	100.425	75.479	24.066	0.455
70	50.487	0.000	0.068	2.640	31.937	0.094	15.294	0.225	100.877	75.892	23.706	0.402
75	50.083	0.000	0.072	2.603	31.738	0.008	15.486	0.205	100.327	76.353	23.225	0.423
80	50.113	0.000	0.066	2.209	30.739	0.029	15.582	0.212	99.082	79.265	20.335	0.400
85	50.671	0.000	0.090	2.898	31.758	0.113	15.250	0.178	101.090	74.024	25.456	0.520
90	50.854	0.000	0.083	2.793	31.680	0.056	14.905	0.178	100.681	74.309	25.198	0.493
95	50.361	0.000	0.090	2.941	31.736	0.009	14.751	0.203	100.223	73.096	26.373	0.531
100	51.510	0.000	0.097	3.009	31.916	0.000	15.065	0.208	101.937	73.040	26.400	0.560
105	51.101	0.000	0.059	3.056	31.446	0.014	14.974	0.194	100.976	72.780	26.879	0.341
110	51.048	0.000	0.069	3.035	31.417	0.055	15.057	0.215	101.028	72.981	26.621	0.398
115	50.992	0.000	0.080	3.058	31.601	0.014	15.257	0.199	101.333	73.049	26.495	0.456
120	50.845	0.000	0.067	2.917	31.766	0.000	15.112	0.192	101.031	73.824	25.787	0.390
125	50.722	0.000	0.084	2.966	31.848	0.000	14.566	0.172	100.490	72.709	26.792	0.499
130	50.995	0.000	0.066	3.011	31.592	0.007	15.187	0.156	101.146	73.316	26.304	0.379
135	50.887	0.000	0.076	3.037	31.031	0.010	14.925	0.188	100.286	72.765	26.794	0.441
140	50.853	0.000	0.056	2.946	31.980	0.000	15.016	0.193	101.176	73.558	26.115	0.327
150	50.710	0.000	0.083	2.959	31.946	0.077	15.243	0.194	101.344	73.650	25.872	0.477

For the analyses, FeO was set at 0.122 and TiO_2 was set at 0.01.

Table F.5. Electron Microprobe Traverse Analyses of Plagioclase P6, Traverse A from Crystal Spring Sample CSWY1E (continued)

Length (μm)	SiO_2	BaO	K_2O	Na_2O	Al_2O_3	SrO	CaO	MgO	Total	An	Ab	Or
155	50.428	0.000	0.056	2.916	31.827	0.000	15.282	0.201	100.842	74.093	25.584	0.323
160	50.932	0.000	0.061	2.919	31.956	0.034	15.165	0.170	101.369	73.904	25.742	0.354
165	50.534	0.000	0.080	2.919	31.961	0.000	15.526	0.202	101.354	74.275	25.270	0.456
170	50.914	0.000	0.061	2.979	31.943	0.000	15.470	0.195	101.694	73.901	25.752	0.347
175	50.599	0.000	0.082	2.881	32.147	0.003	15.389	0.177	101.410	74.343	25.186	0.472
180	50.005	0.000	0.091	2.753	32.021	0.070	15.554	0.167	100.793	75.343	24.132	0.525
185	50.122	0.000	0.118	2.930	31.302	0.000	15.098	0.161	99.863	73.503	25.813	0.684
190	53.221	0.000	0.278	4.291	28.722	0.030	12.480	0.113	99.267	60.653	37.738	1.609

For the analyses, FeO was set at 0.122 and TiO_2 was set at 0.01.

Table F.6. Electron Microprobe Traverse Analyses of Plagioclase P6, Traverse B from Crystal Spring Sample CSWY1E

Length (μm)	SiO_2	BaO	K_2O	Na_2O	Al_2O_3	SrO	CaO	MgO	Total	An	Ab	Or
0	57.732	0.000	0.441	5.526	26.837	0.163	9.829	0.053	100.713	48.290	49.130	2.580
5	53.318	0.000	0.282	4.202	29.160	0.119	12.534	0.108	99.855	61.220	37.140	1.640
10	50.159	0.000	0.124	2.888	31.337	0.024	14.902	0.124	99.690	73.496	25.775	0.728
15	50.383	0.000	0.103	3.012	31.582	0.046	14.998	0.172	100.428	72.908	26.496	0.596
20	50.505	0.000	0.099	2.994	31.128	0.000	15.024	0.163	100.045	73.074	26.352	0.573
25	50.701	0.000	0.087	2.996	31.550	0.000	14.545	0.190	100.201	72.471	27.013	0.516
30	51.238	0.000	0.075	3.101	31.648	0.003	15.201	0.166	101.564	72.725	26.847	0.427
35	51.262	0.000	0.068	3.151	31.653	0.000	15.030	0.176	101.472	72.214	27.397	0.389
40	51.037	0.000	0.082	3.091	31.702	0.000	15.089	0.190	101.323	72.613	26.918	0.470
45	50.932	0.000	0.083	2.961	30.723	0.000	15.316	0.185	100.332	73.730	25.794	0.476
50	50.770	0.000	0.073	2.919	32.159	0.028	15.267	0.171	101.519	73.982	25.597	0.421
55	50.531	0.000	0.058	2.935	31.754	0.014	15.294	0.210	100.928	73.976	25.690	0.334
60	51.287	0.000	0.071	3.076	31.719	0.000	15.330	0.205	101.820	73.066	26.531	0.403
65	49.796	0.000	0.067	3.102	31.369	0.022	15.256	0.197	99.941	72.824	26.795	0.381
70	50.217	0.000	0.069	3.055	31.720	0.033	14.843	0.183	100.252	72.569	27.029	0.402
75	50.668	0.000	0.081	2.996	31.791	0.022	15.022	0.191	100.903	73.135	26.395	0.470
80	50.360	0.000	0.087	2.949	31.730	0.000	15.377	0.160	100.795	73.867	25.635	0.498
85	50.470	0.000	0.064	2.899	32.133	0.063	15.578	0.193	101.532	74.535	25.101	0.365
95	50.202	0.000	0.077	2.847	30.925	0.000	15.704	0.201	100.088	74.968	24.595	0.438
100	50.853	0.000	0.082	3.122	31.763	0.077	15.115	0.185	101.329	72.451	27.081	0.468
110	51.369	0.000	0.079	3.136	31.145	0.000	14.281	0.208	100.350	71.227	28.304	0.469
115	51.149	0.000	0.083	3.196	31.422	0.000	14.646	0.165	100.793	71.345	28.173	0.481
120	51.590	0.000	0.082	3.255	31.604	0.127	14.891	0.209	101.890	71.321	28.212	0.468
125	51.557	0.000	0.093	3.290	31.326	0.033	14.800	0.180	101.411	70.934	28.535	0.531
130	50.303	0.000	0.090	3.020	30.832	0.000	14.536	0.224	99.137	72.289	27.178	0.533
135	49.733	0.000	0.064	2.631	31.619	0.046	15.510	0.404	100.139	76.226	23.399	0.375
140	48.839	0.000	0.044	2.163	33.192	0.060	16.428	0.147	101.005	80.551	19.192	0.257
150	50.192	0.000	0.069	2.923	31.526	0.101	15.302	0.208	100.453	74.017	25.586	0.397
155	49.334	0.000	0.061	1.886	32.791	0.055	16.203	0.186	100.648	82.296	17.335	0.369
160	49.042	0.000	0.058	1.943	32.539	0.056	16.407	0.161	100.338	82.067	17.587	0.345
165	50.787	0.000	0.069	2.538	31.580	0.113	14.908	0.205	100.332	76.127	23.453	0.420

For the analyses, FeO was set at 0.122 and TiO_2 was set at 0.01.

Table F.6. Electron Microprobe Traverse Analyses of Plagioclase P6, Traverse B from Crystal Spring Sample CSWY1E (continued)

Length (μm)	SiO_2	BaO	K_2O	Na_2O	Al_2O_3	SrO	CaO	MgO	Total	An	Ab	Or
170	51.196	0.000	0.088	2.544	30.838	0.036	14.829	0.191	99.854	75.900	23.563	0.536
175	51.260	0.000	0.078	2.560	31.406	0.000	14.953	0.180	100.569	75.987	23.542	0.472
180	50.969	0.000	0.073	2.567	31.181	0.186	14.807	0.240	100.155	75.781	23.774	0.445
185	50.669	0.000	0.074	2.470	30.928	0.000	14.927	0.223	99.423	76.608	22.940	0.452
190	50.908	0.000	0.090	2.585	31.136	0.000	14.876	0.214	99.941	75.662	23.793	0.545
195	51.201	0.000	0.084	2.638	31.149	0.099	14.530	0.201	100.034	74.882	24.602	0.515
200	51.355	0.000	0.085	2.586	31.515	0.000	14.863	0.182	100.718	75.662	23.823	0.515
205	50.724	0.000	0.094	2.622	31.415	0.010	14.949	0.212	100.158	75.478	23.957	0.565
210	51.797	0.000	0.082	2.668	31.707	0.024	14.796	0.224	101.430	75.024	24.481	0.495
215	50.998	0.000	0.072	3.109	31.096	0.020	14.754	0.179	100.360	72.091	27.490	0.419
220	51.066	0.000	0.079	3.175	31.075	0.000	14.319	0.220	100.066	71.032	28.502	0.467
225	51.388	0.000	0.075	3.200	31.212	0.065	14.459	0.205	100.736	71.090	28.471	0.439
230	50.724	0.000	0.077	3.026	31.022	0.000	14.913	0.176	100.070	72.815	26.737	0.448
235	50.486	0.000	0.075	3.023	31.839	0.000	15.261	0.181	100.997	73.297	26.274	0.429
240	50.970	0.000	0.078	2.858	31.626	0.000	14.904	0.208	100.776	73.896	25.643	0.460
245	51.081	0.000	0.083	2.941	31.457	0.000	14.847	0.203	100.744	73.254	26.259	0.488
250	51.203	0.000	0.081	2.964	31.973	0.130	14.737	0.166	101.386	72.966	26.557	0.478
255	50.283	0.000	0.078	2.984	31.953	0.000	15.300	0.190	100.920	73.583	25.970	0.447
260	50.222	0.000	0.078	3.016	31.140	0.000	15.215	0.220	100.023	73.270	26.283	0.447
265	51.297	0.000	0.069	3.072	31.780	0.000	14.051	0.173	100.574	71.353	28.230	0.417
270	51.151	0.000	0.076	2.996	31.932	0.000	15.236	0.194	101.717	73.433	26.131	0.436
275	51.389	0.000	0.070	3.038	31.968	0.017	15.052	0.191	101.857	72.951	26.645	0.404
280	51.137	0.000	0.069	2.946	31.133	0.081	14.965	0.198	100.661	73.436	26.161	0.403
285	51.098	0.000	0.078	3.112	31.363	0.000	15.176	0.186	101.145	72.611	26.945	0.444
290	50.872	0.000	0.064	3.046	31.724	0.067	14.666	0.167	100.738	72.409	27.214	0.376
295	50.816	0.000	0.072	3.031	31.256	0.108	14.711	0.191	100.317	72.533	27.044	0.423
300	50.956	0.000	0.075	2.893	31.755	0.029	15.102	0.157	101.099	73.933	25.630	0.437
310	51.186	0.000	0.086	3.126	31.500	0.069	15.049	0.188	101.336	72.322	27.186	0.492
315	50.861	0.000	0.079	2.888	31.364	0.000	14.966	0.194	100.484	73.774	25.762	0.464
320	50.747	0.000	0.077	3.023	31.404	0.049	14.910	0.188	100.530	72.831	26.722	0.448
325	51.089	0.000	0.079	3.195	31.426	0.099	14.633	0.192	100.845	71.350	28.191	0.459

For the analyses, FeO was set at 0.122 and TiO_2 was set at 0.01.

Table F.6. Electron Microprobe Traverse Analyses of Plagioclase P6, Traverse B from Crystal Spring Sample CSWY1E (continued)

Length (μm)	SiO_2	BaO	K_2O	Na_2O	Al_2O_3	SrO	CaO	MgO	Total	An	Ab	Or
330	50.204	0.000	0.081	3.093	31.346	0.043	14.839	0.220	99.958	72.270	27.260	0.470
335	50.540	0.000	0.128	2.849	31.597	0.000	14.764	0.203	100.213	73.555	25.686	0.759
340	50.899	0.000	0.084	2.952	31.632	0.000	15.034	0.186	100.919	73.423	26.089	0.488
345	50.923	0.000	0.084	3.023	31.671	0.070	15.427	0.192	101.522	73.471	26.053	0.476
350	50.533	0.000	0.088	2.893	31.460	0.065	14.885	0.224	100.280	73.597	25.885	0.518
355	49.123	0.000	0.098	2.955	32.059	0.000	15.234	0.188	99.789	73.601	25.835	0.564
360	50.329	0.000	0.075	2.324	31.626	0.000	15.165	0.191	99.842	77.930	21.611	0.459
365	50.367	0.000	0.068	2.342	31.546	0.022	15.080	0.219	99.776	77.736	21.847	0.417
370	50.453	0.000	0.095	2.303	31.305	0.087	14.997	0.192	99.564	77.795	21.619	0.587
375	50.328	0.000	0.090	2.404	31.631	0.000	14.848	0.170	99.603	76.911	22.534	0.555
380	50.703	0.000	0.076	2.373	31.510	0.000	14.785	0.187	99.766	77.127	22.401	0.472
385	49.589	0.000	0.079	2.387	31.564	0.027	15.141	0.160	99.079	77.429	22.090	0.481
390	51.487	0.000	0.077	2.341	32.267	0.013	15.335	0.220	101.873	77.989	21.545	0.466
395	51.186	0.000	0.108	2.542	31.203	0.000	14.511	0.180	99.862	75.422	23.909	0.668
400	51.486	0.000	0.174	2.592	30.629	0.000	14.781	0.199	99.993	75.112	23.836	1.053

For the analyses, FeO was set at 0.122 and TiO_2 was set at 0.01.

Table F.7. Electron Microprobe Traverse Analyses of Pyroxene P1, Traverse B from Crystal Spring Sample CSWY2

Length (μm)	SiO_2	FeO	K_2O	Na_2O	Al_2O_3	TiO_2	CaO	MgO	Total	Wo	En	Fs	Ac
0	52.314	17.711	0.023	0.078	1.363	0.274	1.848	24.677	98.288	3.69	68.55	27.48	0.28
15	54.181	13.428	0.021	0.013	0.667	0.184	1.648	28.429	98.571	3.19	76.55	20.21	0.05
20	54.209	13.228	0.000	0.020	0.669	0.158	1.628	28.503	98.415	3.15	76.84	19.94	0.07
25	54.363	13.081	0.008	0.008	0.621	0.161	1.638	28.805	98.685	3.16	77.22	19.60	0.03
30	53.808	12.992	0.024	0.010	0.758	0.196	1.912	28.530	98.230	3.70	76.76	19.51	0.03
35	53.451	13.055	0.082	0.038	1.466	0.282	2.548	27.522	98.444	4.99	75.00	19.87	0.13
40	53.569	13.064	0.005	0.010	0.829	0.219	2.411	28.366	98.473	4.63	75.86	19.47	0.03
45	53.962	13.015	0.002	0.003	0.843	0.193	2.104	28.915	99.037	4.01	76.73	19.25	0.01
50	53.714	13.244	0.005	0.012	0.887	0.240	2.079	28.063	98.244	4.04	75.90	20.01	0.04
55	53.627	12.975	0.012	0.000	1.062	0.234	2.089	28.600	98.599	4.02	76.60	19.38	0.00
60	53.826	12.655	0.016	0.020	0.966	0.193	2.091	28.409	98.176	4.06	76.77	19.10	0.07
65	54.026	12.372	0.009	0.017	0.933	0.206	2.094	28.946	98.603	4.03	77.44	18.47	0.06
70	54.357	12.556	0.000	0.014	1.005	0.220	2.156	29.205	99.513	4.10	77.31	18.54	0.05
85	54.635	12.389	0.000	0.038	0.883	0.209	2.179	28.549	98.882	4.22	76.95	18.70	0.13
90	54.120	12.534	0.000	0.011	1.008	0.207	2.172	29.476	99.528	4.10	77.51	18.35	0.04
95	54.256	12.453	0.009	0.018	1.270	0.226	2.200	29.055	99.487	4.20	77.26	18.48	0.06
100	54.053	12.351	0.000	0.017	1.361	0.266	2.470	28.864	99.382	4.73	76.87	18.35	0.06
105	54.010	12.546	0.008	0.015	1.347	0.252	2.439	28.780	99.397	4.67	76.65	18.63	0.05
110	53.936	12.239	0.002	0.006	1.424	0.269	2.282	29.026	99.184	4.37	77.40	18.21	0.02
115	53.233	12.378	0.000	0.000	1.387	0.307	2.394	29.053	98.752	4.57	77.15	18.28	0.00
120	53.748	12.485	0.000	0.014	1.398	0.299	2.325	28.624	98.893	4.48	76.78	18.69	0.05
125	53.434	12.251	0.013	0.003	1.426	0.264	2.295	28.518	98.204	4.46	77.06	18.48	0.01
130	53.836	12.459	0.007	0.010	1.409	0.243	2.475	28.563	99.002	4.77	76.56	18.64	0.03
135	54.362	12.368	0.032	0.047	1.521	0.298	2.684	28.849	100.161	5.11	76.45	18.28	0.16
140	53.822	12.326	0.011	0.014	1.343	0.290	2.607	28.776	99.189	4.99	76.66	18.30	0.05
145	53.534	12.197	0.013	0.000	1.319	0.305	2.624	28.534	98.526	5.07	76.66	18.28	0.00
160	53.572	12.115	0.000	0.028	1.437	0.296	2.717	27.997	98.162	5.31	76.16	18.42	0.10
165	54.135	12.423	0.005	0.009	1.445	0.256	2.488	28.927	99.688	4.75	76.82	18.40	0.03

Table F.7. Electron Microprobe Traverse Analyses of Pyroxene P1, Traverse B from Crystal Spring Sample CSWY2 (continued)

Length (μm)	SiO_2	FeO	K_2O	Na_2O	Al_2O_3	TiO_2	CaO	MgO	Total	Wo	En	Fs	Ac
205	53.502	11.959	0.004	0.023	2.116	0.303	2.677	28.293	98.877	5.21	76.62	18.09	0.08
210	53.616	12.363	0.017	0.011	1.469	0.247	2.479	28.741	98.943	4.76	76.79	18.41	0.04
215	54.240	12.116	0.003	0.017	0.957	0.239	2.180	29.038	98.790	4.19	77.65	18.10	0.06
220	53.743	12.523	0.000	0.026	0.983	0.207	1.972	28.874	98.328	3.80	77.39	18.72	0.09
225	53.232	13.497	0.014	0.029	1.589	0.250	2.323	27.922	98.856	4.49	75.16	20.25	0.10
235	54.106	13.290	0.007	0.023	0.792	0.225	2.125	28.760	99.328	4.05	76.24	19.64	0.08
240	53.969	12.940	0.019	0.031	0.791	0.183	1.906	28.636	98.475	3.68	76.84	19.38	0.11
245	54.344	13.512	0.000	0.000	0.791	0.229	2.006	28.581	99.463	3.84	76.08	20.08	0.00
250	53.092	14.308	0.023	0.023	0.831	0.227	2.022	27.838	98.364	3.90	74.66	21.36	0.08
255	53.074	16.584	0.048	0.036	0.878	0.264	1.886	25.693	98.463	3.73	70.66	25.49	0.13

APPENDIX G

TWO-FELDSPAR GEOTHERMOMETRY ANALYSES OF GIBBON RIVER RHYOLITE SAMPLES

Table G.1. Electron Microprobe Feldspar Analyses Used to Calculate Two-Feldspar Temperatures for Gibbon River Sample GRWY1

Sanidine Analysis Number [a]	An	Ab	Or	2-Feldspar Temp. Analysis No. [b]
S1-30	2.27	46.75	50.98	T01
S1-1010	1.63	48.27	50.09	T02
S2-0	3.41	47.15	49.45	T03
S2-895	2.27	48.14	49.59	T04
S4-0	3.11	58.02	38.87	T05
S4-300	3.10	55.92	40.98	T06
S5-0	3.15	54.95	41.90	T07
S5-550	2.79	48.53	48.67	T08
S6-0	3.17	50.84	45.98	T09
S6-1610	4.66	52.87	42.48	T10
S1R1	2.35	42.73	54.92	T11
S2R1	2.24	46.11	51.65	T12
S4R1	3.40	52.83	43.77	T13
S6R1	2.23	44.53	53.24	T14
Plagioclase Analysis				
P1R1	24.58	68.26	7.16	

[a] Sanidine analysis numbers correspond to the analyzed GRWY1 sanidine number (S1 to S6) combined with the length along the analyzed traverse of the specific analysis (Tables D.1 through D.5, Appendix D) or the GRWY1 rim point analysis number (Table C.1, Appendix C).

[b] The listed sanidine analyses were paired with plagioclase analysis P1R1 (Table C.5, Appendix C) to calculate the corresponding two-feldspar temperature analyses (found in Table G.2).

Table G.2. Calculated Two-Feldspar Temperatures for Gibbon River Sample GRWY1

Calculated Equilibrium Temperatures (°C)				
2-Feldspar Temp. Analysis No. [a]	T_{Ab}	T_{Or}	T_{An}	Calculated Temperature (°C) [b]
T01	901.17	745.77	735.95	-
T02	958.24	746.38	633.70	-
T03	885.22	787.45	826.37	806.9
T04	926.43	745.23	697.32	-
T05	830.58	715.94	715.94	-
T06	848.91	729.98	729.98	-
T07	857.79	738.51	738.51	-
T08	910.32	743.88	733.74	-
T09	937.21	740.77	697.14	-
T10	868.91	776.51	824.79	-
T11	860.66	793.34	841.53	851.1
T12	892.85	751.69	751.69	-
T13	969.10	737.45	653.83	-
T14	882.22	797.42	798.42	797.9
			Average:	818.6

[a] Analysis numbers from Table G.1.

[b] Analysis T03, T11, and T14 produced close-to-equilibrium temperatures and their calculated temperature is the average of the two concordant temperatures (i.e. those within ± 40°C of each other). The other analyses produced discordant, nonequilibrium feldspar pairs and have no calculated crystallization temperature (Fuhrman and Lindsley, 1988).

Table G.3. Electron Microprobe Feldspar Analyses Used to Calculate Two-Feldspar Temperatures for Gibbon River Sample GRWY7P

				2-Feldspar Temp. Analysis No. [a]		
				Plagioclase Analysis Number [b]		
Sanidine Analysis Number [c]	An	Ab	Or	P1-0	P1-1020	P1R1
S2-0	2.02	39.26	58.72	T01	T18	T35
S2-840	2.26	39.90	57.84	T02	T19	T36
S3-0	1.91	38.78	59.31	T03	T20	T37
S3-890	2.24	41.60	56.16	T04	T21	T38
S5-0	2.12	39.57	58.31	T05	T22	T39
S5-770	2.56	46.03	51.41	T06	T23	T40
S6-0	2.48	40.87	56.65	T07	T24	T41
S6-610	2.07	39.07	58.86	T08	T25	T42
S1R1	2.30	40.37	57.33	T09	T26	T43
S1R2	2.17	40.48	57.35	T10	T27	T44
S2R1	2.37	41.72	55.91	T11	T28	T45
S3R1	2.01	40.17	57.82	T12	T29	T46
S3R2	2.14	40.56	57.30	T13	T30	T47
S4R1	2.27	40.39	57.35	T14	T31	T48
S5R1	2.02	39.45	58.53	T15	T32	T49
S5R2	2.19	41.49	56.31	T16	T33	T50
S6R1	2.12	40.64	57.24	T17	T34	T51
Plagioclase Analysis						
P1-0	19.89	70.60	9.51			
P1-1020	19.20	71.65	9.14			
P1R1	19.16	71.38	9.46			

[a] The listed sanidine analyses were paired with each listed plagioclase analysis to calculate the corresponding two-feldspar temperature analyses (found in Table G.4).

[b] Plagioclase analysis numbers correspond to the analyzed GRWY7P plagioclase number (P1) combined with the length along the analyzed traverse of the specific analysis (Table D.13, Appendix D) or the GRWY7P rim point analysis number (Table C.6, Appendix C).

[c] Sanidine analysis numbers correspond to the analyzed GRWY7P sanidine number (S2 to S6) combined with the length along the analyzed traverse of the specific analysis (Tables D.9 through D.12, Appendix D) or the GRWY7P rim point analysis number (Table C.4, Appendix C).

Table G.4. Calculated Two-Feldspar Temperatures for Gibbon River Sample GRWY7P

Calculated Equilibrium Temperatures (°C)				
2-Feldspar Temp. Analysis No. [a]	T_{Ab}	T_{Or}	T_{An}	Calculated Temperature (°C) [b]
T01	825.07	809.62	825.07	819.9
T02	819.88	806.78	819.88	815.5
T03	814.51	803.06	814.51	810.7
T04	834.78	809.99	834.78	826.5
T05	823.77	807.69	823.77	818.4
T06 [c]	854.83	815.12	854.83	841.6 [c]
T07	825.31	810.60	825.31	820.4
T08	813.45	804.90	813.45	810.6
T09	823.33	808.19	823.33	818.3
T10	825.66	805.81	825.66	819.0
T11	835.64	810.08	835.64	827.1
T12	824.43	806.26	824.43	818.4
T13	825.77	805.66	825.77	819.1
T14	825.47	810.30	825.47	820.4
T15	816.41	801.74	816.41	811.5
T16	830.73	808.42	830.73	823.3
T17	829.52	808.90	829.52	822.6
T18	808.18	797.10	808.18	804.5
T19	810.81	805.37	810.81	809.0
T20	805.48	796.28	805.48	802.4
T21	830.23	791.94	830.23	817.5
T22	819.58	800.23	819.58	813.1
T23 [c]	824.19	782.95	782.95	783.0 [c]
T24	816.72	797.66	816.72	810.4
T25	802.21	782.61	802.21	795.7
T26	819.37	805.37	819.37	814.7
T27	813.26	795.65	813.26	807.4
T28	826.99	799.65	826.99	817.9
T29	811.11	796.42	811.11	806.2
T30	817.33	795.45	817.33	810.0
T31	819.71	799.14	819.71	812.9
T32	810.71	794.38	810.71	805.3
T33	820.50	794.77	820.50	811.9
T34	820.37	800.29	820.37	813.7
T35	806.62	797.93	806.62	803.7
T36	817.88	800.90	817.88	812.2
T37	805.23	799.69	805.23	803.4
T38	826.72	806.53	826.72	820.0
T39	809.18	799.21	809.18	805.9
T40 [c]	803.86	760.49	760.49	760.5 [c]
T41	824.43	805.76	824.43	818.2
T42	810.86	798.47	810.86	806.7
T43	821.63	803.20	821.63	815.5

Table G.4. Calculated Two-Feldspar Temperatures for Gibbon River Sample GRWY7P (continued)

Calculated Equilibrium Temperatures (°C)				
2-Feldspar Temp. Analysis No. [a]	T_{Ab}	T_{Or}	T_{An}	Calculated Temperature (°C) [b]
T44	815.72	801.58	815.72	811.0
T45	824.25	804.25	824.25	817.6
T46	819.43	801.72	819.43	813.5
T47	818.29	803.58	818.29	813.4
T48	825.99	805.68	825.99	819.2
T49	807.84	797.11	807.84	804.3
T50	819.61	796.84	819.61	812.0
T51	825.08	804.61	825.08	818.3
			Average [c]:	813.5

[a] Analysis numbers from Table G.3.

[b] All analyses, except T23 and T40, produced equilibrium temperatures and their calculated temperature is the average of all three concordant temperatures. Analyses T23 and T40 produced close-to-equilibrium temperatures and their calculated temperature is the average of the two concordant temperatures (i.e. those within ± 40°C of each other) (Fuhrman and Lindsley, 1988).

[c] Temperatures calculated utilizing sanidine analysis S5-770 were omitted from the average calculated feldspar crystallization temperature.

APPENDIX H

TITANIUM-IN-QUARTZ GEOTHERMOMETRY ANALYSES OF GIBBON RIVER RHYOLITE SAMPLES

Table H.1. Electron Microprobe Traverse Analyses of Quartz QA from Gibbon River Sample GRWY1

											Temperature [a]	
Length (μm)	SiO_2	TiO_2	CaO	Na_2O	Al_2O_3	K_2O	MgO	FeO	Total	Ti (ppm)	K	°C
0	99.130	0.019	0.011	0.002	0.026	0.002	0.000	0.000	99.190	190	1180.3	907.2
80	98.836	0.010	0.000	0.003	0.025	0.000	0.000	0.000	98.874	100	1087.6	814.5
100	98.930	0.009	0.008	0.004	0.018	0.000	0.000	0.006	98.975	90	1073.8	800.6
140	99.378	0.011	0.012	0.008	0.039	0.002	0.000	0.009	99.459	110	1100.4	827.3
160	99.225	0.007	0.001	0.002	0.022	0.003	0.002	0.020	99.282	70	1042.1	769.0
180	99.526	0.008	0.034	0.020	0.084	0.014	0.007	0.031	99.724	80	1058.7	785.5
200	99.482	0.013	0.010	0.007	0.036	0.000	0.001	0.010	99.559	130	1123.7	850.5
220	98.136	0.012	0.011	0.000	0.064	0.000	0.000	0.017	98.240	120	1112.4	839.3
360	99.407	0.007	0.062	0.011	0.346	0.009	0.010	0.039	99.891	70	1042.1	769.0
380	99.295	0.009	0.000	0.000	0.018	0.001	0.000	0.018	99.341	90	1073.8	800.6
420	98.947	0.009	0.000	0.000	0.019	0.001	0.000	0.000	98.976	90	1073.8	800.6
440	93.199	0.008	0.108	0.031	5.441	0.002	0.026	0.024	98.839	80	1058.7	785.5
460	99.327	0.006	0.000	0.007	0.013	0.004	0.000	0.000	99.357	60	1023.6	750.5
520	99.731	0.012	0.003	0.000	0.014	0.000	0.000	0.000	99.760	120	1112.4	839.3
540	99.634	0.009	0.023	0.009	0.041	0.000	0.000	0.009	99.725	90	1073.8	800.6
560	98.822	0.012	0.004	0.000	0.019	0.000	0.001	0.010	98.868	120	1112.4	839.3
580	99.016	0.011	0.006	0.000	0.022	0.005	0.000	0.001	99.061	110	1100.4	827.3
600	99.365	0.011	0.011	0.000	0.019	0.000	0.000	0.003	99.409	110	1100.4	827.3
620	99.289	0.009	0.008	0.004	0.015	0.000	0.000	0.000	99.325	90	1073.8	800.6
640	99.674	0.009	0.007	0.000	0.017	0.002	0.000	0.019	99.728	90	1073.8	800.6
700	99.588	0.007	0.008	0.001	0.024	0.000	0.000	0.013	99.641	70	1042.1	769.0
720	98.872	0.006	0.006	0.000	0.027	0.000	0.000	0.007	98.918	60	1023.6	750.5
760	98.995	0.009	0.007	0.002	0.030	0.000	0.000	0.000	99.043	90	1073.8	800.6
800	99.087	0.006	0.000	0.000	0.019	0.001	0.000	0.010	99.123	60	1023.6	750.5
820	99.013	0.006	0.012	0.000	0.013	0.001	0.003	0.000	99.048	60	1023.6	750.5
840	99.509	0.009	0.018	0.006	0.017	0.006	0.000	0.001	99.566	90	1073.8	800.6
860	99.359	0.006	0.001	0.000	0.021	0.000	0.000	0.006	99.393	60	1023.6	750.5
880	98.477	0.009	0.010	0.001	0.281	0.000	0.002	0.001	98.781	90	1073.8	800.6
960	100.136	0.006	0.001	0.000	0.015	0.003	0.000	0.009	100.170	60	1023.6	750.5

[a] Quartz crystallization temperatures calculated using the TitaniQ method (Wark and Watson, 2006; Wark *et al.*, 2007).

Table H.1. Electron Microprobe Traverse Analyses of Quartz QA from Gibbon River Sample GRWY1 (continued)

											Temperature [a]	
Length (μm)	SiO_2	TiO_2	CaO	Na_2O	Al_2O_3	K_2O	MgO	FeO	Total	Ti (ppm)	K	°C
1000	100.173	0.010	0.003	0.000	0.017	0.000	0.000	0.009	100.212	100	1087.6	814.5
1020	98.523	0.008	0.006	0.003	0.027	0.003	0.004	0.000	98.574	80	1058.7	785.5
1100	98.114	0.011	0.020	0.002	0.109	0.007	0.005	0.019	98.287	110	1100.4	827.3
1160	99.096	0.009	0.025	0.005	0.287	0.004	0.003	0.000	99.429	90	1073.8	800.6
1180	99.310	0.007	0.011	0.000	0.024	0.004	0.000	0.013	99.369	70	1042.1	769.0
1220	98.302	0.007	0.026	0.001	0.111	0.009	0.003	0.080	98.539	70	1042.1	769.0
1240	98.920	0.005	0.018	0.000	0.114	0.006	0.006	0.002	99.071	50	1002.6	729.4
1300	99.763	0.006	0.014	0.006	0.153	0.000	0.002	0.000	99.944	60	1023.6	750.5
1340	99.552	0.008	0.003	0.000	0.019	0.004	0.001	0.004	99.591	80	1058.7	785.5
1380	99.516	0.010	0.007	0.000	0.020	0.001	0.000	0.004	99.558	100	1087.6	814.5
1400	99.614	0.011	0.010	0.003	0.019	0.004	0.000	0.000	99.661	110	1100.4	827.3
1440	99.437	0.010	0.008	0.005	0.024	0.000	0.000	0.000	99.484	100	1087.6	814.5
1560	99.058	0.010	0.007	0.000	0.017	0.001	0.002	0.000	99.095	100	1087.6	814.5
1620	98.788	0.006	0.000	0.000	0.019	0.000	0.005	0.008	98.826	60	1023.6	750.5
1640	98.252	0.011	0.016	0.000	0.055	0.000	0.002	0.010	98.346	110	1100.4	827.3
1660	98.301	0.009	0.010	0.001	0.024	0.002	0.001	0.000	98.348	90	1073.8	800.6

[a] Quartz crystallization temperatures calculated using the TitaniQ method (Wark and Watson, 2006; Wark *et al.*, 2007).

Table H.2. Electron Microprobe Traverse Analyses of Quartz QB from Gibbon River Sample GRWY1

											Temperature [a]	
Length (μm)	SiO_2	TiO_2	CaO	Na_2O	Al_2O_3	K_2O	MgO	FeO	Total	Ti (ppm)	K	°C
20	98.435	0.021	0.006	0.001	0.163	0.000	0.000	0.005	98.631	210	1196.2	923.1
40	98.892	0.023	0.007	0.000	0.027	0.004	0.006	0.008	98.967	230	1211.1	937.9
60	97.045	0.023	0.033	0.012	0.959	0.015	0.005	0.013	98.105	230	1211.1	937.9
100	98.808	0.025	0.008	0.000	0.025	0.000	0.000	0.000	98.866	250	1225.0	951.8
120	98.888	0.023	0.005	0.000	0.029	0.009	0.000	0.000	98.954	230	1211.1	937.9
140	99.470	0.024	0.006	0.005	0.022	0.000	0.000	0.015	99.542	240	1218.1	945.0
160	98.650	0.025	0.027	0.003	0.070	0.002	0.004	0.018	98.799	250	1225.0	951.8
180	99.062	0.021	0.011	0.001	0.024	0.002	0.001	0.000	99.122	210	1196.2	923.1
220	99.604	0.016	0.009	0.001	0.021	0.008	0.003	0.000	99.662	160	1154.0	880.8
240	99.634	0.019	0.006	0.001	0.024	0.002	0.000	0.000	99.686	190	1180.3	907.2
260	99.609	0.010	0.000	0.003	0.024	0.000	0.000	0.000	99.646	100	1087.6	814.5
300	99.843	0.010	0.002	0.000	0.024	0.000	0.002	0.011	99.892	100	1087.6	814.5
320	99.846	0.004	0.003	0.003	0.020	0.003	0.000	0.012	99.891	40	977.9	704.8
340	99.477	0.011	0.000	0.001	0.017	0.000	0.003	0.000	99.509	110	1100.4	827.3
360	99.521	0.007	0.005	0.000	0.024	0.001	0.000	0.014	99.572	70	1042.1	769.0
380	98.793	0.012	0.010	0.000	0.025	0.001	0.000	0.000	98.841	120	1112.4	839.3
400	99.295	0.009	0.006	0.000	0.019	0.010	0.004	0.005	99.348	90	1073.8	800.6
420	99.337	0.010	0.003	0.000	0.028	0.004	0.001	0.004	99.387	100	1087.6	814.5
460	99.830	0.011	0.003	0.003	0.027	0.002	0.001	0.003	99.880	110	1100.4	827.3
480	98.972	0.010	0.004	0.005	0.017	0.000	0.004	0.008	99.020	100	1087.6	814.5
500	98.647	0.011	0.038	0.020	0.021	0.004	0.009	0.000	98.750	110	1100.4	827.3
520	98.934	0.010	0.014	0.006	0.018	0.003	0.004	0.000	98.989	100	1087.6	814.5
540	99.000	0.011	0.018	0.000	0.020	0.000	0.004	0.003	99.056	110	1100.4	827.3
560	99.429	0.009	0.009	0.008	0.019	0.004	0.000	0.003	99.481	90	1073.8	800.6
580	99.024	0.009	0.008	0.000	0.014	0.000	0.000	0.000	99.055	90	1073.8	800.6
600	99.104	0.009	0.015	0.003	0.020	0.003	0.003	0.000	99.157	90	1073.8	800.6
620	98.857	0.008	0.007	0.003	0.012	0.001	0.005	0.010	98.903	80	1058.7	785.5
640	99.127	0.009	0.011	0.007	0.018	0.001	0.001	0.000	99.174	90	1073.8	800.6
660	99.308	0.005	0.029	0.010	0.016	0.004	0.002	0.001	99.375	50	1002.6	729.4

[a] Quartz crystallization temperatures calculated using the TitaniQ method (Wark and Watson, 2006; Wark *et al.*, 2007).

Table H.2. Electron Microprobe Traverse Analyses of Quartz QB from Gibbon River Sample GRWY1 (continued)

											Temperature [a]	
Length (μm)	SiO_2	TiO_2	CaO	Na_2O	Al_2O_3	K_2O	MgO	FeO	Total	Ti (ppm)	K	°C
680	99.784	0.006	0.000	0.000	0.011	0.002	0.000	0.000	99.803	60	1023.6	750.5
700	99.815	0.005	0.002	0.001	0.028	0.001	0.000	0.003	99.855	50	1002.6	729.4
720	99.493	0.009	0.003	0.000	0.015	0.003	0.000	0.003	99.526	90	1073.8	800.6
740	99.679	0.008	0.000	0.000	0.013	0.003	0.002	0.000	99.705	80	1058.7	785.5
760	99.263	0.005	0.003	0.000	0.017	0.000	0.000	0.000	99.288	50	1002.6	729.4
780	99.671	0.008	0.007	0.004	0.018	0.005	0.000	0.011	99.724	80	1058.7	785.5
800	99.668	0.008	0.014	0.000	0.035	0.005	0.005	0.002	99.737	80	1058.7	785.5
820	99.586	0.010	0.003	0.000	0.017	0.003	0.000	0.000	99.619	100	1087.6	814.5
840	99.742	0.009	0.007	0.001	0.022	0.007	0.000	0.000	99.788	90	1073.8	800.6
860	100.197	0.006	0.003	0.000	0.018	0.000	0.000	0.005	100.229	60	1023.6	750.5
880	100.176	0.009	0.007	0.000	0.021	0.000	0.000	0.011	100.224	90	1073.8	800.6
900	98.333	0.012	0.010	0.000	0.060	0.001	0.000	0.000	98.416	120	1112.4	839.3
920	100.168	0.011	0.014	0.000	0.025	0.000	0.003	0.007	100.228	110	1100.4	827.3
940	100.042	0.006	0.007	0.000	0.023	0.005	0.000	0.000	100.083	60	1023.6	750.5
960	99.524	0.009	0.000	0.000	0.022	0.000	0.000	0.008	99.563	90	1073.8	800.6
980	98.515	0.007	0.005	0.002	0.133	0.000	0.000	0.008	98.670	70	1042.1	769.0
1000	98.582	0.005	0.004	0.008	0.026	0.000	0.000	0.000	98.625	50	1002.6	729.4
1020	99.446	0.004	0.009	0.001	0.018	0.005	0.000	0.000	99.483	40	977.9	704.8
1040	99.595	0.010	0.004	0.004	0.021	0.000	0.000	0.000	99.634	100	1087.6	814.5
1060	99.652	0.009	0.005	0.006	0.016	0.000	0.000	0.000	99.688	90	1073.8	800.6
1080	99.842	0.007	0.003	0.001	0.021	0.001	0.000	0.000	99.875	70	1042.1	769.0
1100	99.571	0.010	0.006	0.006	0.021	0.001	0.002	0.004	99.621	100	1087.6	814.5
1140	99.445	0.009	0.002	0.000	0.018	0.002	0.000	0.001	99.477	90	1073.8	800.6
1160	99.263	0.007	0.001	0.004	0.022	0.001	0.000	0.000	99.298	70	1042.1	769.0
1180	99.630	0.004	0.001	0.000	0.037	0.000	0.001	0.000	99.673	40	977.9	704.8
1200	99.992	0.007	0.006	0.005	0.023	0.001	0.000	0.009	100.043	70	1042.1	769.0
1220	100.114	0.020	0.011	0.009	0.026	0.008	0.000	0.000	100.188	200	1188.4	915.3
1240	99.840	0.014	0.003	0.003	0.035	0.000	0.000	0.000	99.895	140	1134.3	861.2
1260	99.430	0.017	0.010	0.000	0.031	0.000	0.000	0.000	99.488	170	1163.2	890.0

[a] Quartz crystallization temperatures calculated using the TitaniQ method (Wark and Watson, 2006; Wark *et al.*, 2007).

Table H.2. Electron Microprobe Traverse Analyses of Quartz QB from Gibbon River Sample GRWY1 (continued)

											Temperature [a]	
Length (μm)	SiO_2	TiO_2	CaO	Na_2O	Al_2O_3	K_2O	MgO	FeO	Total	Ti (ppm)	K	°C
1280	99.139	0.019	0.011	0.007	0.029	0.004	0.003	0.000	99.212	190	1180.3	907.2
1300	99.341	0.028	0.002	0.008	0.026	0.000	0.001	0.000	99.406	280	1244.4	971.3
1320	99.113	0.024	0.003	0.000	0.025	0.001	0.001	0.002	99.169	240	1218.1	945.0
1340	99.264	0.019	0.004	0.000	0.028	0.009	0.001	0.015	99.340	190	1180.3	907.2
1360	98.884	0.023	0.002	0.000	0.035	0.005	0.001	0.007	98.957	230	1211.1	937.9
1400	99.338	0.022	0.000	0.005	0.029	0.005	0.005	0.007	99.411	220	1203.8	930.6
1420	99.649	0.022	0.006	0.000	0.020	0.000	0.000	0.000	99.697	220	1203.8	930.6
1440	99.909	0.023	0.010	0.003	0.023	0.002	0.000	0.012	99.982	230	1211.1	937.9
1460	100.081	0.023	0.004	0.000	0.029	0.000	0.000	0.000	100.137	230	1211.1	937.9
1500	99.616	0.023	0.006	0.003	0.027	0.002	0.002	0.000	99.679	230	1211.1	937.9
1520	99.655	0.019	0.021	0.001	0.209	0.003	0.001	0.001	99.910	190	1180.3	907.2
1540	100.030	0.018	0.005	0.005	0.038	0.003	0.000	0.018	100.117	180	1171.9	898.8
1560	99.272	0.018	0.007	0.000	0.033	0.002	0.000	0.000	99.332	180	1171.9	898.8
1580	99.557	0.016	0.002	0.000	0.017	0.005	0.000	0.000	99.597	160	1154.0	880.8
1600	99.669	0.019	0.002	0.000	0.025	0.007	0.000	0.000	99.722	190	1180.3	907.2

[a] Quartz crystallization temperatures calculated using the TitaniQ method (Wark and Watson, 2006; Wark *et al.*, 2007).

Table H.3. Electron Microprobe Traverse Analyses of Quartz QA from Gibbon River Sample GRWY6

											Temperature [a]	
Length (μm)	SiO_2	TiO_2	CaO	Na_2O	Al_2O_3	K_2O	MgO	FeO	Total	Ti (ppm)	K	°C
0	98.124	0.020	0.033	0.003	0.115	0.010	0.008	0.029	98.342	200	1188.4	915.3
40	98.808	0.027	0.061	0.063	0.345	0.088	0.008	0.045	99.445	270	1238.1	965.0
60	98.341	0.021	0.023	0.022	0.048	0.013	0.004	0.020	98.492	210	1196.2	923.1
80	98.129	0.024	0.011	0.003	0.023	0.006	0.000	0.010	98.206	240	1218.1	945.0
120	97.431	0.025	0.033	0.058	0.398	0.077	0.007	0.017	98.046	250	1225.0	951.8
180	99.063	0.017	0.005	0.006	0.029	0.013	0.002	0.006	99.141	170	1163.2	890.0
200	99.046	0.021	0.011	0.029	0.023	0.023	0.006	0.010	99.169	210	1196.2	923.1
220	98.635	0.018	0.022	0.012	0.046	0.012	0.007	0.020	98.772	180	1171.9	898.8
240	98.669	0.023	0.011	0.001	0.029	0.005	0.000	0.000	98.738	230	1211.1	937.9
260	98.861	0.024	0.009	0.000	0.024	0.000	0.000	0.017	98.935	240	1218.1	945.0
280	99.394	0.025	0.007	0.000	0.016	0.002	0.000	0.000	99.444	250	1225.0	951.8
300	99.337	0.023	0.006	0.000	0.020	0.006	0.000	0.004	99.396	230	1211.1	937.9
340	99.376	0.021	0.069	0.042	0.417	0.050	0.018	0.040	100.033	210	1196.2	923.1
380	98.932	0.026	0.008	0.003	0.014	0.005	0.000	0.024	99.012	260	1231.7	958.5
400	98.898	0.023	0.042	0.018	0.152	0.021	0.015	0.006	99.175	230	1211.1	937.9
420	98.370	0.019	0.043	0.153	0.098	0.121	0.012	0.008	98.824	190	1180.3	907.2
440	99.257	0.018	0.014	0.004	0.034	0.012	0.000	0.013	99.352	180	1171.9	898.8
460	98.172	0.021	0.046	0.032	0.127	0.047	0.010	0.032	98.487	210	1196.2	923.1
480	99.073	0.028	0.087	0.026	0.541	0.038	0.026	0.429	100.248	280	1244.4	971.3
540	98.282	0.025	0.015	0.004	0.076	0.005	0.005	0.012	98.424	250	1225.0	951.8
560	97.107	0.020	0.062	0.065	0.702	0.058	0.007	0.014	98.035	200	1188.4	915.3
880	99.691	0.027	0.028	0.007	0.101	0.016	0.005	0.016	99.891	270	1238.1	965.0
920	98.321	0.026	0.011	0.007	0.015	0.017	0.006	0.004	98.407	260	1231.7	958.5
940	98.826	0.025	0.034	0.232	0.036	0.132	0.009	0.000	99.294	250	1225.0	951.8
960	98.302	0.021	0.018	0.021	0.067	0.031	0.005	0.007	98.472	210	1196.2	923.1
1000	98.465	0.020	0.017	0.032	0.019	0.030	0.000	0.000	98.583	200	1188.4	915.3
1060	98.562	0.023	0.009	0.000	0.036	0.002	0.001	0.029	98.662	230	1211.1	937.9
1080	99.008	0.021	0.010	0.000	0.029	0.000	0.006	0.009	99.083	210	1196.2	923.1
1100	98.537	0.019	0.008	0.000	0.031	0.000	0.004	0.007	98.606	190	1180.3	907.2

[a] Quartz crystallization temperatures calculated using the TitaniQ method (Wark and Watson, 2006; Wark *et al.*, 2007).

Table H.3. Electron Microprobe Traverse Analyses of Quartz QA from Gibbon River Sample GRWY6 (continued)

											Temperature [a]	
Length (μm)	SiO_2	TiO_2	CaO	Na_2O	Al_2O_3	K_2O	MgO	FeO	Total	Ti (ppm)	K	°C
1120	98.771	0.024	0.009	0.000	0.034	0.002	0.000	0.000	98.840	240	1218.1	945.0
1260	96.358	0.020	0.087	0.017	1.559	0.023	0.019	0.187	98.270	200	1188.4	915.3
1280	98.752	0.026	0.018	0.003	0.093	0.004	0.000	0.024	98.920	260	1231.7	958.5
1300	98.054	0.026	0.072	0.031	0.178	0.020	0.005	0.039	98.425	260	1231.7	958.5
1320	98.599	0.026	0.026	0.000	0.068	0.012	0.001	0.009	98.741	260	1231.7	958.5
1340	98.613	0.024	0.018	0.004	0.035	0.004	0.003	0.000	98.701	240	1218.1	945.0
1380	99.248	0.028	0.064	0.034	0.260	0.054	0.004	0.055	99.747	280	1244.4	971.3

[a] Quartz crystallization temperatures calculated using the TitaniQ method (Wark and Watson, 2006; Wark *et al.*, 2007).

Table H.4. Electron Microprobe Traverse Analyses of Quartz QB from Gibbon River Sample GRWY6

											Temperature [a]	
Length (μm)	SiO_2	TiO_2	CaO	Na_2O	Al_2O_3	K_2O	MgO	FeO	Total	Ti (ppm)	K	°C
0	99.693	0.032	0.002	0.008	0.028	0.015	0.006	0.024	99.808	320	1268.2	995.0
20	98.860	0.029	0.000	0.004	0.015	0.011	0.000	0.004	98.923	290	1250.6	977.4
40	99.319	0.034	0.002	0.005	0.023	0.009	0.000	0.005	99.397	340	1279.2	1006.1
60	99.309	0.030	0.003	0.004	0.025	0.010	0.000	0.000	99.381	300	1256.6	983.4
80	99.206	0.027	0.004	0.000	0.018	0.011	0.003	0.000	99.269	270	1238.1	965.0
100	99.043	0.027	0.005	0.001	0.026	0.002	0.002	0.000	99.106	270	1238.1	965.0
120	99.411	0.025	0.006	0.000	0.024	0.014	0.000	0.000	99.480	250	1225.0	951.8
140	100.057	0.026	0.002	0.008	0.018	0.010	0.000	0.002	100.123	260	1231.7	958.5
160	99.637	0.024	0.005	0.005	0.021	0.015	0.000	0.000	99.707	240	1218.1	945.0
180	99.101	0.028	0.002	0.000	0.021	0.012	0.000	0.021	99.185	280	1244.4	971.3
200	98.859	0.028	0.004	0.006	0.088	0.015	0.003	0.014	99.017	280	1244.4	971.3
220	99.576	0.025	0.001	0.000	0.019	0.013	0.000	0.003	99.637	250	1225.0	951.8
240	99.326	0.027	0.006	0.005	0.028	0.016	0.001	0.006	99.415	270	1238.1	965.0
260	99.398	0.027	0.006	0.005	0.023	0.017	0.000	0.000	99.476	270	1238.1	965.0
280	98.707	0.026	0.008	0.012	0.034	0.023	0.000	0.022	98.832	260	1231.7	958.5
300	98.902	0.028	0.016	0.008	0.039	0.020	0.001	0.008	99.022	280	1244.4	971.3
320	98.187	0.027	0.013	0.005	0.095	0.036	0.001	0.009	98.373	270	1238.1	965.0
340	99.185	0.023	0.000	0.000	0.022	0.009	0.003	0.002	99.244	230	1211.1	937.9
360	98.970	0.026	0.002	0.000	0.018	0.014	0.000	0.000	99.030	260	1231.7	958.5
480	99.044	0.028	0.003	0.000	0.020	0.008	0.000	0.002	99.105	280	1244.4	971.3
500	98.760	0.030	0.015	0.006	0.039	0.010	0.004	0.010	98.874	300	1256.6	983.4
520	98.240	0.025	0.011	0.010	0.032	0.010	0.000	0.000	98.328	250	1225.0	951.8
540	98.827	0.031	0.009	0.002	0.029	0.010	0.005	0.000	98.913	310	1262.4	989.3
560	99.210	0.027	0.007	0.004	0.023	0.012	0.004	0.008	99.295	270	1238.1	965.0
600	99.159	0.028	0.004	0.000	0.021	0.007	0.000	0.000	99.219	280	1244.4	971.3
620	99.413	0.030	0.004	0.000	0.023	0.006	0.000	0.003	99.479	300	1256.6	983.4
640	99.556	0.029	0.009	0.000	0.021	0.002	0.001	0.004	99.622	290	1250.6	977.4
660	99.560	0.027	0.007	0.000	0.022	0.007	0.000	0.009	99.632	270	1238.1	965.0
680	99.577	0.028	0.006	0.001	0.023	0.007	0.000	0.000	99.642	280	1244.4	971.3

[a] Quartz crystallization temperatures calculated using the TitaniQ method (Wark and Watson, 2006; Wark *et al.*, 2007).

Table H.4. Electron Microprobe Traverse Analyses of Quartz QB from Gibbon River Sample GRWY6 (continued)

											Temperature [a]	
Length (μm)	SiO_2	TiO_2	CaO	Na_2O	Al_2O_3	K_2O	MgO	FeO	Total	Ti (ppm)	K	°C
700	99.529	0.026	0.003	0.001	0.024	0.009	0.000	0.005	99.597	260	1231.7	958.5
720	99.636	0.023	0.004	0.000	0.025	0.008	0.003	0.000	99.699	230	1211.1	937.9
740	99.511	0.027	0.001	0.000	0.014	0.008	0.003	0.012	99.576	270	1238.1	965.0
760	99.435	0.026	0.000	0.000	0.018	0.013	0.000	0.002	99.494	260	1231.7	958.5
780	99.715	0.030	0.000	0.000	0.012	0.007	0.000	0.000	99.764	300	1256.6	983.4
800	99.865	0.027	0.007	0.002	0.029	0.011	0.000	0.007	99.948	270	1238.1	965.0
820	100.064	0.026	0.007	0.000	0.020	0.009	0.000	0.000	100.126	260	1231.7	958.5
840	99.565	0.025	0.000	0.004	0.023	0.010	0.000	0.024	99.651	250	1225.0	951.8
860	99.902	0.022	0.007	0.003	0.021	0.008	0.004	0.003	99.970	220	1203.8	930.6
880	98.900	0.022	0.008	0.000	0.020	0.004	0.000	0.000	98.954	220	1203.8	930.6
900	99.301	0.025	0.003	0.000	0.018	0.010	0.001	0.000	99.358	250	1225.0	951.8
920	98.947	0.027	0.010	0.009	0.031	0.005	0.000	0.000	99.029	270	1238.1	965.0
940	99.902	0.025	0.005	0.002	0.032	0.016	0.000	0.000	99.982	250	1225.0	951.8
960	99.589	0.029	0.007	0.002	0.023	0.008	0.000	0.000	99.658	290	1250.6	977.4
980	99.043	0.024	0.004	0.004	0.017	0.013	0.000	0.013	99.118	240	1218.1	945.0
1000	98.566	0.030	0.000	0.000	0.021	0.011	0.000	0.000	98.628	300	1256.6	983.4
1020	98.308	0.028	0.009	0.000	0.023	0.009	0.000	0.000	98.377	280	1244.4	971.3
1040	98.778	0.028	0.001	0.000	0.024	0.008	0.000	0.000	98.839	280	1244.4	971.3
1060	99.158	0.023	0.000	0.000	0.023	0.009	0.002	0.002	99.217	230	1211.1	937.9
1080	99.292	0.028	0.009	0.000	0.026	0.011	0.000	0.015	99.381	280	1244.4	971.3
1100	99.334	0.028	0.000	0.004	0.023	0.006	0.000	0.000	99.395	280	1244.4	971.3
1120	98.981	0.027	0.003	0.000	0.023	0.013	0.003	0.017	99.067	270	1238.1	965.0

[a] Quartz crystallization temperatures calculated using the TitaniQ method (Wark and Watson, 2006; Wark *et al.*, 2007).

Table H.5. Electron Microprobe Traverse Analyses of Quartz QA from Gibbon River Sample GRWY7P

											Temperature [a]	
Length (μm)	SiO_2	TiO_2	CaO	Na_2O	Al_2O_3	K_2O	MgO	FeO	Total	Ti (ppm)	K	°C
0	98.951	0.017	0.002	0.000	0.022	0.013	0.000	0.020	99.025	170	1163.2	890.0
20	99.957	0.023	0.006	0.001	0.016	0.002	0.000	0.006	100.011	230	1211.1	937.9
40	99.867	0.019	0.003	0.002	0.022	0.002	0.003	0.010	99.928	190	1180.3	907.2
60	99.924	0.020	0.006	0.000	0.019	0.006	0.001	0.032	100.008	200	1188.4	915.3
80	100.144	0.022	0.003	0.000	0.025	0.000	0.000	0.002	100.196	220	1203.8	930.6
100	100.031	0.024	0.003	0.008	0.026	0.003	0.001	0.002	100.098	240	1218.1	945.0
120	99.967	0.023	0.002	0.000	0.024	0.000	0.000	0.018	100.034	230	1211.1	937.9
140	99.785	0.024	0.044	0.000	0.500	0.007	0.006	0.039	100.405	240	1218.1	945.0
160	99.556	0.027	0.006	0.002	0.024	0.002	0.006	0.019	99.642	270	1238.1	965.0
180	99.011	0.023	0.005	0.000	0.022	0.003	0.000	0.002	99.066	230	1211.1	937.9
200	99.210	0.025	0.003	0.005	0.023	0.000	0.000	0.012	99.278	250	1225.0	951.8
220	99.003	0.026	0.027	0.002	0.026	0.000	0.004	0.000	99.088	260	1231.7	958.5
240	98.705	0.028	0.049	0.028	0.025	0.004	0.010	0.008	98.857	280	1244.4	971.3
260	98.721	0.028	0.027	0.020	0.033	0.002	0.009	0.021	98.861	280	1244.4	971.3
280	99.034	0.027	0.011	0.026	0.027	0.008	0.000	0.000	99.133	270	1238.1	965.0
300	98.879	0.026	0.000	0.004	0.025	0.000	0.000	0.000	98.934	260	1231.7	958.5
320	98.726	0.029	0.000	0.008	0.030	0.000	0.003	0.023	98.819	290	1250.6	977.4
340	98.498	0.032	0.000	0.000	0.031	0.002	0.000	0.010	98.573	320	1268.2	995.0
360	98.189	0.030	0.010	0.001	0.096	0.004	0.001	0.024	98.355	300	1256.6	983.4
400	98.800	0.029	0.006	0.007	0.032	0.000	0.003	0.000	98.877	290	1250.6	977.4
420	98.789	0.027	0.006	0.000	0.022	0.002	0.000	0.005	98.851	270	1238.1	965.0
440	98.695	0.028	0.002	0.000	0.023	0.000	0.001	0.002	98.751	280	1244.4	971.3
460	97.835	0.023	0.037	0.007	0.410	0.011	0.017	0.042	98.382	230	1211.1	937.9
480	98.467	0.030	0.004	0.000	0.036	0.000	0.000	0.002	98.539	300	1256.6	983.4
500	98.849	0.030	0.005	0.000	0.029	0.009	0.000	0.000	98.922	300	1256.6	983.4
520	98.836	0.028	0.004	0.002	0.022	0.003	0.000	0.012	98.907	280	1244.4	971.3
560	98.105	0.029	0.033	0.012	0.464	0.013	0.012	0.015	98.683	290	1250.6	977.4
580	98.809	0.027	0.001	0.001	0.026	0.003	0.000	0.015	98.882	270	1238.1	965.0
600	99.007	0.030	0.004	0.001	0.028	0.004	0.001	0.000	99.075	300	1256.6	983.4

[a] Quartz crystallization temperatures calculated using the TitaniQ method (Wark and Watson, 2006; Wark *et al.*, 2007).

Table H.5. Electron Microprobe Traverse Analyses of Quartz QA from Gibbon River Sample GRWY7P (continued)

											Temperature [a]	
Length (μm)	SiO_2	TiO_2	CaO	Na_2O	Al_2O_3	K_2O	MgO	FeO	Total	Ti (ppm)	K	°C
620	98.944	0.032	0.004	0.002	0.030	0.000	0.003	0.011	99.026	320	1268.2	995.0
640	98.821	0.026	0.008	0.000	0.029	0.000	0.000	0.000	98.884	260	1231.7	958.5
660	99.301	0.029	0.002	0.005	0.038	0.003	0.007	0.008	99.393	290	1250.6	977.4
680	99.070	0.031	0.032	0.020	0.025	0.000	0.005	0.000	99.183	310	1262.4	989.3
700	98.567	0.023	0.003	0.008	0.026	0.006	0.004	0.019	98.656	230	1211.1	937.9
720	99.304	0.029	0.011	0.008	0.029	0.000	0.000	0.000	99.381	290	1250.6	977.4
740	99.307	0.030	0.000	0.000	0.025	0.000	0.000	0.000	99.362	300	1256.6	983.4
760	99.439	0.027	0.006	0.000	0.031	0.000	0.000	0.000	99.503	270	1238.1	965.0
780	99.322	0.026	0.000	0.000	0.023	0.006	0.000	0.000	99.377	260	1231.7	958.5
800	98.743	0.027	0.004	0.000	0.033	0.005	0.001	0.003	98.816	270	1238.1	965.0
820	97.908	0.027	0.046	0.013	0.425	0.015	0.011	0.008	98.453	270	1238.1	965.0
840	98.774	0.023	0.010	0.000	0.054	0.001	0.003	0.012	98.877	230	1211.1	937.9
860	98.882	0.021	0.014	0.001	0.079	0.001	0.000	0.025	99.023	210	1196.2	923.1
880	98.965	0.020	0.004	0.000	0.022	0.000	0.000	0.000	99.011	200	1188.4	915.3
900	99.037	0.020	0.002	0.001	0.023	0.000	0.000	0.000	99.083	200	1188.4	915.3
920	99.305	0.019	0.002	0.000	0.027	0.003	0.002	0.026	99.384	190	1180.3	907.2

[a] Quartz crystallization temperatures calculated using the TitaniQ method (Wark and Watson, 2006; Wark *et al.*, 2007).

Table H.6. Electron Microprobe Traverse Analyses of Quartz QB from Gibbon River Sample GRWY7P

											Temperature [a]	
Length (μm)	SiO_2	TiO_2	CaO	Na_2O	Al_2O_3	K_2O	MgO	FeO	Total	Ti (ppm)	K	°C
0	99.244	0.024	0.009	0.000	0.029	0.004	0.000	0.016	99.326	240	1218.1	945.0
40	99.487	0.025	0.002	0.000	0.026	0.002	0.000	0.008	99.550	250	1225.0	951.8
60	99.083	0.023	0.000	0.003	0.025	0.005	0.000	0.007	99.146	230	1211.1	937.9
80	98.766	0.021	0.005	0.000	0.035	0.003	0.001	0.005	98.836	210	1196.2	923.1
100	99.828	0.023	0.013	0.002	0.054	0.002	0.006	0.008	99.936	230	1211.1	937.9
120	98.870	0.023	0.003	0.008	0.023	0.000	0.002	0.000	98.929	230	1211.1	937.9
160	99.254	0.019	0.004	0.001	0.026	0.005	0.000	0.000	99.309	190	1180.3	907.2
220	101.275	0.024	0.007	0.008	0.099	0.000	0.003	0.000	101.416	240	1218.1	945.0
240	101.334	0.022	0.015	0.012	0.254	0.003	0.003	0.005	101.648	220	1203.8	930.6
260	99.434	0.021	0.008	0.000	0.018	0.006	0.001	0.016	99.504	210	1196.2	923.1
280	99.077	0.025	0.004	0.009	0.047	0.005	0.001	0.014	99.182	250	1225.0	951.8
300	99.322	0.021	0.004	0.007	0.026	0.000	0.000	0.000	99.380	210	1196.2	923.1
320	99.271	0.020	0.008	0.013	0.027	0.002	0.000	0.000	99.341	200	1188.4	915.3
340	98.970	0.018	0.004	0.000	0.027	0.003	0.000	0.006	99.028	180	1171.9	898.8
360	100.073	0.020	0.006	0.001	0.036	0.002	0.000	0.007	100.145	200	1188.4	915.3
380	99.215	0.020	0.003	0.004	0.040	0.000	0.002	0.000	99.284	200	1188.4	915.3
400	99.670	0.021	0.003	0.000	0.037	0.005	0.000	0.000	99.736	210	1196.2	923.1
420	99.130	0.024	0.001	0.002	0.028	0.004	0.002	0.000	99.191	240	1218.1	945.0
440	99.107	0.025	0.014	0.006	0.038	0.000	0.000	0.000	99.190	250	1225.0	951.8
460	99.721	0.024	0.000	0.000	0.033	0.000	0.000	0.004	99.782	240	1218.1	945.0
480	98.942	0.022	0.003	0.000	0.045	0.004	0.000	0.011	99.027	220	1203.8	930.6
500	99.317	0.024	0.002	0.001	0.027	0.001	0.000	0.024	99.396	240	1218.1	945.0
520	98.763	0.027	0.000	0.000	0.028	0.000	0.000	0.000	98.818	270	1238.1	965.0
540	98.794	0.022	0.003	0.000	0.018	0.000	0.000	0.000	98.837	220	1203.8	930.6
560	98.655	0.024	0.002	0.000	0.027	0.003	0.000	0.003	98.714	240	1218.1	945.0
580	100.069	0.025	0.031	0.013	0.476	0.007	0.006	0.006	100.633	250	1225.0	951.8
600	98.343	0.021	0.015	0.000	0.094	0.004	0.005	0.020	98.502	210	1196.2	923.1
660	98.608	0.019	0.007	0.000	0.075	0.000	0.000	0.008	98.717	190	1180.3	907.2
680	98.290	0.020	0.008	0.000	0.039	0.003	0.000	0.019	98.379	200	1188.4	915.3
700	99.145	0.021	0.003	0.001	0.030	0.004	0.000	0.010	99.214	210	1196.2	923.1

[a] Quartz crystallization temperatures calculated using the TitaniQ method (Wark and Watson, 2006; Wark *et al.*, 2007).

Table H.7. Electron Microprobe Traverse Analyses of Quartz QC from Gibbon River Sample GRWY7P

											Temperature [a]	
Length (μm)	SiO_2	TiO_2	CaO	Na_2O	Al_2O_3	K_2O	MgO	FeO	Total	Ti (ppm)	K	°C
20	100.117	0.020	0.007	0.000	0.032	0.009	0.004	0.014	100.203	200	1188.4	915.3
60	100.035	0.019	0.006	0.000	0.046	0.004	0.000	0.027	100.137	190	1180.3	907.2
80	99.807	0.016	0.006	0.000	0.027	0.004	0.002	0.000	99.862	160	1154.0	880.8
100	99.726	0.017	0.006	0.001	0.031	0.000	0.000	0.007	99.788	170	1163.2	890.0
120	99.633	0.017	0.000	0.000	0.029	0.000	0.000	0.018	99.697	170	1163.2	890.0
140	99.537	0.014	0.000	0.005	0.021	0.000	0.001	0.000	99.578	140	1134.3	861.2
160	99.443	0.014	0.008	0.000	0.023	0.000	0.000	0.000	99.488	140	1134.3	861.2
180	99.357	0.017	0.004	0.000	0.026	0.000	0.000	0.009	99.413	170	1163.2	890.0
200	99.465	0.020	0.000	0.000	0.030	0.000	0.000	0.016	99.531	200	1188.4	915.3
220	99.304	0.016	0.000	0.000	0.022	0.001	0.001	0.000	99.344	160	1154.0	880.8
260	99.793	0.016	0.006	0.003	0.025	0.001	0.000	0.000	99.844	160	1154.0	880.8
340	98.976	0.016	0.002	0.000	0.025	0.000	0.004	0.001	99.024	160	1154.0	880.8
360	98.661	0.015	0.007	0.000	0.030	0.000	0.002	0.000	98.715	150	1144.4	871.3
380	98.271	0.016	0.024	0.005	0.834	0.000	0.003	0.021	99.174	160	1154.0	880.8
440	100.301	0.019	0.008	0.003	0.036	0.002	0.000	0.016	100.385	190	1180.3	907.2
460	99.851	0.023	0.007	0.000	0.036	0.004	0.000	0.003	99.924	230	1211.1	937.9
480	99.807	0.018	0.000	0.006	0.028	0.003	0.000	0.003	99.865	180	1171.9	898.8
520	99.459	0.017	0.005	0.000	0.031	0.003	0.000	0.000	99.515	170	1163.2	890.0
540	99.366	0.018	0.003	0.005	0.028	0.000	0.004	0.000	99.424	180	1171.9	898.8
560	99.216	0.019	0.005	0.000	0.029	0.001	0.001	0.009	99.280	190	1180.3	907.2
580	99.382	0.022	0.006	0.000	0.018	0.001	0.000	0.012	99.441	220	1203.8	930.6
600	99.641	0.017	0.001	0.000	0.022	0.000	0.005	0.000	99.686	170	1163.2	890.0
620	99.830	0.020	0.009	0.002	0.025	0.006	0.000	0.000	99.892	200	1188.4	915.3
660	97.710	0.021	0.047	0.021	0.545	0.043	0.017	0.045	98.449	210	1196.2	923.1
680	99.622	0.019	0.000	0.000	0.028	0.000	0.000	0.002	99.671	190	1180.3	907.2
700	99.515	0.012	0.000	0.000	0.028	0.007	0.000	0.000	99.562	120	1112.4	839.3
720	99.120	0.016	0.011	0.002	0.022	0.001	0.008	0.006	99.186	160	1154.0	880.8
740	99.082	0.016	0.009	0.005	0.086	0.000	0.004	0.022	99.224	160	1154.0	880.8
780	93.557	0.021	0.136	0.039	4.389	0.028	0.049	0.124	98.343	210	1196.2	923.1

[a] Quartz crystallization temperatures calculated using the TitaniQ method (Wark and Watson, 2006; Wark *et al.*, 2007).

Table H.7. Electron Microprobe Traverse Analyses of Quartz QC from Gibbon River Sample GRWY7P (continued)

											Temperature [a]	
Length (μm)	SiO_2	TiO_2	CaO	Na_2O	Al_2O_3	K_2O	MgO	FeO	Total	Ti (ppm)	K	°C
800	99.903	0.019	0.004	0.000	0.027	0.002	0.005	0.036	99.996	190	1180.3	907.2
820	99.504	0.016	0.005	0.003	0.025	0.005	0.002	0.004	99.564	160	1154.0	880.8
840	99.562	0.018	0.008	0.000	0.024	0.001	0.000	0.010	99.623	180	1171.9	898.8
920	99.394	0.014	0.005	0.000	0.029	0.000	0.003	0.014	99.459	140	1134.3	861.2
940	98.426	0.017	0.047	0.018	0.413	0.021	0.021	0.007	98.970	170	1163.2	890.0
960	98.882	0.019	0.005	0.001	0.024	0.005	0.001	0.017	98.954	190	1180.3	907.2

[a] Quartz crystallization temperatures calculated using the TitaniQ method (Wark and Watson, 2006; Wark *et al.*, 2007).

APPENDIX I

U-TH GEOCHRONOLOGY DATA

Table I.1. U-Th Ion Microprobe Data and Calculated Ages for Zircons from Gibbon River Sample GRWY6

Zircon Grain	Analysis Spot	$^{230}Th/^{232}Th$	1 σ	$^{238}U/^{232}Th$	1 σ	Age (k.y.) [a]	1 σ (k.y.) [a]	U (ppm)
1	1	2.85×10^{-5}	3.62×10^{-6}	2.559	6.15×10^{-3}	131	34	72
1	2	1.80×10^{-5}	2.20×10^{-6}	1.678	4.70×10^{-3}	120	29	129
1	3	2.53×10^{-5}	2.22×10^{-6}	1.864	1.86×10^{-2}	211	64	105
2	4	1.94×10^{-5}	9.98×10^{-7}	1.686	3.64×10^{-3}	138	17	275
3	5	1.80×10^{-5}	1.30×10^{-6}	1.637	2.85×10^{-3}	126	19	191
3	6	2.08×10^{-5}	1.51×10^{-6}	1.838	4.11×10^{-3}	133	21	188
4	7	2.21×10^{-5}	8.49×10^{-7}	1.799	1.79×10^{-2}	160	20	379
5	8	2.06×10^{-5}	1.60×10^{-6}	1.667	6.63×10^{-3}	162	33	135
6	9	2.01×10^{-5}	1.37×10^{-6}	1.794	2.70×10^{-2}	130	21	142
6	10	1.74×10^{-5}	1.30×10^{-6}	1.643	6.55×10^{-3}	116	18	153
6	11	1.95×10^{-5}	1.47×10^{-6}	1.684	9.97×10^{-3}	139	24	139
7	12	2.09×10^{-5}	1.55×10^{-6}	1.813	2.53×10^{-2}	138	25	127
7	13	1.90×10^{-5}	1.43×10^{-6}	1.602	3.73×10^{-3}	148	27	167
8	14	2.22×10^{-5}	1.91×10^{-6}	1.976	2.55×10^{-2}	132	26	125
8	15	2.32×10^{-5}	1.82×10^{-6}	1.860	2.77×10^{-2}	166	36	137
9	16	2.72×10^{-5}	2.69×10^{-6}	1.626	2.38×10^{-2}	- [b]	-206	72
9	17	2.00×10^{-5}	1.82×10^{-6}	1.640	3.52×10^{-3}	156	35	108
10	18	1.95×10^{-5}	6.70×10^{-7}	1.502	1.16×10^{-2}	184	24	487
11	19	2.41×10^{-5}	1.96×10^{-6}	2.146	3.81×10^{-3}	132	23	126
11	20	2.40×10^{-5}	9.00×10^{-7}	2.096	4.39×10^{-3}	137	13	418

[a] Activity and age calculations used the following decay constants: $\lambda_{230} = 9.158 \times 10^{-6}$ a^{-1}; $\lambda_{232} = 4.9475 \times 10^{-11}$ a^{-1}; $\lambda_{238} = 1.55125 \times 10^{-10}$ a^{-1}.

[b] Age calculations for analysis 16 result in an imaginary number and analysis 16 is excluded in further age calculations and comparisons.

APPENDIX J

AR-AR GEOCHRONOLOGY DATA

Table J.1. Ar-Ar Data and Calculated Ages for Basalt Groundmass from Crystal Spring Sample CSWY1E (Analysis #1)

Step	T(°C)	t (min.)	^{36}Ar	^{37}Ar	^{38}Ar	^{39}Ar	^{40}Ar	$\%^{40}Ar^*$	Ca/K	$^{40}Ar^*/^{39}ArK$	Age (ka)	1 σ (ka)
1	500	12	45.526	2.899	9.310	63.229	12311.77	-6.5	1.18944272	-3605.641433	-6088.00	-551.00
2	580	12	38.742	8.068	8.282	77.751	11129.84	-0.2	2.69319551	-303.571238	-153.00	-358.00
3	660	12	23.535	20.193	5.329	63.004	6853.14	1.3	8.33251759	1739.399807	690.00	274.00
4	740	12	15.700	32.275	3.436	40.177	4583.31	2.0	20.9640554	3037.561997	1074.00	287.00
5	835	12	3.202	48.642	1.054	36.394	907.77	3.2	35.0259555	883.015997	383.00	64.00
6	945	12	2.168	35.201	0.622	18.857	604.58	2.6	49.1258235	893.262974	387.00	116.00
7	1070	12	2.721	11.455	0.570	5.893	785.11	2.0	51.1860071	3756.282730	1256.00	346.00
8	1400	12	11.406	149.418	2.223	7.806	4224.24	25.5	583.538278	2.48442×10^{22}	78192.00	2102.00
										Total gas age =	2317.49	106.51
										Plateau Age [1] =	420.13	53.90
										[1] Steps 3-6, 50.6% ^{39}Ar released		
										Isochron Age [2] =	212.00	4.25
										[2] Steps 3-7, 52.5% ^{39}Ar released		

Note: ^{36}Ar through ^{40}Ar are measured beam intensities (mV), corrected for decay for the age calculations, error in age includes J error, all errors 1 sigma
200.96 mg basalt groundmass, J = 0.000267849 ± 0.5283%
4 amu discrimination = 1.02601 ± 0.52%, 40/39K = 0.0600 ± 34.8%, 36/37Ca = 0.00027787 ± 1.34%, 39/37Ca = 0.0006897 ± 8.84

Table J.2. Ar-Ar Data and Calculated Ages for Basalt Groundmass from Crystal Spring Sample CSWY1E (Analysis #2)

Step	T(°C)	t (min.)	^{36}Ar	^{37}Ar	^{38}Ar	^{39}Ar	^{40}Ar	$\%^{40}Ar^*$	Ca/K	$^{40}Ar^*/^{39}ArK$	Age (ka)	1 σ (ka)
1	425	12	16.415	1.041	3.395	24.658	4708.65	-0.4	1.100088635	-694.189732	-366.00	-478.00
2	500	12	22.802	2.530	4.913	46.359	6535.36	-0.5	1.422208686	-624.993481	-326.00	-353.00
3	560	12	23.100	5.596	5.081	50.565	6634.80	-0.2	2.885330642	-293.903110	-146.00	-331.00
4	620	12	17.873	12.691	4.027	47.527	5217.92	1.5	6.970376642	2139.254131	809.00	281.00
5	690	12	18.549	24.829	3.930	36.804	5425.57	1.9	17.6667761	4311.895813	1373.00	376.00
6	780	12	3.192	45.587	1.056	37.584	913.45	3.8	31.89897667	1060.300506	446.00	63.00
7	875	12	1.543	40.002	0.553	23.744	416.45	2.0	44.47240205	368.972102	168.00	57.00
8	1020	12	2.468	23.804	0.602	12.308	694.27	1.0	51.15473844	612.776977	271.00	152.00
9	1200	12	5.640	53.017	1.149	4.687	1598.78	1.5	323.3114175	12607.5963	2646.00	1021.00
10	1400	12	19.222	81.753	3.624	3.888	5571.59	1.9	655.7882283	33775729.3	16413.00	4641.00
										Total gas age =	547.56	78.72
										No plateau		
										No isochron		

Note: ^{36}Ar through ^{40}Ar are measured beam intensities (mV), corrected for decay for the age calculations, error in age includes J error, all errors 1 sigma
206.27 mg basalt groundmass, J = 0.000264508 ± 0.4442%
4 amu discrimination = 1.02601 ± 0.52%, 40/39K = 0.0600 ± 34.8%, 36/37Ca = 0.00027787 ± 1.34%, 39/37Ca = 0.0006897 ± 8.84

Table J.3. Ar-Ar Data and Calculated Ages for Basalt Groundmass from Crystal Spring Sample CSWY1E (Analysis #3)

Step	T(°C)	t (min.)	^{36}Ar	^{37}Ar	^{38}Ar	^{39}Ar	^{40}Ar	$\%^{40}Ar^*$	Ca/K	$^{40}Ar^*/^{39}ArK$	Age (ka)	1 σ (ka)
1	450	12	20.718	1.312	4.327	36.771	5882.38	-0.4	1.058598944	-646.733422	-334.00	-150.00
2	510	12	19.931	2.213	4.206	40.054	5674.57	-0.2	1.639511421	-208.344408	-101.00	-128.00
3	570	12	23.976	6.113	5.188	52.987	6920.36	1.2	3.425288205	2033.903364	769.00	123.00
4	630	12	16.296	12.448	3.658	44.960	4744.93	2.3	8.23213024	3387.942249	1144.00	92.00
5	700	12	17.183	24.199	3.739	36.135	5026.57	4.1	19.9819057	13648.262962	2740.00	187.00
6	790	12	2.430	40.954	0.909	36.572	688.30	13.9	33.54852606	3790.687361	1242.00	117.00
7	890	12	1.585	33.937	0.556	22.044	435.87	23.3	46.29719599	10111.257611	2332.00	195.00
8	1090	12	3.931	20.058	0.890	11.424	1115.72	1.3	52.90437565	195.740622	90.00	629.00
9	1400	12	8.564	127.083	1.666	6.926	2430.07	5.0	650.7509547	905195.545713	9869.00	441.00
										Total gas age =	1184.82	97.00
										No plateau		
										No isochron		

Note: ^{36}Ar through ^{40}Ar are measured beam intensities (mV), corrected for decay for the age calculations, error in age includes J error, all errors 1 sigma
209.73 mg basalt groundmass, J = 0.000261327 ± 0.4726%
4 amu discrimination = 1.03622 ± 0.18%, 40/39K = 0.0600 ± 34.8%, 36/37Ca = 0.00027787 ± 1.34%, 39/37Ca = 0.0006897 ± 8.84

Table J.4. Ar-Ar Data and Calculated Ages for 600 μm Volcanic Glass from Obsidian Cliff Sample OCWY2 (Analysis #1)

Step	T(°C)	t (min.)	^{36}Ar	^{37}Ar	^{38}Ar	^{39}Ar	^{40}Ar	%^{40}Ar*	Ca/K	^{40}Ar*/^{39}ArK	Age (ka)	1 σ (ka)
1	675	12	13.554	0.548	5.110	177.329	3970.93	2.4	0.09231928	584.011249	251.00	26.00
2	750	12	2.714	0.233	1.502	67.912	796.95	2.4	0.102494921	285.341828	127.00	16.00
3	800	12	0.313	0.486	2.330	158.466	118.76	18.0	0.091620297	130.064451	59.00	10.00
4	820	12	0.200	0.655	3.104	212.745	96.63	30.3	0.091975786	130.064451	59.00	10.00
5	840	12	0.176	0.653	3.107	216.128	89.02	32.0	0.090259618	123.347859	56.00	10.00
6	865	12	0.182	0.690	3.245	225.409	92.61	32.2	0.091446974	125.585482	57.00	10.00
7	890	12	0.215	0.756	3.492	237.606	103.59	29.5	0.095050928	123.347859	56.00	10.00
8	950	12	0.415	1.316	6.323	436.934	196.74	28.6	0.089976968	125.585482	57.00	10.00
9	1000	12	0.336	1.219	5.994	409.506	171.19	32.1	0.088927198	130.064451	59.00	10.00
10	1050	12	0.191	0.937	4.496	313.356	112.64	38.9	0.089329067	132.305798	60.00	10.00
11	1100	12	0.138	0.636	2.940	201.360	76.76	42.7	0.094357362	134.548388	61.00	10.00
12	1170	12	0.154	0.634	3.010	206.391	83.00	40.8	0.091767742	136.792221	62.00	10.00
13	1400	12	0.701	1.412	6.708	463.358	291.07	24.5	0.091035226	143.531189	65.00	10.00
										Total gas age =	71.05	5.89
										Plateau age [1] =	59.18	6.03
										[1] Steps 3-13, 92.6% ^{39}Ar released		
										Isochron age 1 [2] =	56.00	0.7
										[2] Steps 1-9, 64.4% ^{39}Ar released		
										Isochron age 2 [3] =	62.50	1.60
										[3] Steps 3-12, 78.7% ^{39}Ar released		

Note: ^{36}Ar through ^{40}Ar are measured beam intensities (mV), corrected for decay for the age calculations, error in age includes J error, all errors 1 sigma
200.39 mg 600 μm volcanic glass, J = 0.000255599 ± 0.5035%
4 amu discrimination = 1.03622 ± 0.18%, 40/39K = 0.0600 ± 34.8%, 36/37Ca = 0.00027787 ± 1.34%, 39/37Ca = 0.0006897 ± 8.84

Table J.5. Ar-Ar Data and Calculated Ages for 600 μm Volcanic Glass from Obsidian Cliff Sample OCWY2 (Analysis #2)

Step	T(°C)	t (min.)	^{36}Ar	^{37}Ar	^{38}Ar	^{39}Ar	^{40}Ar	$\%^{40}Ar^*$	Ca/K	$^{40}Ar^*/^{39}ArK$	Age (ka)	1 σ (ka)
1	675	12	11.345	0.771	5.825	254.214	3357.94	3.2	0.091412303	456.580481	208.00	20.00
2	750	12	3.410	1.006	5.521	342.335	1040.90	4.7	0.088571917	145.666054	69.00	11.00
3	800	12	0.485	1.005	4.904	328.380	186.99	16.5	0.09224423	92.243786	44.00	10.00
4	820	12	0.432	0.784	3.771	255.791	170.13	19.7	0.092380576	128.490317	61.00	10.00
5	840	12	0.436	0.645	3.231	219.364	160.32	15.1	0.088622445	107.127475	51.00	10.00
6	865	12	0.440	0.612	3.045	205.852	161.12	15.3	0.089607803	117.794094	56.00	10.00
7	890	12	0.451	0.599	2.928	197.690	163.36	14.8	0.091325455	119.930968	57.00	11.00
8	950	12	0.559	0.921	4.463	308.733	218.88	20.0	0.089913751	139.216226	66.00	11.00
9	1000	12	0.592	0.917	4.501	302.801	220.08	16.2	0.091277082	115.658405	55.00	10.00
10	1050	12	0.554	0.759	3.707	252.083	200.03	14.5	0.090750258	113.523899	54.00	10.00
11	1100	12	0.641	0.681	3.301	222.780	220.41	12.3	0.092134173	115.658405	55.00	10.00
12	1170	12	0.780	1.136	5.518	380.621	293.81	18.0	0.089957035	134.922295	64.00	10.00
13	1400	12	3.292	1.198	6.292	398.155	1020.27	5.9	0.090688932	152.126617	72.00	10.00
										Total gas age =	69.90	5.85
										Plateau Age[1] =	58.43	2.95
										[1] Steps 2-13, 93.1% ^{39}Ar released		
										No isochron		

Note: ^{36}Ar through ^{40}Ar are measured beam intensities (mV), corrected for decay for the age calculations, error in age includes J error, all errors 1 sigma
206.97 mg 600 μm volcanic glass, J = 0.00026765 ± 0.5%
4 amu discrimination = 1.03622 ± 0.18%, 40/39K = 0.0600 ± 34.8%, 36/37Ca = 0.00027787 ± 1.34%, 39/37Ca = 0.0006897 ± 8.84

Table J.6. Ar-Ar Data and Calculated Ages for 600 μm Volcanic Glass from Obsidian Cliff Sample OCWY2 (Analysis #3)

Step	T(°C)	t (min.)	^{36}Ar	^{37}Ar	^{38}Ar	^{39}Ar	^{40}Ar	$\%^{40}Ar^*$	Ca/K	$^{40}Ar^*/^{39}ArK$	Age (ka)	1 σ (ka)
1	675	12	6.878	0.847	5.352	283.911	2021.03	2.2	0.07698153	159.917052	71.00	16.00
2	750	12	1.734	0.924	4.787	309.195	547.47	6.5	0.077112516	116.503735	52.00	10.00
3	800	12	1.451	1.067	5.412	356.815	479.74	9.6	0.07716257	130.163841	58.00	10.00
4	820	12	1.227	0.899	4.539	300.598	403.18	9.0	0.077171861	121.052057	54.00	10.00
5	840	12	1.110	0.784	4.005	263.943	360.37	8.1	0.076646304	109.690700	49.00	10.00
6	865	12	1.079	0.787	3.877	258.354	355.08	9.3	0.078604082	127.884001	57.00	10.00
7	890	12	1.051	0.758	3.809	251.594	345.62	9.2	0.07774176	127.884001	57.00	10.00
8	950	12	1.314	0.981	5.096	335.732	434.79	9.6	0.075398275	125.605424	56.00	10.00
9	1000	12	1.336	1.001	5.058	335.156	445.12	10.3	0.077067707	139.295851	62.00	10.00
10	1050	12	1.298	0.861	4.440	293.281	428.07	9.8	0.075753797	143.869454	64.00	10.00
11	1100	12	1.212	0.691	3.447	223.875	393.62	9.4	0.079644931	164.513529	73.00	10.00
12	1170	12	1.203	0.577	2.967	192.943	384.39	8.3	0.077167096	162.214654	72.00	10.00
13	1400	12	1.901	0.399	2.166	128.750	572.63	4.2	0.079967109	185.260848	82.00	11.00
										Total gas age =	60.64	5.72
										Plateau Age [1] =	59.86	2.96
										[1] Steps 1-12, 96.4% ^{39}Ar released		
										No isochron		

Note: ^{36}Ar through ^{40}Ar are measured beam intensities (mV), corrected for decay for the age calculations, error in age includes J error, all errors 1 sigma
208.84 mg 600 μm volcanic glass, J = 0.000251005 ± 1.1422%
4 amu discrimination = 1.03622 ± 0.18%, 40/39K = 0.0600 ± 34.8%, 36/37Ca = 0.00027787 ± 1.34%, 39/37Ca = 0.0006897 ± 8.84

Table J.7. Ar-Ar Data and Calculated Ages for 850 μm Volcanic Glass from Obsidian Cliff Sample OCWY2 (Analysis #4)

Crystal	T(°C)	t (min.)	^{36}Ar	^{37}Ar	^{38}Ar	^{39}Ar	^{40}Ar	%^{40}Ar*	Ca/K	^{40}Ar*/^{39}ArK	Age (ka)	1 σ (ka)
1	1600	4	0.018	0.189	0.330	21.911	7.611	62.1	0.119949362	161.6452	76	21
2	1600	4	0.035	0.252	0.440	29.648	12.553	29.3	0.118196137	105.5776	50	17
3	1600	4	0.022	0.193	0.347	23.078	9.651	64.8	0.116293937	227.3508	106	16
4	1600	4	0.029	0.162	0.286	19.192	9.427	40.0	0.117379656	161.6452	76	19
5	1600	4	0.033	0.228	0.395	26.699	10.724	31.1	0.118751214	105.5776	50	15
										Mean age =	71.60	20.76
										No isochron		

Note: ^{36}Ar through ^{40}Ar are measured beam intensities (mV), corrected for decay for the age calculations, error in age includes J error, all errors 1 sigma
Individual 850 μm fragments of volcanic glass, J = 0.00026618 ± 0.5%
4 amu discrimination = 1.03042 ± 0.39%, 40/39K = 0.0600 ± 34.8%, 36/37Ca = 0.00027787 ± 1.34%, 39/37Ca = 0.00068970 ± 8.84%

Table J.8. Ar-Ar Data and Calculated Ages for 600 μm Sanidine from Gibbon River Sample GRWY6 (Analysis #1)

Step	T(°C)	t (min.)	^{36}Ar	^{37}Ar	^{38}Ar	^{39}Ar	^{40}Ar	$\%^{40}Ar^*$	Ca/K	$^{40}Ar^*/^{39}ArK$	Age (ka)	1 σ (ka)
1	650	12	1.003	0.046	0.269	5.920	287.50	0.7	0.238800457	338.722091	151.00	54.00
2	750	12	0.589	0.079	0.303	15.732	177.68	4.4	0.154323174	515.360050	225.00	18.00
3	850	12	0.826	0.178	0.688	44.070	239.81	0.6	0.124125497	32.393861	15.00	19.00
4	920	12	0.855	0.218	0.946	63.283	257.76	4.2	0.105864682	169.182918	77.00	15.00
5	990	12	0.990	0.337	1.346	94.798	304.08	5.6	0.109247833	178.170491	81.00	10.00
6	1060	12	1.131	0.441	1.802	129.691	357.19	7.8	0.104498543	218.862085	99.00	10.00
7	1110	12	1.212	0.478	1.924	137.162	370.56	4.9	0.107096656	131.207267	60.00	10.00
8	1150	12	1.238	0.487	1.987	140.431	380.30	5.4	0.106573131	142.339453	65.00	10.00
9	1190	12	1.364	0.611	2.540	184.065	433.18	8.2	0.102011974	191.689270	87.00	10.00
10	1230	12	1.677	1.412	5.558	421.981	576.33	13.3	0.102830765	182.671756	83.00	10.00
11	1260	12	1.599	0.918	3.682	279.127	512.21	8.2	0.101069908	149.033589	68.00	10.00
12	1290	12	1.339	0.337	1.448	99.611	404.64	4.5	0.103969035	180.420500	82.00	11.00
13	1400	12	1.822	0.137	0.772	35.630	532.42	2.1	0.11816477	315.402990	141.00	19.00
										Total gas age =	79.35	6.61
										Plateau Age[1] =	77.98	3.48
										[1] Steps 4-12, 93.9% ^{39}Ar released		
										No isochron		

Note: ^{36}Ar through ^{40}Ar are measured beam intensities (mV), corrected for decay for the age calculations, error in age includes J error, all errors 1 sigma
72.64 mg 600 μm sanidine, J = 0.000257739 ± 0.1467%
4 amu discrimination = 1.03622 ± 0.18%, 40/39K = 0.0600 ± 34.8%, 36/37Ca = 0.00027787 ± 1.34%, 39/37Ca = 0.0006897 ± 8.84

Table J.9. Ar-Ar Data and Calculated Ages for 600 μm Sanidine from Gibbon River Sample GRWY6 (Analysis #2)

Step	T(°C)	t (min.)	^{36}Ar	^{37}Ar	^{38}Ar	^{39}Ar	^{40}Ar	$\%^{40}Ar^*$	Ca/K	$^{40}Ar^*/^{39}ArK$	Age (ka)	1 σ (ka)
1	650	12	1.562	0.148	0.402	6.648	470.074	3.7	9.450253569	3690.867326	1206	133
2	750	12	0.275	0.144	0.277	16.971	83.427	11.4	3.595542383	547.146197	238	18
3	850	12	0.292	0.164	0.613	42.677	84.292	4.3	1.627430281	78.200148	36	23
4	920	12	0.277	0.158	0.844	62.655	89.038	14.8	1.067777321	189.433017	86	10
5	990	12	0.309	0.179	1.260	95.683	103.776	16.4	0.792066375	162.455303	74	11
6	1060	12	0.304	0.170	1.752	135.616	122.528	29.5	0.530697668	250.792986	113	10
7	1110	12	0.292	0.186	1.868	145.913	107.208	22.4	0.539671295	149.033589	68	10
8	1150	12	0.232	0.175	1.885	148.908	103.581	38.1	0.497536418	241.644573	109	10
9	1190	12	0.233	0.177	2.208	173.227	157.288	59.8	0.432567665	534.893642	233	10
10	1230	12	0.390	0.204	4.016	318.277	252.643	53.1	0.271331502	423.749260	187	10
11	1260	12	0.403	0.252	5.887	469.972	222.309	40.6	0.226985477	187.178014	85	10
12	1290	12	0.246	0.217	3.853	311.232	127.967	39.7	0.295157559	151.267443	69	10
13	1400	12	0.186	0.179	2.052	169.223	83.367	38.3	0.447808159	133.431236	61	10
										Total gas age =	114.05	6.22
										Pseudo-plateau age [1] =	71.67	5.77
										[1] Steps 11-13, 45.3% ^{39}Ar released		
										No isochron		

Note: ^{36}Ar through ^{40}Ar are measured beam intensities (mV), corrected for decay for the age calculations, error in age includes J error, all errors 1 sigma
73.51 mg 600 μm sanidine, J = 0.000257739 ± 0.1467%
4 amu discrimination = 1.00826 ± 0.40%, 40/39K = 0.0600 ± 34.8%, 36/37Ca = 0.00027787 ± 1.34%, 39/37Ca = 0.0006897 ± 8.84

Table J.10. Ar-Ar Data and Calculated Ages for 600 μm Sanidine from Gibbon River Sample GRWY6 (Analysis #3)

Step	T(°C)	t (min.)	^{36}Ar	^{37}Ar	^{38}Ar	^{39}Ar	^{40}Ar	$\%^{40}Ar^*$	Ca/K	$^{40}Ar^*/^{39}ArK$	Age (ka)	1 σ (ka)
1	650	12	0.649	0.151	0.193	4.563	196.195	5.8	14.31480401	3422.951990	1141	91
2	750	12	0.230	0.153	0.220	13.056	66.506	9.0	5.055149264	430.911742	190	14
3	850	12	0.245	0.149	0.461	32.977	72.577	8.8	1.94725222	178.170491	81	11
4	920	12	0.220	0.148	0.659	48.881	73.685	21.7	1.304622308	289.900832	130	12
5	990	12	0.277	0.172	0.994	75.025	86.248	11.0	0.987743601	113.459818	52	10
6	1060	12	0.274	0.167	1.406	106.977	100.213	23.6	0.672522263	202.989315	92	10
7	1110	12	0.261	0.167	1.489	114.853	93.321	21.3	0.626395619	155.738867	71	10
8	1150	12	0.303	0.172	1.593	122.870	110.095	24.6	0.603051113	184.924261	84	10
9	1190	12	0.298	0.188	1.824	141.902	112.023	24.6	0.570737813	178.170491	81	10
10	1230	12	0.407	0.212	3.734	299.002	193.799	36.0	0.305417855	225.683576	102	10
11	1260	12	0.355	0.224	4.519	353.160	172.060	34.9	0.273215264	173.674214	79	10
12	1290	12	0.244	0.193	2.477	197.285	103.428	31.3	0.42141603	149.033589	68	10
13	1400	12	0.254	0.180	1.300	103.898	88.457	18.0	0.746372403	111.246915	51	10
										Total gas age =	85.19	6.02
										Plateau Age[1] =	82.43	7.56
										[1] Steps 6-12, 82.8% ^{39}Ar released		
										No isochron		

Note: ^{36}Ar through ^{40}Ar are measured beam intensities (mV), corrected for decay for the age calculations, error in age includes J error, all errors 1 sigma
67.09 mg 600 μm sanidine, J = 0.000257739 ± 0.1467%
4 amu discrimination = 1.00826 ± 0.40%, 40/39K = 0.0600 ± 34.8%, 36/37Ca = 0.00027787 ± 1.34%, 39/37Ca = 0.0006897 ± 8.84

Table J.11. Ar-Ar Data and Calculated Ages for 850 μm Sanidine from Gibbon River Sample GRWY6 (Analysis #4)

Crystal	T(°C)	t (min.)	^{36}Ar	^{37}Ar	^{38}Ar	^{39}Ar	^{40}Ar	$\%^{40}Ar^*$	Ca/K	$^{40}Ar^*/^{39}ArK$	Age (ka)	1 σ (ka)
1	1600	6	0.032	0.256	0.346	27.490	16.260	57.5	0.127208916	309.0256	140	12
2	1600	6	0.062	0.370	0.509	39.441	24.534	31.4	0.128146349	184.7551	85	11
3	1600	6	0.044	0.320	0.448	35.651	17.693	35.8	0.122611182	160.3524	74	10
4	1600	4	0.126	0.384	0.591	45.100	44.126	16.6	0.116306985	162.5647	75	11
5	1600	4	0.032	0.274	0.381	30.179	12.943	33.4	0.123996048	125.1222	58	11
6	1600	4	0.060	0.316	0.459	36.134	30.262	48.1	0.119435288	408.8560	183	11
7	1600	4	0.026	0.258	0.350	27.773	10.386	46.9	0.126870122	149.3094	69	11
8	1600	4	0.069	0.244	0.314	23.827	23.808	24.0	0.139857046	234.0092	107	11
9	1600	4	0.076	0.323	0.514	41.619	30.356	29.8	0.105991491	216.0291	99	12
10	1600	4	0.082	0.340	0.519	41.102	29.521	21.3	0.112973572	149.3094	69	11
11	1600	4	0.206	0.384	0.639	46.659	650.189	91.1	0.112397495	111954.06	6150	120
12	1600	4	0.092	0.351	0.544	42.779	34.565	24.4	0.112056559	195.8965	90	11
										Mean age =	599.92	1673.75
										Mean age [1] =	95.36	36.90
										[1] Omitting Crystal 11		
										Weighted mean age [2] =	80.19	3.66
										[2] Omitting Crystals 1, 6 & 11		
										Isochron age [3] =	52	8.5
										[3] Crystals 6, 7, 8, 9, 11, 12 & 14		

Note: ^{36}Ar through ^{40}Ar are measured beam intensities (mV), corrected for decay for the age calculations, error in age includes J error, all errors 1 sigma
Individual 850 μm sanidine crystals, J = 0.000261119 ± 0.1601%
4 amu discrimination = 1.03042 ± 0.39%, 40/39K = 0.0600 ± 34.8%, 36/37Ca = 0.00027787 ± 1.34%, 39/37Ca = 0.00068970 ± 8.84%

Table J.12. Ar-Ar Data and Calculated Ages for 1.4 mm Sanidine from Gibbon River Sample GRWY6 (Analysis #5)

Crystal	T(°C)	t (min.)	^{36}Ar	^{37}Ar	^{38}Ar	^{39}Ar	^{40}Ar	$\%^{40}Ar^*$	Ca/K	$^{40}Ar^*/^{39}ArK$	Age (ka)	1 σ (ka)
1	1600	4	0.124	0.180	1.055	80.358	55.483	48.7	1.167226605	337.1767	156	11
2	1600	4	0.180	0.182	1.312	102.084	81.956	43.2	0.92896423	355.2663	164	10
3	1600	4	0.277	0.185	1.713	134.534	133.859	42.6	0.716475448	442.2957	202	11
4	1600	4	0.115	0.173	1.329	103.758	78.586	65.7	0.86876656	517.0189	234	10
5	1600	4	0.432	0.183	1.533	117.688	164.066	26.0	0.810197642	375.7131	173	11
6	1600	4	0.169	0.184	1.778	139.883	80.441	43.7	0.68534786	252.3383	118	10
7	1600	4	0.167	0.192	1.836	143.698	107.459	58.6	0.696161311	456.2055	208	10
8	1600	4	0.184	0.177	1.643	129.369	88.057	44.2	0.712860059	305.7124	142	10
9	1600	4	0.227	0.181	1.548	120.534	102.469	40.2	0.782416467	350.7364	162	10
10	1600	4	0.145	0.192	1.781	140.631	82.334	53.9	0.711346555	321.4140	149	10
11	1600	4	0.138	0.183	2.002	158.975	77.740	52.2	0.599750898	256.7591	120	10
12	1600	4	0.139	0.187	1.579	124.956	98.727	64.5	0.779746029	533.5420	241	11
13	1600	4	0.473	0.188	1.862	144.564	188.223	28.4	0.677571302	384.8334	177	11
14	1600	4	0.243	0.185	2.194	172.123	103.458	33.3	0.559985843	201.8502	95	10
15	1600	4	0.116	0.200	2.011	160.618	73.469	58.7	0.648768697	270.0509	126	10
16	1600	4	0.177	0.188	1.748	137.005	70.051	32.2	0.714961907	162.7843	77	10
17	1600	4	0.177	0.205	2.318	183.106	134.092	63.2	0.583308234	484.1643	220	10
18	1600	4	1.054	0.211	3.374	255.810	385.408	19.1	0.429729006	299.0017	139	11
19	1600	4	0.228	0.200	2.383	186.821	119.448	45.6	0.557761177	299.0017	139	10
20	1600	4	0.238	0.200	2.462	192.676	99.690	31.2	0.540809692	162.7843	77	10

Note: ^{36}Ar through ^{40}Ar are measured beam intensities (mV), corrected for decay for the age calculations, error in age includes J error, all errors 1 sigma
Individual 1.4 mm crystals of volcanic glass, J = 0.000267870 ± 0.1553%
4 amu discrimination = 1.00826 ± 0.40% , 40/39K = 0.0600 ± 34.8%, 36/37Ca = 0.00027787 ± 1.34%, 39/37Ca = 0.00068970 ± 8.84%

Table J.12. Ar-Ar Data and Calculated Ages for 1.4 mm Sanidine from Gibbon River Sample GRWY6 (Analysis #5) (continued)

Crystal	T(°C)	t (min.)	^{36}Ar	^{37}Ar	^{38}Ar	^{39}Ar	^{40}Ar	$\%^{40}Ar^*$	Ca/K	$^{40}Ar^*/^{39}ArK$	Age (ka)	1 σ (ka)
21	1600	4	0.247	0.217	3.062	243.436	136.826	46.2	0.464417442	265.6154	124	10
22	1600	4	0.211	0.178	1.118	85.435	67.356	18.6	1.085642643	145.5464	69	11
23	1600	4	0.162	0.179	1.454	114.140	61.977	32.4	0.817124066	173.5969	82	10
										Mean age =	147.57	50.52
										1st Peak [1] =	80.40	4.55
										[1] Crystals 14, 16, 20, 22 & 23		
										2nd Peak [2] =	144.41	2.85
										[2] Crystals 1, 2, 5, 6, 8, 9, 10, 11, 13, 15, 18, 19 & 21		
										3rd Peak [3] =	220.97	4.63
										[3] Crystals 3, 4, 7, 12 & 17		

Note: ^{36}Ar through ^{40}Ar are measured beam intensities (mV), corrected for decay for the age calculations, error in age includes J error, all errors 1 sigma
Individual 1.4 mm crystals of volcanic glass, J = 0.000267870 ± 0.1553%
4 amu discrimination = 1.00826 ± 0.40% , 40/39K = 0.0600 ± 34.8%, 36/37Ca = 0.00027787 ± 1.34%, 39/37Ca = 0.00068970 ± 8.84%

REFERENCES

Armstrong, R.L., Leeman, W.P., and Malde, H.E., 1975, K-Ar dating, Quaternary and Neogene volcanic rocks of the Snake River Plain, Idaho: American Journal of Science, v. 275, p. 225-251.

Bachmann, O., and Bergantz, G.W., 2004, On the origin of crystal-poor rhyolites: extracted from batholithic crystal mushes: Journal of Petrology, v. 45, p. 1565-1582.

Bachmann, O., and Bergantz, G., 2008, The magma reservoirs that feed supereruptions: Elements, v. 4, p. 17-21.

Bennett, K., 2006, [Monograph] Petrogenesis of Pleistocene basalts in the Norris-Mammoth Corridor, Yellowstone National Park: University of Nevada, Las Vegas Masters Thesis, 124 p.

Bindeman, I.N., Valley, J.W., Wooden, J.L., and Persing, H.M., 2001, Post-caldera volcanism: in situ measurement of U-Pb age and O-isotope ratio in Pleistocene zircons from Yellowstone caldera: Earth and Planetary Science Letters, v. 189, p. 197-206.

Carr, M.J., 2000, IgPet for Windows: Somerset, New Jersey, Terra Softa Inc, version June 12, 2002.

Cathey, H.E., and Nash, B.P., 2004, The Cougar Point Tuff: implications for thermochemical zonation and longevity of high-temperature, large-volume silicic magmas of the Miocene Yellowstone Hotspot: Journal of Petrology, v. 45, p.27-58.

Cebula, G.T., Kunk, M.J., Mehnert, H.H., Naeser, C.W., Obradovich, J.D., and Sutter, J.F., 1986, A potential standard for the ^{40}Ar-^{39}Ar and fission-track dating methods [abs.]: Terra Cognita, v. 6, p. 139-140.

Chang, W.-L., Smith, R.B., Wicks, C., Farrell, J.M., and Puskas, C.M., 2007, Accelerated uplift and magmatic intrusion of the Yellowstone Caldera, 2004 to 2006: Science, v. 318, p. 952-956.

Cherniak, D.J., Watson, E.B., and Wark, D.A., 2007, Ti diffusion in quartz: Chemical Geology, v. 236, p. 65-74.

Christensen, J.N., and DePaolo, D.J., 1993, Time scales of large volume silicic magma systems: Sr isotopic systematic of phenocrysts and glass from the Bishop Tuff, Long Valley, California: Contributions to Mineralogy and Petrology, v. 113, p. 100-114.

Christensen, J.N., and Halliday, A.N., 1996, Rb-Sr ages and Nd isotopic compositions of melt inclusions from the Bishop Tuff and the generation of silicic magma: Earth and Planetary Science Letters, v. 144, p. 547-561.

Christiansen, R.L., 2001, The Quaternary and Pliocene Yellowstone Plateau Volcanic Field of Wyoming, Idaho, and Montana: U.S. Geological Survey Professional Paper 729-G, 145 p.

Christiansen, R.L., and Blank, H.R., 1972, Volcanic stratigraphy of the Quaternary rhyolite plateau in Yellowstone National Park: Geology of Yellowstone National Park, U.S. Geological Survey Professional Paper 729-B, 18 p.

Christiansen, R.L., Foulger, G.R., and Evans, J.R., 2002, Upper-mantle origin of the Yellowstone hotspot: Geological Society of America Bulletin, v. 114, p. 1245-1256.

Christiansen, R.L., Lowenstern, J.B., Smith, R.B., Heasler, H., Morgan, L.A., Nathenson, M., Mastin, L.G., Muffler, L.J.P., and Robinson, J.E., 2007, Preliminary assessment of volcanic and hydrothermal hazards in Yellowstone National Park and vicinity: U.S. Geological Survey Open-File Report 2007-1071, 94 p.

Couch, S., Sparks, R.S.J., and Carroll, M.R., 2001, Mineral disequilibrium in lavas explained by convective self-mixing in open magma chambers: Nature, v. 411, p. 1037-1039.

DePaolo, D.J., 1981, Trace element and isotopic effects of combined wallrock assimilation and fractional crystallization: Earth and Planetary Science Letters, v. 53, p. 189-202.

Ewart, A., and Griffin, W.L., 1994, Application of proton-microprobe data to trace-element partitioning in volcanic-rocks: Chemical Geology, v. 117, p. 251-284.

Fenner, C.N., 1938, Contact relations between rhyolite and basalt on Gardiner River, Yellowstone Park: Geological Society of America Bulletin, v. 49, p. 1441-1483.

Fuhrman, M.L., and Lindsley, D.L., 1988, Ternary-feldspar modeling and thermometry: American Mineralogist, v. 73, p. 201-215.

Funkhouser, J.G., Fisher, D.E., and Bonatti, E., 1968, Excess argon in deep-sea rocks: Earth and Planetary Science Letters, v. 5, p. 95-100.

Gibler, K., 2007, [Monograph] Postcollapse volcanism in the Valles Caldera, New Mexico: the transition from large volume explosive to small volume effusive eruptions: University of Nevada, Las Vegas Masters Thesis, 191 p.

Ginibre, C., Wörner, G., and Kronz, A, 2004, Structure and dynamics of the Laacher See magma chamber (Eifel, Germany) from major and trace element zoning in sanidine: a cathodoluminescence and electron microprobe study: Journal of Petrology, v. 45, p. 2197-2223.

Hall, C.M., and Farrell, J.W., 1995, Laser $^{40}Ar/^{39}Ar$ ages of tephra from Indian Ocean deep-sea sediments: tie points for the astronomical and geomagnetic polarity time scales: Earth and Planetary Science Letters, v. 133, p. 327-338.

Halliday, A.N., Mahood, G.A., Holden, P., Metz, J.M., Dempster, T.J., and Davidson, J.P., 1989, Evidence for long residence times of rhyolitic magma in the Long Valley magmatic system: the isotopic record in precaldera lavas of Glass Mountain: Earth and Planetary Science Letters, v. 94, p. 274-290.

Hamilton, W., 1963, Petrology of rhyolite and basalt, northwestern Yellowstone Plateau, *in* Short Papers in Geology and Hydrology, U.S. Geological Survey Professional Paper 475-C, p. C78-C81.

Hamilton, W., 1965, Geology and petrogenesis of the Island Park caldera of rhyolite and basalt, eastern Idaho: U.S. Geological Survey Professional Paper 504-C, 37 p.

Hayden, L.A., and Watson, E.B., 2007, Rutile saturation in hydrous siliceous melts and its bearsing on Ti-thermometry of quartz and zircon: Earth and Planetary Science Letters, v. 258, p. 561-568.

Hildreth, W., 1979, The Bishop Tuff: evidence for the origin of compositional zonation in silicic magma chambers: Geological Society of America Special Paper 180, p. 43-75.

Hildreth, W., 1981, Gradients in silicic magma chambers: implications for lithospheric magmatism: Journal of Geophysical Research, v. 86, p. 10153-10192.

Hildreth, W., Christiansen, R.L., and O'Neil, J.R., 1984, Catastrophic isotopic modification of rhyolitic magma at times of caldera subsidence, Yellowstone Plateau Volcanic Field: Journal of Geophysical Research, v. 89, p.8339-8369.

Hildreth, W., Halliday, A.N., and Christiansen, R.L., 1991, Isotopic and chemical evidence concerning the genesis and contamination of basaltic and rhyolitic magma beneath the Yellowstone Plateau Volcanic Field: Journal of Petrology, v. 32, p. 63-138.

Honjo, N., Bonnichsen, B., Leeman, W.P., and Stormer, J.C., 1992, Mineralogy and geothermometry of high-temperature rhyolites from the central and western Snake River Plain: Bulletin of Volcanology, v. 54, p. 220-237.

Hooper, P.R., Binger, G.B., and Lees, K.R., 2002, Ages of the Steens and Columbia River flood basalts and their relationship to extension-related calc-alkalic volcanism in eastern Oregon: Geological Society of America Bulletin, v. 114, p.43-50.

Huber, C., Bachmann, O., and Manga, M., 2009, Homogenization processes in silicic magma chambers by stirring and mushification (latent heat buffering): Earth and Planetary Science Letters, v. 283, p. 38-47.

Husen, S., Smith, R.B., and White, G.P., 2004, Evidence for gas and magmatic sources beneath the Yellowstone Volcanic Field from seismic tomographic imaging: Journal of Volcanology and Geothermal Research, v. 131, p. 397-410.

Idleman, B.D., 2006, LabSpec: Lehigh University, Bethlehem, Pennsylvania.

Jaworowski, C., Heasler, H.P., Hardy, C.C., and Queen, L.P, 2006, Control of hydrothermal fluids by natural fractures at Norris Geyser Basin: Yellowstone Science, v. 14, p. 13-23.

Johnson, D.M., Hooper, P.R., and Conrey, R.M., 1999, XRF analysis of rocks and minerals for major and trace elements on a single low dilution Li-tetraborate fused bead: Advances in X-ray Analysis, v. 41, p. 843-867.

Jurek, K., and Gedeon, O., 2003, Analysis of alkali-silicate glasses by electron probe analysis: Spectrochimica Acta Part B, v. 58, p. 741-744.

Kharaka, Y.K., Sorey, M.L., and Thordsen, J.J., 2000, Large-scale hydrothermal fluid discharges in the Norris-Mammoth Corridor, Yellowstone National Park, USA: Journal of Geochemical Exploration, v. 69-70, p. 201-205.

Knaack, C., Cornelius, S.B., and Hooper, P.R., 1994, Trace element analyses of rocks and minerals by ICP-MS: Washington State University GeoAnalytical Lab Technical Notes, http://www.sees.wsu.edu/Geolab/index.html.

LaBas, M.J., LeMaitre, R.W., Streckeisen, A., and Zanettin, B., 1986, A chemical classification of volcanic rocks based on the total alkali-silica diagram: Journal of Petrology, v. 27, p.745-750.

Lanphere, M.A., Champion, D.E., Christiansen, R.L., Izett, G.A., and Obradovich, J.D., 2002, Revised ages for tuffs of the Yellowstone Plateau Volcanic Field: assignment of the Huckleberry Ridge Tuff to a new geomagnetic polarity event: Geological Society of America Bulletin, v. 114, p. 559-568.

Lipman, P.W., 1965, Chemical comparison of glassy and crystalline volcanic rocks: Geological Society of America Bulletin, v. 1201-D, 24 p.

Lipman, P.W., 1984, The roots of ash flow calderas in western North America: windows into the tops of granitic batholiths: Journal of Geophysical Research, v. 89, p. 8801-8841.

Lowry, A.R., Ribe, N.M., and Smith, R.B., 2000, Dynamic elevation of the Cordillera, western United States: Journal of Geophysical Research, v. 105, p. 23,371-23,390.

Ludwig, K.R., 2003, Isoplot 3.00: a geochronological toolkit for Microsoft *Excel*: Berkeley Geochronology Center Special Publication 4, 73 p.

Mahood, G.A., and Hildreth, E.W., 1983, Large partition coefficients for trace elements in high-silica rhyolites: Geochimica et Cosmochimica Acta, v. 47, p. 11-30.

McDougall, I., and Harrison, T.M., 1999, Geochronology and Thermochronology by the $^{40}Ar/^{39}Ar$ Method, 2nd edition: New York, Oxford University Press, 269 p.

Miyashiro, A., 1974, Volcanic rock series in island arcs and active continental margins: American Journal of Science, v. 274, p. 321-355.

Morgan, L.E., Renne, P.R., and Watkins, J.M., 2007, $^{40}Ar/^{39}Ar$ dating of volcanic glass: American Geophysical Union, Fall Meeting 2007, Abstract V31G-05.

Morgan, W.J., 1972, Plate motions and deep Mantle convection: *in* Geological Society of America Memoir 132, p. 7-22.

Nastanski, N.M., 2005, [Monograph] Petrogenesis of extracaldera rhyolites at Yellowstone Volcanic Field: evidence for an evolving silicic magma system north of Yellowstone Caldera: University of Nevada, Las Vegas Masters Thesis, 192 p.

Nastanski, N.M, and Spell, T.L., 2004a, Do the young extracaldera rhyolites north of Yellowstone caldera mark the beginnings of a 4th volcanic cycle in the Yellowstone Plateau Volcanic Field?: Geological Society of America Abstracts with Programs, v. 36, n. 4, p. 11.

Nastanski, N.M, and Spell, T.L., 2004b, Extracaldera rhyolites north of the Yellowstone Plateau Volcanic Field caldera complex: an evolving silicic magma system and site of future large volume eruptions?: Geological Society of America Abstracts with Programs, v. 36, n. 5, p. 431.

Noble, D.C., 1967, Sodium, potassium, and ferrous iron contents of some secondarily hydrated natural silicic glasses: The American Mineralogist, v. 52, p. 280-286.

Obradovich, J.D., 1992, Geochronology of the late Cenozoic volcanism of Yellowstone National Park and adjoining areas, Wyoming and Idaho: U.S. Geological Survey Open-File Report 92-408, 45 p.

Paces, J.B., and Miller, J.D., 1993, Precise U-Pb ages of Duluth Complex and related mafic intrusions, Northeastern Minnesota: geochronological insights to physical, petrogenetic, paleomagnetic, and techonomagmatic processes associated with the 1.1 Ga midcontinent rift system: Journal of Geophysical Research, v. 98, p. 13,997-14,013.

Pierce, K.L., and Morgan, L.A., 2009, Is the track of the Yellowstone hotspot driven by a deep mantle plume? – Review of volcanism, faulting, and uplift in light of new data: Journal of Volcanology and Geothermal Research, v. 188, p. 1-25.

Reid, M.R., and Coath, C.D., 2000, In situ U-Pb ages of zircons from the Bishop Tuff: no evidence for long crystal residence times: Geology, v. 28, p. 443-446.

Reid, M.R., Coath, C.D., Harrison, T.M., and McKeegan, K.D., 1997, Prolonged residence times for the youngest rhyolite associated with Long Valley Caldera: $^{230}Th/^{238}U$ ion microprobe dating of young zircons: Earth and Planetary Science Letters, v. 150, p. 27-39.

Schmitt, A.K., Stockli, D.F., and Hausback, B.P., 2006, Eruption and magma crystallization ages of Las Tres Virgenes (Baja California) constrained by combined $^{230}Th/^{238}U$ and (U-Th)/He dating of zircon: Journal of Volcanology and Geothermal Research, v. 158, p. 281-295.

Simon, J.I., and Reid, M.R., 2005, The pace of rhyolite differentiation and storage in an "archetypical" silicic magma system, Long Valley, California: Earth and Planetary Science Letters, v. 235, p. 123-140.

Smith, E.I., and Bennett, K., 2006, Panther Creek Volcano: Yellowstone Science, v. 14, p. 5-12.

Smith, R.B., Jordan, M., Steinberger, B., Puskas, C.M., Farrell, J., Waite, G.P., Husen, S., Chang, W.-l., and O'Connell, R., 2009, Geodynamics of the Yellowstone hotspot and mantle plume: seismic and GPS imaging, kinematics, and mantle flow: Journal of Volcanology and Geothermal Research, v. 188, p. 26-56.

Spell, T.L., and Nastanski, N.M., 2004, Ion-microprobe $^{206}Pb/^{238}U$ and $^{230}Th/^{238}U$ zircon ages for extracaldera rhyolites at Yellowstone: constraints on magma residence times and evolution: Geological Society of America Abstracts with Programs, v. 36, n. 5, p. 431.

Spell, T.L., Smith, E.I., Nastanski, N.M., and Bennett, K., 2004, Establishment and evolution of a new silicic magma system north of Yellowstone Caldera: geochronology, geochemistry and petrographic relationships of extracaldera basalts and rhyolites in the Norris-Mammoth Corridor: American Geophysical Union, Fall Meeting 2004, Abstract V52B-08.

Stix, J., and Gorton, M.P., 1990, Variations in trace-element partition-coefficients in sanidine in the Cerro Toledo Rhyolite, Jemez Mountains, New-Mexico - Effects of composition, temperature, and volatiles: Geochimica et Cosmochimica Acta, v. 54, p. 2697-2708.

Streck, M.J., and Grunder, A.L., 1997, Compositional gradients and gaps in high-silica rhyolites of the Rattlesnake Tuff, Oregon: Journal of Petrology, v. 38, p. 133-163.

Sun, S.-s., 1980, Lead isotopic study of young volcanic rocks from mid-ocean ridges, oceanic ridges and island arcs: Philosophical Transactions of the Royal Society of London Series A, v. 297, p. 409-445.

Sun, S.-s., and McDonough, W.F., 1989, Chemical and isotopic systematics of oceanic basalts: implications for mantle composition and processes, *in* Saunders, A.D., and Norry, M.J., eds., Magmatism in the Ocean Basins: Geological Society of London Special Publication 42, p. 313-345.

Tetley, N., McDougall, I., and Heydegger, H.R., 1980, Thermal neutron interferences in the $^{40}Ar/^{39}Ar$ dating technique: Journal of Geophysical Research, v. 85, p. 7201-7205.

U.S.G.S., 1986a, Norris Junction Quadrangle, Wyoming: U.S. Geological Survey 7.5 Minute Series (Topographic) Map 44110-F6-TF-024, scale 1:24 000, 1 sheet.

U.S.G.S., 1986b, Obsidian Cliff Quadrangle, Wyoming – Park Co.: U.S. Geological Survey 7.5 Minute Series (Topographic) Map 44110-G6-TF-024, scale 1:24 000, 1 sheet.

Vazquez, J.A., and Reid, M.R., 2002, Time scales of magma storage and differentiation of voluminous high-silica rhyolites at Yellowstone caldera, Wyoming: Contributions to Mineralogy and Petrology, v. 144, p. 274-285.

Vazquez, J.A., Kyriazis, S.F., Reid, M.R., Sehler, R.C., and Ramos, F.C., 2009, Thermochemical evolution of young rhyolites at Yellowstone: evidence for a cooling but periodically replenished postcaldera magma reservoir: Journal of Volcanology and Geothermal Research, v. 188, p. 186-196.

Wark, D.A., Hildreth, W., Spear, F.S., Cherniak, D.J., and Watson, E.B., 2007, Pre-eruption recharge of the Bishop magma system: Geology, v. 35, p. 235-238.

Wark, D.A., and Watson, E.B., 2006, TitaniQ: a titanium-in-quartz geothermometer: Contributions to Mineralogy and Petrology, v. 152, p. 743-754.

Wen, S., and Nekvasil, H., 1994, SOLVCALC: An interactive graphics program package for calculating the ternary feldspar solvus and for two-feldspar geothermometry: Computers & Geosciences, v. 20, p. 1025-1040.

Wendt, I., and Carl, C., 1991, The statistical distribution of the mean squared weighted deviation: Chemical Geology (Isotope Geoscience Section), v. 86, p. 275-285.

Wicks, C.W., Thatcher, W., Dzurisin, D., and Svarc, J., 2006, Uplift, thermal unrest and magma intrusion at Yellowstone caldera: Nature, v. 440, p. 72-75.

Wolff, J.A., and Gardner, J.N., 1995, Is the Valles caldera entering a new cycle of activity?: Geology, v. 23, p. 411-414.

York, D., 1969, Least squares fitting of a straight line with correlated errors: Earth and Planetary Science Letters, v. 5, p. 320-324.

VITA

Graduate College
University of Nevada, Las Vegas

Kathleen Marie Wooton

Degrees:
Bachelor of Science, Geology, 2005
The College of William & Mary

Publications:

Forte, A.M., **Wooton, K.M.**, Hasty, B.A., and Bailey, C.M., 2005, Bedrock geology of the Swift Run Gap 7.5' quadrangle, Blue Ridge province, Virginia: Geological Society of America Abstracts with Programs, v.37, n.2, p.34, 11-8.

Wooton, K.M., 2005, The nature and timing of deformation in the Blue Ridge province, Greene County, Virginia: Geological Society of America Abstracts with Programs, v.37, n.2, p.36, 13-8.

Wooton, K.M., 2005, [Monograph] The nature and timing of deformation in the Blue Ridge province, Greene County, Virginia: College of William & Mary Bachelors Thesis, 66 p.

Wooton, K.M., and Spell, T.L., 2007, Latest Yellowstone volcanism: Roaring Mountain rhyolites, Yellowstone Volcanic Field, Wyoming: Geological Society of America Abstracts with Programs, v.39, n.6, p.393, 143-46.

Spell, T.L., **Wooton, K.**, Nastanski, N.M., and Smith, E.I., 2008, The role of basalt in eruption of Quaternary rhyolites north of the Yellowstone Caldera: Geological Society of America Abstracts with Programs, v.40, n.1, p.62, 14-2.

Thesis Title: Age and Petrogenesis of the Roaring Mountain Rhyolites, Yellowstone Volcanic Field, Wyoming

Thesis Examination Committee:
Chairperson, Dr. Terry L. Spell, Ph.D.
Committee Member, Dr. Eugene I. Smith, Ph.D.
Committee Member, Dr. Michael L. Wells, Ph.D.
Graduate Faculty Representative, Dr. Stephen H. Lepp, Ph.D.